ANTENNAS FOR GLOBAL NAVIGATION SATELLITE SYSTEMS

ANTENNAS FOR GLOBAL NAVIGATION SATELLITE SYSTEMS

Xiaodong Chen
Queen Mary University of London, UK

Clive G. Parini
Queen Mary University of London, UK

Brian Collins
Antenova Ltd, UK

Yuan Yao
Beijing University of Posts and Telecommunications, China

Masood Ur Rehman
Queen Mary University of London, UK

A John Wiley & Sons, Ltd., Publication

This edition first published 2012

Registered office
John Wiley & Sons Ltd, The Atrium, Southern Gate, Chichester, West Sussex, PO19 8SQ, United Kingdom

Library of Congress Cataloging-in-Publication Data

Antennas for global navigation satellite systems / Xiaodong Chen ... [et al.].
p. cm.
Includes bibliographical references and index.
ISBN 978-1-119-99367-4 (cloth)
1. Antennas (Electronics) 2. Global Positioning System. 3. Space vehicles–Radio antennas.
4. Radio wave propagation. 5. Mobile communication systems. I. Chen, Xiaodong.
TK7871.6.A532 2012
621.382–dc23

2011043939

A catalogue record for this book is available from the British Library.

ISBN: 9781119993674

Set in 10.5/13pt Times by Laserwords Private Limited, Chennai, India

Contents

Preface

The global navigation satellite system (GNSS) is becoming yet another pillar technology in today's society along with the Internet and mobile communications. GNSS offers a range of services, such as navigation, positioning, public safety and surveillance, geographic surveys, time standards, mapping, and weather and atmospheric information. The usage of GNSS applications has become nearly ubiquitous from the ever-growing demand of navigation facilities made available in portable personal navigation devices (PNDs). Sales of mobile devices including smart phones with integrated GNSS are expected to grow from 109 million units in 2006 to 444 million units in 2012, and this sector of industry is second only to the mobile phone industry. The navigation industry is predicted to earn a gross total of $130 billion in 2014. The current developments and expected future growth of GNSS usage demand the availability of more sophisticated terminal antennas than those previously deployed.

The antenna is one of most important elements on a GNSS device. GNSS antennas are becoming more complex every day due to the integration of different GNSS services on one platform, miniaturisation of these devices and performance degradations caused by the user and the local environment. These factors should be thoroughly considered and proper solutions sought in order to develop efficient navigation devices. The authors have been active in this research area over the last decade and are aware that a large amount of information on GNSS antenna research is scattered in the literature. There is thus a need for a coherent text to address this topic, and this book intends to fill this knowledge gap in GNSS antenna technology. The book focuses on both the theory and practical designs of GNSS antennas. Various aspects of GNSS antennas, including the fundamentals of GNSS and circularly polarised antennas, design approaches for the GNSS terminal and satellite antennas, performance enhancement techniques used for such antennas, and the effects of a user's presence and the surrounding environment on these antennas, are discussed

in the book. Many challenging issues of GNSS antenna design are addressed giving solutions from technology and application points of view.

The book is divided into eight chapters.

Chapter 1 introduces the concept of GNSS by charting its history starting from DECCA land-based navigation in the Second World War to the latest versions being implemented by the USA (GPS), Europe (GLONASS and Galileo) and China (Compass). The fundamental principles of time delay navigation are addressed and the operation of the US NAVSTAR GPS is described. The enhanced applications of the GPS are addressed including its use as a time reference and as an accurate survey tool in its differential form.

Chapter 2 describes radio wave propagation between the GNSS satellite and the ground receiver and the rationale for selecting circularly polarised (CP) waves. It also introduces the relevant propagation issues, such as multipath interference, RF interference, atmospheric effects, etc. The fundamental issues in GNSS antenna design are highlighted by presenting the basic approaches for designing a CP antenna.

Chapter 3 covers the requirements for spacecraft GNSS antennas illustrating the descriptions of typical deployed systems for both NAVSTAR GPS and Galileo. The various special performance requirements and tests imposed on spacecraft antennas, such as passive intermodulation (PIM) testing and multipactor effects, are also discussed.

Chapter 4 deals with the specifications, technical challenges, design methodology and practical designs of portable terminal GNSS antennas. It introduces various intrinsic types of terminal antennas deployed in current GNSSs, including microstrip, spiral, helical and ceramic antennas.

Chapter 5 is dedicated to multimode antennas for an integrated GNSS receiver. The chapter presents three kinds of multimode GNSS antennas, namely dual-band, triple-band and wideband antennas. Practical and novel antenna designs, such as multi-layer microstrip antennas and couple feed slot antennas, are discussed. It also covers high-precision terminal antennas for the differential GPS system, including phase centre determination and stability.

Chapter 6 discusses the effects of the multipath environment on the performance of GNSS antennas in mobile terminals. It highlights the importance of statistical models defining the environmental factors in the evaluation of GNSS antenna performance and proposes such a model. It then presents a detailed analysis of the performance of various types of mobile terminal GNSS antennas in real working scenarios using the proposed model. Finally, it describes the performance enhancement of the terminal antennas in difficult environments by employing the techniques of beamforming, antenna diversity, A-GPS and ESTI standardised reradiating.

Chapter 7 deals with the effects of the human user's presence on the GNSS antennas, presenting details of the dependency of antenna performance on varying antenna–body separations, different on-body antenna placements and varying body postures. It also considers the effects of homogeneous and inhomogeneous human body models in the vicinity of the GNSS antennas. Finally, it discusses the performance of these antennas in the whole multipath environment operating near the human body, using a statistical modelling approach and considering various on-body scenarios.

Chapter 8 describes the limitations of both antenna size and shape that are imposed when GNSS functions are to be added to small devices such as mobile handsets and personal trackers. It is shown how the radiation patterns and polarisation properties of the antenna can be radically changed by factors such as the positioning of the antenna on the platform. The presence of a highly sensitive receiver system imposes severe constraints on the permitted levels of noise that may be generated by other devices on the platform without impairing the sensitivity of the GPS receiver. The chapter gives the steps which must be taken to reduce these to an acceptable level. The case studies cover a range of mobile terminal antennas, such as small backfire helices, CP patches and various microstrip antennas.

This is the first dedicated book to give such a broad and in-depth treatment of GNSS antennas. The organisation of the book makes it a valuable practical guide for antenna designers who need to apply their skills to GNSS applications, as well as an introductory text for researchers and students who are less familiar with the topic.

1

Fundamentals of GNSS

1.1 History of GNSS

GNSS is a natural development of localised ground-based systems such as the DECCA Navigator and LORAN, early versions of which were used in the Second World War. The first satellite systems were developed by the US military in trial projects such as *Transit, Timation* and then *NAVSTAR*, these offering the basic technology that is used today. The first NAVSTAR was launched in 1989; the 24th satellite was launched in 1994 with full operational capability being declared in April 1995. NAVSTAR offered both a civilian and (improved accuracy) military service and this continues to this day. The system has been continually developed, with more satellites offering more frequencies and improved accuracy (see Section 1.3).

The Soviet Union began a similar development in 1976, with GLONASS (GLObal NAvigation Satellite System) achieving a fully operational constellation of 24 satellites by 1995 [1]. GLONASS orbits the Earth, in three orbital planes, at an altitude of 19 100 km, compared with 20 183 km for NAVSTAR. Following completion, GLONASS fell into disrepair with the collapse of the Soviet economy, but was revived in 2003, with Russia committed to restoring the system. In 2010 it achieved full coverage of the Russian territory with a 20-satellite constellation, aiming for global coverage in 2012.

The European Union and European Space Agency *Galileo* system consists of 26 satellites positioned in three circular medium Earth orbit (MEO) planes at 23 222 km altitude. This is a global system using dual frequencies, which aims to offer resolution down to 1 m and be fully operational by 2014. Currently (end 2010) budgetary issues mean that by 2014 only 18 satellites will be operational (60% capacity).

Antennas for Global Navigation Satellite Systems, First Edition.
Xiaodong Chen, Clive G. Parini, Brian Collins, Yuan Yao and Masood Ur Rehman.

Compass is a project by China to develop an independent regional and global navigation system, by means of a constellation of 5 geostationary orbit (GEO) satellites and 30 MEO satellites at an altitude of 21 150 km. It is planned to offer services to customers in the Asia-Pacific region by 2012 and a global system by 2020.

QZSS (Quasi-Zenith Satellite System) is a Japanese regional proposal aimed at providing at least one satellite that can be observed at near zenith over Japan at any given time. The system uses three satellites in elliptical and inclined geostationary orbits (altitude 42 164 km), 120° apart and passing over the same ground track. It aims to work in combination with GPS and Galileo to improve services in city centres (so called *urban canyon*s) as well as mountainous areas. Another aim is for a 1.6 m position accuracy for 95% availability, with full operational status expected by 2013.

It is likely that many of these systems will offer the user interoperability leading to improved position accuracy in the future. It has already been shown that a potential improvement in performance by combining the GPS and Galileo navigation systems comes from a better satellite constellation compared with each system alone [2]. This combined satellite constellation results in a lower dilution of precision value (see Section 1.3), which leads to a better position estimate. A summary of the various systems undertaken during the first quarter of 2011 is shown in Table 1.1.

1.2 Basic Principles of GNSS

1.2.1 Time-Based Radio Navigation

The principle of GNSSs is the accurate measurement of distance from the receiver of each of a number (minimum of four) of satellites that transmit accurately timed signals as well as other coded data giving the satellites' position. The distance between the user and the satellite is calculated by knowing the time of transmission of the signal from the satellite and the time of reception at the receiver, and the fact that the signal propagates at the speed of light. From this a 3D ranging system based on knowledge of the precise position of the satellites in space can be developed. To understand the principles, the simple offshore maritime 2D system shown in Figure 1.1 can be considered. Imagine that transmitter 1 is able to transmit continually a message that says 'on the next pulse the time from transmitter 1 is . . . ', this time being sourced from a highly accurate (atomic) clock. At the mobile receiver (a ship in this example) this signal is received with a time delay ΔT_1; the distance D_1 from the transmitter can then be determined based on the signal propagating at the

Table 1.1 Summary of GNSS systems undertaken during Q1 2011

GNSS	GPS/NAVSTAR	GLONASS	Galileo	Compass	QZSS
Operational	Now	Now	2014 (for 14 satellites)	2012 regional 2020 global	2013
Constellation	24 MEO	24 MEO	27 MEO	5 GEO + 30 MEO	3 highly inclined elliptical orbits
Orbital altitude (km)	20 183	19 100	23 222	21 150 + GEO	42 164
Coverage	Global	Regional (Russia) then global	Global	Regional (Asia-Pacific) then global	Regional (East Asia and Oceania), augmentation with GPS
Position accuracy (civilian)	7.1 m 95%	7.5 m 95%	4 m (dual freq.)	10 m	1.6 m 95%
User Frequency bands (MHz)	L1 = 1575.420 L2 = 1227.6 L5 = 1176.45	G1 = 1602.0 G2 = 1246.0 G3 = 1204.704	E1 = 1575.42 E6 = 1278.75 E5 = 1191.795 E5a = 1176.45 E5b = 1207.14	B1 = 1561.098 B2 = 1207.14 B3 = 1268.52	L1 L2 L5 LEX = 1278.75 (for Differential GPS)
User coding and modulation	CDMA BPSK	FDMA BPSK + CDMA on GLONASS-K1	CDMA BOC and BPSK	QPSK and BOC	CDMA BPSK, BOC
Services and bandwidth	SPS on L1 with 2.046 MHz BW PPS on L1 & L2 with 20.46 MHz BW L2C (by 2016) L5 (by 2018) 20.46 MHz BW		Open on E1 with 24.552 MHz BW Open on E5a + E5b both 20.46 MHz BW	Open on B1 with 4.092 MHz BW Open on B2 with 24 MHz BW	L1 24 MHz BW, L2 24 MHz BW, L5 24.9 MHz BW

CDMA: Code Division Multiple Access; FDMA: Frequency Division Multiple Access; BPSK: Binary Phase Shift Keying; QPSK: Quadrature Phase Shift Keying; BOC: Binary Offset Carrier; SPS: Standard Positioning Service; PPS: Precision Positioning Service.

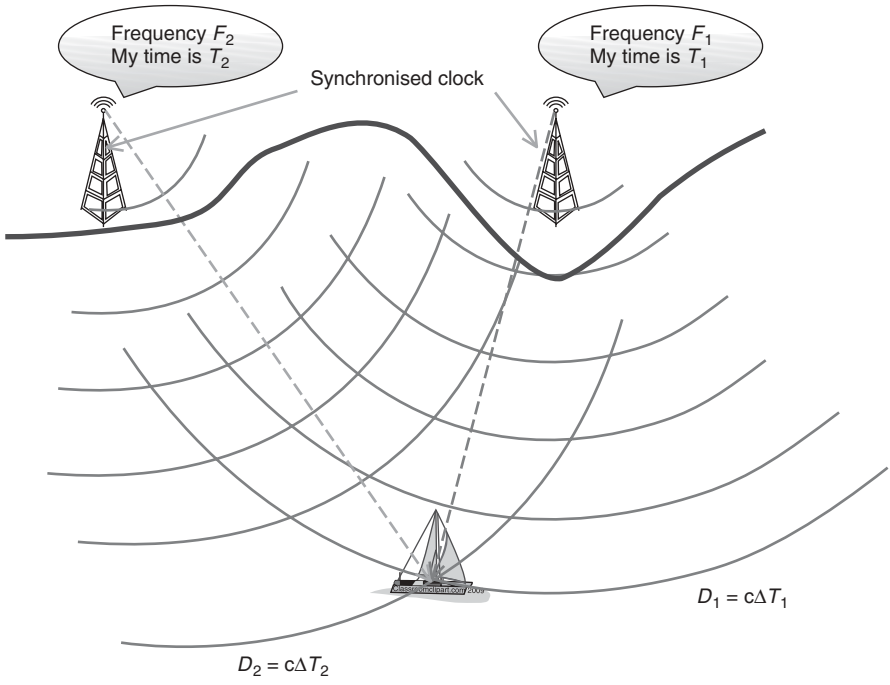

Figure 1.1 Simple 2D localised ship-to-shore location system.

speed of light c, from $D_1 = c\Delta T_1$. The same process can be repeated for transmitter 2, yielding a distance D_2. If the mobile user then has a chart showing the accurate location of the shore-based transmitter 1 and transmitter 2, the user can construct the arcs of constant distance D_1 and D_2 and hence find his or her location. For this system to be accurate all three clocks (at the two transmitters and on board the ship) must be synchronised. In practice it may not be that difficult to synchronise the two land-based transmitters but the level of synchronisation of the ship-based clock will fundamentally determine the level of position accuracy achievable. If the ship's clock is in error by $\pm 1\,\mu s$ then the position error will be $\pm 300\,m$, since light travels 300 m in a microsecond. This is the fundamental problem with this simplistic system which can be effectively thought of as a problem of *two equations with two unknowns* (the unknowns being the ship's u_x, u_y location). However, in reality we have a third unknown, which is the ship's clock offset with respect to the synchronised land-based transmitters' clock. This can be overcome by adding a third transmitter to the system, providing the ability to add a third equation determining the u_x, u_y location of the ship and so giving a three-equation,

three-unknown solvable system of equations. We will explore this in detail later when we consider the full 3D location problem that is GNSS. As a local coastal navigation system this is practical since all ships will be south of the transmitters shown in Figure 1.1.

At this point it is worth noting the advantages of this system, the key one being that the ship requires no active participation in the system; it is only required to listen to the transmissions to determine its position. Thus, there is no limit on the number of system users and, because they are receive only, they will be relatively low cost for the ship owner.

1.2.2 A 3D Time-Based Navigation System

We can extend this basic concept of time-delay-based navigation to determine a user's position in three dimensions by moving our transmitters into space and forming a constellation surrounding the Earth's surface, Figure 1.2. In order

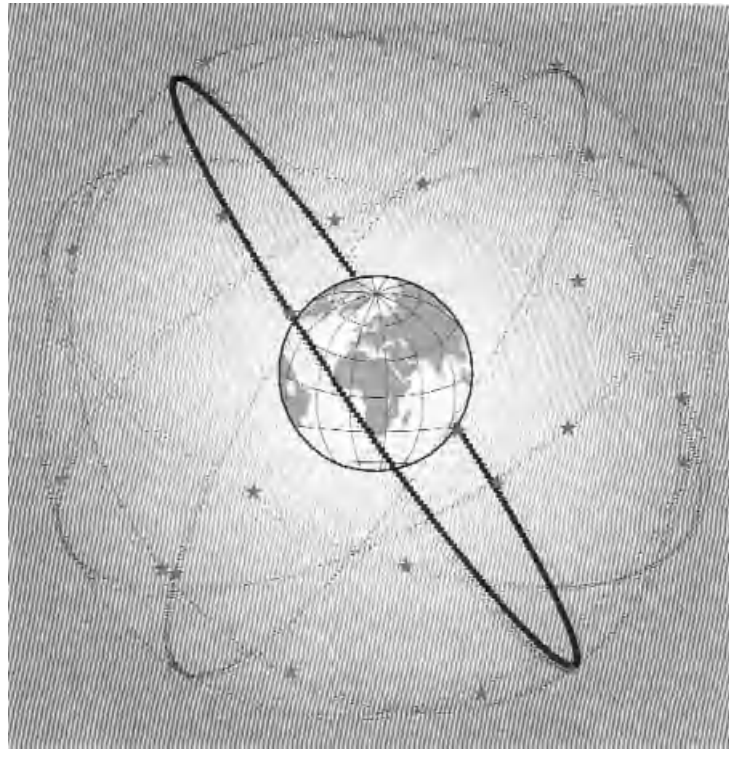

Figure 1.2 Satellite constellation [5].

for such a system to operate the user would be required to see (i.e. have a direct line of sight to) at least four satellites at any one time. This time *four* transmitters are required as there are now four unknowns in the four equations that determine the distance from a satellite to a user, these being the user's coordinates (u_x, u_y, u_z) and the user's clock offset ΔT with respect to *GPS time*. The concept of GPS time is that all the clocks on board all the satellites are reading exactly the same time. In practice they use one (or more) atomic clocks, but by employing a series of ground-based monitoring stations each satellite clock can be checked and so any offset from GPS time can be transmitted to the satellite and passed on to the user requiring a position fix.

The (x, y, z) location of each satellite used in a position fix calculation must be accurately known, and although Kepler's laws of motion do a very good job in predicting the satellite's location, use of the above-mentioned monitoring stations can offer minor position corrections. These monitoring stations (whose accurate position is known) can be used to determine accurately the satellite's orbital location and thus send to each satellite its orbital position corrections, which are then reported to the users via the GPS transmitted signal to all users. So each satellite would effectively transmit 'on the next pulse the time is ..., my clock offset from GPS time is ..., my orbital position correction is ...'.

A sketch of a four-satellite position location is shown in Figure 1.3 and the corresponding equation for the raw distance R_1 between the user terminal and satellite 1 is

$$R_1 = c(\Delta t_1 + \Delta T - \tau_1) \tag{1.1}$$

where Δt_1 is the true propagation delay from satellite 1 to the user terminal, τ_1 is the GPS time correction for satellite 1, and ΔT is the unknown user terminal clock offset from GPS time. Let the corrected range to remove the satellite 1 clock error be R_1'. Then

$$R_1' = c(\Delta t_1 + \Delta T) \tag{1.2}$$

The true distance between satellite 1 and the user terminal is then

$$C\Delta t_1 = R_1' - c\Delta t = R_1' - C_B \tag{1.3}$$

where C_B is fixed for a given user terminal at a given measurement time. In Cartesian coordinates the equation for the distance between the true satellite 1 position (x_1, y_1, z_1), which has been corrected at the user terminal

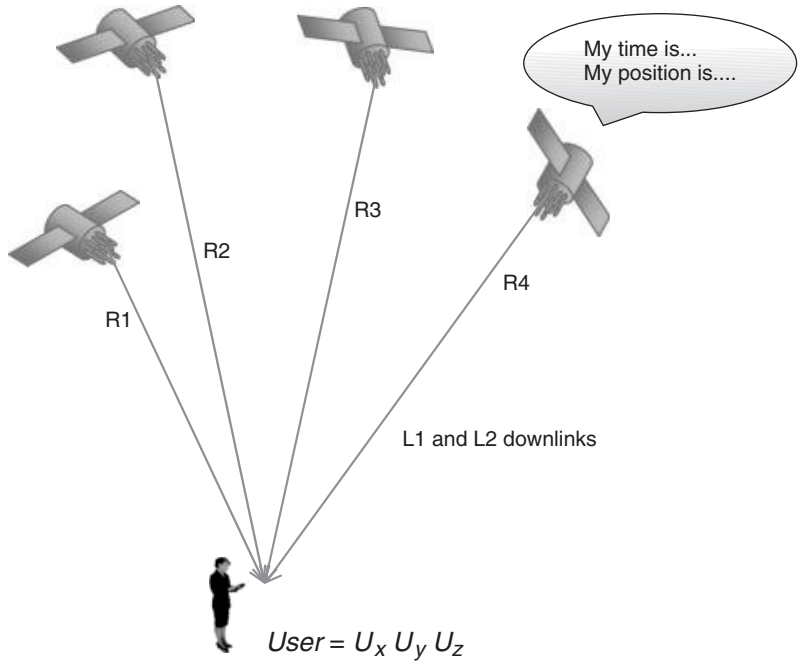

Figure 1.3 Sketch of four-satellite fix.

by the transmitted orbital correction data, and the user terminal position (u_x, u_y, u_z) is

$$(x_1 - u_x)^2 + (y_1 - u_y)^2 + (z_1 - u_z)^2 = (R_1' - C_B)^2 \tag{1.4}$$

The corresponding equations for the remaining three satellites are

$$\begin{aligned}(x_2 - u_x)^2 + (y_2 - u_y)^2 + (z_2 - u_z)^2 &= (R_2' - C_B)^2\\ (x_3 - u_x)^2 + (y_3 - u_y)^2 + (z_3 - u_z)^2 &= (R_3' - C_B)^2\\ (x_4 - u_x)^2 + (y_4 - u_y)^2 + (z_4 - u_z)^2 &= (R_4' - C_B)^2\end{aligned} \tag{1.5}$$

Equations 1.4 and 1.5 constitute four equations in four unknowns (u_x, u_y, u_z, C_B) and so enable the user terminal location to be determined.

In a similar way the user terminal's velocity can be determined by measuring the Doppler shift of the received carrier frequency of the signal from each of the four satellites. As in the case of time, an error due to the offset of the

receiver oscillator frequency with GPS time can be removed using a four-satellite measurement. A set of equations with the three velocity components plus this offset again gives four equations with four unknowns (V_x, V_y, V_z and the user oscillator offset).

1.3 Operation of GPS

In this section we will take the basic concept described above and describe how a practical system (NAVSTAR GPS) can be implemented. As explained above, the user must be able to see four satellites simultaneously to get a fix, so the concept of a constellation of MEO satellites (altitude 20 183 km) with 12 h circular orbits inclined at 55° to the equator in six orbital planes was conceived [3]. With four satellites per orbital plane the operational constellation is 24 satellites (Figure 1.2); in 2010 the constellation had risen to 32 satellites. Figure 1.4 shows the satellite trajectories as viewed from the Earth for two orbits (24 hours) with one satellite's orbit shown by the heavy line for clarity.

This pattern repeats every day, although a given satellite in a given place is seen four minutes earlier each day. Assuming an open (non-urban) environment, the four 'seen' satellites need to be above a 15° elevation angle in order to avoid problems with multipath propagation. As we can see from Figure 1.5, this can be achieved at all points on the Earth's surface, even at the poles.

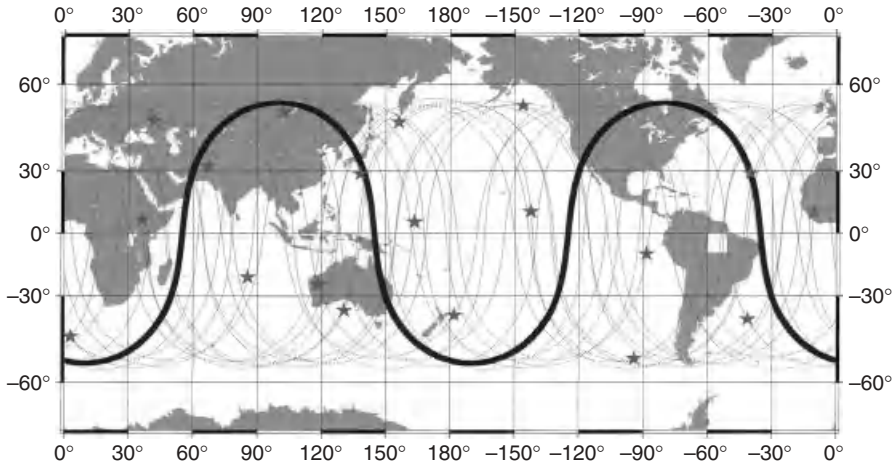

Figure 1.4 Satellite trajectories as viewed from Earth for two orbits (24 hours) with one satellite's orbit emphasised for clarity [5].

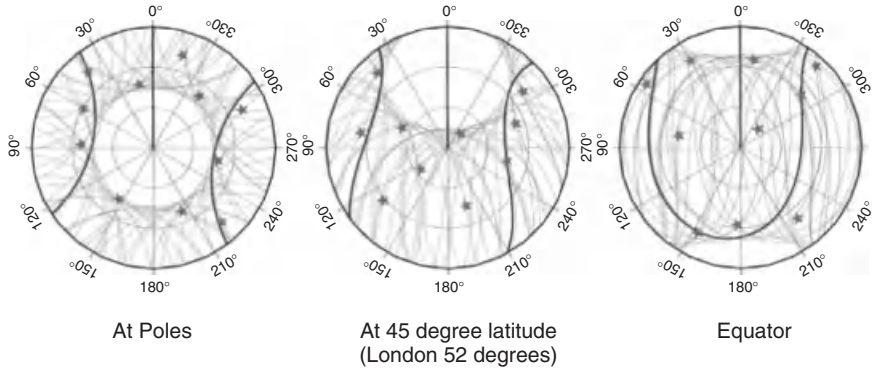

Figure 1.5 View of constellation from a user [5].

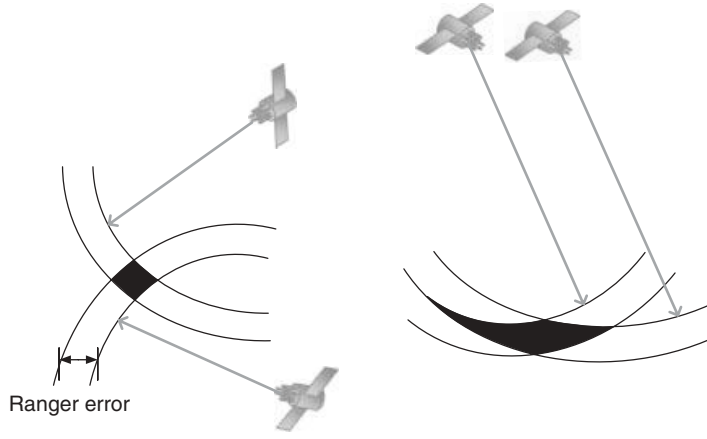

Figure 1.6 A 2D representation of range error as a function of satellite relative position (Shaded area represents region of position uncertainty).

Careful choice of location of the four satellites used for a fix can help accuracy, as can be simply illustrated in the 2D navigation system shown in Figure 1.6 and termed *dilution of precision*. The concept is of course extendable to the full 3D constellation of GPS.

GPS time is maintained on board the satellites by using a caesium and pair of rubidium atomic clocks providing an accuracy of better than 1 ns, which is improved by passing onto the user the clock adjustments determined by

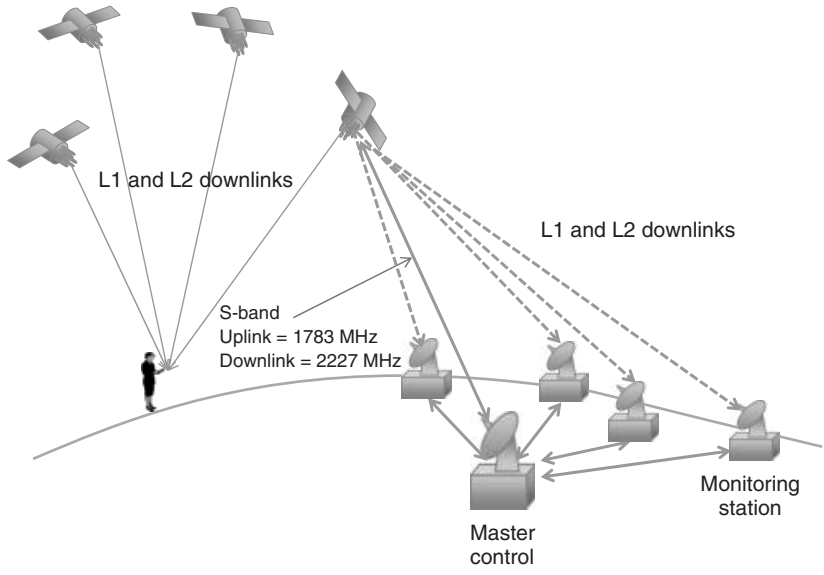

Figure 1.7 Ground control segment monitoring one satellite in the constellation.

the ground control segment of the GPS system. An overview of the ground control segment is shown in Figure 1.7 and consists of a master control station (MCS) and a number of remote monitoring stations distributed around the globe. These monitoring stations passively track the GPS satellites as they pass overhead, making accurate range measurements and forwarding this data to the MCS via other satellite and terrestrial communication links. The MCS then processes the data for each satellite in the constellation in order to provide: (i) clock corrections; (ii) corrections to the satellite's predicted position in space (ephemeris)[1] (i.e. its deviation from Kepler's modified laws), typically valid for four hours; (iii) almanac data that tells the receiver which satellites should be visible at a given time in the future and valid for up to 180 days. This data is combined with the normal TT&C (Telemetry Tracking and Command) data and uplinked to each satellite via the TT&C communications link, which for the GPS satellites operates in the S band (2227 MHz downlink, 1783 MHz uplink). The uplink ground stations are located at a number of the remote monitoring stations.

[1] A table of values that gives the positions of astronomical objects in the sky at a given time.

The user communications downlink (Figure 1.7) is transmitted using RHCP (Right Hand Circular Polarisation) and has two operating modes:

1. Standard Positioning Service (SPS) – unrestricted access using the band L1 = 1575.42 MHz.
2. Precision Positioning Service (PPS) – DoD (US Department of Defense) authorised users only using both bands L1 = 1575.42 MHz and L2 = 1227.6 MHz.

Both L1 and L2 use CDMA (Code Division Multiple Access) as the multiplexing process and BPSK (Binary Phase Shift Keying) as the modulation method. As in all CDMA systems, all the satellites transmit at the same frequency but each uses a different and unique 'gold code' as the spreading code for this spread-spectrum form of communication. The basic CDMA process is that of multiplying each bit of information to be sent by a unique pseudo-random 'gold code' (called the spreading code). If the information bit is logic 1 the gold code is sent; if logic 0, the inverse of the gold code is sent. The encoded information is then sent on a microwave carrier using a suitable form of modulation (in this case BPSK). To decode a signal from a given satellite the receiver simply needs to load the particular gold code into its correlation receiver (Appendix A shows the recovery process for a simplistic case of a 4 bit gold code). For SPS the spreading code is 1023 bits long and is called the C/A (Coarse/Acquisition) code with a chip rate of 1.023 Mbits/s. The spectrum of this modulated code is 1.023 MHz either side of the L1 carrier, so the receiver and antenna require a bandwidth of 2.046 MHz.

Details of the content of the C/A code are shown in Figure 1.8, where the 1023 bit spreading code is continually transmitted every 1 ms, giving a chip rate of 1.023 Mbits/s. The code is modulated by a 50 bit/s navigation message so each bit of data spans 20 spreading code transmissions (i.e. the coded message is repeated 20 times). The 1500 bit message is subdivided into five subframes of 300 bits each, taking six seconds to transmit.

Each subframe begins with a telemetry word (TLM), which enables the receiver to detect the beginning of a subframe and determine the receiver clock time at which the navigation subframe begins. The next word is the handover word (HOW), which gives the GPS time (the time when the first bit of the next subframe will be transmitted) and identifies the specific subframe within a complete frame. The remaining eight words of the subframe contain the actual data specific to that subframe. Subframe 1 contains the GPS date (week number) and

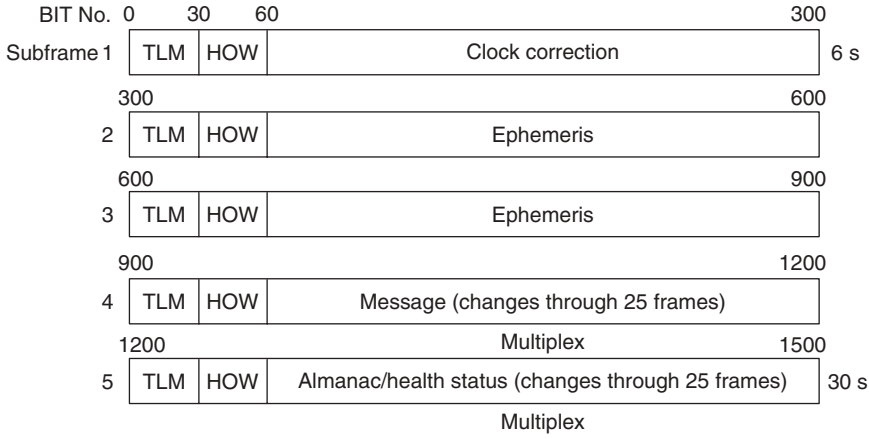

Figure 1.8 C/A code detail.

information to correct the satellite's time to GPS time, together with satellite status and health. Subframes 2 and 3 together contain the transmitting satellite's ephemeris data. Subframes 4 and 5 contain components of the almanac. Each frame contains only 1/25th of the total almanac, so 25 frames are required to retrieve the entire 15 000 bit message. The almanac contains coarse orbit and status information for the whole constellation, as well as an ionospheric model to help mitigate this error when only one frequency is received. Once each subframe is processed, the time for the start of the next subframe from the satellite is known, and once the leading edge of the TLM is detected, the raw transmission time is known. Thus a new range measurement is available at the beginning of each subframe or every six seconds.

A block diagram of a typical GPS user receiver is shown in Figure 1.9. The received CDMA signal is split into a number of parallel channels enabling navigation messages from individual satellites to be received in parallel, thus achieving fastest 'lock' time; 12 channel receivers are common today. For each digital signal processing (DSP) channel, the raw propagation time is determined for a given satellite by loading into the CDMA receiver correlator the gold code for the desired satellite and delaying it one chip at a time until correlation is achieved with the incoming signal. This form of timing is often called code phase timing as it attempts to match the phase of the incoming code with the receiver's own generated code, as illustrated in Figure 1.10a. Since the chip rate is about one microsecond and the accuracy to which the code phase can be locked is about 1% of its period, then the timing accuracy is about

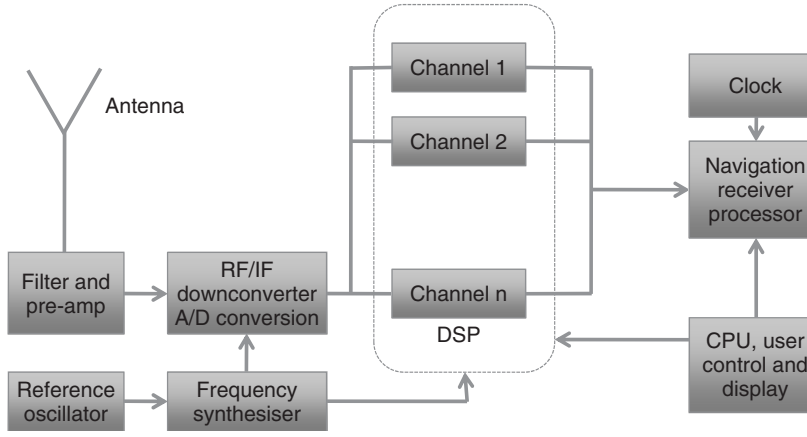

Figure 1.9 Block diagram of user receiver.

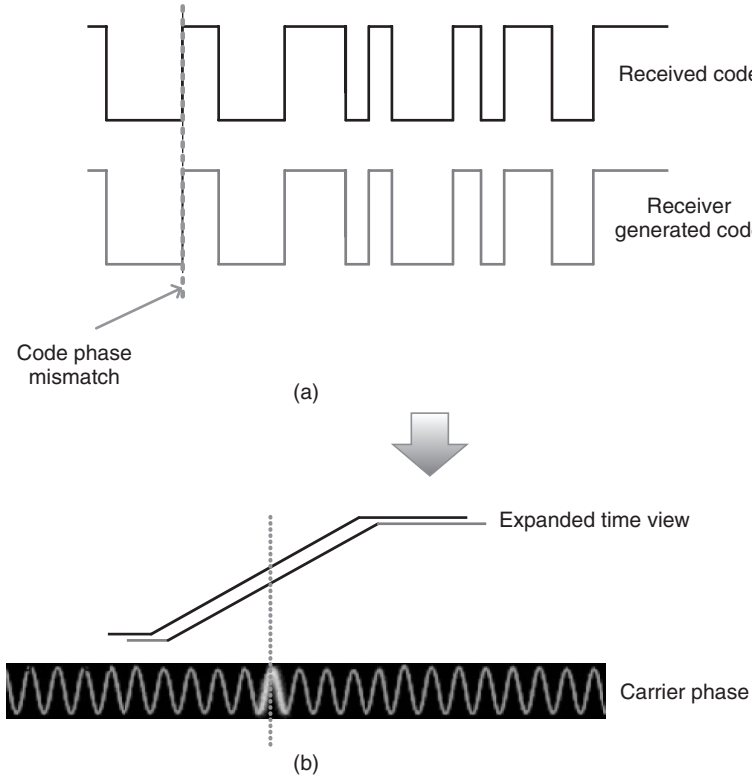

Figure 1.10 (a) Code phase timing and (b) carrier phase timing.

± 10 ns, corresponding to a position error of ± 3 m. This can be improved if carrier phase is used to give a finer timing for the received edge of the incoming pseudo-random code, as shown in Figure 1.10b. The receiver can measure the carrier phase to about 1% accuracy by keeping a running count of the Doppler frequency shift of the carrier since satellite acquisition and the overall phase measurement contains an unknown number of carrier cycles, N, between the satellite and the user. If this *carrier cycle integer ambiguity* can be determined, accuracies of the order of 1 mm can be achieved. The techniques employed by differential GPS (DGPS), described in the next section, aim to determine N.

GPS was originally a US military system and is still today administered by the US DoD, which explains the background for the PPS and why the precise P code can be encrypted so that only military equipment with a proper decryption key can access it. Here an additional code P is transmitted on L1 and a second on L2. In both cases the chip rate is 10.23 Mbits/s with a bandwidth of 20.46 MHz. The P code is pseudo-random and 37 weeks long but only about 1 week is used. For protection against interfering signals transmitted by a possible enemy, the P code can be transmitted encrypted. During this anti-spoofing (AS) mode the P code is encrypted by binary summing it with a slower rate pseudo-random noise code (W code) forming the so-called Y code (called P(Y) mode) which requires a special key to extract the gold code. Even SPS was subject to 'selective availability', its role being to deny accurate positioning to non-authorised users. This is achieved by dithering the satellite clocks in a pseudo-random fashion to corrupt the range measurements, with authorised users having a key to enable them to remove the dithering before processing. When enabled, the SPS location accuracy was limited to about 100 m horizontally and about 150 m vertically, but in the year 2000 it was permanently turned off.

Besides redundancy and increased resistance to jamming, the benefit of having two frequencies transmitted from one satellite is the ability to measure directly, and therefore remove, the ionospheric delay error for that satellite. As the ionosphere is a highly dynamic charged medium, its permittivity is also dynamic and so the speed of light fluctuates by a small frequency-dependent amount, thus leading to positional errors. Ionospheric delay is one of the largest remaining sources of error in the GPS signal for a static receiver. Without such a two-frequency measurement, a GPS receiver must use a generic model or receive ionospheric corrections from another source. As part of a general development of NAVSTAR GPS the introduction of a second civilian signal channel L2C was begun in 2006 (with the IIR-M satellites), which by about 2016 will provide a 24-satellite constellation with this capability. In addition a third new civilian radio channel L5 has been allocated with a carrier frequency

of 1176.45 MHz (20.46 MHz bandwidth), which is in the Aeronautical Radio Navigation Service (ARNS) band authorised for use in emergencies and safety of life applications. The first launch was in 2009 and the 24-satellite constellation with this capability will be achieved by about 2018. It is anticipated that use of the pilot carrier in this band combined with L1 will achieve improved tracking in poor signal and multipath environments.

While most systems employ CDMA-based[2] coding with BPSK modulation, Galileo uses binary offset carrier (BOC) modulation. BPSK has its spectral energy concentrated around the carrier frequency, while BOC-modulated signals have low energy around the carrier frequency and two main spectral lobes further away from the carrier (hence the name of split-spectrum modulation); this reduces the interference with BPSK and hence other GPS services.

1.4 Applications Including Differential GPS

The concept of local area differential GPS (LADGPS) is to place a GPS reference receiver at a surveyed (known) location and to compute the differences in latitude, longitude and geodetic height between the GPS measured position and the known surveyed location. The GPS reference receiver is a survey-grade GPS that performs GPS carrier tracking and can work out its own position to a few millimetres. For real-time LADGPS these differences are immediately transmitted to the local receivers by a low-frequency radio link (VHF or UHF) and they employ this data to correct their own GPS position solutions. This requires that all the receivers make pseudo-range measurements to the same set of satellites to ensure that errors are common. Where there is no need for real-time measurement, such as in terrain mapping, the local receiver needs to record all of its measured positions and the exact time, satellite data, etc., then post-processing the data along with that from the reference receiver yields the required accurate locations. In both cases the basic measurement errors (or *biases*) related to each satellite measurement, such as ionospheric and tropospheric delay errors, receiver noise and clock offset, orbital errors, etc., can be determined and corrected for. Table 1.2 [4] gives estimates of the pseudo-range error components from various sources in SPS mode. The total rms range error is estimated at 7.1 m, and with LADGPS the error drops by a factor of 10.

Protocols have been defined for communicating between reference station and remote users and one such is that from the Radio Technical Commission for Maritime Services (RTCM-104). The data rate is low (200 baud) and so

[2] GLONASS originally used an FDMA-based system but is transferring to a CDMA-based approach.

Table 1.2 GPS C/A code pseudo-range error budget (after [4])

Segment source	Error source	GPS 1 sigma error (m)	LADGPS 1 sigma error (m)
Space	Satellite clock stability	1.1	0
	Satellite perturbations	1	0
	Broadcast ephemeris	0.8	0.1–0.6 mm/km*
User	Ionospheric delay	7.0	0.2–4 cm/km*
	Tropospheric delay	0.2	14 cm/km*
	Receiver noise and resolutions	0.1	0.1
	Multipath + others (interchannel bias etc.)	0.2	0.3
System	Total (RSS)	7.1	0.3 m + 16 cm × baseline in km

*Baseline distance in km.
RSS: Received Signal Strength.

can be transmitted to the remote receiver in a number of ways including a GPRS (General Packet Radio Service) mobile phone connection. The error in the estimated corrections will be a direct function of the distance between the reference and remote receivers; it is possible to use a number of reference receivers to provide a perimeter to the roving remote receiver [4].

As mentioned previously, the receiver can measure the carrier phase to about 1% accuracy by keeping a running count of the Doppler frequency shift of the carrier since satellite acquisition by the receiver, but the overall phase measurement contains an unknown number of carrier cycles, N, between the satellite and the user (Figure 1.11). The recording of this data over time can be done at both the reference and roving receiver for the *same* set of satellites at the *same* time. Combining this data in the form of interferometry leads to a set of equations over time that can be solved to determine the values of N (*carrier cycle integer ambiguity*) for each satellite received by the reference and roving receivers. The corresponding code-phase-measured data can be used to limit the size of the integer ambiguity to about $\pm 10\ \lambda$ to aid the solution. A brute force solution to determining N could then be applied by calculating the least squares solution for each time iteration and finding the minimum residual, but this is a large computational task (of the order of 300 000 residuals for each time point for a $\pm 10\ \lambda$ ambiguity [4])! A better approach uses advanced

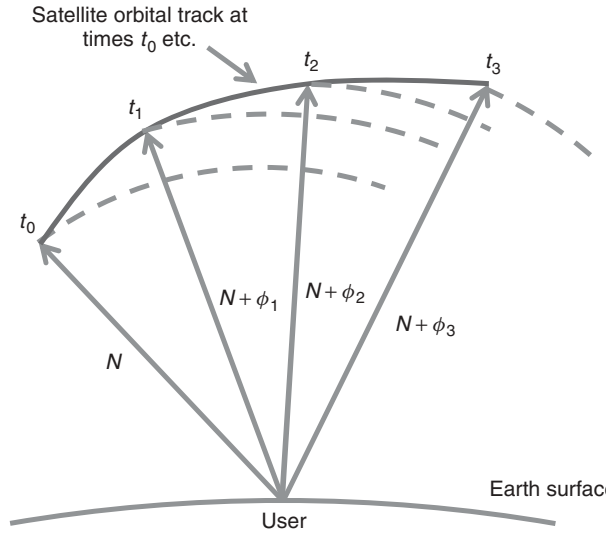

Figure 1.11 Carrier phase as a function of time for a given satellite link.

processing techniques to choose suitable trial values for N [4] leading to 20 cm accuracy in near real time and 1 mm accuracy with post-processing.

When millimetre accuracies are involved the location of the receive antenna's *phase centre* is a vital component in achieving positional accuracy, as the phase centre defines the point at which the electromagnetic energy is received by the antenna, and hence the location for the 3D point of measurement for GPS. The phase centre for an antenna is where the spherical phase fronts of the far-field radiation pattern of an antenna appear to emanate from in transmit mode. Since antennas are reciprocal devices, so long as they are isotropically passive and linear this will also be the point at which the energy is received by the antenna. For a given antenna the phase centre is a function of the operating frequency and polarisation, and has a range of validity in terms of the solid angle surrounding the antenna boresight. The phase centre is easily determined by far-field radiation pattern phase measurement as shown in Figure 1.12 for a set of planar pattern cuts for a given polarisation at different points about which the antenna is rotated. For a given operating frequency and polarisation, such measurements need to be undertaken in both the **E** plane and **H** plane to determine the 3D coordinates of the phase centre. The phase centre data is then referred to some fixed physical reference point on the antenna, such data normally being provided by the manufacturer for antennas to be used for precision GPS.

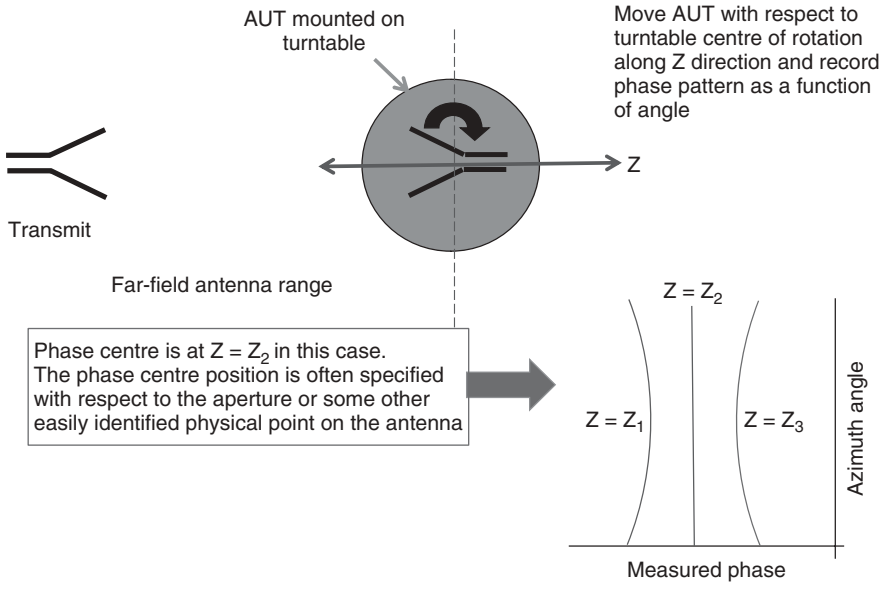

Figure 1.12 Antenna phase centre measurement. AUT: Antenna Under Test.

A key issue for high-precision measurements is the effect of multipath, where a delayed version of the GPS signal is received by reflection from a nearby building or the ground. Techniques to mitigate this include correlator designs to separate the multipath components, spectral techniques, multiple receive antennas as well as sensible choice of site (where that is possible). Today multipath mitigation extends to mobile receivers in urban environments, and the use of multiple antennas on vehicles is a possible solution.

Regional area and wide area DGPSs, as the names suggest, cover much wider areas and often use satellites to provide the differential data (e.g. the LEX frequencies of the QZSS system in Table 1.1). Another significant application for GPS is its use as a time standard, for example to synchronise master clocks in telecommunication systems.

References

1. Hofmann-Wellenhof, B., Lichtenegger, H. and Wasle, E., *GNSS – Global Navigation Satellite Systems, GPS, GLONASS, Galileo and more*, Springer, Vienna, 2008.

2. Engel, U., 'Improving position accuracy by combined processing of Galileo and GPS satellite signals', Proceedings of the ISIF Fusion 2008 Conference, Cologne, Germany, 30 June–3 July 2008.
3. NAVISTAR-GPS Joint Programme Office, *NAVSTAR-GPS user equipment: introduction*, public release version, February 1991.
4. Kaplan, E.D., *Understanding GPS: Principles and applications*, 2nd edn, Artech House, London, 2006.
5. MIT course web site '12.540 Principles of the Global Positioning System'. http://www-gpsg.mit.edu/~tah/12.540/12.540_HW_01_soln.htm, last accessed on 23 December, 2011.

2

Fundamental Considerations for GNSS Antennas

This chapter starts by describing radio wave propagation between a satellite and a ground receiver and the rationale for selecting circularly polarised (CP) waves. It also introduces the relevant propagation issues, such as multipath interference and the effects of ionospheric, tropospheric and RF interference, and covers fundamental issues in antenna design for GNSS applications. Finally, it presents the basic approaches for designing a CP antenna and highlights the technical challenges involved.

2.1 GNSS Radio Wave Propagation

Satellite navigation relies on signals carried by electromagnetic (EM) waves (radio waves). In order to design better GNSS antennas, we need to have a good understanding of radio wave propagation and related effects on satellite navigation systems.

2.1.1 Plane Waves and Polarisation

A radio wave propagating over a long distance, as in a satellite navigation system, is always in the form of a plane wave. A plane EM wave is characterised by having no field components in the propagation direction and the field only varying in the propagation direction. A typical plane wave and its attributes are shown in Figure 2.1. The electric and magnetic fields are in phase and vary sinusoidally along the propagation direction.

Antennas for Global Navigation Satellite Systems, First Edition.
Xiaodong Chen, Clive G. Parini, Brian Collins, Yuan Yao and Masood Ur Rehman.

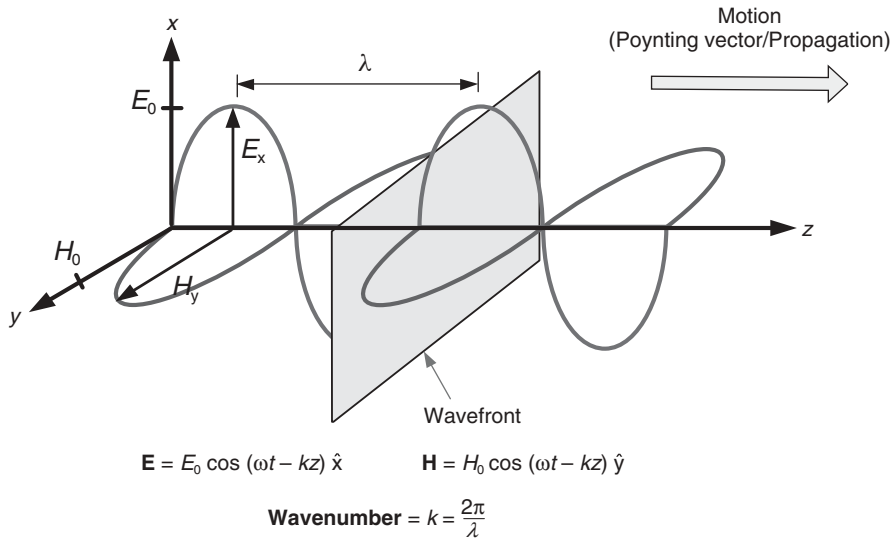

Figure 2.1 Illustration of a plane EM wave.

The polarisation of a plane EM wave can be characterised as being linear, circular or elliptical, depending on the direction of its electric field vector $\mathbf{E} = [E_x, E_y]$. A constant direction of $\mathbf{E}$ characterises linear polarisation, as indicated in Figure 2.2a. A CP plane wave is characterised by the equal amplitude transverse components of the electric field, out of phase by 90°. The electric field vector rotates along the propagation direction – tracing a circle on the $x-y$ plane, as indicated in Figure 2.2b. When the two transverse components have different magnitudes or if the phase difference between them is different from 90°, the electric field vector traces an ellipse on the $x-y$ plane, as shown in Figure 2.2c, and the polarisation is described as elliptical.

Circular polarisation can be classified into right hand circular polarisation (RHCP) and left hand circular polarisation (LHCP). An RHCP wave is defined as if the right hand thumb points in the direction of propagation, while the fingers curl along the direction of the $\mathbf{E}$ field vector rotation. It is considered to be clockwise because, from the point of view of the source, looking in the direction of propagation, the field rotates in a clockwise direction. An LHCP wave is defined as if the left thumb points in the direction of propagation while the fingers curl along the direction of the $\mathbf{E}$ field vector rotation. This convention is also applied to elliptical polarisation. Different types of polarisations are summarised in Figure 2.2.

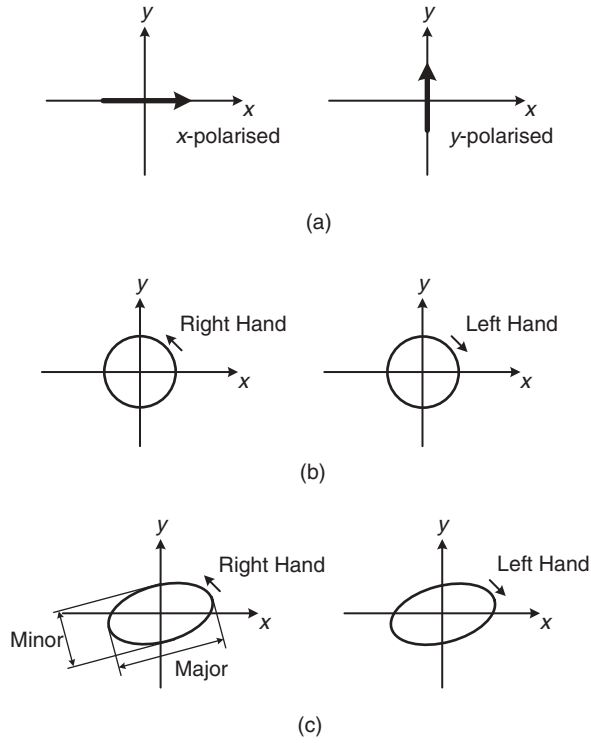

Figure 2.2 Different types of plane wave polarisations: (a) Linear polarisation, (b) Circular polarisation and (c) Elliptical polarisation.

When a plane radio wave propagates in a homogeneous medium, it has a constant velocity and remains in its original polarisation. However, the radio wave will experience many changes in its attributes when propagating through different media, as it does in the case of satellite navigation systems.

2.1.2 GNSS Radio Wave Propagation and Effects

The radio wave transmitted from a moving GNSS satellite propagates through the atmosphere (ionosphere and troposphere) and reaches the ground receiver, as shown in Figure 2.3. It encounters several impairments, such as attenuation, Doppler shift, propagation delay in the ionosphere and troposphere, multipath and interference. The link budget between a satellite and a ground station must take into account the attenuations caused by distance, and the effects of absorption and scattering in the ionosphere and troposphere. Other impairments

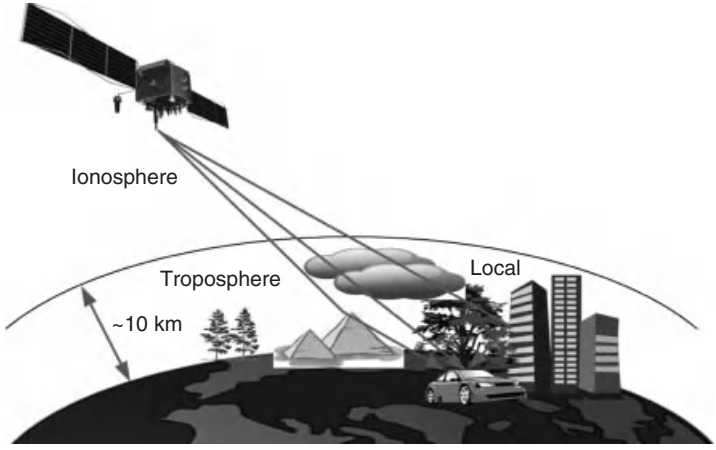

Figure 2.3 Radio wave propagation between a GNSS satellite and a ground receiver.

cause navigation errors. Together with their associated mitigation methods, these are discussed briefly below.

2.1.2.1 Doppler Shift

The Doppler shift is caused by the well-known physical fact that relative motion between a transmitter and receiver will cause a perceived frequency shift in the received signal. An approaching transmitter increases the received frequency, whereas a receding transmitter decreases it. In satellite navigation, a Doppler shift of about 5 kHz maximum is created by satellite motion when the satellite is moving directly towards or away from the receiver. Motion of the receiver also creates a small Doppler shift at a rate of 1.46 Hz/km/h. Taking into account receiver oscillator frequency offset, the total maximum frequency uncertainty at the receiver is roughly ± 10 kHz. The receiver must search in this 20 kHz band to find detectable GNSS signals [1]. Within this band each satellite will have its own characteristic Doppler shift according to its orbital characteristics and the position of the receiver.

2.1.2.2 Effects of the Ionosphere

The ionosphere is a layer of electrons and charged atoms and molecules (ions) that surround the Earth, stretching from a height of 50 to 1000 km. The ionosphere can be characterised by its total electron content (TEC). The TEC is influenced by solar activity, diurnal and seasonal variations, and the Earth's

magnetic field. Radio waves travelling through the ionosphere can undergo a change in their polarisation, which is known as Faraday rotation. This effect may cause linearly polarised (LP) radio waves to become elliptically or circularly polarised. The major effect of the ionosphere on a GNSS signal is the frequency-dependent phase shift (group delay), caused by the dispersive characteristics of the ionosphere. We can reduce the effect of ionospheric dispersion by employing two widely spaced frequencies. By employing a diversity scheme at the receiver, we can correct almost all the ionospheric effects. It is for this reason that GPS satellites transmit signals at two carrier frequencies, L1 at 1575.42 MHz and L2 at 1227.60 MHz.

2.1.2.3 Effects of the Troposphere

The troposphere, extending from the Earth's surface to a height of about 50 km, is non-dispersive at GNSS frequencies. The troposphere delays radio waves by refraction. The reasons for the refraction are different concentrations of water vapour in the troposphere, caused by different weather conditions. The resulting error is smaller than the ionospheric error, but it cannot be eliminated by calculation. It can only be approximated by a general calculation model.

2.1.2.4 Multipath Propagation

Multipath propagation occurs when the receiver picks up signals from the originating satellite that have travelled by more than one path. Multipath is mainly caused by reflecting surfaces near the receiver. In the example in Figure 2.3, the satellite signal arrives at the receiver through three different paths, one direct and two reflected. As a consequence, the received signals have relative phase offsets, which results in pseudo-range error. The range error caused by the multipath may grow to about 100 m in the vicinity of buildings [1]. The methods of mitigating multipath effects can be classified as (i) antenna based and (ii) signal processing based. One of the antenna-based approaches is to improve the antenna radiation pattern by using choke rings to suppress signals received from directions below the horizon. Another approach is to choose an antenna that takes advantage of the radio wave polarisation. If transmitted GNSS signals are right-handed circularly polarised, then after one reflection the signals are left-handed polarised. So if the receiver antenna is designed to be right hand polarised, it will reject many reflected multipath signals. Signal processing methods for mitigating multipath have recently progressed substantially [1]; however, even with high-performance correlator receivers, multipath errors still occur frequently.

We have only discussed radio wave propagation in a general environment. Nowadays, GPS receivers are often integrated with mobile phone handsets. Radio wave propagation is more complicated in this scenario, in which we need to consider the effects of the human body and the mobile terminal.

2.1.3 Why CP Waves in GNSS?

Having discussed radio wave propagation and its impairments in the previous section, we can easily see the benefits of employing CP waves in satellite navigation (RHCP in GNSS).

Firstly, a CP radio wave enhances the polarisation efficiency of the receiving antenna. Maximising the received signal using LP or elliptically polarised (EP) antennas requires the receiving antenna to be correctly aligned relative to the direction of propagation. Using RHCP antennas at the satellite and at the receiver means that no polarisation alignment is needed. Secondly, a CP wave is capable of combating Faraday rotation in the ionosphere. If an LP wave is adopted, the signal becomes EP or even CP after passing through ionosphere, so an LP antenna on the receiver can only pick up a fraction of the incoming signal. Thirdly, a CP radio wave can be utilised to reject multipath signals. As mentioned earlier, a right hand polarised signal becomes left hand polarised after reflection from a surface. An RHCP receiving antenna would reject these reflected signals.

The design of a CP antenna is more complicated and difficult compared with that of an LP antenna, especially in GNSS applications. Thus this text provides comprehensive coverage of this topic.

2.2 Antenna Design Fundamentals

An antenna can be regarded as a transducer between EM waves travelling in free space and guided EM waves in RF circuits [2]. Antennas are characterised by a number of parameters and can be classified into a number of different categories.

2.2.1 Antenna Fundamental Parameters

In the design of antennas, a number of fundamental parameters must be specified. These key parameters are reviewed in the following subsections.

2.2.1.1 Impedance Bandwidth

We may define impedance bandwidth as the frequency range over which 90% of the incident power is delivered to the antenna – the reflection coefficient $S_{11} < -10\,\text{dB}$ and the voltage standing wave ratio (VSWR) is less than 2:1. The absolute impedance bandwidth can be calculated as the difference between the upper and lower frequencies at which these criteria are met. Alternatively, the fractional impedance bandwidth can be calculated as the percentage of the upper and lower frequency difference divided by the centre frequency of the bandwidth:

$$\text{BW} = \frac{f_{\max} - f_{\min}}{f_{\text{centre}}} \times 100\% \tag{2.1}$$

2.2.1.2 Radiation Pattern

The radiation pattern is a graphical representation of the radiation characteristics of the antenna as a function of spatial coordinates. For a small antenna it is generally determined in the far-field region and is represented as a function of directional coordinates. Spherical coordinates are typically used, where the $x-z$ plane (measuring θ with fixed φ at 0°) is called the elevation plane and the $x-y$ plane (measuring θ with fixed φ at 90°) is called the azimuth plane, as shown in Figure 2.4a.

Figure 2.4b illustrates an example of an antenna scalar radiation pattern [3]. Its major features are as follows:

- *Major lobe or main beam*: The part that contains the direction of maximum radiation. The direction of the centre of an essentially symmetrical main beam is called the electrical boresight of an antenna.
- *Back lobe*: A radiation lobe that is directly opposite to the main lobe. Back lobes may refer to any radiation lobes between 90° and 180° from the boresight direction.
- *Minor lobes*: Any lobe apart from the main beam.
- *Half-power beamwidth* (HPBW): The angle subtended by the half-power points of the main lobe.

2.2.1.3 Antenna Phase Centre

As discussed in Chapter 1, antenna phase centre is a concept related to the phase pattern, that is the equiphase surfaces of an antenna, shown as dashed

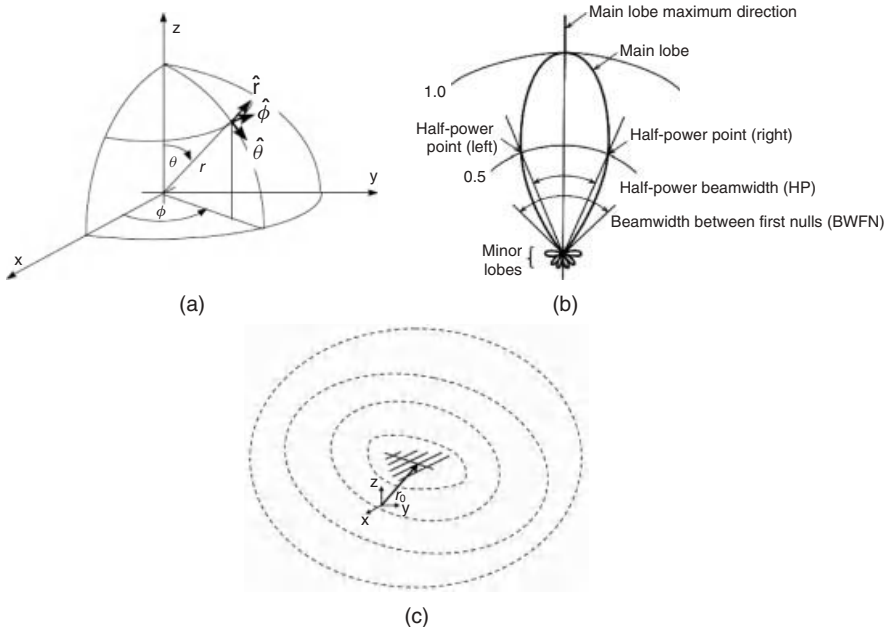

Figure 2.4 (a) Spherical coordinates, (b) an example of a radiation pattern and (c) the phase pattern (equiphase surfaces) of an antenna on an azimuth plane.

lines on a particular azimuth plane in Figure 2.4c. In the far-field region, the equiphase surface is close to a spherical surface, indicated as the outermost circle in Figure 2.4c. The centre of the sphere is the equivalent phase centre of the antenna.

In most cases of antenna design, we are only concerned with the scalar radiation pattern, the spatial distribution of the field strength. However, in satellite surveying and other precision measurements, the phase of the received signal is used to obtain a greater precision of position, so the antenna phase centre and its characteristics need to be taken into account.

2.2.1.4 Directivity and Gain

The directivity of a receiving antenna is the ratio of the sensitivity to signals arriving from the direction of the maximum of the main lobe to the mean sensitivity to signals arriving from all directions in 3D space.

The gain of a receiving antenna is the ratio of the signal received by the antenna compared with that received by a lossless isotropic antenna in the same signal environment.

2.2.1.5 Efficiency

Total antenna efficiency describes the losses incurred in the process of converting the input power to radiated power:

$$\text{Total efficiency} = \text{radiation efficiency} \times \text{reflection efficiency}$$

Radiation efficiency takes into account conduction and the dielectric losses (heating) of the antenna. Reflection (mismatch) efficiency accounts for the power loss due to impedance mismatch.

2.2.1.6 Polarisation

As mentioned earlier, polarisation can be described as the property of the EM waves that defines the directional variation of the electric field vector. The polarisation of a receiving antenna may be defined by reference to the polarisation of an incoming wave of a given field strength for which the antenna delivers maximum received power.

Generally speaking, the polarisation of a receiving antenna is not the same as the polarisation of the incident wave. The polarisation loss factor (PLF) characterises the loss of received power due to *polarisation mismatch*.

Antennas can be classified in accordance with their polarisation characteristics as LP, CP and EP.

For an EP antenna, there is an additional characteristic – the *axial ratio* (AR) defined as the ratio of the major axis to the minor axis of the polarisation ellipse, as shown in Figure 2.2c:

$$\text{AR} = \frac{\text{major axis}}{\text{minor axis}} \tag{2.2}$$

The AR is unity (0 dB) for a perfect CP antenna. In practice, when the AR is less than 3 dB, the antenna is usually accepted as a CP antenna.

2.2.2 LP Antenna Design and Example

The LP antenna usually has a simple structure, such as a dipole, which we use as a straightforward example to illustrate the characteristics of an LP antenna.

A half-wavelength dipole antenna working at the GPS L1 band is shown in Figure 2.5. The length of the dipole is approximately $\lambda/2$, so since the central frequency is 1575.42 MHz, $l = 95.2$ mm. The antenna illustrated is LP in the vertical direction.

Figure 2.5 Schematic of an ideal dipole.

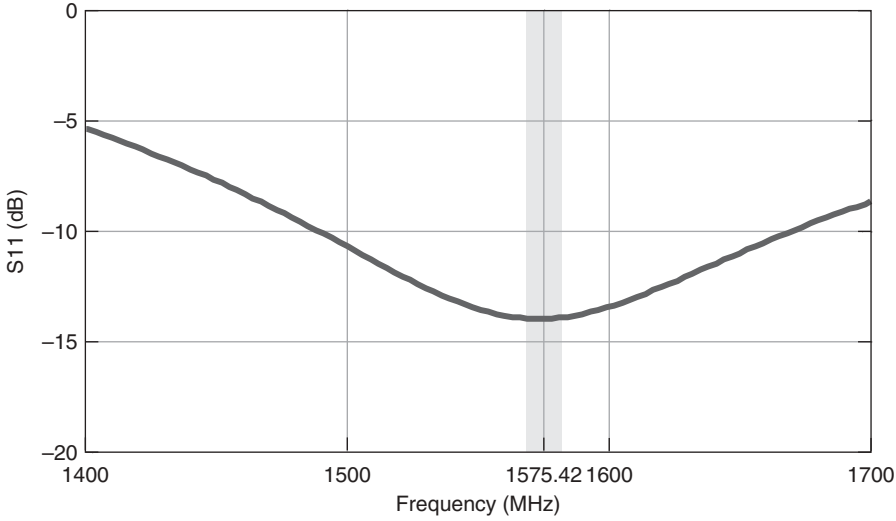

Figure 2.6 Simulated S_{11} curve of a half-wavelength dipole.

The dipole antenna is modelled by using CST Microwave Studio [4]. Figure 2.6 shows the simulated S_{11} for the antenna. The antenna performs well in the L1 frequency band with a -10 dB bandwidth of 153 MHz.

The radiation patterns of the dipole antenna in the elevation and azimuth planes are illustrated in Figure 2.7. The pattern in the azimuth plane is a circle, indicating that the dipole is an omnidirectional antenna. The pattern in the elevation plane indicates the major lobe is directed towards the horizontal axis ($\theta = 90^\circ$) with a directivity of 2.14 dB and with a 3 dB beamwidth of 78°. A practical dipole will be discussed again in Chapter 6.

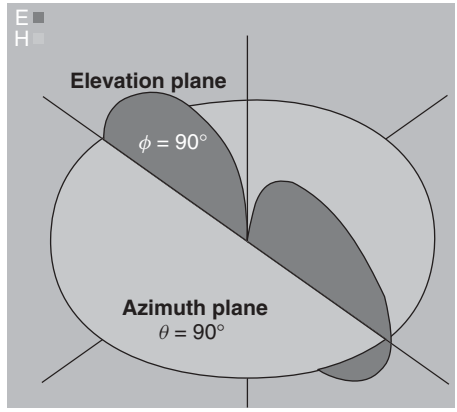

Figure 2.7 The 2D radiation pattern of a half-wavelength dipole.

2.3 CP Antenna Design

As we mentioned earlier, CP antennas are required for optimum reception of GNSS signals. We will cover CP antenna design issues in this section.

2.3.1 CP Antenna Fundamentals and Types

CP antennas can be realised in design through different structures and feeding techniques. In terms of structures, CP antennas can be classified into helical, spiral and microstrip patch types.

2.3.1.1 Helical Antennas

A helical antenna can easily generate circular polarisation since the current follows a helical path like the CP EM wave. In practice, it comprises a helix with a ground plane, where a clockwise winding provides RHCP and anti-clockwise provides LHCP. An example is shown in Figure 2.8.

The geometry of a helix consists of N turns, diameter D and spacing S between turns, as shown in Figure 2.8. The axial (endfire) mode is usually used to achieve circular polarisation over a wide bandwidth. To excite this mode, the diameter D and spacing S must be large fractions of the wavelength. In practice, the circumference of the helix must be in the range of $3/4 < \pi D/\lambda < 4/3$ and

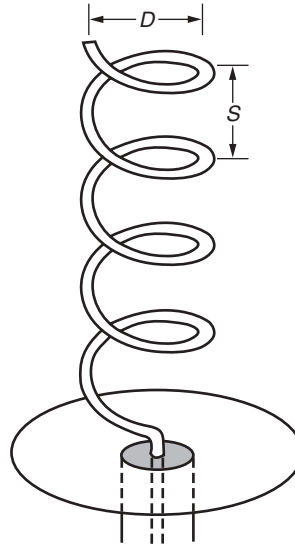

Figure 2.8 Helical antenna geometry.

the spacing about λ/4. Most often the helix is fed by a coaxial line and is supported by a ground plane with a diameter of at least λ/2.

The helix provides high gain and broad bandwidth, but is large in size, so it is normally used as a transmitting antenna on a satellite, or as a high-gain receiving antenna. One variation of the helix, the quadrifilar helix, can be made in compact form. Thus it has also been employed on the receiving terminals. The features of the quadrifilar antenna will be addressed in the following chapters.

2.3.1.2 Spiral Type

Flat spiral antennas belong to the class of frequency-independent antennas which operate over a wide range of frequencies. Figure 2.9 shows a typical configuration of a two-arm flat spiral antenna. The lowest frequency of operation occurs when the total arm length is comparable with the wavelength. For all frequencies above this and below a frequency defined by the extent to which the spiral geometry is maintained near the central feed point, the pattern and impedance characteristics are sensibly frequency independent. Spiral antennas are inherently CP, with low gain. Lossy cavities are usually placed behind the spiral to eliminate back lobes, because the structure is intrinsically bidirectional, while a unidirectional pattern is usually preferred. Spiral antennas are classified

Figure 2.9 A two-arm log-spiral antenna backed with a cavity.

into different types: Archimedean spiral, square spiral, log spiral, etc. [2]. A typical cavity-backed two-arm log-spiral antenna is shown in Figure 2.9.

Different designs of spiral antenna can be obtained by varying the number of turns, the spacing between turns and the width of the arms. The properties of the antenna also depend on the permittivity of the dielectric medium on which the spiral is supported.

The antenna comprises usually two conductive spiral arms, extending outwards from the centre. The antenna may be a flat disc, with conductors resembling a pair of loosely nested clock springs, or the spirals may extend in a 3D shape like a tapered screw thread (a conical spiral). The direction of rotation of the spiral, as viewed from behind, defines the sense of polarisation. Additional spirals may be included to form a multi-spiral structure.

2.3.1.3 Patch Antennas

To understand how a patch CP antenna works, we need to see how a microstrip patch antenna operates. A simple rectangular patch antenna can be viewed as a dielectric-loaded cavity, having various resonant modes. The fundamental mode is the TM^x_{010} mode, as shown in Figure 2.10a. The equivalent magnetic current is shown in Figure 2.10b. The currents flowing along the y-direction (sides 2 and 4) cancel each other, while the currents flowing along the x-direction (sides 1 and 3) add. So the net exciting current in the TM^x_{010} mode flows in the x-direction. The other fundamental mode of a patch cavity is the TM^y_{010} mode

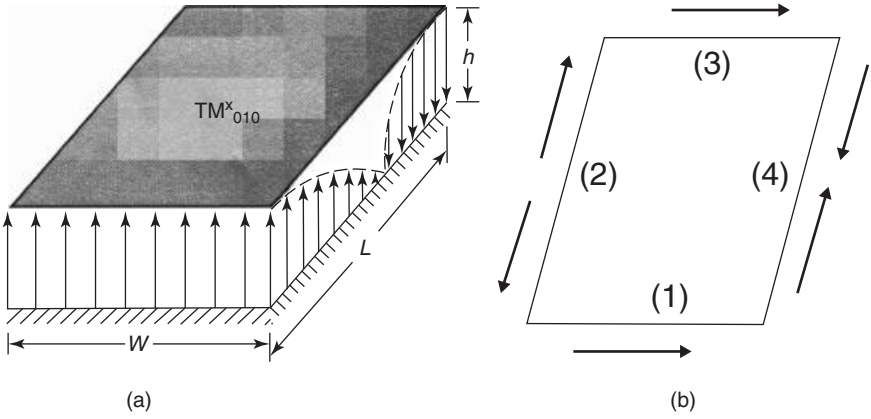

Figure 2.10 (a) Patch cavity mode, TM^x_{010}, and (b) equivalent magnetic current flows.

in the y-direction, similar to the patterns in Figure 2.10, but rotated by 90°. The net exciting current in TM^y_{010} mode flows in the y-direction.

In a square patch antenna, the TM^x_{010} and TM^y_{010} modes have the same resonant frequency, so if we excite these two modes simultaneously with a 90° time–phase difference, a CP wave can be launched. A similar analysis can be applied to a circular patch antenna which supports the fundamental TM_{110} mode in both the x- and y-directions.

Basically, there are two feeding approaches to achieve CP on a patch antenna:

1. *Dual-fed CP patch antenna*: In this design, two feed ports are excited with orthogonal currents having 90° phase difference. For a square patch antenna, the ideal method is to feed the patch at the centre of two adjacent edges. A power divider or 90° hybrid can be used to obtain the quadrature phase difference between the feeds. Another method is to use offset feeding where one feed line is one quarter wavelength longer than the other. Figure 2.11 shows two different types of dual feeding.
2. *Single-fed CP patch antenna*: The antenna is fed at a single point where the generated mode is separated into two orthogonal modes by the effect of an offset feed point together with geometrical perturbations of the patch such as slots or truncations on its edges or corners, as shown in Figure 2.12. The radiated fields excited by these two generated modes are orthogonally polarised with equal amplitude, and are 90° out of phase at the centre frequency when the perturbed segment is optimally adjusted. This arrangement enables the antenna to act as a CP radiator despite being fed only at a single point. This antenna has several advantages over the dual-fed ones, such as

no need for an external feed network and its compact size. However, the AR bandwidth of a patch antenna of this type is normally smaller than that of a dual-fed patch and is only suitable for coverage of one of the GNSS frequency bands.

There are other types of CP patch antennas, such as pentagonal, triangular and elliptical patches and composite CP antennas [4]. Also, various variations of CP patch antennas have been designed in practical GNSS applications. These practical patch antenna designs will be discussed in the following chapters.

2.3.2 *Simple CP Antenna Design Example*

Here we design a corner-truncated square patch CP antenna to cover the GPS L1 band to demonstrate CP antenna characteristics.

The geometry of the probe-fed truncated corner square patch antenna is shown in Figure 2.13.

The optimised dimensions of the antenna are $L_p = 53.4\,\text{mm}$, $L_s = 100\,\text{mm}$, $a = 49.9\,\text{mm}$, $\Delta a = 3.5\,\text{mm}$, $b = 26.7\,\text{mm}$ and $c = 16\,\text{mm}$. An FR4 dielectric

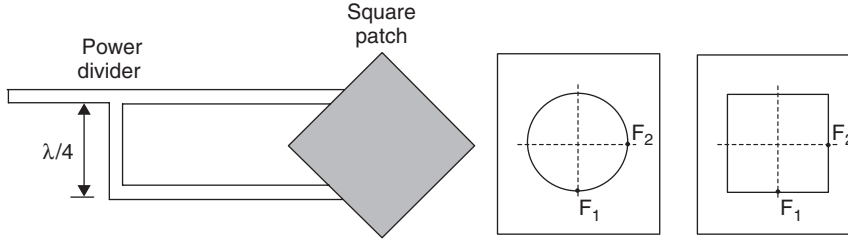

Figure 2.11 Dual-feed types of circularly polarized antenna [5]. Reproduced with permission from IET.

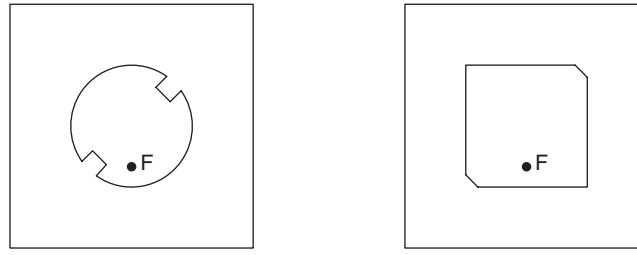

Figure 2.12 Singly fed types of CP patch antennas [5]. Reproduced with permission from IET.

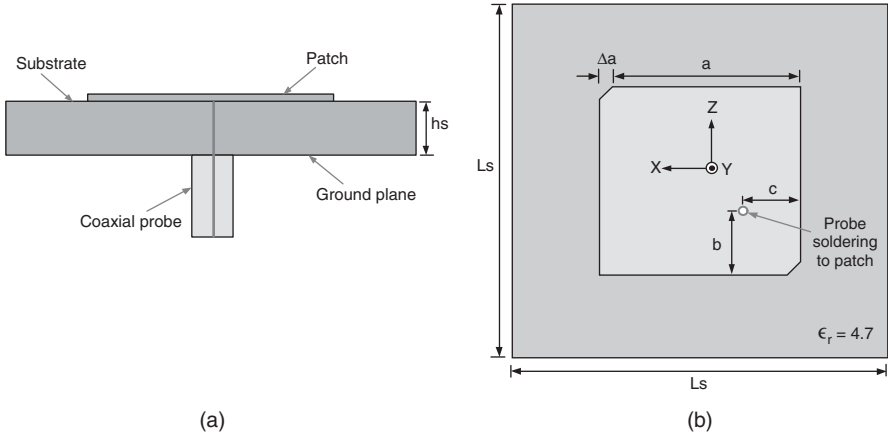

Figure 2.13 Configuration of the designed CP antenna: (a) Side view; (b) Front view.

substrate with a permittivity of $\varepsilon_r = 4.7$ and thickness $h_s = 1.6$ mm is used. The position of the feed probe was varied to achieve proper impedance matching for the antenna.

The antenna design was simulated using CST Microwave Studio [5]. The simulated s parameter gives an impedance bandwidth of 1561–1592 MHz (31 MHz) while the acceptable AR bandwidth is 1566–1578 MHz (12 MHz), as shown in Figure 2.14.

The AR in the broadside direction is 1.39 dB while the minimum AR of 0.16 dB is achieved at 60°. The beamwidth of the antenna for an AR of less than 3 dB is about 160°. A Cartesian plot of the AR as a function of angle from boresight at 1575.42 MHz is shown in Figure 2.15. The RHCP and LHCP patterns in the $x-y$ and $y-z$ planes, as illustrated in Figure 2.16, show that the cross-polar discrimination is greater than 10 dB over a wide angle. The gain of the antenna is 7.0 dBi and the radiation efficiency is above 88%. The back lobe of the RHCP radiation pattern is below −22 dB.

2.3.3 Technical Challenges in Designing GNSS Antennas

The design of GNSS antennas is becoming more complex day by day due to miniaturisation of user devices and performance degradations caused by the user and the local environment. These factors should be considered in order to develop an efficient navigation device.

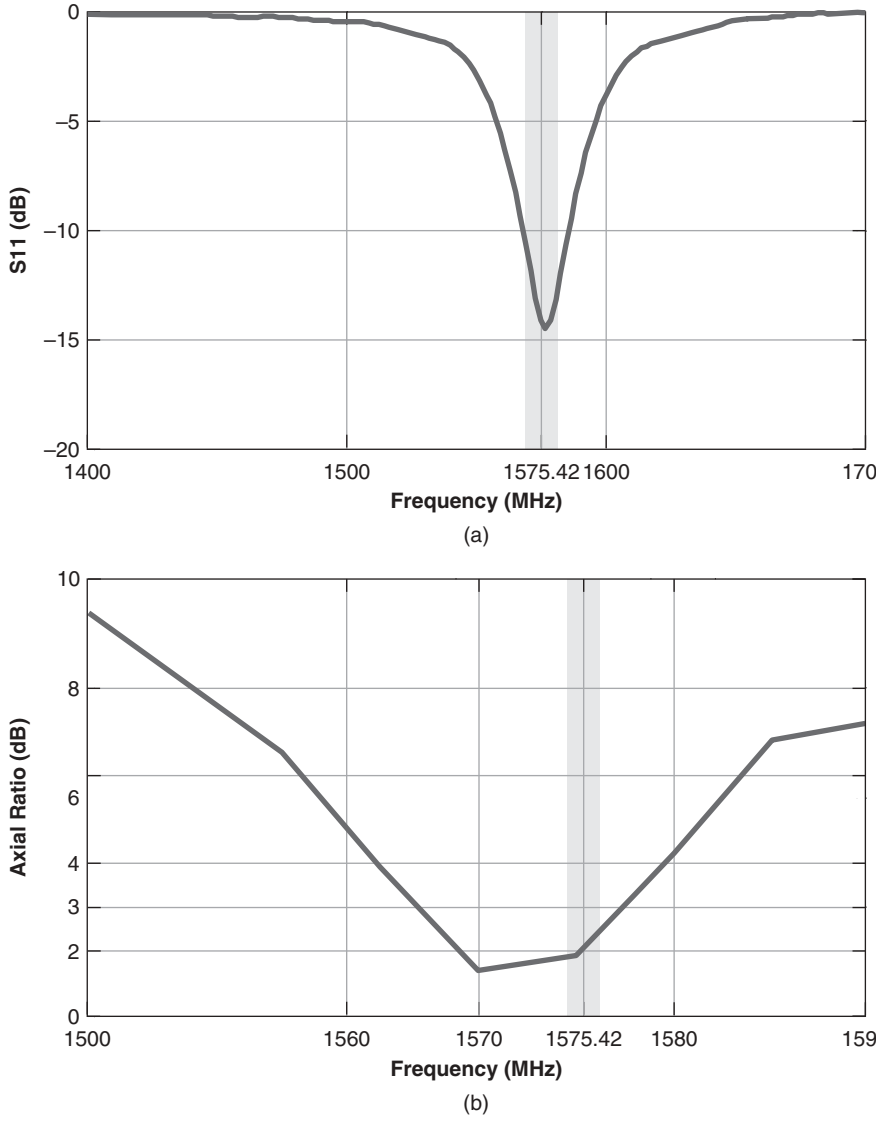

Figure 2.14 Reflection coefficient and AR plots of the CP antenna.

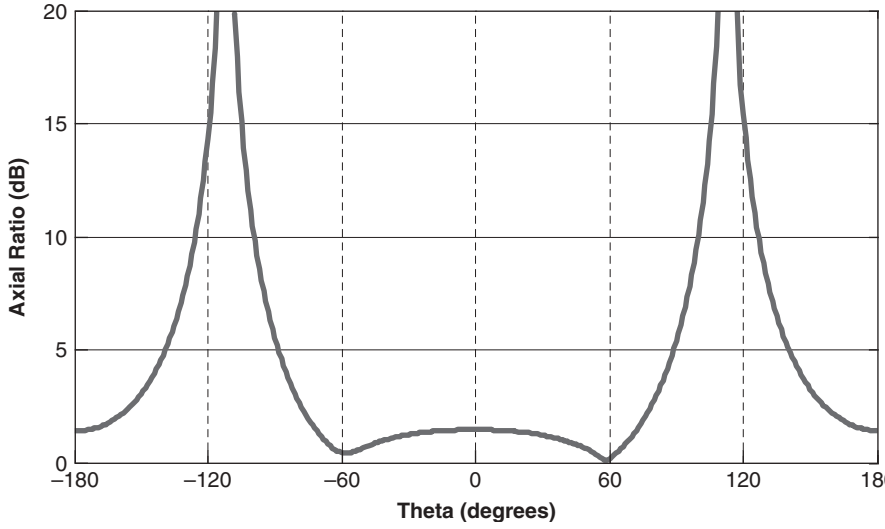

Figure 2.15 Cartesian plot of AR in $x-y$ plane at 1575.42 MHz.

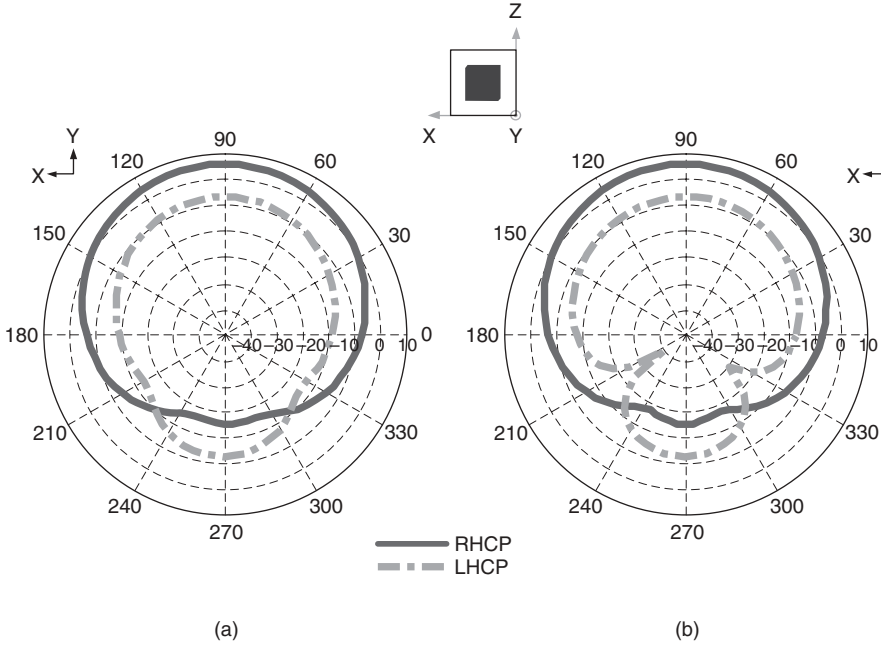

Figure 2.16 Radiation pattern RHCP (solid curve) and LHCP (dot–dashed curve) at 1575.42 MHz: (a) $x-y$ Plane; (b) $y-z$ Plane.

2.3.3.1 Limitation on the Size and Shape of Antennas

A major technical challenge comes from the limitation on the size and shape of antennas when adding GNSS functions to small devices such as mobile handsets and personal trackers. As the size of average mobile handsets continues to fall, the space for installing the GPS antenna on the PCB is really limited. To combat this challenge, the majority of GPS antennas on mobile phones are of the space-saving LP type, in the form of PIFAs (Planar Inverted-F Antennas) or IFAs (Inverted-F Antennas). In order to compensate the lower effective antenna gain of an LP antenna, a low-noise amplifier (LNA) is usually used together with the antenna. Though CP patch antennas, usually on a high-permittivity ceramic substrate, are still employed in some handsets, studies have shown that the advantage of a CP antenna disappears in a complex operating environment with rich multipath [6]. This issue is further addressed in the following chapters.

2.3.3.2 Multiband and Broadband Operation

With the development of integrated GNSS receivers covering GPS, GLONASS, Galileo and the Chinese Compass systems, there is a demand for multiband or broadband CP receiving antennas. This demand poses another challenge in designing antennas for compact GNSS receivers since small CP antennas are usually narrow band. Considerable research work has been carried out in this area and different approaches have been proposed to meet such a demand. This is the main topic of Chapter 5.

2.3.3.3 The Effects of the Environment, Human Body and Platform

The performance of a GNSS antenna on a mobile terminal is affected substantially by its surroundings. Firstly, the antenna will pick up multipath signals due to reflections, refractions and scattering of incident radio waves in cluttered environments, such as city streets and indoors. These multipath signals have arbitrary polarisation and can cause substantial positioning errors. Secondly, the antenna is greatly affected by the human body in its vicinity. It is well known that the human body, being a lossy medium, can reduce the radiation efficiency of an antenna, degrade its radiation pattern and detune the impedance matching at its feed point. Finally, other components on the mobile platform can also affect GNSS antenna performance, distorting the radiation pattern, reducing gain and causing EM interference. These effects and relevant mitigation measures are the main topics in Chapters 6, 7 and 8.

2.3.3.4 EM Interference

EM interference can be categorised as intentional and unintentional interference. Any intentional interference is unlawful, but GNSS receivers for some purposes, for example military and law enforcement applications, must be able to function in its presence. Sources of unintentional interference include out-of-band emissions from other services and in-band emissions, in particular from other GNSS systems. Spread-spectrum GNSS signals reduce the effect of narrowband interfering signals. Interference can be further mitigated by using adaptive antenna and filter designs to filter the signal in the spatial, time and frequency domains. On a mobile platform, EM interference may be emitted from other components or devices. It is challenging to isolate and mitigate this type of EM interference in designing a mobile platform. Further discussion of this issue is provided in Chapter 8.

2.3.3.5 Other Issues

There are other issues to be considered in the design of GNSS antennas for various applications. For example, in the high-precision positioning service (differential GPS), stability of the phase centre of the antenna is required. This imposes another constraint in the design of GNSS antennas. This issue is addressed in the following chapters.

References

1. Van Diggelen, F., *A-GPS: Assisted GPS, GNSS, and SBAS*, Artech House, London, 2009.
2. Balanis, C.A., *Antenna Theory: Analysis and Design*, 2nd edn, John Wiley & Son, Inc., New York, 1997.
3. Stutzman, W.L. and Thiele, G.A., *Antennas Theory & Design*, John Wiley & Sons, Ltd, Chichester, 1981.
4. CST Microwave Studio, *User Manual*, 2009.
5. James, J.R. and Hall, P.S., *Handbook of microstrip antennas*, Peter Peregrinus, London, 1989.
6. Pathak, V., Thornwall, S., Krier, M. *et al*., 'Mobile handset system performance comparison of a linearly polarized GPS internal antenna with a circularly polarized antenna', Proceedings of IEEE Antennas and Propagation Society International Symposium 2003, Columbus, OH, June 22–27, 2003, Vol. 3, pp. 666–669.

3

Satellite GNSS Antennas

3.1 Navigation Antenna Requirements

This chapter will take an overview of the antenna requirements and design techniques used for the spacecraft segment of the GPS system. Although the antenna farms are complex high-value systems, the antenna designer can infer useful techniques that can be translated into constructing specialised GNSS user antennas. Figure 3.1 shows the level of complexity of an antenna farm for the GPS III satellite. A typical spacecraft antenna farm consists of a number of antenna systems including:

- L-band downlink array that provides the L1, L2 and L5 navigation signals.
- UHF uplink array for search and rescue.
- S-B and TT&C (Tracking Telemetry & Control) up- and downlinks.
- UHF antennas for satellite control.

Here we will concern ourselves with the first two that are specific to GNSS antenna design.

3.2 Types of Antenna Deployed

As an example of a modern navigation antenna array we will consider the design for Galileo. Table 3.1 summarises the specification.

This performance is achieved by using a 1.4 m diameter planar array of 45 stacked patch antenna elements forming six triangular subarrays, as shown in Figure 3.2 [1]. There are two types of subarray (type A = six elements and type B = nine elements) and they are placed alternatively in a radial pattern around

Antennas for Global Navigation Satellite Systems, First Edition.
Xiaodong Chen, Clive G. Parini, Brian Collins, Yuan Yao and Masood Ur Rehman.

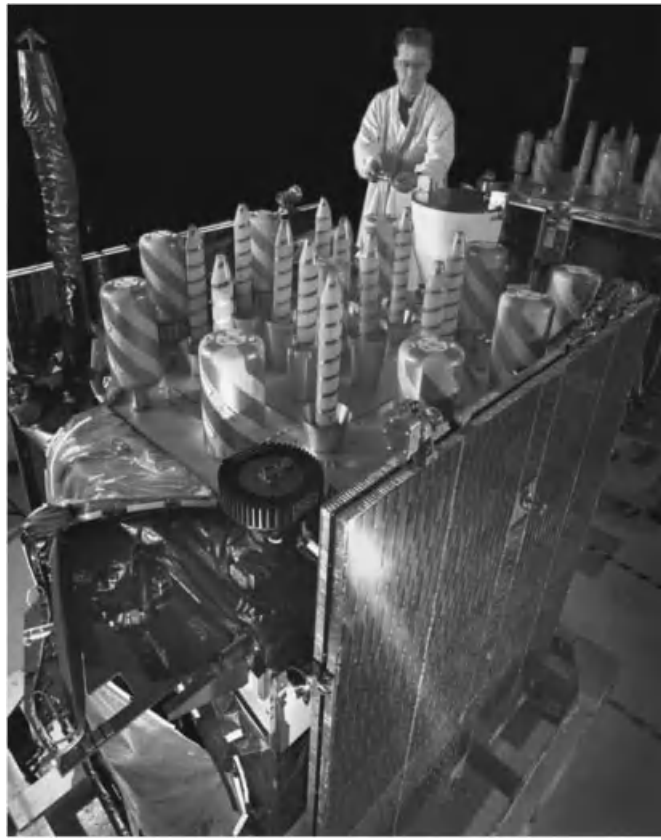

Figure 3.1 GPS III antenna farm (Lockheed Martin).

the centre of the array structure. The array element is a cavity-backed stacked microstrip patch with coaxial probe feeding as illustrated in Figure 3.3 [2].

The high-band element is a circular ring patch with two notches to achieve circular polarisation from a single coaxial feed point. The low-band element is excited by a pair of coaxial probes fed in quadrature to achieve the circular polarisation. An additional patch between the two elements acts as a ground plane for the high-band antenna. Between the metallic layers is a lightweight foam spacer, and each coaxial feed point includes a capacitive gap to improve matching. The measured radiation pattern for this element is shown in Figure 3.4 [3].

The array beamformer employs a fully corporate feed in order to achieve the bandwidth requirements; the equal length lines also provide low dispersion in

Table 3.1 Galileo navigation antenna array specification

Frequency plan:	
Low band	1145–1237 and 1259–1299 MHz
High band	1555–1595 MHz
Coverage pattern	12.67° from boresight with 2 dB isoflux window
Group delay variability across the field of view	Better than 30 mm pseudo-range error
Minimum gain at limit of coverage (LoC)	15.35 dBi low band, 14.85 dBi high band
Polarisation	Right hand circular
Maximum axial ratio	1.2 dB
Return loss	>20 dB
Mutual coupling to adjacent elements	<−30 dB

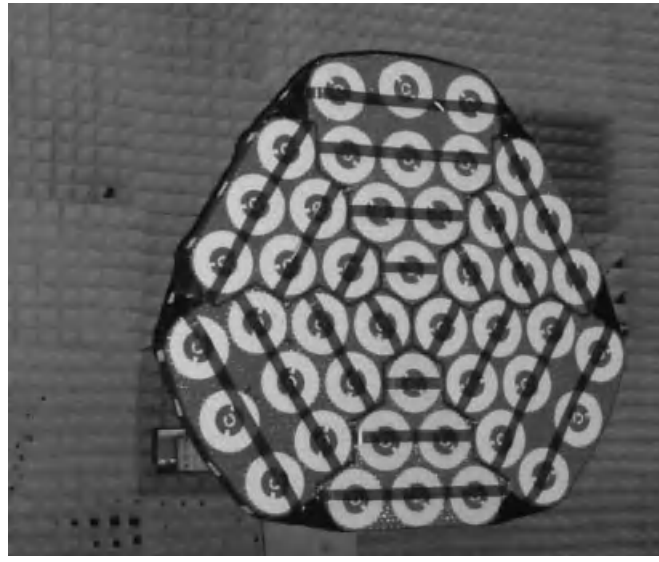

Figure 3.2 Flight model of Galileo navigation antenna array. Taken from [1]; copyright EurAAP; used with permission.

the signal transit time. The type A and B subarrays have their own beamformers and are fed by a central power divider (1:6) splitter with unequal arm lengths to implement sequential rotation [4] of the subarray feed elements (60° rotation and phase difference between adjacent subarrays). The radiation patterns for the complete array are shown in Figures 3.5 and 3.6 [1] for the two bands. In

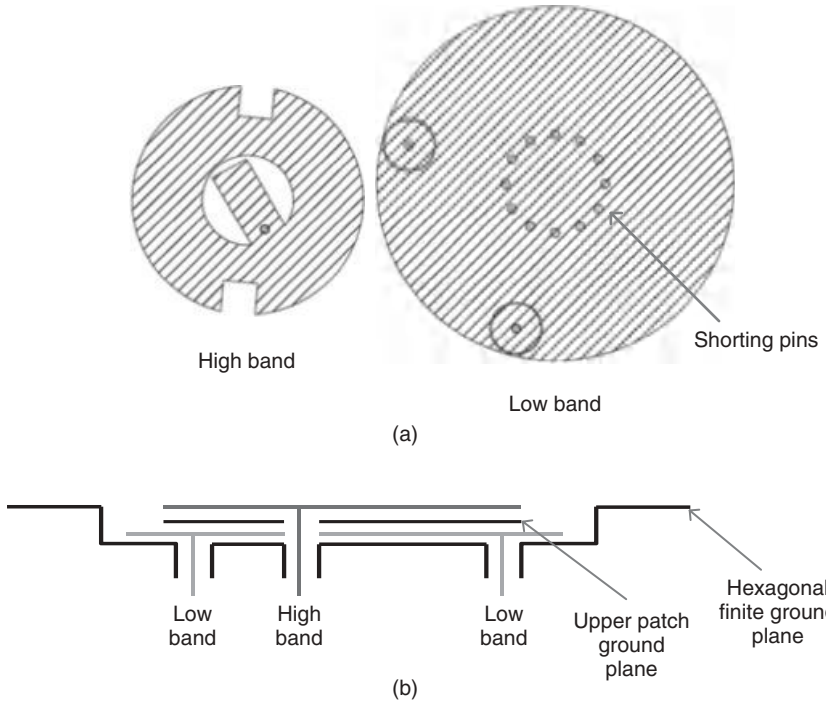

Figure 3.3 Stacked patch antennas: (a) plan view; (b) side view [2].

order to achieve the same limit of coverage angle for both bands the design has to accept a large gain dip at boresight for the upper band performance.

Of particular importance to a GNSS navigation beam is the group delay variation across the coverage zone, which can be calculated from the phase pattern in the coverage region at several frequencies within the operating band [5]. An example of this is shown in Figure 3.7 for the low band of Galileo (see also [6]), calculated using a simulated radiation pattern, the result showing a total variation that will manifest as a pseudo-range error of around 30 mm across the coverage region [7].

To achieve this level of accuracy in prediction of the group delay requires highly specialised modelling of the array that will take into account the effects of array mutual coupling and the effects of the spacecraft body. The results shown in Figure 3.6 were obtained using the finite integral time domain technique [8] giving a full electromagnetic model of the array, using the structure shown in Figure 3.8 [7]. The subtle effects of the spacecraft body

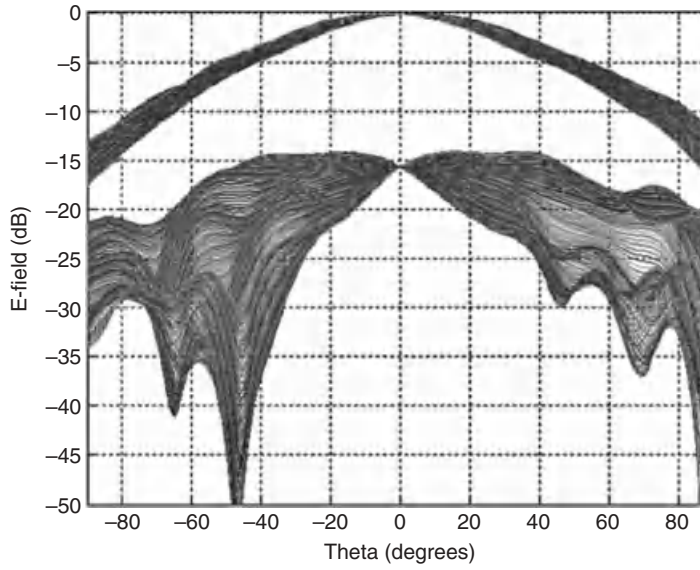

Figure 3.4 Measured co-polar and cross-polar radiation pattern for isolated element at 1228 MHz (for a number of phi cuts). Taken from [3]; copyright EurAAP; used with permission.

can be seen in Figure 3.9 where the edges of coverage gain levels are plotted both with the array in isolation and mounted on the spacecraft body model of Figure 3.8. Such a model required up to 7 million mesh cells with run times of the order of 24 hours.

Such a process is acceptable for final performance evaluation, but not suitable as a design process. The approach was to undertake a full wave simulation of the isolated array element including its ground plane; a generalised scattering matrix (GSM) of each element is then obtained using coaxial and spherical modal expansions from a hybrid 3D finite element modal analysis. The GSMs of the array elements are analytically connected by rotating and translating spherical modes to obtain the GSM for the whole array. This brings the modelling time down to a few minutes per frequency point, which is much more suitable for the design process; details of the analytical method can be found in [4]. It is essential to realise that, to achieve the level of modelling accuracy required, particularly in determining the accurate mutual coupling effect, an accurate model of the beam-forming network (BFN) must be achieved so that each array antenna element is terminated in the true complex impedance

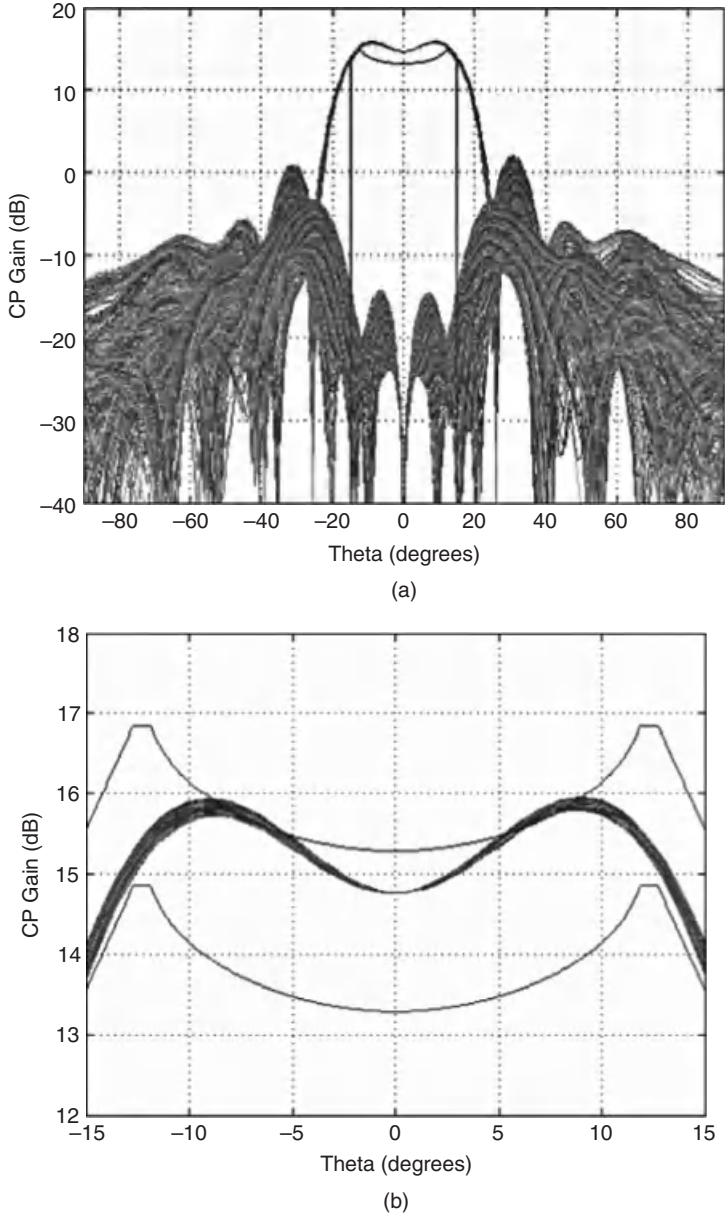

Figure 3.5 Co- and cross-polar gain radiation pattern for the low band (1237 MHz) for various phi cuts: (a) full pattern; (b) expanded region of coverage area. Taken from [1]; copyright EurAAP; used with permission.

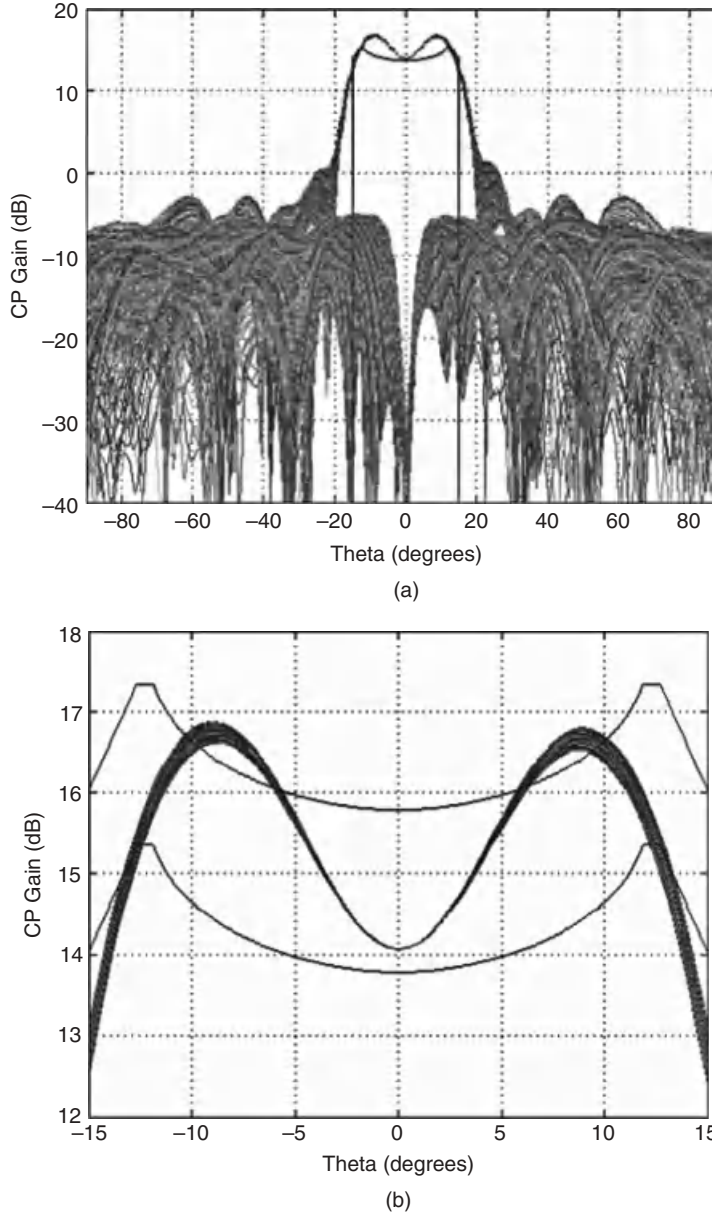

Figure 3.6 Co- and cross-polar gain radiation pattern for the high band (1575 MHz) for various phi cuts: (a) full pattern; (b) expanded region of coverage area. Taken from [1]; copyright EurAAP; used with permission.

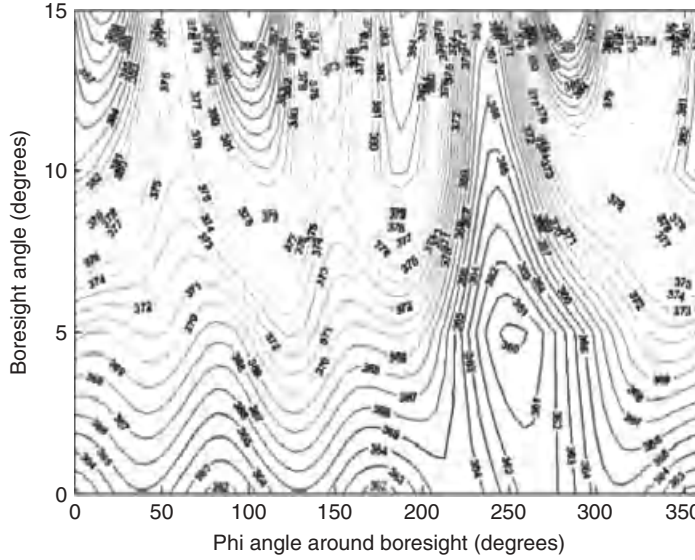

Figure 3.7 Simulated group delay (pseudo range in mm) for the 1150–1220 MHz band. Taken from [7]; copyright EurAAP; used with permission.

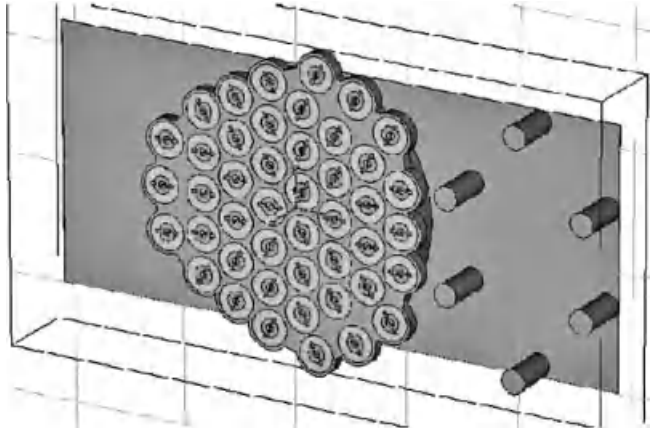

Figure 3.8 Galileo navigation array on spacecraft body model. Taken from [7]; copyright EurAAP; used with permission.

presented to it by the BFN. Details of the method employed for Galileo can be found in [6].

Helical arrays are a very popular choice of antenna for spacecraft and indeed the Sputnik satellite in 1957 brandished a helical antenna [9]. The use of helical

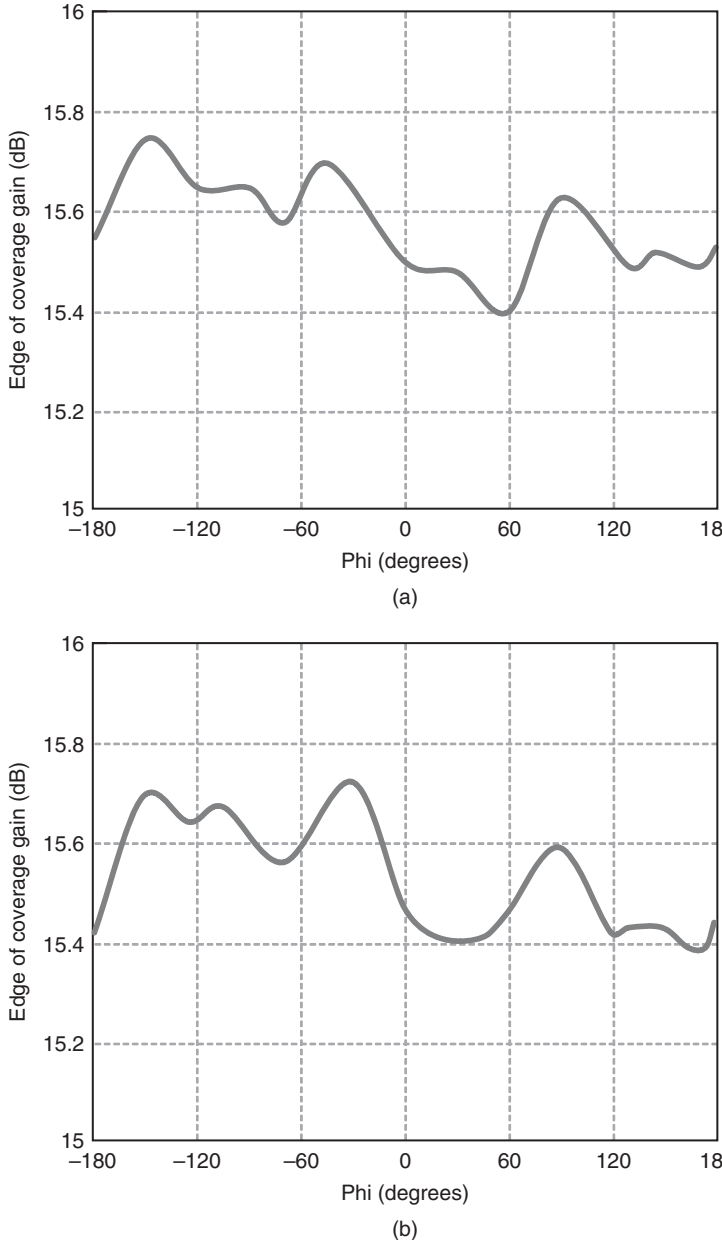

Figure 3.9 Edge of coverage gain value for 1220 MHz: (a) on infinite ground plane; (b) on spacecraft body model of Figure 3.8. Taken from [7]; copyright EurAAP; used with permission.

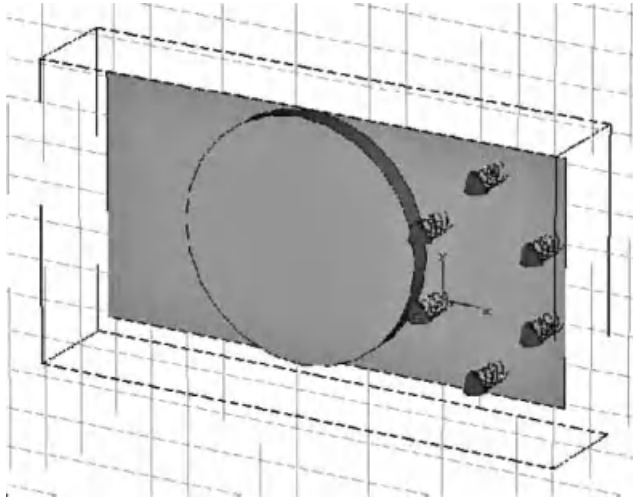

Figure 3.10 Galileo search and rescue helical antenna array on spacecraft body model. Taken from [7]; copyright EurAAP; used with permission.

antennas in space reflects their high gain, ease of fabrication and ease of generation of circular polarisation, details of which are given in Chapter 2.

Here we consider the Galileo search and rescue array antenna operating at 400 MHz, a spacecraft model of which is shown in Figure 3.10 [7] and a prototype photograph in Figure 3.11. Because of the 3D curved structure of the helical antenna modelling, using a rectangular grid for the finite integral time domain technique requires very small cell sizes ($\lambda/40$). Again the effect of the spacecraft body model, rather than an infinite ground plane, influenced the edge of coverage gain pattern by as much as 0.3 dB [7].

3.3 Special Considerations for Spacecraft Antenna Design

3.3.1 Passive Intermodulation Effects

It is essential that all transmit antennas on board a spacecraft do not interfere with other receivers via the process of passive intermodulation (PIM). Here an interfering frequency component is generated by combining several of the transmit frequencies (e.g. E5, E6 and L1 for Galileo) seeing a nonlinear input–output characteristic and so generating a mixing effect [10]. Such nonlinearity can

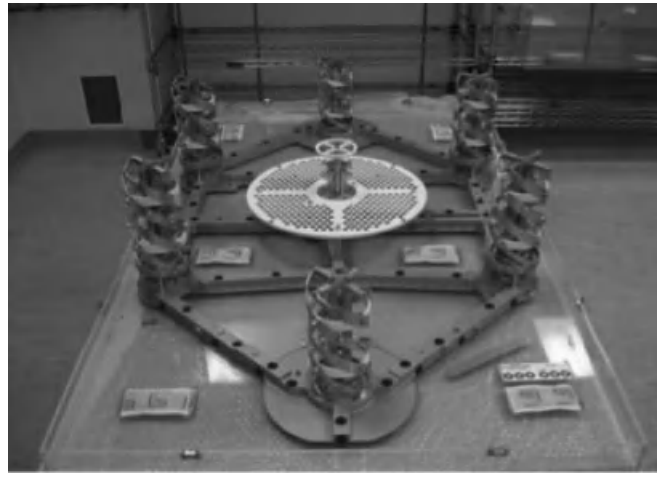

Figure 3.11 Prototype search and rescue antenna array for Galileo (Surrey Satellite Technology Ltd.).

occur even at a junction between different metals that form the transmission line or antenna input terminals. Possible sources of PIM include:

- Non-homogeneous contacts between metals of different types.
- Presence of oxides, particularly across gaps and joints (often associated with RF connectors).
- Local lack of uniformity in the conductivities of the materials involved.
- Intrinsically nonlinear materials (ferromagnetic, ferrites, stainless steel, dielectrics loaded with conductive powders or granules).

For example, with metal surfaces separated by oxide layers 0.1 μm thick, nonlinear electron tunnelling through the barrier occurs, giving rise to low-level PIM. Nonlinearities also arise due to micro-cracks or voids in metal structures and surface contamination. Such levels of PIM generation need to be very low: for example, the Galileo search and rescue UHF band needs to be less than −145 dBm which is over 30 dB below the thermal noise floor [2]. A self-diplexed antenna is more prone to PIM effects. If there are three frequencies f_1, f_2, f_3 then the order of the PIM is second order, $(f_1 - f_2)$ or $(f_1 + f_2)$; third order, $(f_1 - f_2 + f_3)$ or $(2f_1 - f_2)$, etc. PIM effects often

manifest themselves while thermal cycling is undertaken and so this usually forms part of the PIM testing programme for a spacecraft antenna.

3.3.2 Multipactor Effects

The multipactor effect is an electron resonance phenomenon associated with operating with high RF powers in a near vacuum ($<10^{-5}$ torr) and results in electrical breakdown that can destroy RF components or transmission lines.

If one considers a simple parallel plate structure with near the peak of an RF voltage across it, any available free electrons are accelerated across the gap by the RF field. In a near vacuum the mean free path of an electron is considerably larger than the spacing between the electrodes. On hitting the temporarily positive electrode, these 'primary' electrons liberate 'secondary' electrons from the electrode surface. If the number of secondary electrons liberated per primary electron is greater than unity then a net increase of free electrons occurs. A reversal of the RF field now accelerates these newly created free electrons back across the gap, and if the electron transit time across the gap is approximately equal to an odd number of half periods of the applied RF voltage, multipactor breakdown is experienced after a number of RF cycles [11]. Thus gaps in the antenna and transmission line construction need to be avoided, as should sharp edges that can act to concentrate electric field strength. Surface contamination can often increase secondary emission, as can thermal effects on the material. With multiple high-power carriers feeding the same antenna/transmission line, adverse phasing can result in high peak voltages in a very short time period and so multipactor testing often occurs with much higher RF powers than would be the normal operating case. As for PIM tests, multipactor testing includes thermal cycling.

References

1. Monjas, F., Montesano, A., Montesano, C. *et al.*, 'Test campaign of the IOV (In Orbit Validation) Galileo system navigation antenna for global positioning,' Proceedings of the Fourth European Conference on Antennas and Propagation (EuCAP), 2010.
2. Montesano, A., Montesano, C., Caballero, R. *et al.*, 'Galileo system navigation antenna for global positioning', Second European Conference on Antennas and Propagation (EuCAP), 2007.
3. Rubio, J., Gonzalez, M.A., Zapata, J. *et al.*, 'Full-wave analysis of the GALILEO system navigation antenna by means of the generalized scattering matrix of a finite array', First European Conference on Antennas and Propagation (EuCAP), 2006.
4. Smith, M.S. and Hall, P.S., 'Analysis of radiation pattern effects in sequentially rotated arrays', *IEE Proceedings (Microwaves, Antennas and Propagation)*, **141** (4), 313–320, 1994.

5. Arenas, S., Monjas, F., Montesano, A. *et al.*, 'Performances of GALILEO system navigation antenna for global positioning', Proceedings of the 5th European Conference on Antennas and Propagation (EUCAP), 2011, pp. 1018–1022.
6. James, P., Maxwell-Cox, G.G. and Potter, S.V., 'Modeling of a complex beam forming network for a phased array antenna', Second European Conference on Antennas and Propagation (EuCAP), 2007.
7. Maxwel-Cox, G.G. and Smith, M.S. 'Full-wave modelling of the antenna for the Galileo satellite', Second European Conference on Antennas and Propagation (EuCAP), 2007.
8. CST Microwave Studio (CST MWS) from Computer Simulation Technology.
9. Kraus, R.J.M., *Antennas for all Applications*, McGraw-Hill, New York, 2002.
10. Dumoulin, J.-G., 'Passive intermodulation and its effect on space programs', IEE Colloquium on Screening Effectiveness Measurements, 1998.
11. Tang, W.-C. and Kudsia, C.M., 'Multipactor breakdown and passive intermodulation in microwave equipment for satellite application', Proceedings of IEEE MILCOM'90, Monterey, CA, September 30–October 3, 1990, Vol. 1, pp. 181–187.

4

Terminal GNSS Antennas

In the last few decades, the variety of electronic terminal devices integrated with global positioning, navigation and time services has grown dramatically, so the design of terminal antennas for GNSS applications is attracting more and more interest. This chapter introduces three kinds of RHCP antennas commonly used for GNSS reception, namely microstrip patch antennas, quadrifilar helices and spirals. In addition, a novel PIFA antenna for GNSS application will be presented in the last section of the chapter.

4.1 Microstrip Antenna for Terminal GNSS Application

As discussed in Chapter 2, the microstrip patch antenna has been successfully modified to radiate a CP wave. Microstrip CP antennas have a compact size for terminal GNSS applications.

There are two kinds of microstrip antennas in terms of the feed: single-feed or multi-feed antennas.

4.1.1 Single-Feed Microstrip GNSS Antennas

The major advantage of single-feed CP microstrip antennas is their simple structure, which does not require an external polariser network. They can be realised more compactly, using less board space than the dual-feed configurations. Many designs of single-feed CP microstrip antennas with square or circular patches have been reported. A corner-truncated square patch printed on an FR4 substrate for RHCP has been discussed in Chapter 2. Other techniques include embedding a cross-slot of unequal arm lengths [1], embedding

Antennas for Global Navigation Satellite Systems, First Edition.
Xiaodong Chen, Clive G. Parini, Brian Collins, Yuan Yao and Masood Ur Rehman.

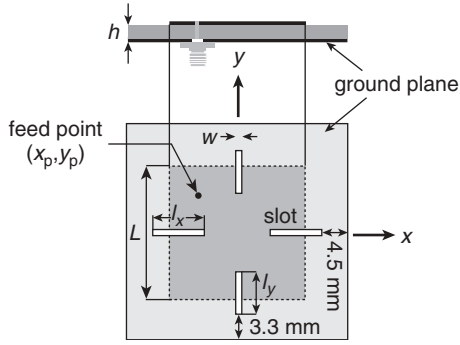

Figure 4.1 Geometry of the single-feed, slotted ground plane microstrip antenna [10]. Reproduced with permission of John Wiley & Sons, Inc.

a Y-shaped slot of unequal arm lengths [2], inserting slits or spur lines at the patch boundary [3, 4], truncating patch corners or tips [5, 6], introducing small peripheral cuts at the boundary of a circular patch [7], adding a tuning stub [8] or a bent tuning stub [9], and so forth.

4.1.1.1 Design with a Slotted Patch and Ground Plane

Two kinds of slotted antennas will be discussed here: a square patch with two pairs of slot on the ground plane [10]; and a GNSS antenna with two pairs of slits on the square patch [10].

The geometry of the first type of single-feed CP microstrip antenna for GNSS application is shown in Figure 4.1. It is etched on an FR4 substrate of thickness 1.6 mm with a relative permittivity of 4.4. The antenna element for the GNSS band is a top square patch of $43 \times 43\,\text{mm}^2$ and the dimension of the finite ground plane is $60 \times 60\,\text{mm}^2$. The width of the slotted pair embedded on the ground plane is 1 mm. To achieve optimum CP radiation at 1575 MHz, the lengths of the slotted pair along the x- and y-axes are selected to be $l_x = 13.5$ mm and $l_y = 11.5$ mm, respectively. To obtain RHCP, the probe feed is located at the coordinate $(x_p, y_p) = (-9, 9)$ mm, assuming that the centre of the patch is the origin.

The simulated and measured return loss and axial ratio for this are shown in Figure 4.2 for a 10 dB impedance bandwidth of 70 MHz and CP bandwidth of 22 MHz centred at 1575 MHz. Figure 4.3 shows the RHCP radiation patterns in two orthogonal planes.

The geometry of the second type of antenna for GNSS application is illustrated in Figure 4.4 [10]. The basic dimension of this antenna is similar to the first one, except that the 1 mm wide slits are formed at the edges of the square

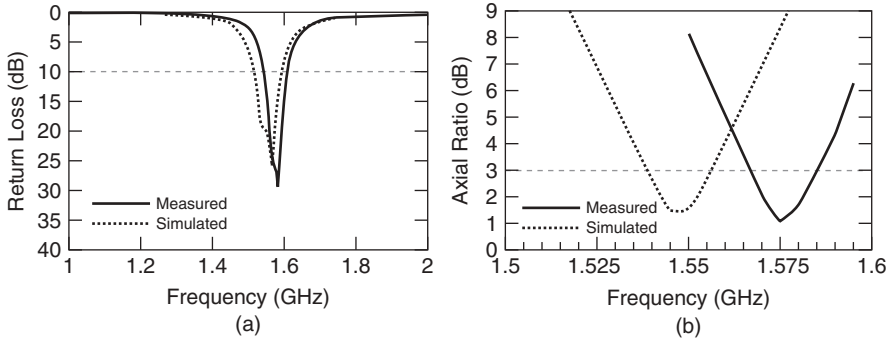

Figure 4.2 Simulated and measured (a) return loss and (b) axial ratio of the single-feed, slotted ground plane microstrip antenna [10]. Reproduced with permission of John Wiley & Sons, Inc.

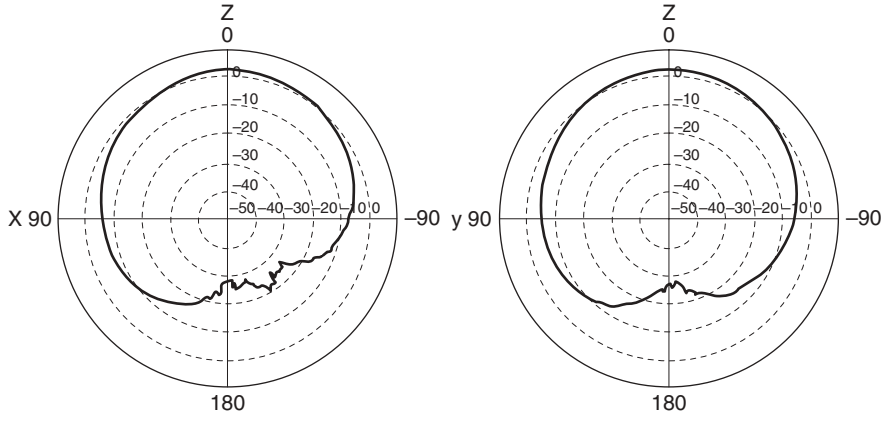

Figure 4.3 RHCP radiation patterns in two principal planes of the single-feed, slotted ground plane microstrip antenna [10]. Reproduced with permission of John Wiley & Sons, Inc.

patch. In order to achieve optimum CP radiation at 1575 MHz, the lengths of the slits along the x- and y-axes are $l_x = 6.5$ mm and $l_y = 5.5$ mm, respectively. To excite an RHCP wave, the probe feed is again located at the coordinate $(x_p, y_p) = (9, 9)$ mm.

Figure 4.5 shows the simulated and measured return loss and axial ratio for the slotted-patch antenna. It has a 10 dB impedance bandwidth of 55 MHz and a CP bandwidth of 18 MHz. The difference between simulated and measured results is caused by fabrication imperfections and the tolerance of the

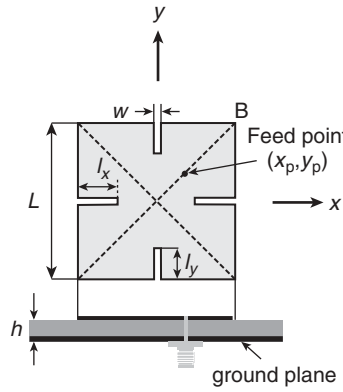

Figure 4.4 Geometry of the slotted square patch microstrip antenna [10]. Reproduced with permission of John Wiley & Sons, Inc.

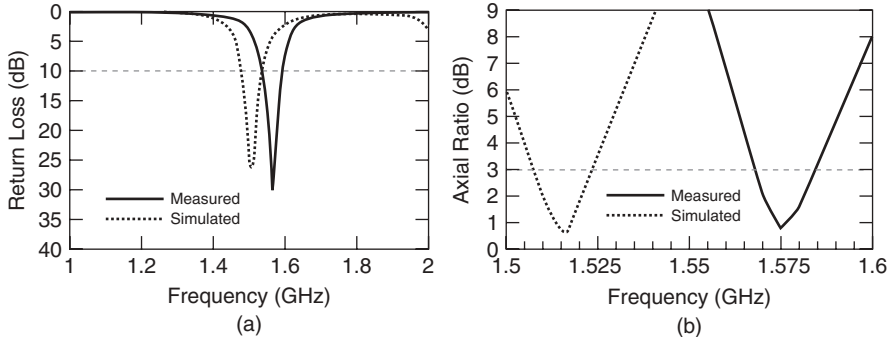

Figure 4.5 Simulated and measured (a) return loss and (b) axial ratio of the slotted square patch microstrip antenna [10]. Reproduced with permission of John Wiley & Sons, Inc.

permittivity of the substrate. Figure 4.6 shows the RHCP radiation patterns in two orthogonal planes.

It can be seen that both kinds of antennas can be used for GNSS applications. Comparing these two designs, it seems that the antenna with the slotted ground plane has a better CP and impedance bandwidth, and also a higher peak gain.

4.1.1.2 Design with Shorting Wall

The size of a microstrip patch antenna is basically determined by its resonant length and width. The reduction in size can be achieved by using a

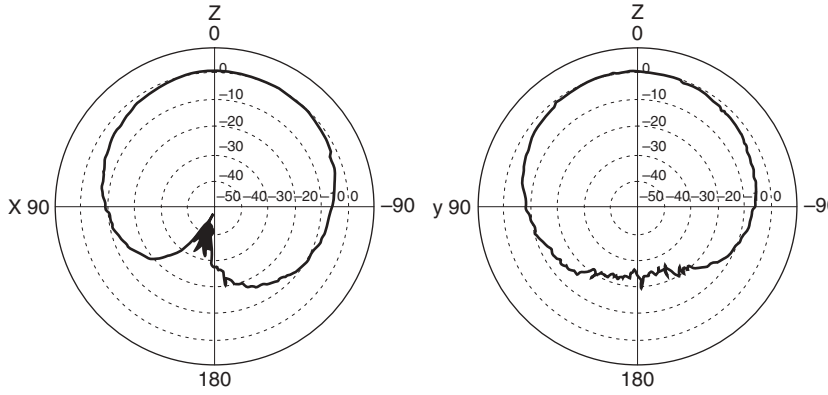

Figure 4.6 RHCP radiation patterns in two principal planes of the slotted square patch microstrip antenna [10]. Reproduced with permission of John Wiley & Sons, Inc.

high-permittivity substrate and/or a smaller substrate height, but this results in a lower radiation efficiency, a lower antenna gain and a narrower bandwidth. Various techniques have been explored to reduce the size of a CP patch antenna. One of these techniques is to use a shorting wall. The side length of a resonant rectangular patch antenna is of the order of a half wavelength. The length of the antenna is reduced by a factor of two if the patch is short-circuited to ground at the zero potential plane. The result is a resonant rectangular patch with length of order $\lambda/4$, called a quarter-wave patch or shorted rectangular patch antenna.

The geometry of a shorted rectangular patch antenna is shown in Figure 4.7 [11]. The feed point is centred on the x-axis and the shorting wall is at the patch edge. The antenna is RHCP, using a single feed with a 45° truncated segment (perturbation area) at the edge of the patch with side length ΔL. The patch has a side length $L/2$ and width W. The input impedance and resonant frequency of the antenna can be controlled by changing the length of the shorting wall. The antenna has the following parameters: permittivity of the substrate, 2.2; thickness of the substrate, 1.6 mm; length $L/2$, 29.0 mm; width, 40.4 mm; width of shorting wall, 28.32 mm; length of truncated corner, 2.2 mm.

Figure 4.8 shows a comparison between the simulated and measured return loss for the proposed GNSS antenna. There is a small deviation between the measured and theoretical results, which may be due to fabrication imperfections. Figure 4.9 shows the simulated radiation pattern of the antenna at 1.575 GHz. Figure 4.10 shows the simulated axial ratio results of the antenna. The measured and simulated results are accepted and satisfy the requirements for a GNSS antenna.

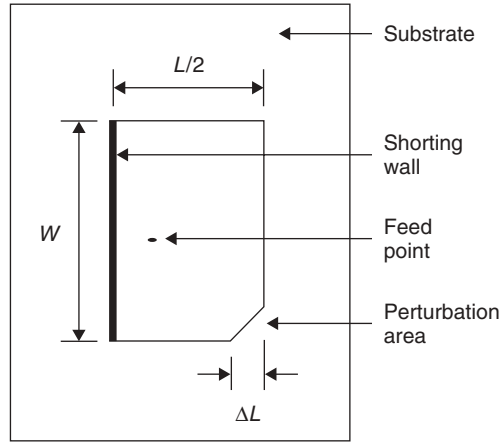

Figure 4.7 Geometry of the shorting-wall rectangular microstrip patch antenna [11]. Reproduced with permission from JATIT.

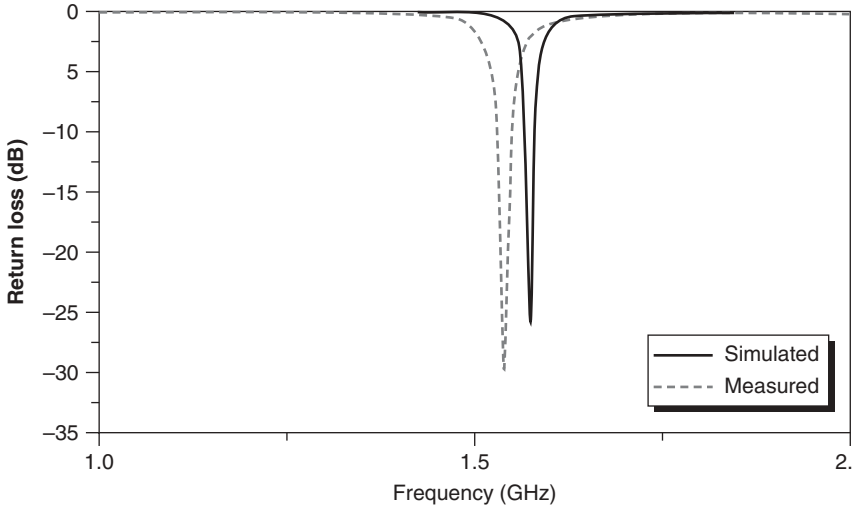

Figure 4.8 Simulated and measured return loss of the shorted rectangular patch antenna [11]. Reproduced with permission from JATIT.

4.1.2 Dual-Feed Microstrip GNSS Antennas

Compared with single-feed structures, dual-feed microstrip GNSS antennas have external polarisers and their structure is more complicated. However, dual-feed microstrip GNSS antennas have high polarisation purity. As shown

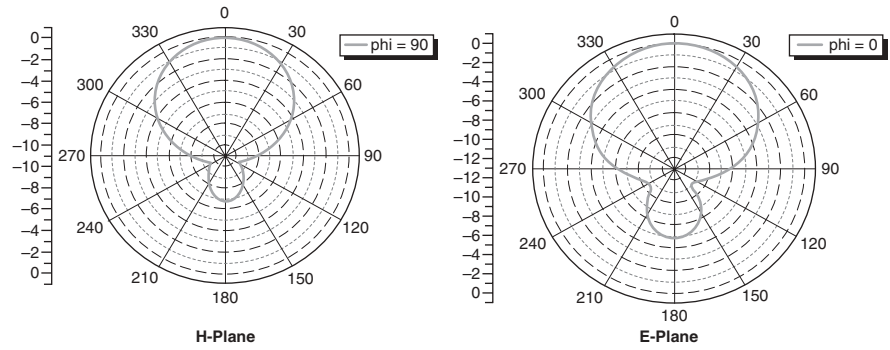

Figure 4.9 Radiation patterns of the shorting-wall rectangular patch antenna [11]. Reproduced with permission from JATIT.

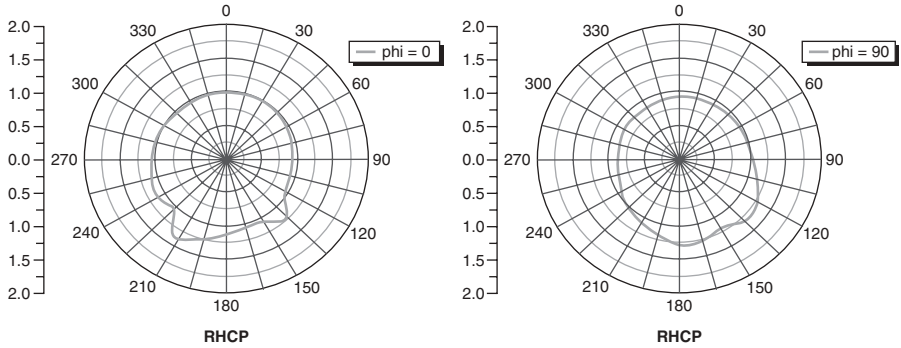

Figure 4.10 Axial ratio of the shorting-wall rectangular patch [11]. Reproduced with permission from JATIT.

in Figure 4.11, the proximity-fed microstrip patch antenna supports two orthogonal modes that combine to deliver RHCP operation. Capacitively coupled probe feeds are used to increase impedance matching and bandwidth. Some methods have been presented in the literature to enhance gain at low angles – for example, employing a folded conducting wall or a dielectric lens and a pyramidal ground, using high-permittivity substrates, or using a four circular slot–rings array. The design described here employs a high-permittivity substrate for encapsulating the patch to increase the gain at low angles. The permittivity of the substrate is 10.2. The schematic of the 90° balun which is required to excite the antenna is shown in Figure 4.12. It comprises a cascaded 3 dB Wilkinson power divider and a 90° phase shifter. It was printed on a microwave substrate with a thickness of 1.5 mm and

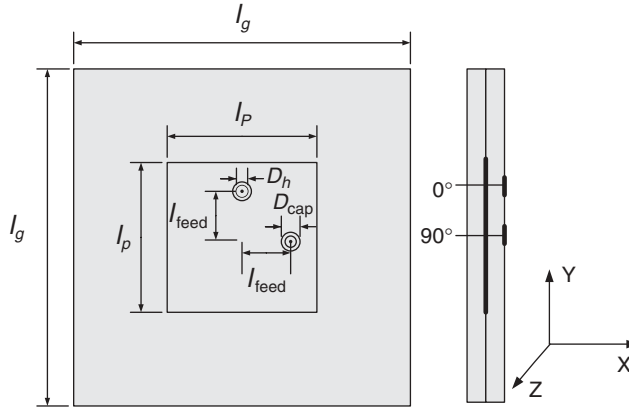

Figure 4.11 Geometry of the dual-feed, capacitively fed microstrip patch antenna. (Length of the patch, 28 mm; diameter of the capacitive cap, 4 mm; distance between the feed and the centre of the patch, 8 mm; length of the ground, 100 mm, diameter of the hole in patch, 3 mm.)

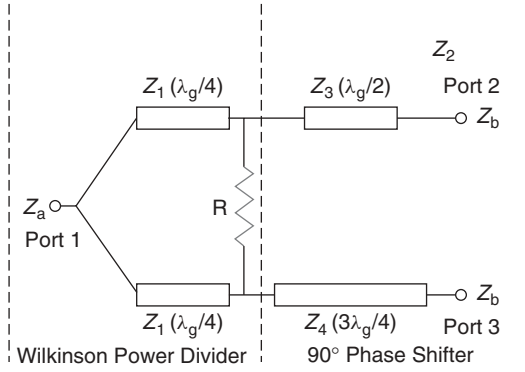

Figure 4.12 Schematic of the 90° balun.

dielectric constant 2.65. For convenience, the characteristic impedances of the input and output ports of the balun are assumed to be 50 Ω.

The antenna layer and the feed layer were fixed together. A 50 Ω SMA connector was fitted at the feed point and the Wilkinson divider was terminated with a 100 Ω surface-mounted chip resistor. The final design antenna is shown in Figure 4.13. Figure 4.14 shows the simulated and measured S_{11}, with reasonable agreement between the simulated and measured data. The measured

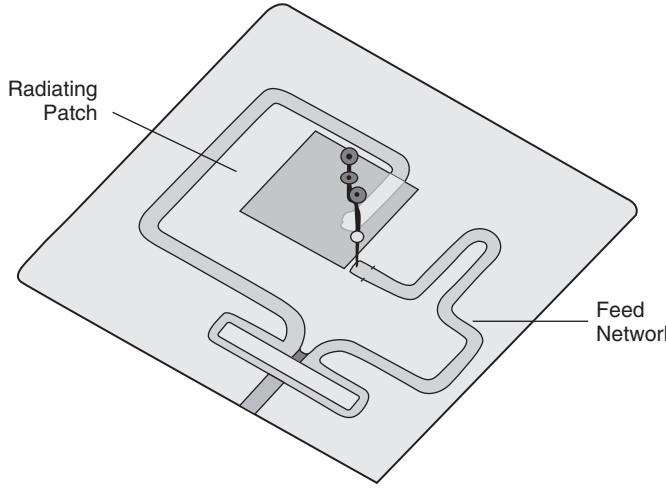

Figure 4.13 Whole geometry of the dual-feed, proximity-fed microstrip patch antenna.

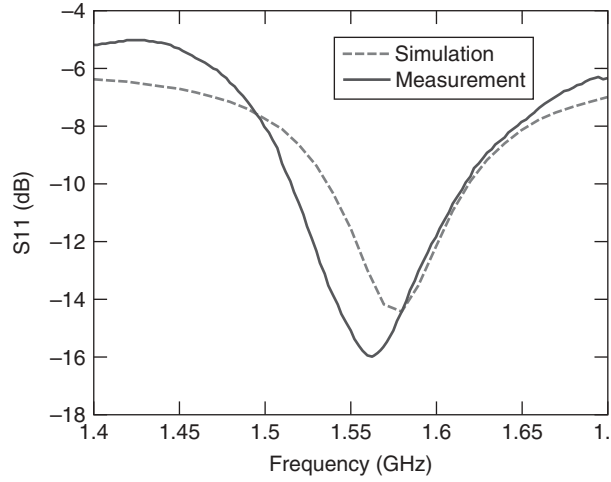

Figure 4.14 Simulated and measured S_{11} of the dual-feed, proximity-fed microstrip patch antenna.

return loss exceeds −15 dB over the operating frequency band of 1.575 GHz. Figure 4.15 shows the radiation pattern at 1575 MHz, indicating that the polarisation purity is rather good as well. As shown, a broad pattern coverage and high gain at low angles are achieved.

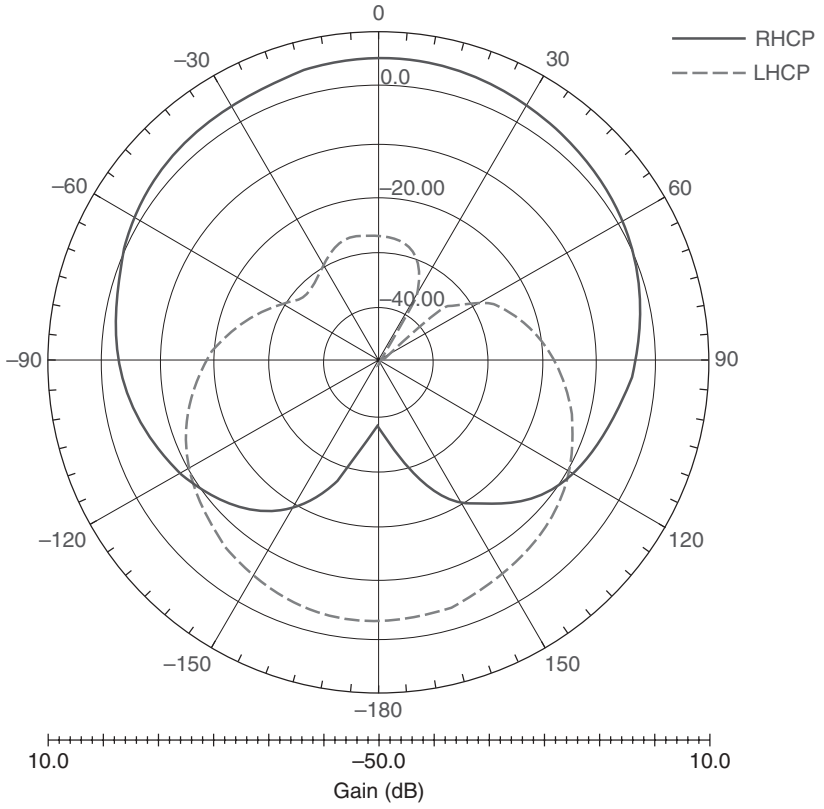

Figure 4.15 Radiation pattern of the dual-feed, proximity-fed microstrip patch antenna at 1575 MHz.

4.1.3 Design with Ceramic Substrate

An effective way to achieve a compact GNSS antenna is to use a high-permittivity substrate such as ceramic. Figure 4.16 shows the geometry of a CP square-disc ceramic chip antenna mounted on a test circuit board for GNSS operation at 1575 MHz [12]. The test circuit board in this study was a 0.8 mm grounded FR4 substrate of dimension $50 \times 50\,\text{mm}^2$. The square-disc ceramic chip had a height of 4 mm and a cross-section of $17.5 \times 17.5\,\text{mm}^2$, and its relative permittivity was 45. A square radiating patch of dimension $12.6 \times 12.6\,\text{mm}^2$ was printed and centred on the top surface of the ceramic. A conducting ground plane is formed on the lower surface of the ceramic. Two identical feeds in the form of conformal strips of width 2.2 mm and length 4 mm were printed at the centres of two adjacent side surfaces of the ceramic chip

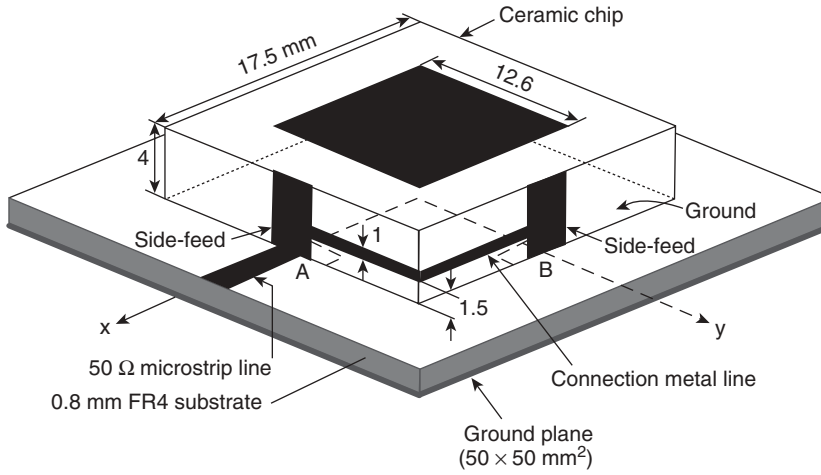

Figure 4.16 Geometry of square-disc ceramic antenna [12]. Reproduced with permission of John Wiley & Sons, Inc.

and were used to excite the antenna by capacitive coupling. Good impedance matching can be obtained by adjusting the width of the two side-feeds, which was chosen to be 2.2 mm.

A connecting metal line 1 mm wide was printed between the two side-feeds. This serves as a delay line to provide a 90° phase difference between the two side-feeds. This phase difference can be obtained by adjusting the distance (1.5 mm in this design) between the connection metal line and the ground conducting patch in the proposed design. Two small notches were cut near points A and B in the ground conducting patch to avoid the short-circuiting of the two side-feeds to the ground. To create RHCP radiation, a 50 Ω microstrip feed line printed on the test circuit board is connected to the side-feed at point A; this provides a 90° phase lead, relative to the feed at point B. This arrangement leads to the excitation of two orthogonal resonant modes of equal amplitude with a 90° phase difference for RHCP operation. If LHCP operation is desired for some other applications, the microstrip feed line can be connected to the side-feed at point B, reversing the relative phases of the feeds.

Figure 4.17 shows the measured return loss of the square-disc ceramic antenna. The impedance bandwidth for a 10 dB return loss is 12 MHz (1570–1582 MHz) centred at 1575 MHz. In addition, there are two resonances excited at very close frequencies, which are contributed by the excitation of the two side-feeds. Figure 4.18 shows the measured axial ratio in the broadside direction of the constructed prototype. With a 3 dB axial ratio a CP bandwidth

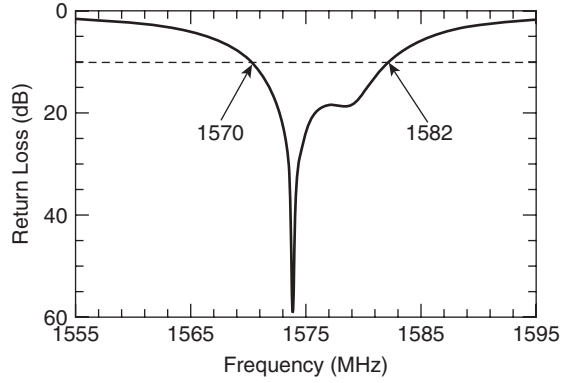

Figure 4.17 Measured return loss of the square-disc ceramic antenna [12]. Reproduced with permission of John Wiley & Sons, Inc.

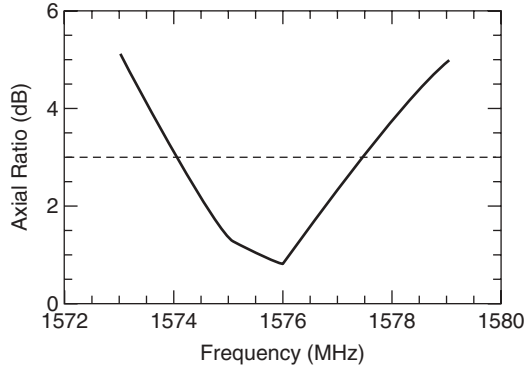

Figure 4.18 Measured axial ratio of the square-disk ceramic antenna [12]. Reproduced with permission of John Wiley & Sons, Inc.

of about 3.5 MHz is obtained, which covers the required bandwidths for GPS operation at 1575 MHz. The radiation patterns at 1575 MHz in two principal planes are also plotted in Figure 4.19, and the gain is shown in Figure 4.20. The measured antenna gain is 3.0–3.4 dBi for operating frequencies across the CP bandwidth with a 3 dB axial ratio.

4.2 Spiral and Helix GNSS Antennas

4.2.1 Helix Antennas

Resonant quadrifilar helical antennas are particularly attractive for GNSS applications because they are small in size and provide circular polarisation and wide

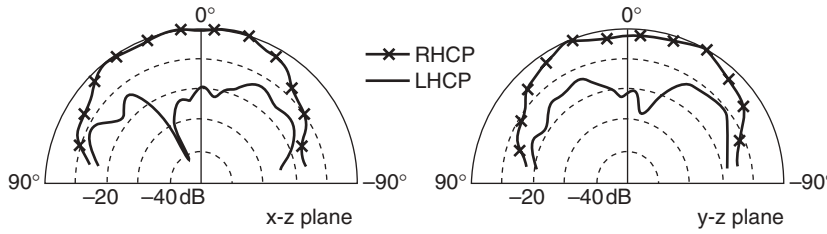

Figure 4.19 Measured radiation patterns in two principal planes at 1575 MHz [12]. Reproduced with permission of John Wiley & Sons, Inc.

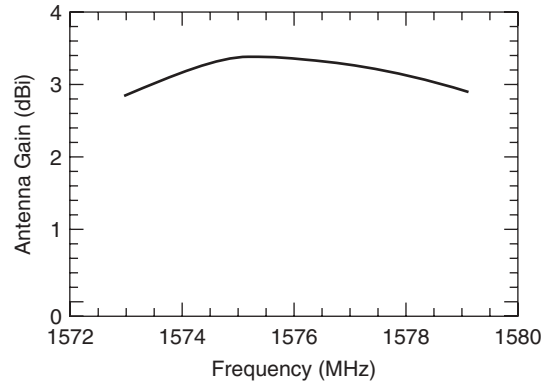

Figure 4.20 Measured antenna gain of the square-disk ceramic antenna [12]. Reproduced with permission of John Wiley & Sons, Inc.

elevation coverage. Gerst and Worden studied four-start, six-start and eight-start helix antennas and showed that the antenna can have different radiation patterns and polarisations, and achieve high gain and wide bandwidth [13]. The resonant fractional-turn quadrifilar helix antenna was introduced by Kilgus [14] in 1968. He described a half-turn, half-wavelength quadrifilar helix as a loop-dipole antenna and showed that circular polarisation is provided, with a wide beamwidth and a cardioid-shaped radiation pattern [15, 16]. The physical structure of the resonant quadrifilar helix proposed in [14] consists of two orthogonal fractional-turn bifilar helical antennas fed in phase quadrature. Each helix produces a toroidal CP pattern. The combination of two orthogonal bifilar helices provides a directive CP pattern with the pattern direction determined by the phasing between the two helices. The arrangement consists of two orthogonally balanced antennas, each of which must be fed through a balun.

An example of a design of a printed half-wavelength quadrifilar helix antenna consisting of four microstrip-fed helical elements with four opposite radial

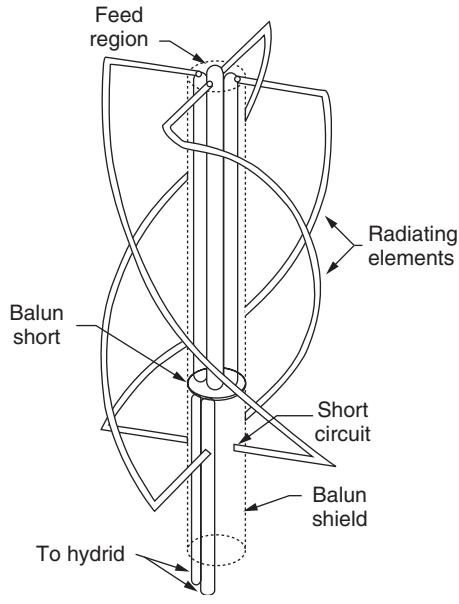

Figure 4.21 Physical configuration of conventional half-turn, half-wavelength quadrifilar helical antenna with Pawsey stub baluns [17]. Reproduced with permission from IET.

strips is shown in Figure 4.21 [17]. This design substitutes microstrip-fed helical elements for conventional folded or split-sheath baluns. Since the centre conductor of each microstrip-fed helical element is connected to the opposite radial strip, this connection causes equal currents of opposite phase to flow on the ground surface of the microstrip feed line and the adjoining radial strip. The ground plane of the microstrip feed line serves as the major radiating element of the resonant quadrifilar helix antenna.

Figure 4.21 shows the configuration of a conventional half-turn, half-wavelength volute with folded baluns. The upper end of each helical element is bent to connect to its feed point and the lower end is connected to the balun shield. At the feed point, opposite helical elements are fed in anti-phase using a Pawsey stub balun to form two independent bifilar (balanced) helices. These two bifilar helices are fed in phase quadrature from a 90° hybrid to produce a cardioidal radiation pattern with circular polarisation over the upper hemisphere.

Figure 4.22 shows a printed half-turn, half-wavelength quadrifilar helix fed with microstrip infinite baluns [17]. The ground plane of each microstrip feed line serves as one of the elements of the bifilar helices. At the feed point, the

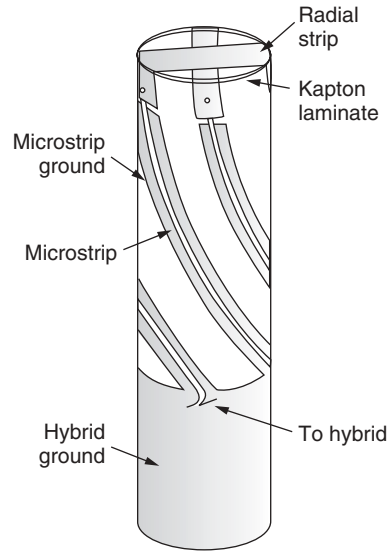

Figure 4.22 Printed half-turn, half-wavelength quadrifilar helix with infinite microstrip baluns [17]. Reproduced with permission from IET.

centre conductor of the microstrip feed line is soldered to the opposite radial strip. This causes balanced currents to flow on the outer ground surface of the microstrip feed line and the connecting radial strip. This type of balun does not cause any impedance transformation, so the input impedance of each microstrip-fed helical element can be matched to a 50 Ω feed line by minor adjustment of the opposite radial strip, without the need for a matching network.

The 90° phase relationship between the two pairs of helices can be achieved by exciting the four microstrip-fed helical elements with 0°, 90°, 180° and 270° phase differentials. The feed networks can be hybrid types such as the branch line or rat-race coupler, or T-splitters of either matched or unmatched form. Feeds using hybrid couplers and matched T-splitters incorporate a fourth port with an absorbing load. These three types of feeding networks give good isolation between the output ports and will generally provide a wider axial ratio bandwidth than simple splitters. In the prototype design we used a branch-line coupler to generate the phase quadrature between two bifilar helices.

Figure 4.23 shows the measured return loss for the microstrip-fed printed half-turn, half-wavelength quadrifilar helix. The resonant frequency of the antenna is at 1.575 GHz with return loss less than −30 dB. The bandwidth with l0 dB return loss is 1.6% of the centre frequency.

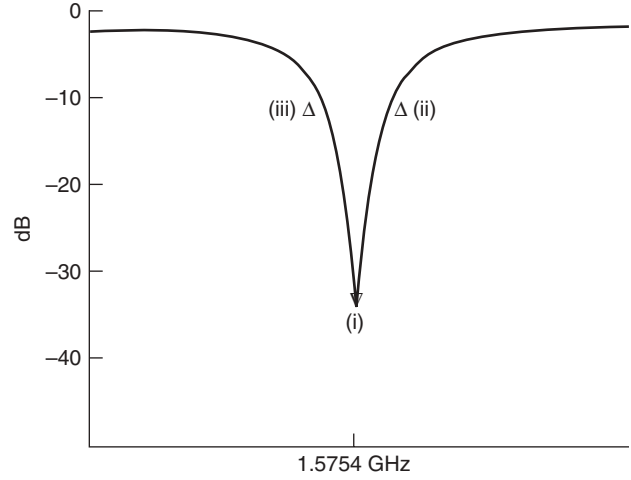

Figure 4.23 Measured return loss of microstrip-fed printed half-turn, half-wavelength quadrifilar helix antenna [17]. Reproduced with permission from IET.

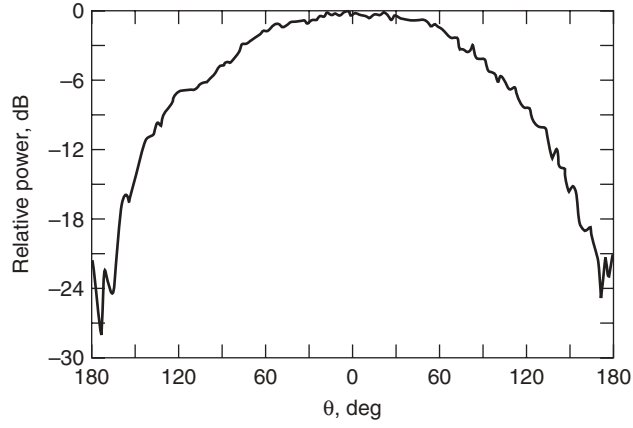

Figure 4.24 Measured radiation pattern for printed microstrip-fed volute antenna [17]. Reproduced with permission from IET.

Figure 4.24 shows the measured radiation pattern of a microstrip-fed printed half-turn, half-wavelength quadrifilar helix antenna. As shown in Figure 4.24, a broad axial beam is obtained with a half-power beamwidth of $\theta > 145^\circ$. The front-to-back ratio exceeds 20 dB, which is good for the rejection of multipath signals reflected from the ground.

4.2.2 Spiral Antennas

As discussed in Chapter 2, a spiral antenna can provide circular polarisation characteristics and desirable impedance matching, radiation pattern and gain as long as the parameters of the antenna are properly chosen. It radiates from a region where the circumference of the spiral equals one wavelength. This is called the active region of the spiral. Each arm of the spiral is fed 180° out of phase, so when its circumference is one wavelength the currents at complementary or opposite points on each arm of the spiral add in phase in the far field. As shown in Figure 4.25 [18], the low-frequency operating point of the spiral is determined theoretically by the outer radius as given by

$$f_{\text{low}} = c/2\pi r_2 \tag{4.1}$$

where c is the speed of light. Similarly the high-frequency operating point is determined by the inner radius r_1,

$$f_{\text{high}} = c/2\pi r_1 \tag{4.2}$$

In practice, the low-frequency point will be greater than the predicted value of Equation 4.1 due to reflections from the end of the spiral. The reflections can be minimised by using resistive loading at the end of each arm or by adding conductivity loss to some part of the outer turn of each arm.

An example is given below of the design of a single-arm Archimedean spiral antenna (ASA) for GNSS application [18]. The antenna operates at a

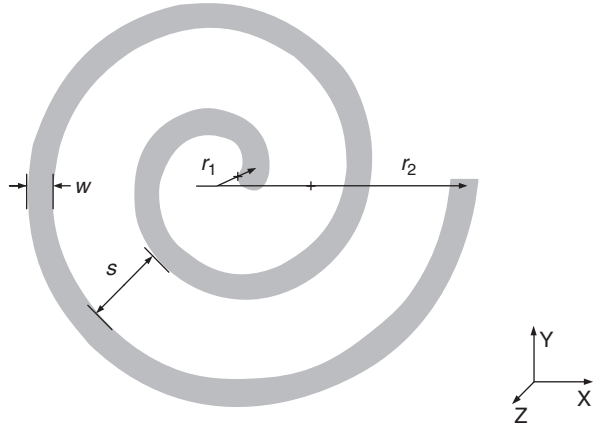

Figure 4.25 Geometry of the Archimedean spiral antenna [18]. Reproduced by permission of © 2010 IEEE.

centre frequency of 1.575 GHz by choosing $N = 3r_1 = s = w = 0.336$ cm, giving $r_2 = 2.7$ cm. The antenna was fed using a coaxial feed and a prototype was fabricated on FR4 of dielectric constant $\varepsilon_r = 4.9$ with a thickness of 1.54 mm. Photographs of the fabricated antenna can be seen in Figure 4.26. Figures 4.27 and 4.28 show the simulated and measured return loss, respectively, indicating a good resonance at 1.575 GHz. The measured radiation patterns at both $x-z$ and $y-z$ planes are shown in Figure 4.29 and the antenna has an omnidirectional radiation pattern.

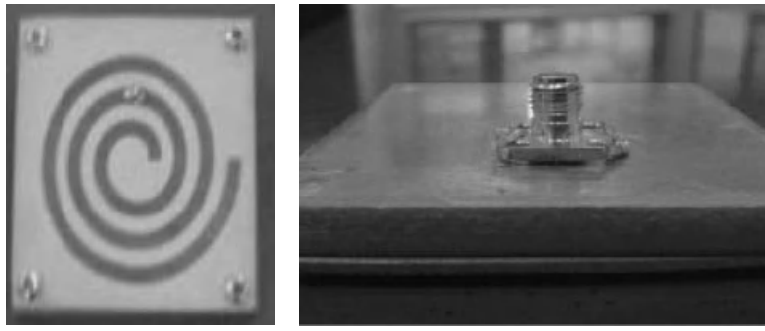

Figure 4.26 Photographs of the coaxial feed for the Archimedean spiral antenna: (a) top view; (b) bottom view [18]. Reproduced by permission of © 2010 IEEE.

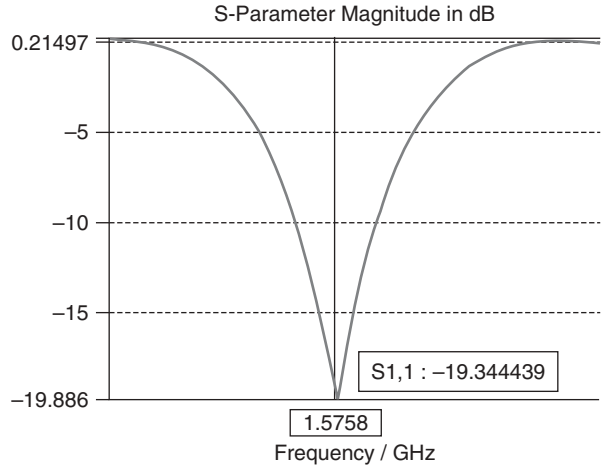

Figure 4.27 Simulated return loss of the Archimedean spiral antenna [18]. Reproduced by permission of © 2010 IEEE.

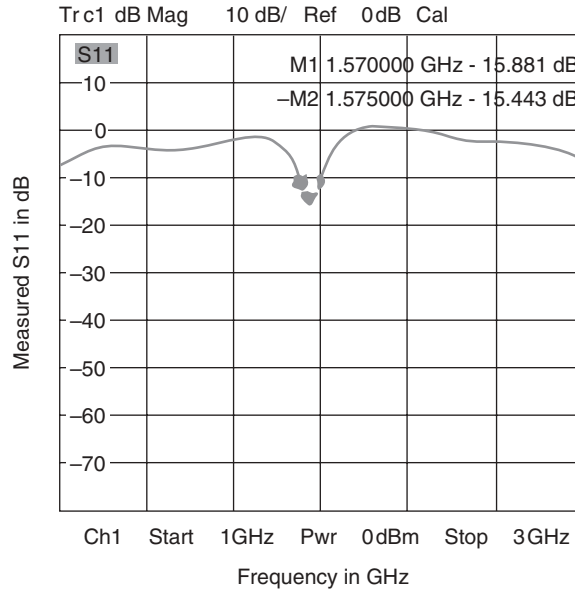

Figure 4.28 Measured return loss of the Archimedean spiral antenna [18]. Reproduced by permission of © 2010 IEEE.

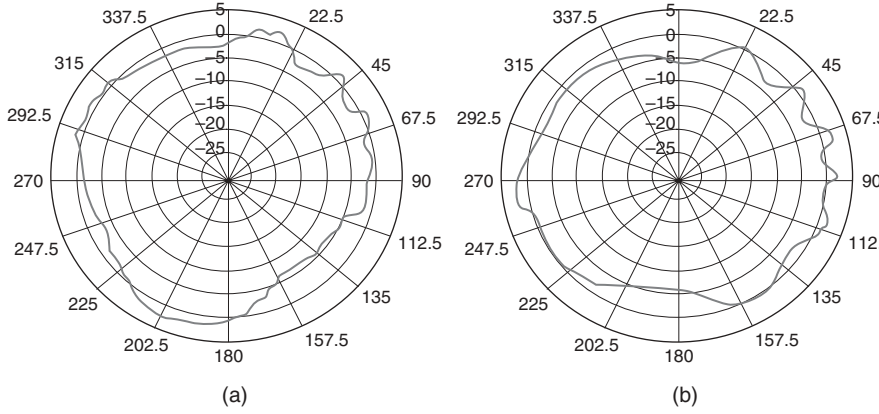

Figure 4.29 Measured radiation patterns of the Archimedean spiral antenna: (a) **E** plane; (b) **H** plane [18]. Reproduced by permission of © 2010 IEEE.

4.3 Design of a PIFA for a GNSS Terminal Antenna

CP antennas have been extensively studied recently for GNSS applications. The general limitations of the CP patch antennas are the achievable impedance and

axial ratio (AR) bandwidths. Traditionally, the 3 dB AR bandwidth is typically less than 10% for the single-feed cases [19, 20]. PIFAs (Planar Inverted-F Antennas) [21–23] have been widely used in wireless communications, as they have wideband characteristics, good radiation patterns, simple structures and easy integration with other active devices, but they are usually used for linear polarisation. Very few designs are available in the open literature for achieving CP radiation using PIFA structures.

A novel broadband single-feed printed PIFA with broadband circular polarisation is described in [24], consisting of a square ground with a cross-shaped branch at its corner and a modified PIFA structure. By introducing a protruding cross at the ground, wideband circular polarisation is generated, and the modified PIFA structure gives the antenna a broad impedance bandwidth. The antenna has a very compact structure with a dimension of $51 \times 13\,\text{mm}^2$ on the substrate, which is suitable for handheld GNSS terminal application.

The geometry of the proposed broadband planar antenna with broadband circular polarisation is shown in Figure 4.30. The antenna uses an FR4 substrate 1.6 mm thick with a permittivity of 4.4. The substrate dimension is fixed at $94 \times 94\,\text{mm}^2$. All the metallic components of the antenna are printed on the same side of the substrate. The antenna consists of a PIFA structure and a square ground with a cross-shaped branch at its corner. The square ground is placed in the left part of the substrate with length 68 mm. The antenna is excited by a coaxial probe. The outer surface of the coaxial is in full conjunction with

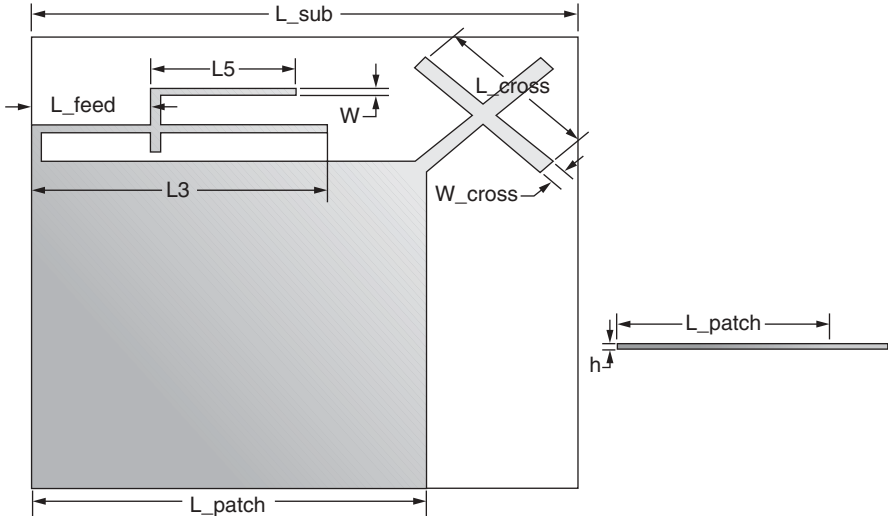

Figure 4.30 Geometry of the broadband printed PIFA with circular polarisation.

the square ground, while the inner copper is connected to the PIFA to excite the antenna.

The simulation indicates that the impedance matching and AR bandwidth are primarily dependent on the PIFA and the cross-shaped ground, separately. The PIFA structure has a great effect on the impedance bandwidth. In order to increase the impedance bandwidth, another branch is applied for the PIFA structure, which greatly extends the frequency band enabling it to cover the GNSS frequency band. Due to the mutual influence of the PIFA and protruding cross-shaped ground, circular polarisation is produced. The cross is a paramount factor and needs serious consideration in the AR of the designed frequency band. By carefully selecting the parameter of the cross, a broadband circular polarisation is obtained. The finally chosen dimensions of the proposed antenna are given in Table 4.1.

To verify the proposed design, a prototype is fabricated on an FR4 substrate as shown in Figure 4.31. The simulated and measured return loss of

Table 4.1 Dimensions of the broadband printed PIFA

Parameter	L_sub	L_patch	L_feed	L3
Value (mm)	94	68	20.4	51
L5	L_cross	W	W_cross	h
25	30.6	1.7	3	1.6

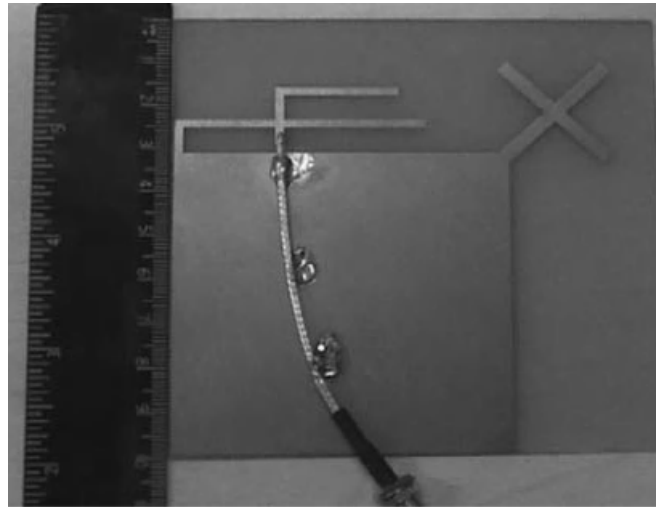

Figure 4.31 Fabricated prototype of the broadband printed PIFA.

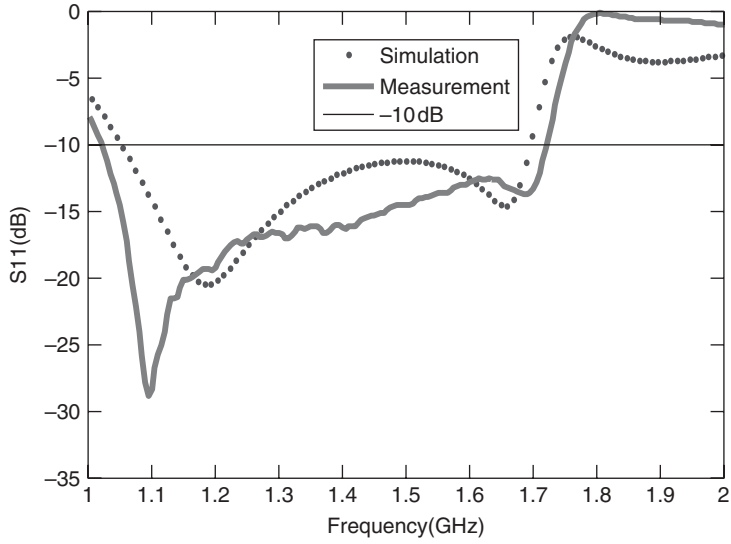

Figure 4.32 Simulated and measured return loss for the broadband printed PIFA.

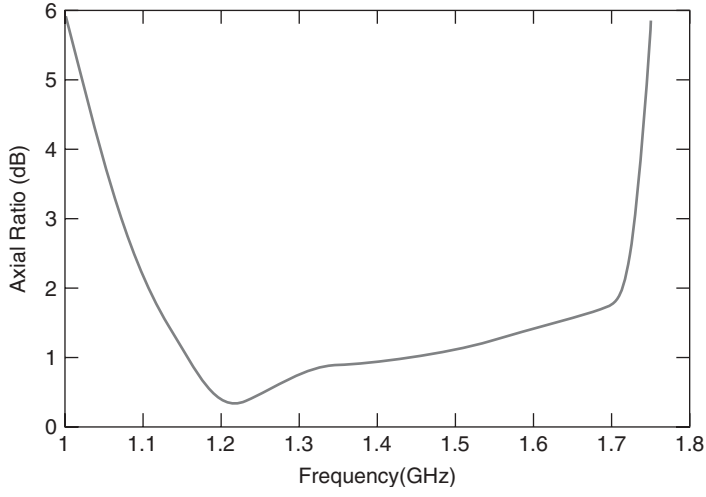

Figure 4.33 Simulated AR of the broadband printed PIFA.

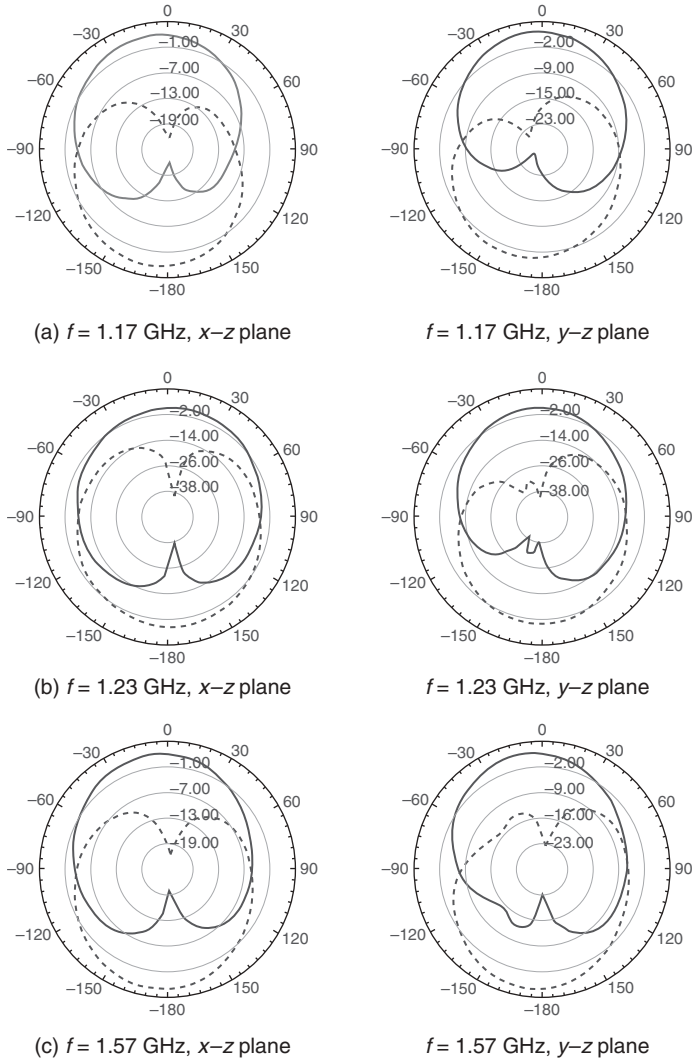

(a) $f = 1.17$ GHz, x–z plane

$f = 1.17$ GHz, y–z plane

(b) $f = 1.23$ GHz, x–z plane

$f = 1.23$ GHz, y–z plane

(c) $f = 1.57$ GHz, x–z plane

$f = 1.57$ GHz, y–z plane

Figure 4.34 The radiation patterns of the broadband printed PIFA at: (a) 1.17 GHz; (b) 1.23 GHz; (c) 1.57 GHz.

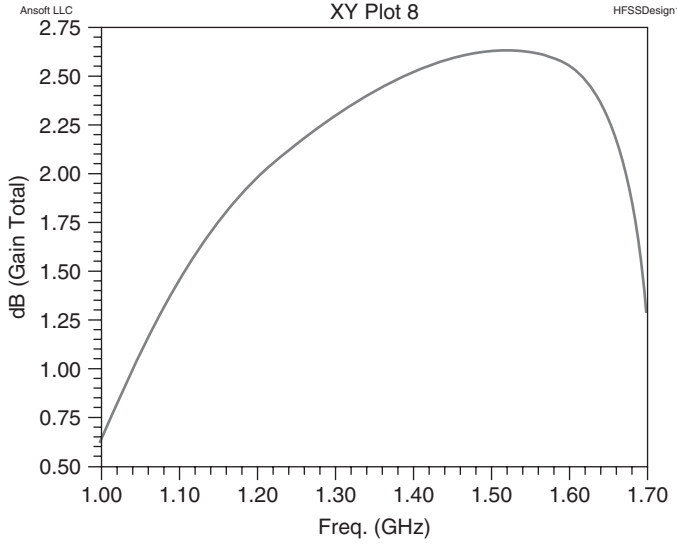

Figure 4.35 Simulated gain characteristic.

the proposed antenna are shown in Figure 4.32. As can be seen, the S_{11} characteristic shows an improved bandwidth of 46.67% (1.02–1.72 GHz) in measurement at less than −10 dB compared with that of 43.33% at less than −10 dB (1.04–1.69 GHz) in simulation.

Figure 4.33 shows the simulated AR in the broadside direction ($\theta = 0^\circ$). We have just measured AR at a series of discrete points (1176.45, 1207.14, 1227.6, 1246, 1268.52, 1278.75, 1561.098, 1575.42, 1605.375 MHz) covering the whole GNSS frequency band. As can be seen, the simulation result shows a broadband AR bandwidth of around 660 MHz from 1.07 to 1.73 GHz for AR ≤3 dB, which is largely enhanced compared with a microstrip antenna.

The radiation patterns in the $x-z$ and $y-z$ planes at three different frequencies (L1, L2, L5 for GPS) are given in Figure 4.34. The solid curve represents the RHCP pattern, while the dashed line represents the LHCP pattern. As can be seen, the antenna achieves good CP radiation in the z-direction.

The simulated gain characteristics of the antenna are shown in Figure 4.35. We find that in all GNSS frequency bands the gain of the antenna is above 1.5 dBi, which is well above the requirement for handheld wireless terminals.

This chapter has introduced practical microstrip patches, quadrifilar helices and spirals for application with GNSS receivers. Most of these antenna designs

can only operate in a single frequency band. Antenna designs for operating in multiple GNSS frequency bands and for other special scenarios are discussed in the next chapter.

References

1. Lu, J.H., Tang, C.L. and Wong, K.L., 'Single feed slotted equilateral-triangular microstrip antenna for circular polarization', *IEEE Transactions on Antennas and Propagation*, **47**, 1174–1178, 1999.
2. Yang, K.P., Wong, K.L. and Lu, J.H., 'Compact circularly-polarized equilateral-triangular microstrip antenna with Y-shaped slot', *Microwave and Optical Technology Letters*, **20**, 31–34, 1999.
3. Chen, W.S., Wu, C.K. and Wong, K.L., 'Novel compact circularly polarized square microstrip antenna', *IEEE Transactions on Antennas and Propagation*, **49**, 340–342, 2001.
4. Bokhari, S.A., Zuercher, J.F., Mosig, J.R. and Gardiol, F.E., 'A small microstrip patch antenna with a convenient tuning option', *IEEE Transactions on Antennas and Propagation*, **44**, 1521–1528, 1996.
5. Tang, C.L. and Wong, K.L., 'A modified equilateral-triangular-ring microstrip antenna for circular polarization', *Microwave and Optical Technology Letters*, **23**, 123–126, 1999.
6. Chen, W.S., Wu, C.K. and Wong, K.L., 'Compact circularly polarized microstrip antenna with bent slots', *Electronic Letters*, **34**, 1278–1279, 1998.
7. Chen, W.S., Wu, C.K. and Wong, K.L., 'Compact circularly polarized circular microstrip antenna with cross slot and peripheral cuts', *Electronic Letters*, **34**, 1040–1041, 1998.
8. Lu, J.H. and Wong, K.L., 'Single-feed circularly-polarized equilateral-triangular microstrip antenna with a tuning stub', *IEEE Transactions on Antennas and Propagation*, **48**, 1869–1872, 2000.
9. Wong, K.L. and Chen, M.H., 'Slot-coupled small circularly polarized microstrip antenna with modified cross-slot and bent tuning-stub', *Electronic Letters*, **34**, 1542–1543, 1998.
10. Sim, C.Y.D. and Han, T.Y., 'GPS antenna design with slotted ground plane', *Microwave and Optical Technology Letters*, **50** (3), 818–821, 2008.
11. Abdelaziz, A.A. and Nashaat, D.M., 'Compact GPS microstrip patch antenna', *Journal of Theoretical and Applied Information Technology*, **4**, 530–535, 2007.
12. Su, C.M. and Wong, K.L., 'Surface-mountable dual side-feed circularly polarized ceramic chip antenna', *Microwave and Optical Technology Letters*, **35** (2), 137–138, 2002.
13. Gerst, C. and Worden, R., 'A helix antenna takes turn for better', *Electronics*, **39** (17), 100–110, 1966.
14. Kilgus, C.C., 'Multi-element, fractional turn helices', *IEEE Transactions on Antennas and Propagation*, **16**, 400–500, 1968.
15. Kilgus, C.C., 'Resonant quadrifilar helix', *IEEE Transactions on Antennas and Propagation*, **17**, 349–451, 1969.
16. Kilgus, C.C., 'Resonant quadrifilar helix design', *Microwave Journal*, **13**, 49–54, 1970.
17. Shumaker, P.K., Ho, C.H. and Smith, K.B., 'Printed half-wavelength quadrifilar helix antenna for GPS marine applications', *Electronics Letters*, **32** (3), 153–154, 1996.

18. Mohd Yusop, M.F., Ismail, K., Sulaiman, S. and Haron, M.A., 'Coaxial feed Archimedean spiral antenna for GPS application', Proceedings of the 2010 IEEE Asia-Pacific Conference on Applied Electromagnetics (APACE 2010).
19. Iwasaki, H., 'A circularly polarized small-size microstrip antenna with a cross slot', *IEEE Transactions on Antennas and Propagation*, **44** (10), 1399–1401, 1996.
20. Wang, C.L. and Chang, K., 'A novel CP patch antenna with a simple feed structure', Antenna and Propagation Society International Symposium, Vol. 2, pp. 1000–1003, 2000.
21. Rowell, C.R. and Murch, R.D., 'A compact PIFA suitable for dual-frequency 900/1800-MHz operation', *IEEE Transactions on Antennas and Propagation*, **46**, 596–598, 1998.
22. Wong, K.L. and Huang, C.H., 'Bandwidth-enhanced PIFA with a coupling feed for quad-band operation in the mobile phone', *Microwave and Optical Technology Letters*, **50**, 683–687, 2008.
23. Kuo, Y.L., Chiou, T.W. and Wong, K.L., 'A novel dual-band printed inverted-F antenna', *Microwave and Optical Technology Letters*, **31**, 353–355, 2001.
24. Wang, X., Yao, Y., Lu, Z.J., Yu, J.S. and Chen, X., 'A broadband planar antenna with circular polarization for multi-mode satellite navigation', Asia-Pacific Microwave Conference, Melbourne, Australia, 5–8 December 2011.

5

Multimode and Advanced Terminal Antennas

This chapter introduces multimode antennas for an integrated GNSS receiver, covering the GPS, GLONASS, Compass and Galileo systems. It presents several kinds of multimode GNSS antennas, including microstrip and helix antennas. For each one, some practical and novel designs are presented, such as multi-layer microstrip antennas, slotted-patch antennas, quadrifilar helix antennas, and so on. Finally, the chapter touches on high-precision terminal antennas for differential GPS, including phase centre determination and stability.

5.1 Multiband Terminal Antennas

With the development of satellite navigation technology, many countries have started to build their own satellite navigation systems. Nowadays, these systems are used intensively. The American GPS and the Russian GLONASS are already operating worldwide. The Chinese Compass system has also provided a partial service. Future satellite navigation receivers will provide multimode operation utilising different satellite navigation systems to improve their positioning accuracy and reliability, so the design of terminal antennas for multimode satellite navigation systems is practically desirable.

A multimode satellite navigation receiver is required to cover several frequency bands for the GPS, GLONASS, Galileo and Compass systems, as detailed in Table 1.1. Each GNSS has several frequency bands. The challenges in the design of a multiband receiver antenna come from two requirements: the antenna needs to provide right hand circular polarisation with a low axial ratio

Antennas for Global Navigation Satellite Systems, First Edition.
Xiaodong Chen, Clive G. Parini, Brian Collins, Yuan Yao and Masood Ur Rehman.

and also maintain a low VSWR over multiple frequency bands. In this chapter several designs of dual-band and triple-band GNSS antennas are discussed.

5.1.1 Multiband Microstrip GNSS Antennas

Because of their low profile, CP microstrip antennas are widely used in GNSS applications. However, most of the current antenna designs only cover the GPS L1 band: 1575 MHz. In more demanding operations, such as differential GPS [1], it is necessary that terminal antennas cover multiple GNSS bands. There are generally two kinds of microstrip antennas capable of multiband RHCP operation. One uses stacked patches while the other uses a single patch with loading.

5.1.1.1 Design of a Stacked Patch with a Single Feed

A CP antenna for multi-frequency operation can be achieved by using multi-layer patches. By using a multi-layer structure it is easier to achieve multi-frequency CP operation than can be provided using other approaches. The dimensions of each patch mainly determine the resonant frequencies. By changing one of the patches, a specific frequency can be achieved while the rest of the frequencies remain unchanged [2].

Based on the principle mentioned above, we propose a multi-layer microstrip patch antenna operating at three frequencies with circular polarisation. The geometry of the proposed antenna is shown in Figure 5.1. The triple-layer patch antenna is fed by a single coaxial cable that passes through the ground plane and substrates and is connected to the top patch. The top, middle and bottom layer patches of the antenna are for the 575, 1227 and 1176 MHz bands respectively. RHCP is achieved by placing the feed point in the upper right portion of the diagonal of the square patch.

In Figure 5.1, each square patch is built on a substrate of permittivity $\varepsilon_r = 2.65$ and the same substrate height of $h = 1.5$ mm. The size of ground plane is 100 mm. The dimensions of each patch $(a_i \times b_i)$ and feed position (c, d) need to be optimised in order to minimise the VSWR and AR. The detailed size is: $a_1 = b_1 = 55.5$ mm, $a_2 = b_2 = 71$ mm, $a_3 = b_3 = 74$ mm and $c = d = 8$ mm. Figure 5.2 shows the simulation results for return loss. The resonant frequencies are 1575, 1227 and 1176 MHz, matching the target frequencies well. The bandwidths of VSWR < 2 at each frequency are 35, 16 and 25 MHz for each band. Figure 5.3 shows the AR of the antenna. The antenna radiates RHCP at all three frequencies; the radiation patterns are presented in Figure 5.4.

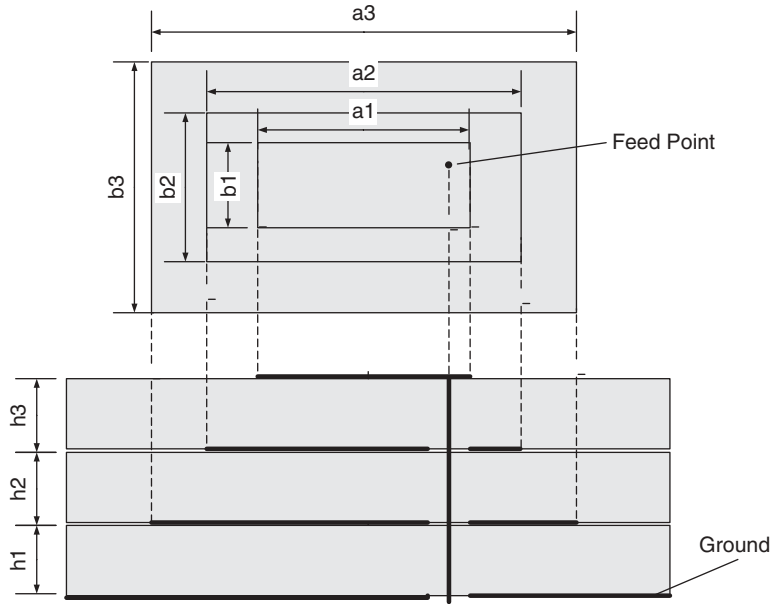

Figure 5.1 Structure of three-layer microstrip CP antenna.

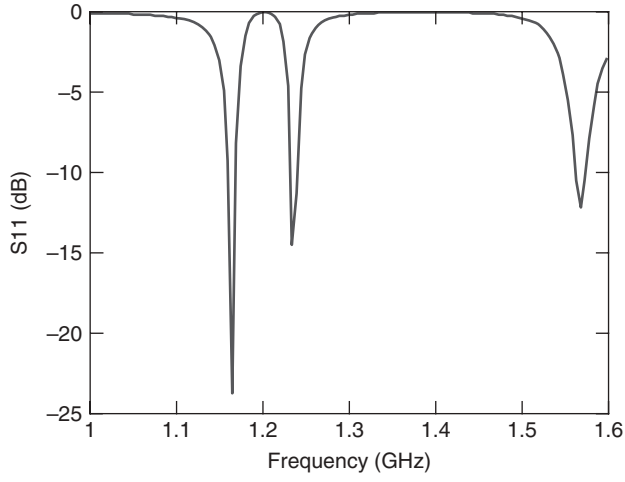

Figure 5.2 Return loss of the three-layer microstrip CP antenna.

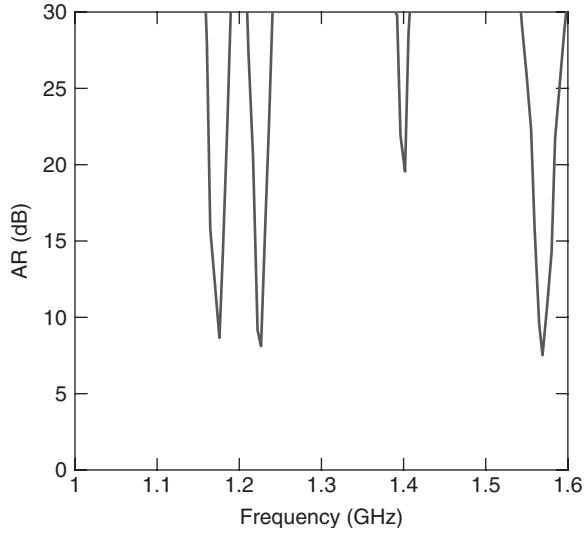

Figure 5.3 Axial ratio of the three-layer microstrip CP antenna.

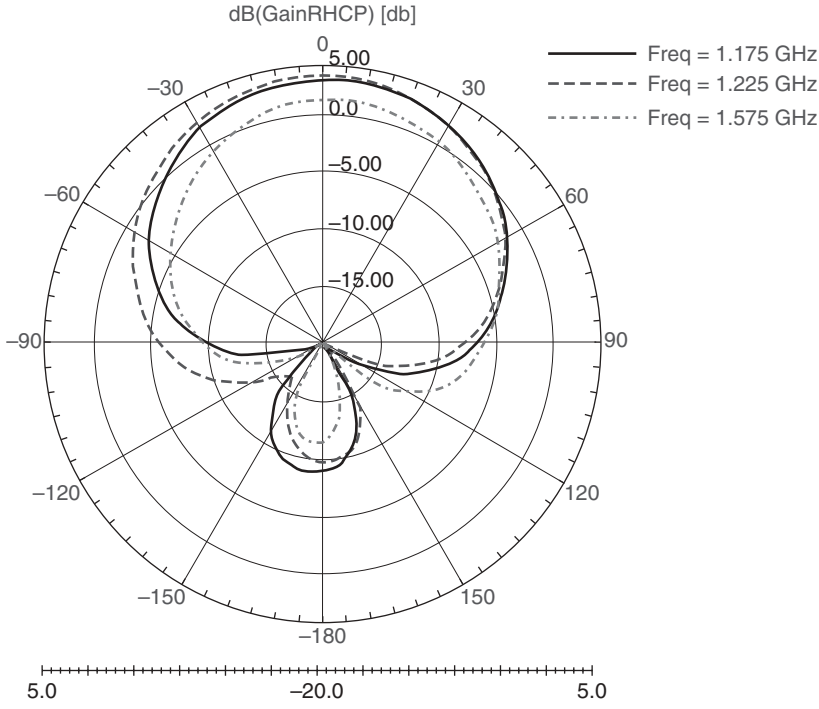

Figure 5.4 RHCP radiation patterns of the three-layer microstrip CP antenna.

5.1.1.2 Design of Stacked Patches with Four Feeds [3]

This antenna design comprises two stacked patches which are fed by four pins placed symmetrically on the two main axes. The amplitude and phase relationship between the four pins to maintain circular polarisation is obtained by two wideband 90° hybrid couplers. Impedance matching of the four-feed structure is easily realised by changing the positions of the feed points. The structure of the antenna is shown in Figure 5.5. The antenna consists of two square patches with tuning stubs, stacked concentrically in the vertical direction. Changing the length of the tuning stubs can alter the resonance frequency, which will decline when the lengths of the tuning stubs increase. The permittivity of both the top two substrates is 9.8 ($\varepsilon_{r1} = \varepsilon_{r2} = 9.8$), and their thicknesses are both 2.5 mm ($h_1 = h_2 = 2.5$ mm). The feed network layer uses a square substrate of FR4. Its thickness is 0.8 mm ($h_3 = 0.8$ mm) and length 48 mm. All the structures have a via with a diameter of 1.5 mm ($D = 1.5$ mm) at their centre, so that the two patches on the top and bottom layers can be connected to the ground. Thus the radiation patterns are directed towards the z-axis. The feed network is composed of two 3 dB wideband 90° hybrids whose ground is common to the ground of the antenna – it is shown as one ground in the figure. The dimensions of the two

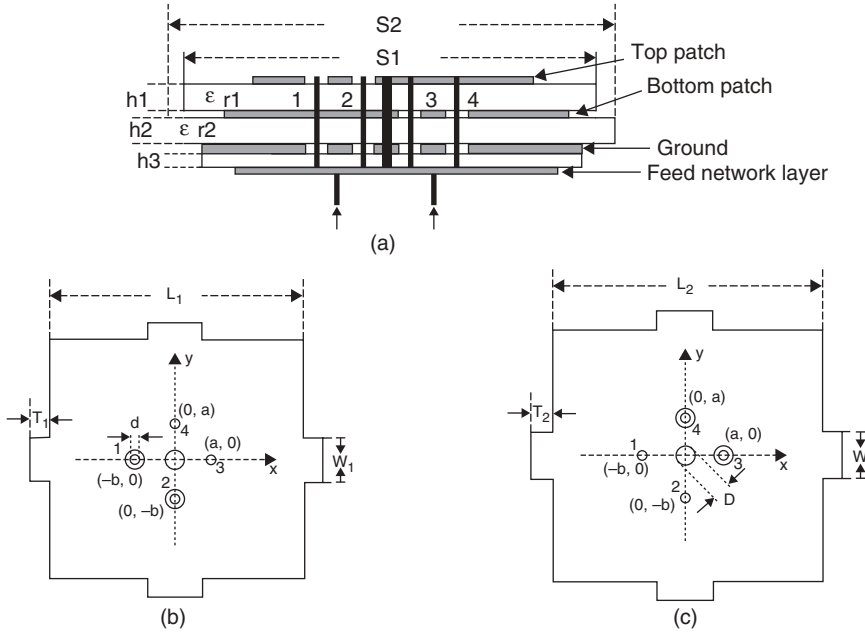

Figure 5.5 Geometry of the four-feed stacked antenna: (a) side view; (b) top patch; (c) bottom patch [3]. Reproduced by permission of © 2007 IEEE.

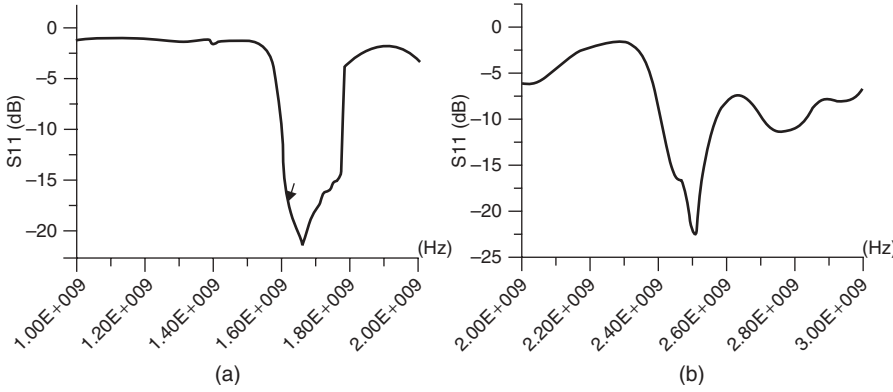

Figure 5.6 Measured S_{11} of the four-feed stacked antenna [3]. Reproduced by permission of © 2007 IEEE.

patches are $L_1 = 17.5$ mm and $L_2 = 26$ mm, and the dimensions of the tuning stubs are $T_1 = 1.5$ mm, $W_1 = 2.5$ mm, $T_2 = 1$ mm, $W_2 = 5$ mm. The two substrates have dimensions $S_1 = 63$ mm and $S_2 = 73$ mm; the lengths from pin to centre are $a = 3$ mm and $b = 5$ mm. Pin 1 and pin 2, used for feed points of the lower frequency band, are connected to the bottom patch but do not touch the top patch. The diameter of the pin is 1 mm ($d = 1$ mm). Pin 3 and pin 4 are used for feed points of the higher frequency band; they too are connected to the top patch but do not touch the bottom patch. The currents fed to pin 1 and pin 2, and that fed also to pin 3 and pin 4, must maintain equal amplitude and 90° phase difference so that the antenna receives RHCP signals at both frequency bands.

As shown in Figure 5.6, the antenna resonates in both the L band (1.6 GHz) and S band (2.5 GHz). Figure 5.7 shows that the measured AR of the antenna is less than 6 dB when the elevation is in the range of 0°–60° at lower frequency, and is less than 3.5 dB when the elevation is in the range of 0°–90° at higher frequency. The measured and simulated results have the same trend, but there are some differences between them. This is due to the errors of the amplitude and phase of the actual feed network. Figure 5.8 shows the linear radiation patterns of the antenna. The 3 dB beamwidth at the lower frequency is larger than 140° and at higher frequency is larger than 160°. It has perfect CP characteristics over a wide angle.

5.1.1.3 Design of Single Patch with Loading

A new design of a single-layer slit-loaded square patch antenna for achieving dual-band circular polarisation has been reported [4]. The antenna size can be

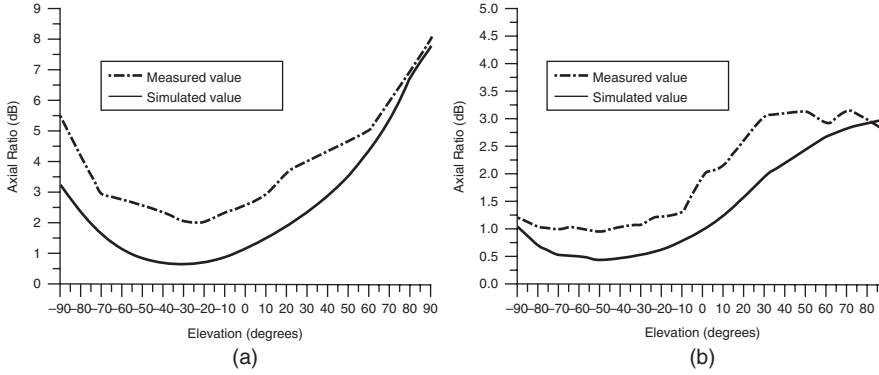

Figure 5.7 AR results of the antenna at (a) lower frequency and (b) higher frequency [3]. Reproduced by permission of © 2007 IEEE.

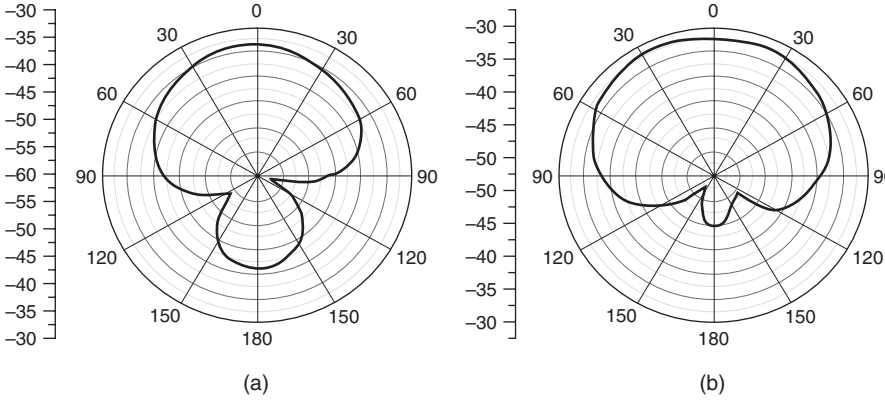

Figure 5.8 Radiation patterns of the antenna at (a) lower frequency and (b) higher frequency [3]. Reproduced by permission of © 2007 IEEE.

significantly reduced compared with conventional stacked-patch CP designs. The proposed slit-loaded square patch antennas are formed by inserting four T-shaped slits at the patch edges or four Y-shaped slits at the patch corners of a square patch as shown in Figure 5.9. The two resonant modes TM_{01} and TM_{03} are excited to provide dual-band CP radiation in the designs. Due to the inserted T-shaped or Y-shaped slits, the surface current path of the TM_{01} mode is greatly lengthened, which effectively lowers its resonant frequency and allows the designs to operate with a reduced patch size for a fixed lower frequency. The inserted slits also considerably lower the resonant frequency of the TM_{03} mode and modify its three-lobe-shaped radiation pattern to become

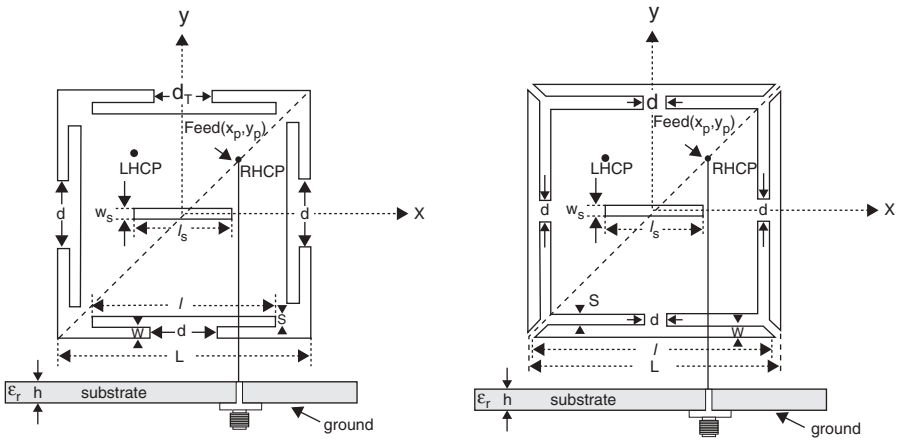

Figure 5.9 Configurations for slit-loaded dual-band CP designs: (a) design A, a square patch with four T-shaped slits; (b) design B, a square patch with four Y-shaped slits [4]. Reproduced by permission of © 2001 IEEE.

similar to that of the TM_{01} mode. By further embedding a narrow slot in the patch centre and using a single-probe feed at the diagonals of the slit-loaded square patch, both the perturbed TM_{01} and TM_{03} modes can be split into two near-degenerate modes for dual-band CP radiation.

A square patch with four T-shaped slits and a square patch with four Y-shaped slits normally have the same excitation mode as well as the same antenna performance. To save space, we only show the measured results of antenna design A in Figures 5.10, 5.11 and 5.12. The dimensions of design A are as follows: $h = 1.6$ mm, ground size $= 75 \times 75$ mm^2, feed point $= (7$ mm, 7 mm), $L = 36$ mm, $l = 28.8$ mm, $d = 1.8$ mm, $d_T = 3.5$ mm, $W_s = 0.9$ mm, $l_s = 13$ mm, $S = 0.9$ mm, $w = 1.80$ mm.

It can be seen that this antenna operates in two frequency bands and has good RHCP radiation patterns. Though in this particular design (for other applications) one frequency band is out of GNSS range, this design principle can be applied to obtain dual-band GNSS operation by varying the dimensions of the centre slot and the inserted T-shaped or Y-shaped slits.

5.1.2 Multiband Helix Antennas for GNSS

The quadrifilar helix antenna (QHA) is one of most commonly used antenna designs for GNSS applications, due to its good circular polarisation property and compactness [5–7]. Since the quadrifilar helix is a resonant antenna, its

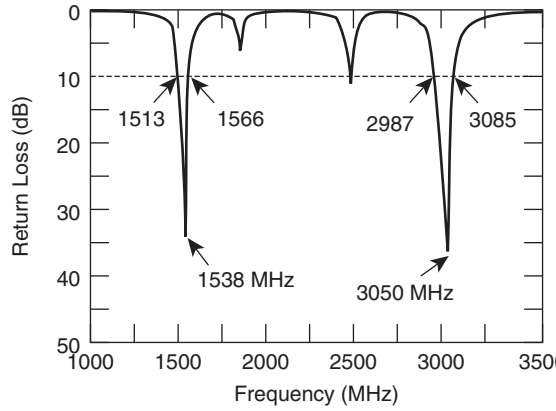

Figure 5.10 Measured return loss for design A: a square patch with four T-shaped slits [4]. Reproduced by permission of © 2001 IEEE.

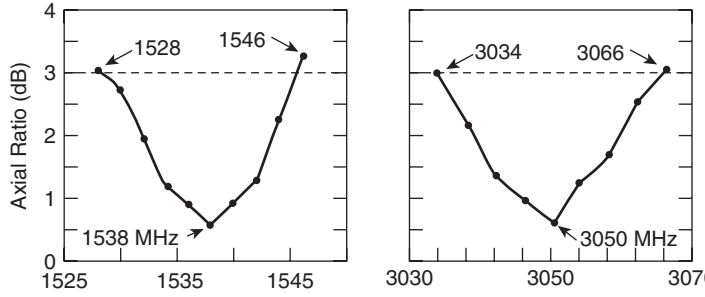

Figure 5.11 Measured AR for design A: a square patch with four T-shaped slits [4]. Reproduced by permission of © 2001 IEEE.

dimensions are chosen to provide optimal performance for one frequency band, and it is difficult to design it to operate at multiple frequency bands. Various methods have been proposed to make the QHA operate at both GPS frequencies of 1.575 and 1.227 GHz. A typical approach is to use volutes of different size and construction [8]. Another technique is to place a parallel LC circuit at appropriate locations in each arm [9]. The antenna provides the same performance in two separate frequency bands and has no impact upon the overall size by this method.

The configuration of a compact printed square QHA antenna for dual-band GNSS application is shown in Figure 5.13 [10]. The antenna is mounted above a substrate and has the shape of a cube, formed by four vertical substrate

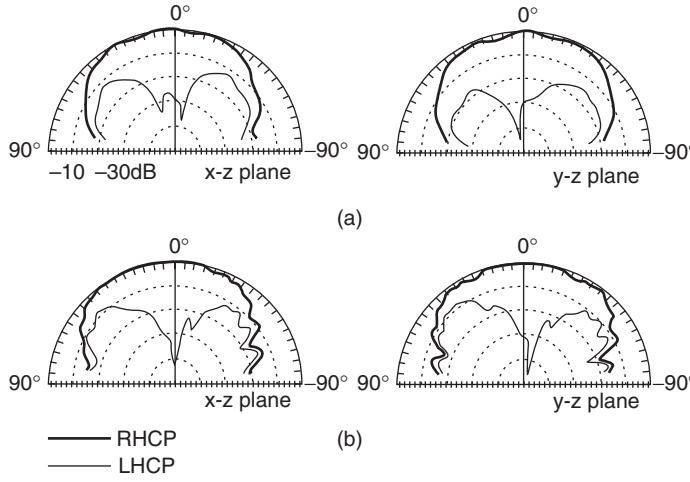

Figure 5.12 Measured radiation patterns for design A: a square patch with four T-shaped slits [4]. Reproduced by permission of © 2001 IEEE.

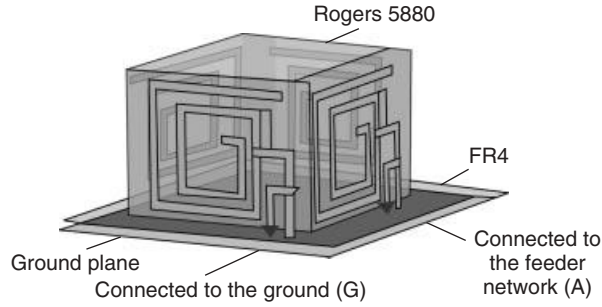

Figure 5.13 Geometry of the dual-band QHA [10]. Reproduced with permission of John Wiley & Sons, Inc.

boards, each of which has a printed helix on one face. These printed helices comprise two loops having different lengths. The total length of the shorter loop is chosen to be about one-quarter of a wavelength at 1575 MHz, and that of the longer loop is about one-quarter of a wavelength at 1227 MHz. The antenna can radiate RHCP, and the sense of polarisation is determined by the direction of rotation of the printed helices. The feed network is required to produce four RF signals of equal amplitude with relative phases of 0°, 90°, 180° and 270°. The antenna, combined with the feed network, generates CP radiation. The volume of the antenna is 1 cm^3.

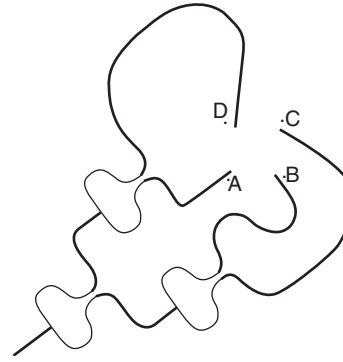

Figure 5.14 Layout of the feed network of the dual-band QHA [10]. Reproduced with permission of John Wiley & Sons, Inc.

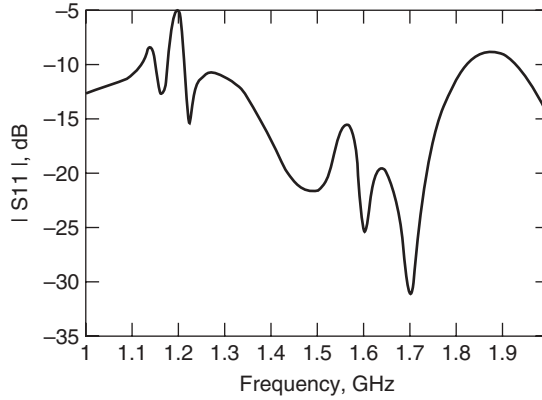

Figure 5.15 Measured S_{11} of the dual-band QHA [10]. Reproduced with permission of John Wiley & Sons, Inc.

The feed network is designed by using microstrip lines printed on the FR4 substrate, which has a permittivity of 4.6 and thickness of 1.6 mm. Figure 5.14 shows the layout of the feed network, which uses three Wilkinson power dividers and different lengths of connecting microstrip lines to achieve the required relative phases. As the feed network needs to operate at both 1227 and 1575 MHz, it is designed at a centre frequency of 1400 MHz.

The measured S_{11}, as shown in Figure 5.15, is below -10 dB at both 1227 and 1575 MHz bands. Figures 5.16 shows the measured radiation patterns at 1227 and 1575 MHz. It can be seen that the cross-polar level is 10 dB below

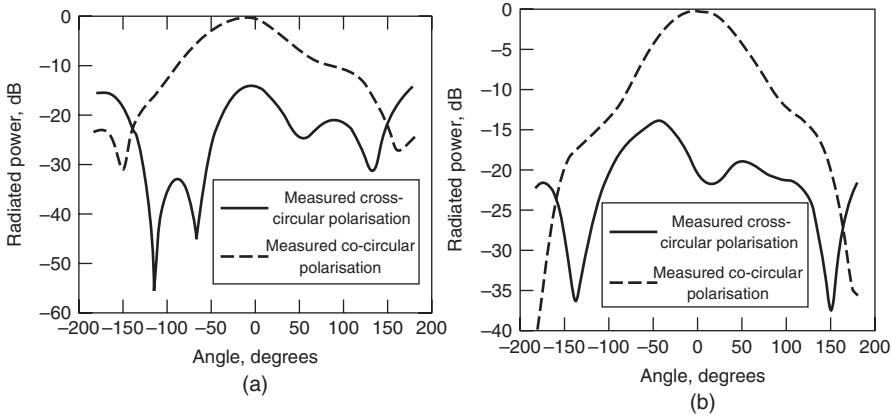

Figure 5.16 Radiation patterns of the dual-band QHA: (a) 1227 MHz; (b) 1575 MHz [10]. Reproduced with permission of John Wiley & Sons, Inc.

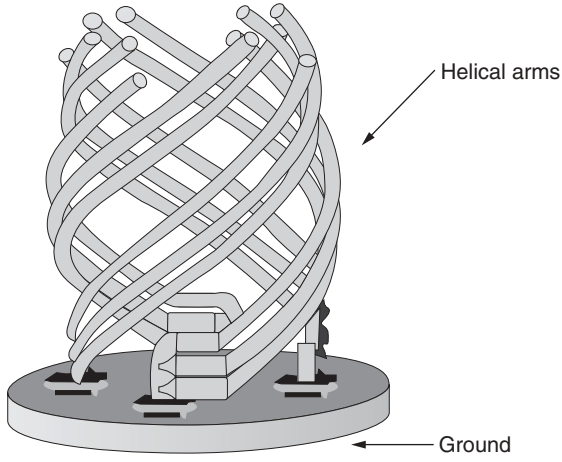

Figure 5.17 Structure of multi-arm helix antenna [2]. Reproduced by permission of © 2006 IEEE.

the co-polar level. The AR values at the boresight are 2.8 and 1.6 dB, at 1.227 and 1.575 GHz, respectively.

As another example, a novel triple-frequency multi-arm helix antenna structure is shown in Figure 5.17 [3]. It operates in three separate frequency bands and has good performance at each frequency. Being similar to a conventional QHA, this antenna has four feed points and four main arms, each of which consists of three elements with differing lengths for triple frequencies.

This structure is superior to those mentioned previously, particularly in the case of a frequency ratio close to one. It is more compact in size and easier to tune.

The modelling of the antenna was conducted for operation in the frequency bands 1.207, 1.268 and 1.561 GHz, with more than 2% bandwidth in each. The parameters of the antenna are chosen based on the standard theory of the QHA for operation at the chosen frequencies. Slim wires are chosen for the helix arms since the antenna has a compact size. In this simulation we chose copper wire with a 1 mm radius. The length of each arm is $\lambda/4$ at each frequency. Figure 5.18 shows the return loss of this antenna. At the three resonant frequencies the return loss is greater than 15 dB, and the widths of each band for VSWR < 2 are about 40, 30 and 31 MHz. The antenna has a good gain at low angle with excellent circular polarisation as shown in Figure 5.19. Figure 5.20 shows the radiation patterns as a function of frequency. The minimum gain is about -2.8 dB at 5° and -2 dB at 10°. The AR and gain over the hemisphere show that the novel antenna can provide triple frequency bands with good performance at each frequency.

This triple-frequency antenna is based on the theory of a QHA. By varying the length of each arm, and its diameter, the three resonant frequencies can be adjusted. The AR is generally better than that of many microstrip antennas, but the fabrication of a quadrifilar helix is more difficult compared with a microstrip patch. The feeding network of the QHA is also more complicated.

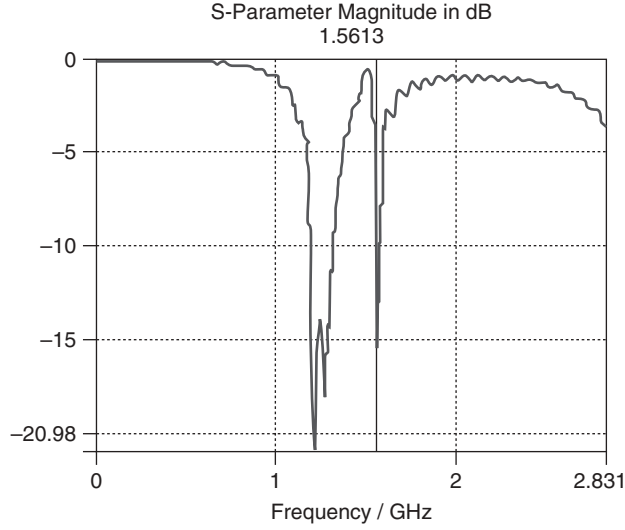

Figure 5.18 Return loss of the antenna [2]. Reproduced by permission of © 2006 IEEE.

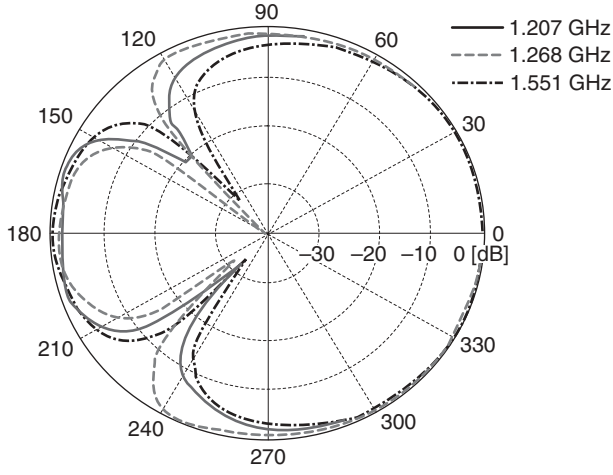

Figure 5.19 AR of the antenna [2]. Reproduced by permission of © 2006 IEEE.

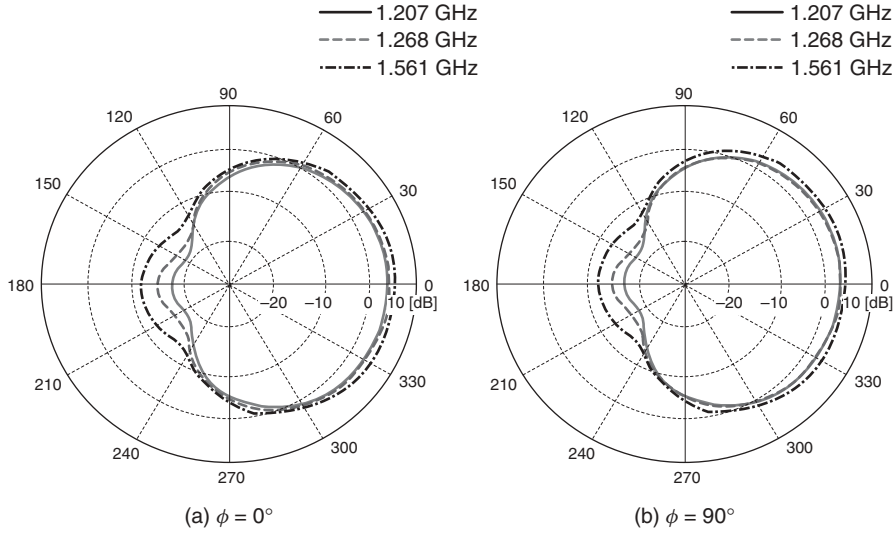

Figure 5.20 Radiation patterns of the antenna [2]. Reproduced by permission of © 2006 IEEE.

5.2 Wideband CP Terminal Antennas

As described previously, the whole frequency band of the four GNSSs (GPS, GLONASS, Compass, Galileo) is between 1164 and 1615.5 MHz and this requires an antenna with a relative impedance bandwidth of 33%. Another way to achieve multimode GNSS operation is to develop a wideband CP antenna to cover this 33% relative impedance bandwidth. In this section, several antennas are discussed to show a broadband GNSS performance.

5.2.1 Wideband Microstrip Antenna Array

A four-element wideband CP array, which utilises multi-layer microstrip patch antenna technology, was successfully designed and tested [11]. Each unit of the array comprised four dielectric substrates that incorporate electromagnetically coupled radiating elements fed by microstrip feed lines through coupling slots. The substrate architecture for the four-layer microstrip antenna design is shown in Figure 5.21, where adjacent substrates (Rogers 4003, $h = 1.524$ mm) are set $d = 10$ mm apart vertically. Three elements located on three separate layers, together with a slot-coupled feed, provide the required bandwidth. Each element has vertical (VP) and horizontal (HP) feed points.

This single-element design was arranged in a 2×2 array with a centre-to-centre separation of 65 mm. The architecture and prototype are illustrated in Figure 5.22. As shown in Figure 5.23, the array has good impedance matching and an excellent boresight AR performance of less than 1.5 dB over the entire

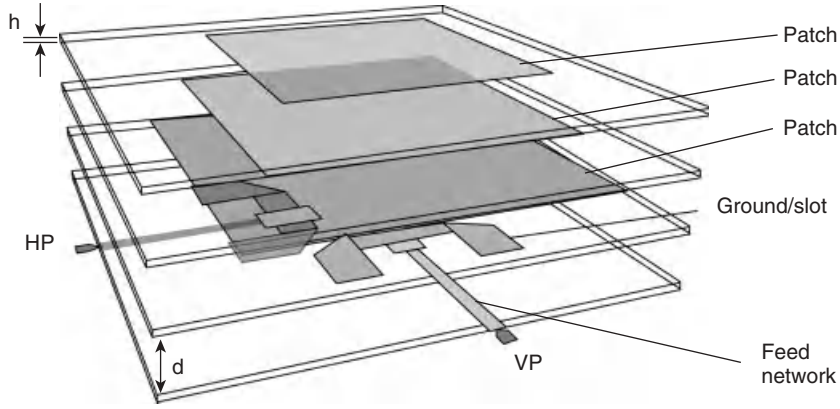

Figure 5.21 Architecture of a four-layer array unit. Taken from [11]; copyright EurAAP; used with permission.

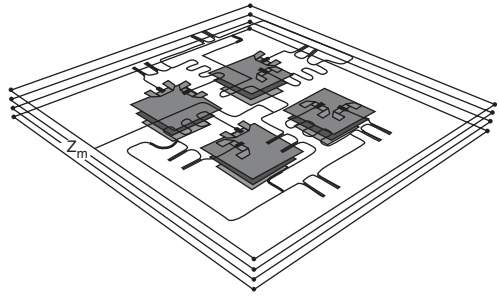

Figure 5.22 Prototype of four-element microstrip antenna array. Taken from [11]; copyright EurAAP; used with permission.

four GNSS system band. The gain of the antenna is above 8.5 dBi for the designated operating band.

5.2.2 High-Performance Universal GNSS Antenna Based on Spiral Mode Microstrip Antenna Technology

A class of high-performance low-cost GNSS antennas that covers all three GNSS services (GPS/GLONASS/Galileo) is described in [12]. This low-cost antenna is platform conformable. The prototype is shown in Figure 5.24, which is a spiral mode microstrip (SMM) antenna 11.5 cm in diameter and 3.0 cm in height. The antenna is a four-arm self-complementary Archimedean spiral. Its characteristics are shown in Figure 5.25, illustrating a broad bandwidth. Its low profile and conformable shape make it suitable for platform mounting.

5.2.3 Wideband CP Hybrid Dielectric Resonator Antenna

Circular polarisation can also be generated by using a dielectric resonator antenna (DRA) with two orthogonal feeds. A recent approach to improve the bandwidth of DRAs consists of merging the resonant band of the dielectric resonator with a band produced by the feed network itself. Such an antenna is referred to as a hybrid dielectric resonator antenna [13].

A hybrid antenna comprising a DRA and four feed slots as shown in Figure 5.26 has been investigated and analysed to enhance the AR bandwidth in order to cover the current GNSS frequency bands in one antenna [14].

The cylindrical DRA has a radius of 31.75 mm, a height of 22 mm and a permittivity of 10. It has been designed to resonate around 1.575 GHz. Circular polarisation is generated by a 90° phase feed network. The slots have to be arranged and their dimensions optimised to ensure proper coupling to the

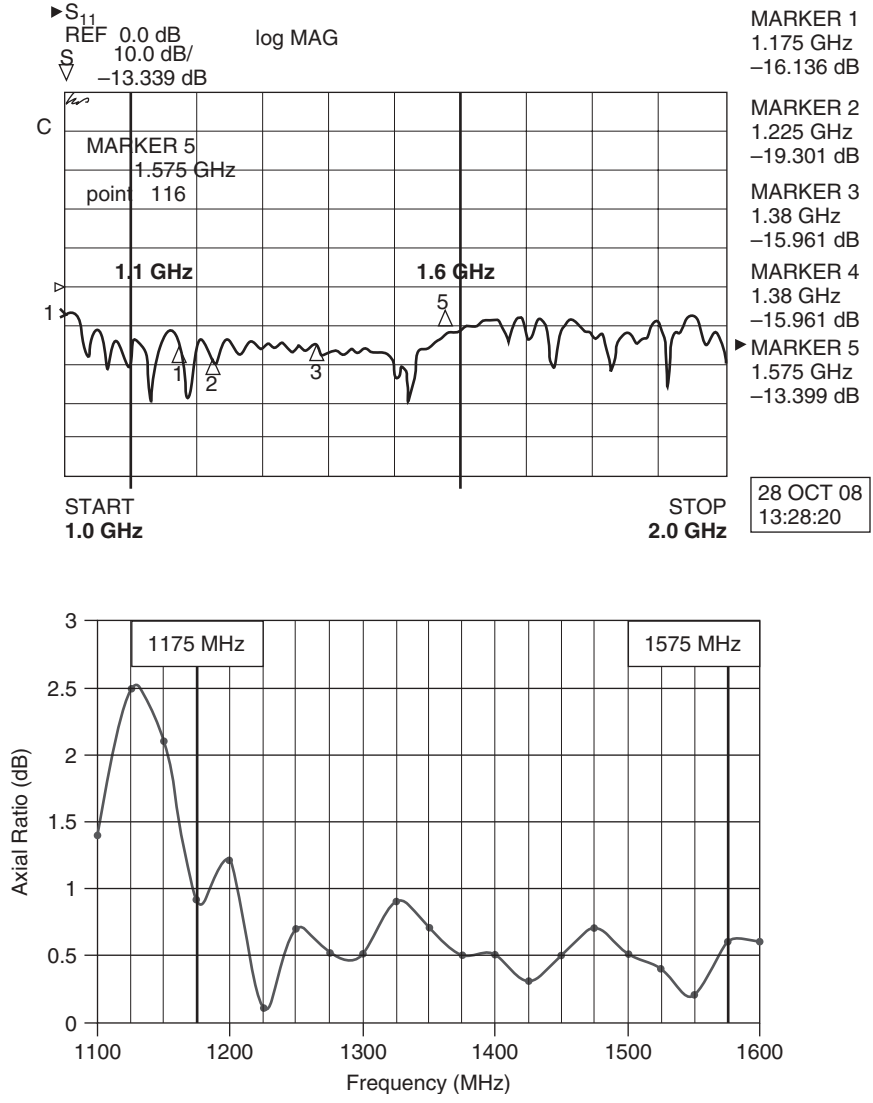

Figure 5.23 Measured S_{11} and AR performance of four-element microstrip antenna array. Taken from [11]; copyright EurAAP; used with permission.

dielectric resonator and to have good impedance matching. A substrate made of FR4 was chosen to accommodate the feed circuit of the DRA and the slots were etched in the ground plane. The ground plane dimensions are $160 \times 160\,\text{mm}^2$; the slot length is 36 mm and its width is 8.8 mm. The coordinates of the slots

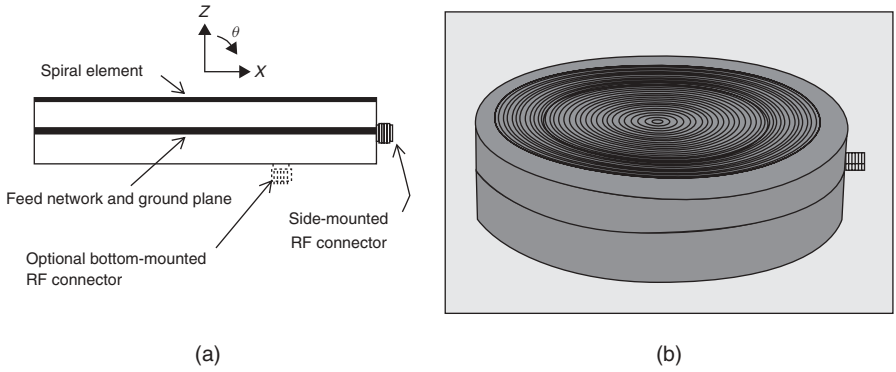

Figure 5.24 (a) Cross-sectional view for layout and (b) photograph of universal GNSS antenna [12]. Reproduced by permission of © 2010 IEEE.

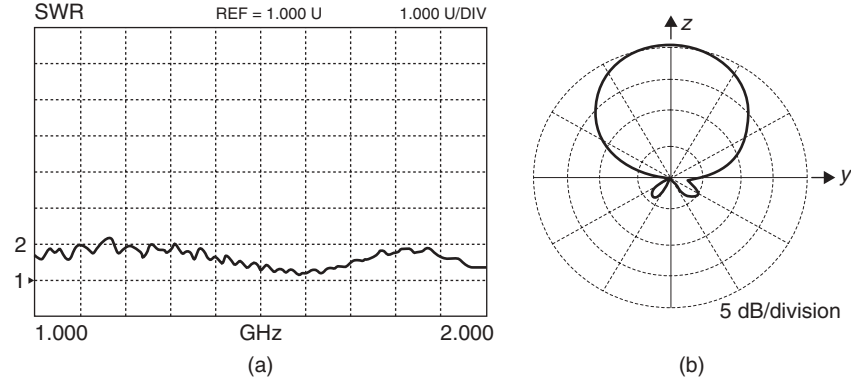

Figure 5.25 Universal GNSS antenna characteristics: (a) SWR performance; (b) measured radiation pattern (RHCP) [12]. Reproduced by permission of © 2010 IEEE.

are 4 mm along the x-direction and 19.4 mm in the y-direction. The feed line is 12.9 mm long and 11 mm away from the slot centre. The prototype of the DRA and its performance are shown in Figures 5.27 and 5.28. The advantage of the hybrid DRA over other GNSS antennas is its compact size.

5.2.4 Multi-Feed Microstrip Patch Antenna for Multimode GNSS

Note that a general limitation on CP microstrip antennas is the achievable AR bandwidth while the impedance bandwidth is satisfied. Traditionally, the

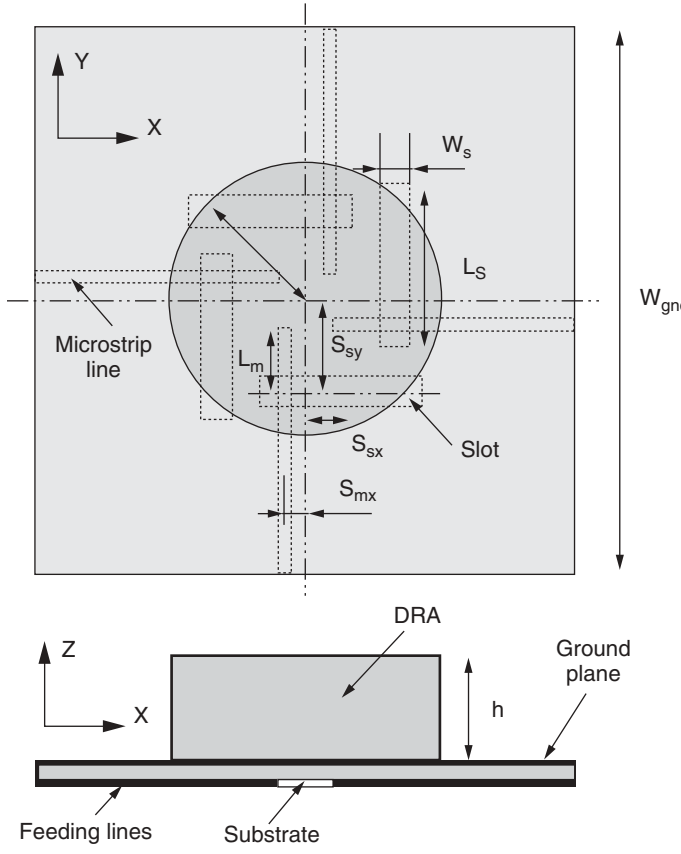

Figure 5.26 Diagram of the hybrid DRA [14]. Reproduced by permission of © 2010 IEEE.

allowable 3 dB AR bandwidth is typically less than 10% for the single-feed cases [15, 16]. Much wider impedance and AR bandwidths can be achieved in dual-feed and quadruple-feed CP patch antennas. Experimental patch antennas with quadruple broadband feeds [16, 17] have been found to achieve −10 dB impedance bandwidths of around 70–80% and 3 dB AR bandwidths of 80%.

Figure 5.29 shows an example of a four-feed microstrip antenna for a wideband GNSS application [17]. Four small, square radiating patches situated under the parasitic patch are excited by four metallic probes mounted symmetrically in the $+z$-direction. In order to enlarge the AR bandwidth, a symmetrical configuration of the antenna elements is necessary. The feed network model for

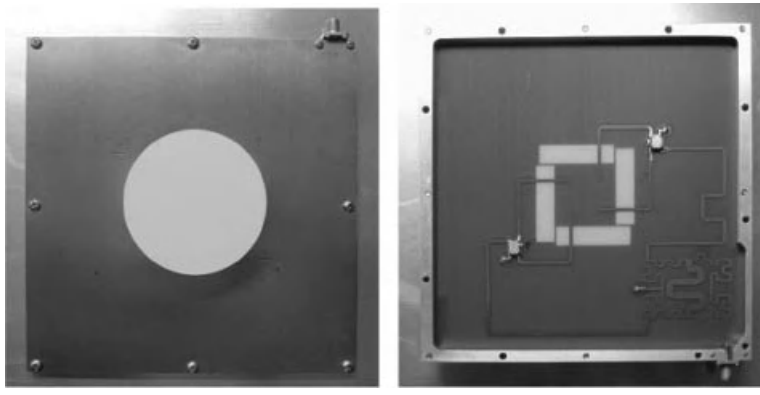

Figure 5.27 Fabricated hybrid DRA: (a) top view; (b) bottom view [14]. Reproduced by permission of © 2010 IEEE.

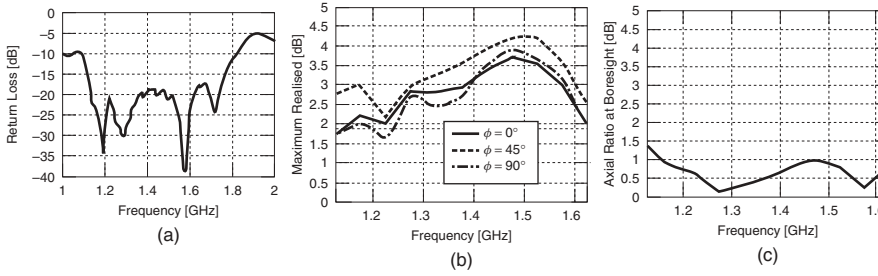

Figure 5.28 Hybrid DRA performance (measured): (a) S_{11}; (b) maximum radiation gain; (c) AR [14]. Reproduced by permission of © 2010 IEEE.

this microstrip antenna is shown in Figure 5.30, and the dimensions are listed in Table 5.1.

The simulated return loss of the proposed multimode GNSS antenna is presented in Figure 5.31. As can be seen from the results, the antenna exhibits a wide impedance bandwidth ($S_{11} < -10$ dB) of 51.6% from 1.14 to 1.93 GHz. Figure 5.32 shows the simulated AR as a function of frequency. The -3 dB AR bandwidth is 1 GHz. It should be noted that the AR bandwidth is wider than the impedance bandwidth. The gain is between 6.69 dBi and 8.429 dBi. This four-feed CP antenna is suitable for multimode GNSS application.

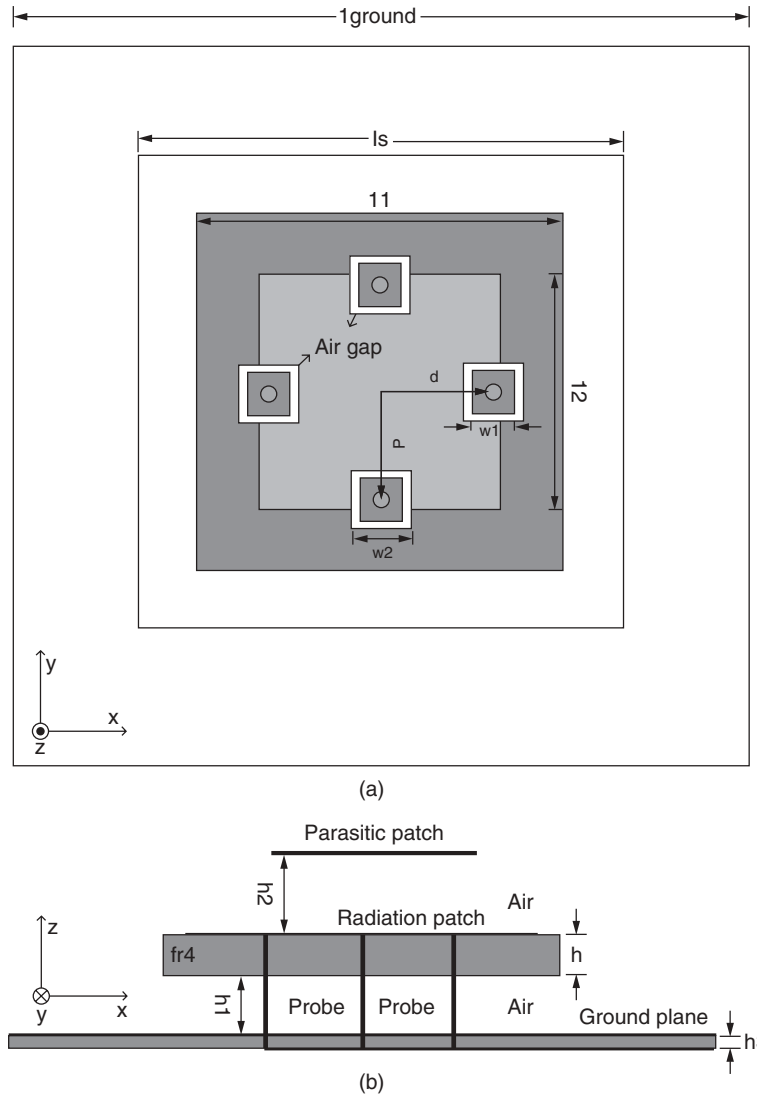

Figure 5.29 Geometry of the wideband CP antenna: (a) top view; (b) side view.

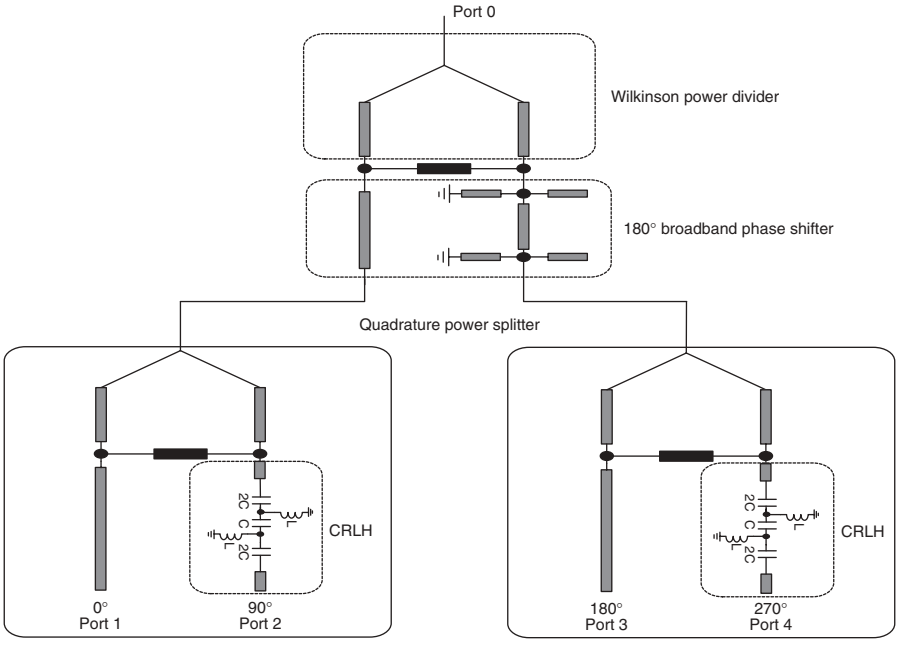

Figure 5.30 Broadband five-port phase shifter and feed network providing currents of equal amplitude and phase of 0°, 90°, 180° and 270°.

Table 5.1 Dimensions of the antenna (units: mm)

d	h	h_1	h_2	l_1	l_2	l_s	l_{ground}	w_1	w_2
25.6	3	12	10	64.8	55	84	100	6	9

5.3 High-Precision GNSS Terminal Antennas

High-precision satellite positioning has been widely used in applications including marine and terrestrial geodesy, geodynamics, astronomy, geophysical exploration, resource exploration, engineering survey deformation monitoring and civil engineering. To provide enhanced accuracy of location, receivers for these applications make use of the information contained in the phase of the incoming satellite, so maintaining the stability of the phase centre of the antenna is very important in the antenna design.

What the satellite navigation system measures is the distance between the phase centres of the transmitting receiving antennas. The satellite navigation

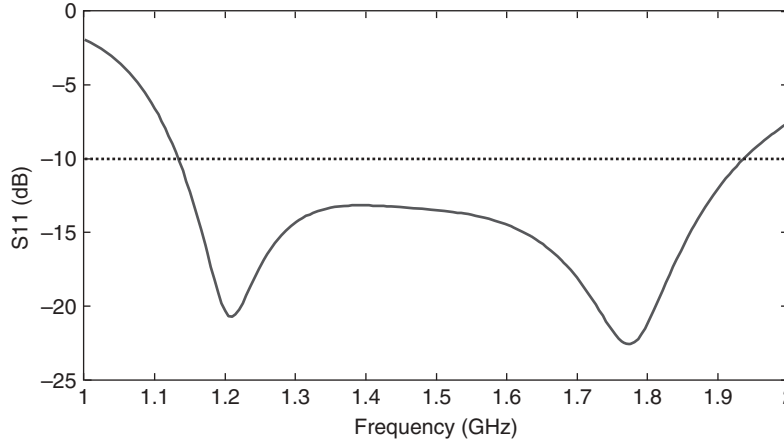

Figure 5.31 Simulated return loss of the wideband CP antenna.

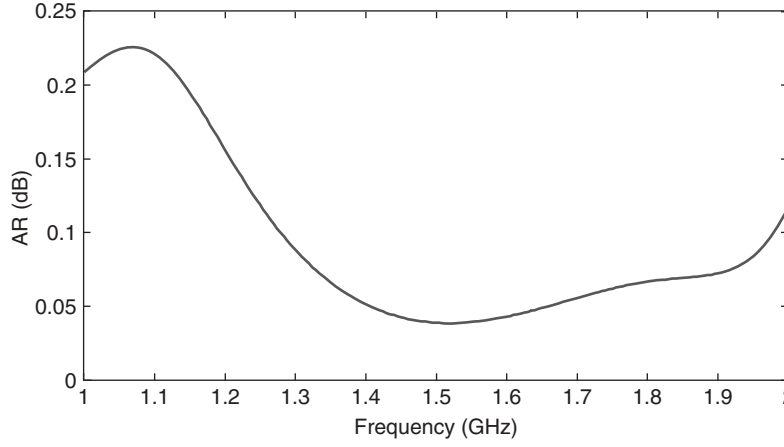

Figure 5.32 Simulated AR of the wideband CP antenna.

receiver needs to track signals from several satellites simultaneously; each satellite has different elevation and azimuth angles as seen from the receiver, so variations in the antenna phase centre when seen from different elevation and azimuth angles will give rise to position errors. The phase centre of the antenna is the benchmark of the observations of the satellite navigation receiver, while the placement of the antenna is based on the geometric centre. Any distance between these two centres will cause some measurement error. Movement of the

phase centre as a function of elevation angle mainly causes altitude errors. Phase centre changes associated with the azimuth will result in errors in positioning in the horizontal plane. According to the stability of the phase centre of the antenna, these errors vary from a millimetre to a few centimetres. For pseudo-code ranging, this error is much smaller than the positioning accuracy, so it can be ignored, but for a carrier phase measurement used for high-precision positioning, this error cannot be ignored. A detailed discussion on the antenna phase centre and evaluation of the phase centre variation is presented in Appendix B.

A typical method of achieving stability of the antenna phase centre is to maintain the symmetry of the antenna structure. In the design of microstrip patch antennas, an axisymmetric multiple feed is often used to obtain antenna phase centre stability, since the antenna structure is itself symmetrical. In general, the more feed points and the better the physical symmetry of the antenna, the higher the stability of the phase centre, but at the cost of more complexity of the feed network. Also, microstrip patch antennas with axisymmetric multiple feeds suffer from narrow bandwidth. A multi-arm spiral antenna ensures the high-stability properties of the phase centre through spiral arms which are symmetrical around the axis.

As an example, we present here a multi-feed dual-band GPS patch antenna developed by Trimble Zephyr [18]. This antenna utilises an innovative n-point symmetrical feed patch design, where n is a positive integer greater than two, as shown in Figure 5.33. There is a significant improvement in terms of phase centre stability compared with a single-feed design. The key feature of this multi-feed design is its perfect symmetry in structure, obtained through combining a phased multiple feed system and precisely located feed points.

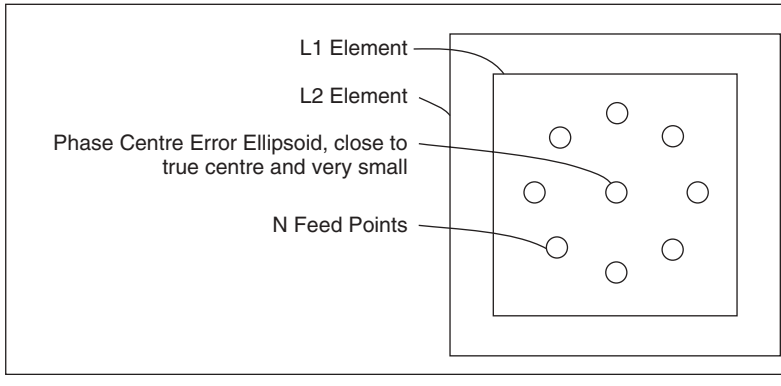

Figure 5.33 The Trimble Zephyr antenna with symmetrical n-point feed [18]. Source: www.Trimble.com.

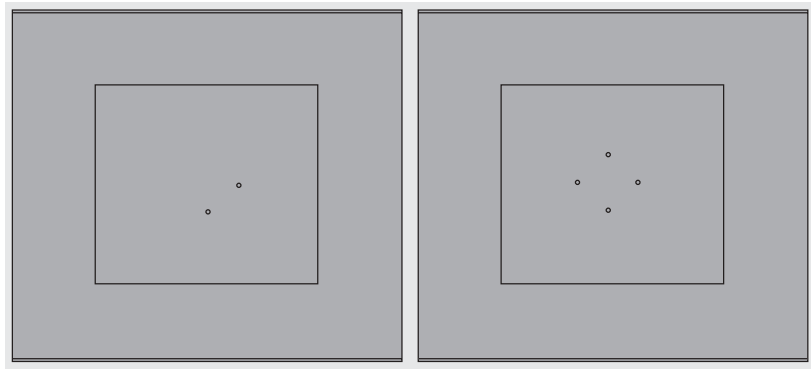

Figure 5.34 The configuration of (a) two-feed and (b) four-feed patch antennas.

The excellent symmetry of this antenna significantly improves its AR and phase centre stability and enables a much wider bandwidth (frequency range) to be provided. This increases the signal-to-noise ratio (SNR) at the receiver, improving the ability of the antenna/receiver system to acquire and track GNSS signals under difficult conditions. It also makes the antenna more immune to multipath.

In order to prove the effectiveness of this method, we can compare the phase centre stability of square patches with two feeds and with four feeds. As shown in Figure 5.34, the antennas are of the same size. The only difference between them is that one is dual feed and the other is quadruple feed. The antennas each have a ground plane 100 mm square and a radiating patch 56.8 mm square. The feed points are located 8 mm from the centre of the antenna. The substrate is 1.5 mm in height with a permittivity of 2.65. Figures 5.35 and 5.36 show the return loss and AR of both antennas. It can be seen that both antennas resonate at 1575 MHz and have good RHCP characteristics.

According to the method discussed in Appendix B, we can calculate the phase centre stability of the two antennas over a range of azimuth angles. For the four-feed antenna, the simulated phase fluctuations on different azimuth planes are shown in Figure 5.37.

Following the procedure in Appendix B, we can obtain the average phase centre location at (−1.4095, 0.6547, 8.1035) and can then calculate the phase centre variation on different azimuth planes, as shown in Figure 5.38.

The phase centre stability on different azimuth planes is calculated using Equation A2.1 and is shown in Table 5.2.

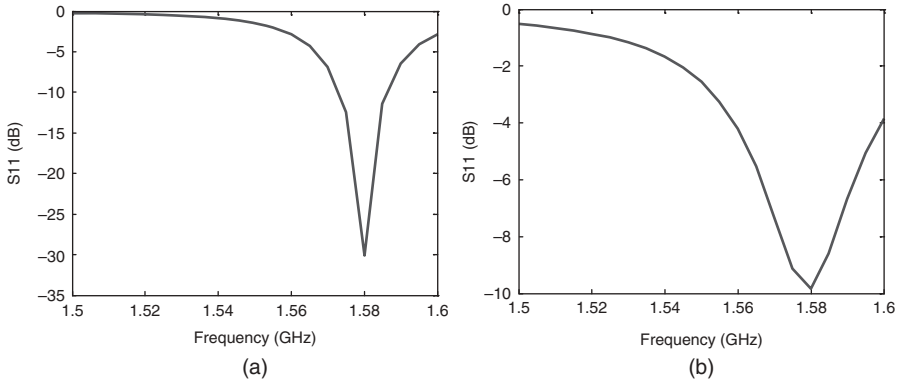

Figure 5.35 Return loss of (a) two-feed and (b) four-feed patch antennas.

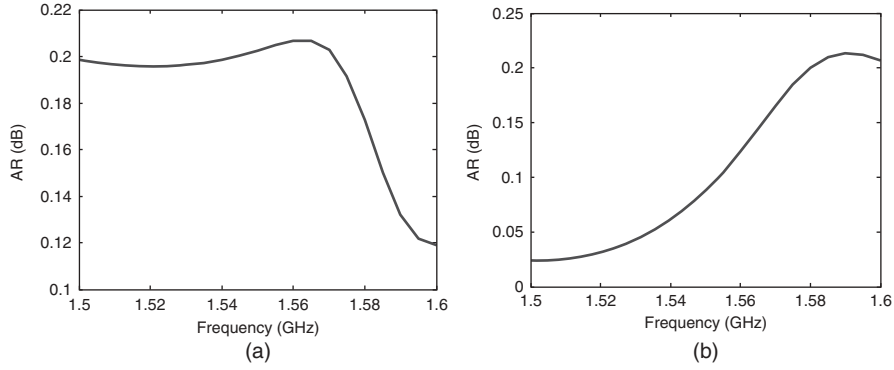

Figure 5.36 The AR of (a) two-feed and (b) four-feed patch antennas.

For the dual-feed patch antenna, the simulated phase fluctuations for different azimuth planes are shown in Figure 5.39.

Following the same procedure in Appendix B, we can obtain the phase centre location (1.1153,–0.8344, 6.9164) and can then calculate the phase centre variation, as shown in Figure 5.40.

So the phase centre stability on different azimuth planes is calculated using Equation A2.1 again, and is shown in Table 5.3. It can be seen that the antenna with four feeds has a more stable phase centre than the one with dual feeds.

We have discussed a variety of multiband and wideband GNSS antennas in this chapter and have addressed the issue of phase centre stability in high-precision GNSS terminal antennas. However, we have not considered the effects

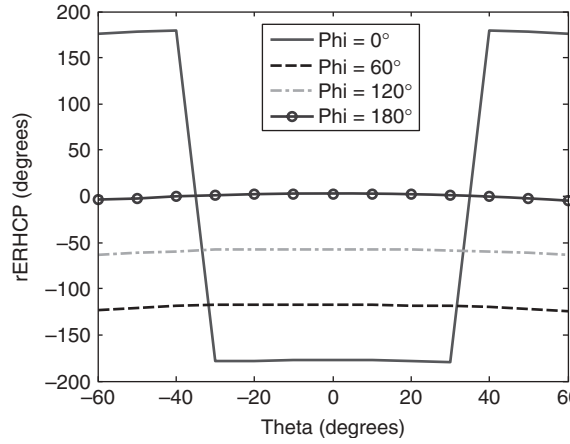

Figure 5.37 The phase pattern of RHCP remote electric field (rERHCP) on different azimuth planes for $\theta = \pm 60^\circ$ of four-feed antenna.

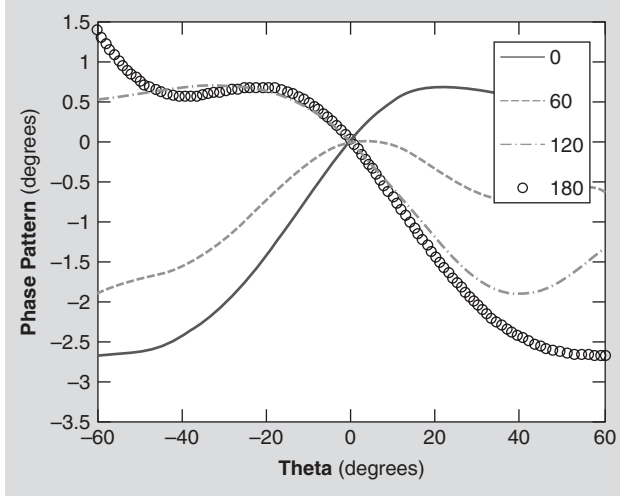

Figure 5.38 Phase centre variation of rERHCP on different azimuth planes for $\theta = \pm 60^\circ$ of four-feed antenna.

Table 5.2 Phase centre stability with respect to azimuthal angles for four-feed patch antenna

Azimuth angle Φ	0°	30°	60°	90°	120°	150°	180°
Phase centre stability (mm)	1.0753	0.9212	0.5112	0.7678	0.6905	1.007	1.0753

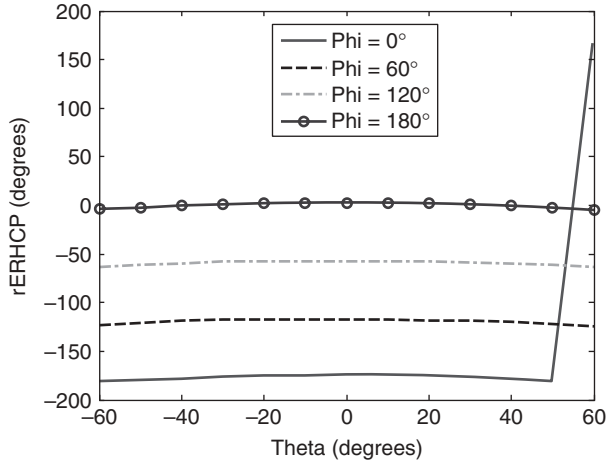

Figure 5.39 The phase pattern of rERHCP at different azimuth planes for $\theta = \pm 60^{\circ}$ of dual-feed antenna.

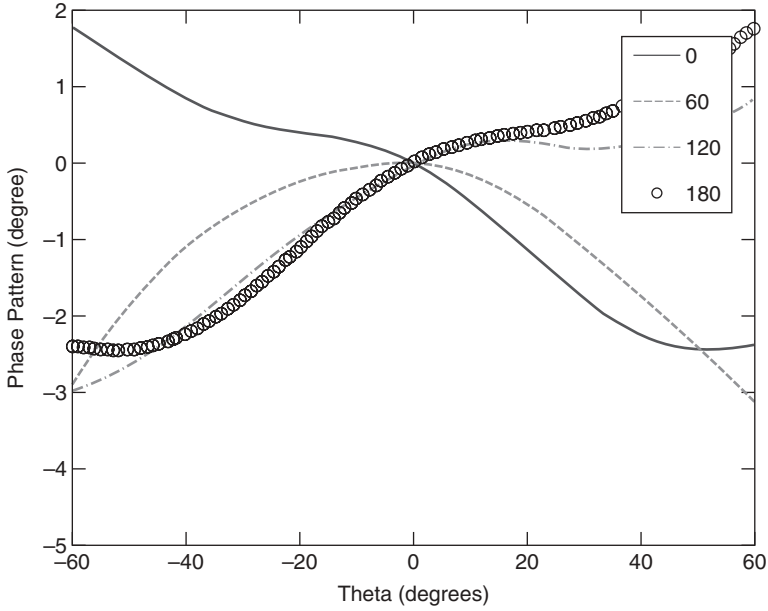

Figure 5.40 Phase centre variation of rERHCP on different azimuth planes for $\theta = \pm 60^{\circ}$ of dual-feed antenna.

Table 5.3 Phase centre stability with respect to azimuthal angles for dual-feed patch antenna

Azimuth angle Φ	0°	30°	60°	90°	120°	150°	180°
Phase centre stability (mm)	2.1115	2.0032	1.8228	1.4515	2.0078	2.3758	2.1115

of the environment, the human body and the terminal platform on the GNSS antenna performance. For portable GNSS terminals, it is very important to address these topics, so next three chapters are devoted to them.

References

1. Pozar, D.M. and Duffy, S.M., 'A dual-band circularly polarized aperture coupled stacked microstrip antenna for global positioning satellite', *IEEE Transactions on Antennas and Propagation*, **45**, 1618–1625, 1997.
2. Qiu, J., Li, W. and Suo, Y., 'Simulation and comparison of two classes of circularly polarized triple-frequency antennas', First International Symposium on Systems and Control in Aerospace and Astronautics, pp. 643–646, 2006.
3. Huang, B., Yao, Y. and Feng, Z., 'A novel wide beam dual-band dual-polarisation stacked microstrip-dielectric antenna', International Conference on Microwave and Millimeter Wave Technology, pp. 33–36, 2007.
4. Yang, K.P. and Wong, K.L., 'Dual-band circularly-polarized square microstrip antenna', *IEEE Transactions on Antennas and Propagation*, **49**, 377–382, 2001.
5. Wang, Y.S. and Chung, S.J., 'A miniature quadrifilar helix antenna for global positioning satellite reception', *IEEE Transactions on Antennas and Propagation*, **57**, 3746–3751, 2009.
6. Kilgus, C.C., 'Multielement fractional turn helices', *IEEE Transactions on Antennas and Propagation*, **16**, 499–500, 1968.
7. Agius, A.A., Saunders, S.R. and Evans, B.G., 'Antenna design for the ICO handheld terminal', 10th IEEE International Conference on Antennas and Propagation, pp. 1385–1389, April 1997.
8. Fujimoto, K. and James, J.R., *Mobile Antenna Systems Handbook*, Boston, MA: Artech House, pp. 411–416, 1994.
9. Lamensdorf, D. and Smolinski, M.A., 'Dual-band quadrifilar helix antenna', Antennas and Propagation Society International Symposium, Vol. 3, pp. 16–21, 2002.
10. Zheng, L. and Gao, S., 'Compact dual-band printed square quadrifilar helix antenna for global navigation satellite system receivers', *Microwave and Optical Technology Letters*, **53** (5), 993–997, 2011.
11. Raut, S. and Petosa, A., 'GPS wideband circularly polarized microstrip antenna array', 3rd European Conference on Antennas and Propagation, Digital Format, Berlin, April 2009.
12. Wang, J.J.H. and Triplett, D.J., 'High-performance universal GNSS antenna based on SMM antenna technology', IEEE International Symposium on Microwave, Antenna, Propagation, and EMC Technologies for Wireless Communications, pp. 644–647, 2007.

13. Clénet, M., Caillet, M. and Antar, Y.M.M., 'Wideband circularly polarized antenna elements for GPS/GNSS applications developed at DRDC Ottawa', 14th International Symposium on Antenna Technology and Applied Electromagnetics (ANTEM) and the American Electromagnetics Conference (AMEREM), pp. 1–4, 2010.
14. Massie, G., Caillet, M., Clenet, M. and Antar, Y.M.M., 'A new wideband circularly polarized hybrid dielectric resonator antenna', *IEEE Antennas and Wireless Propagation Letters*, **9**, 347–350, 2010.
15. Iwasaki, H., 'A circularly polarized small-size microstrip antenna with a cross slot', *IEEE Transactions on Antennas and Propagation*, **44**, 1399–1401, 1996.
16. Wang, C. and Chang, K., 'A novel CP patch antenna with a simple feed structure', Antennas and Propagation Society International Symposium, Vol. 2, pp. 1000–1003, 2000.
17. Tao, J., Yu, J. and Chen, X., 'A design of multi-mode global navigation satellite system antenna', *Chinese Scientific Papers Online*, 18 January 2011.
18. Krantz, E., Riley, S. and Large, P., 'GPS antenna design and performance advancements: The Trimble Zephyr', http://trl.trimble.com/docushare/dsweb/Get/Document-86094/5700WPZephyrE.pdf (accessed 4 November 2011).

6

Terminal Antennas in Difficult Environments

6.1 GNSS Antennas and Multipath Environment

The introduction of built-in GPS in portable personal navigation devices (PNDs), especially in mobile phones, has revolutionised the navigation industry. The ever-growing demand for the availability of navigation facilities in these devices has made the GNSS an essential part of modern wireless personal area network (WPAN) and wireless body area network (WBAN) applications. As the only navigation and positioning service provider to the mobile phone industry in recent times, the GPS is discussed in this chapter.

Portable mobile terminals are affected by multipath due to reflections, diffraction and scattering of the incident radio waves. It depends on the structure of the surrounding environment, as shown in Figure 6.1. This phenomenon has been well studied over time. Analysis of this complex and random nature problem is complicated. Statistical modelling is a powerful tool that offers simple and flexible solutions to such problems. A number of researchers have used this approach to study and characterise the multipath effects on mobile terminals and GPS antennas [1–10]. Axelrad *et al*. have used signal-to-noise ratios (SNRs) to predict and remove multipath errors [7]. Wu and Hsieh have used sidereal filtering of time-series range residual variations based on a least squares model to mitigate the multipath [8]. It requires a comprehensive data set containing multipath delay samples from the previous day and the day before that. Spangenberg *et al*. have modelled the multipath as the variance change in received signals in line-of-sight (LOS) conditions and as mean value jumps

Antennas for Global Navigation Satellite Systems, First Edition.
Xiaodong Chen, Clive G. Parini, Brian Collins, Yuan Yao and Masood Ur Rehman.

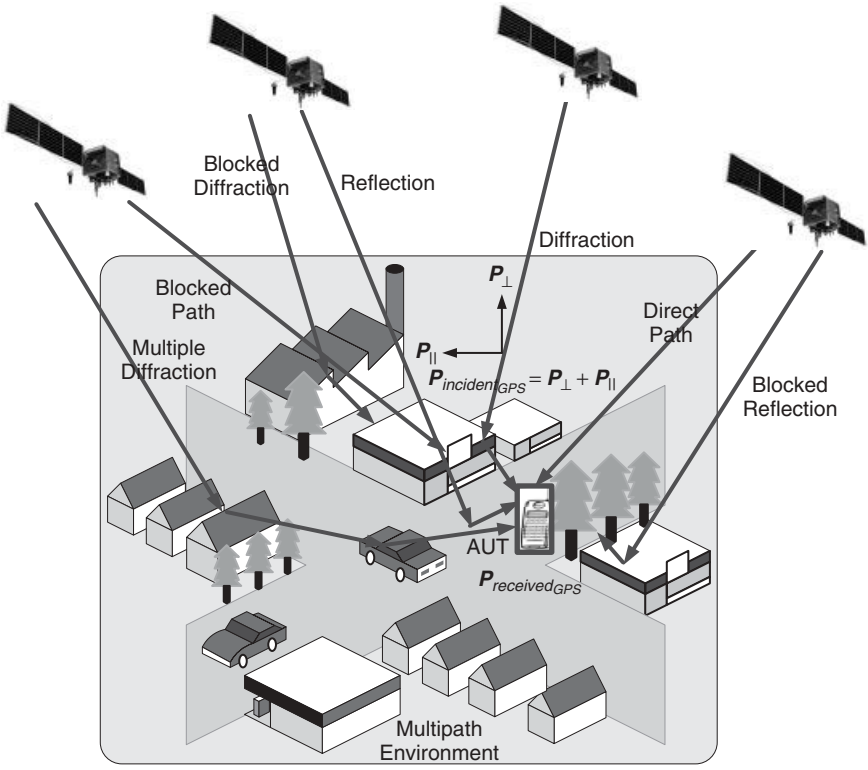

Figure 6.1 GPS environment and multipath signals. Reproduced by permission of © 2012 IEEE.

in non-line-of-sight (NLOS) conditions using an extended Kalman filter [9]. Hannah has proposed a parabolic-equation-based propagation model for GPS multipath employing the concept of coupled polarisation reflection coefficient [10]. However, these studies usually need large measurement data sets and mainly deal with quantification of multipath effects on stand-alone, static GPS receivers with antennas designed according to the theoretical guidelines.

Ideally, the GPS antennas should have good RHCP with a uniform radiation pattern over the entire upper hemisphere to receive the incoming GPS signal efficiently. A good rejection of LHCP is also required to avoid multipath [11–13]. However, these requirements are difficult to fulfil in portable devices, especially in mobile terminals that are required to allow maximum mobility of the user and flexibility of use with multiple functions such as Wi-Fi, Bluetooth, FM radio, digital camera, mobile TV and GPS [14, 15].

In the common scenarios of cluttered environments including indoors and city streets, LOS GPS signals arriving at the mobile terminal are weak while the reflected signals may have arbitrary polarisations. Moreover, mobile phones are hardly used in a fixed position and the 'up' direction of the antenna changes depending on the used orientation. Furthermore, the antenna suffers from electromagnetic absorptions and shielding of clear sky view in hand held positions. Establishing a quick GPS link with good satellite lock is therefore a difficult task in such devices. Use of wide-beam linear polarised (LP) GPS antennas could help to address the uncertainty of antenna orientation, blockage of LOS signal and clear sky view, and losses due to the user's body. Hence, LP antennas are a preferred choice for mobile terminal GPS as they give better performance compared with the conventional RHCP antennas [16–18]. Moreover, it enables use of the multipath signal constructively in order to establish a quick GPS link. Once a GPS lock is achieved, positioning errors can be estimated and removed using software approaches. This necessitates the characterisation of mobile terminal GPS antennas in a multipath environment.

Mean effective gain (MEG) has been used as an important performance metric for mobile handsets in multipath land mobile propagation environments [19, 20]. It describes statistically the impact of the antenna on the link budget considering the angle of arrival and polarisation of the incident waves and antenna gain characteristics [1–4]. Effects of the presence of the human body can also be evaluated using this technique [5, 6]. The applicability of this metric to portable GPS antennas in conjunction with another new parameter of antenna coverage efficiency has been proposed and developed by Ur Rehman *et al*. [21–23]. This chapter investigates the usefulness of this method, presenting a thorough analysis of mobile terminal GPS antennas.

6.2 Statistical Modelling of Multipath Environment for GNSS Operation

Currently, the performance assessment of a mobile terminal GPS antenna is mostly done by field tests. However, it has the drawback of longer procedures where weather, temperature and location hazards make it hard to control the test environment. It results in lack of accuracy due to poor repeatability and efficiency. The statistical models representing the real multipath scenarios provide an excellent alternative to the field tests, predicting the antenna performance while avoiding the shortcomings of the field tests.

A statistical method is developed to characterise the environmental factors on the performance of the GPS antennas, introducing the parameters of GPS

mean effective gain (MEG_{GPS}) and coverage efficiency (η_c). The MEG equation derived by Taga [1] is reformulated to suit the GPS environment with RHCP incoming waves and environmental reflections. An overview of the expected performance of the GPS antennas in the multipath environment can be achieved using this method by knowing the 3D free space antenna gain patterns and the average angular distribution of incident power in the environment.

6.2.1 GPS Mean Effective Gain (MEG_{GPS})

The MEG is the average gain of the antenna performance in a multipath radio environment. The MEG of an antenna in a mobile terminal is defined as [1]

$$\text{MEG} = \frac{\text{mean received power } (P_{\text{received}})}{\text{total mean incident power } (P_{\text{incident}})} \tag{6.1}$$

For spherical coordinates (Figure 6.2), P_{received} can be expressed as [24]

$$P_{\text{received}} = \int_0^{2\pi} \int_0^{\pi} \left[P_1 G_\theta (\theta, \phi)\, p_\theta (\theta, \phi) + P_2 G_\phi (\theta, \phi)\, p_\phi (\theta, \phi) \right] \sin\theta \, d\theta \, d\phi \tag{6.2}$$

where $G_\theta (\theta, \phi)$ and $G_\phi (\theta, \phi)$ are θ and ϕ components of the antenna power gain pattern respectively and $p_\theta (\theta, \phi)$ and $p_\phi (\theta, \phi)$ indicate the θ and ϕ components of angular density functions of the incoming waves, respectively. P_1 is the mean power that would be received by an isotropic antenna in θ polarisation while P_2 is the mean power received by an isotropic antenna in ϕ polarisation. The total mean incident power (P_{incident}) arriving at the antenna is the summation of the mean powers in the two polarisations.

The incident wave in the GPS mobile environment can be split into two components, namely the perpendicular polarised component and the parallel polarised component. Therefore, θ and ϕ components respectively correspond to the perpendicular and parallel polarised components. Reformulating Equation 6.2 to suit the GPS environment results in the following:

$$P_{\text{received}_{\text{GPS}}} = \int_0^{2\pi} \int_0^{\pi} \left[P_\perp G_\perp (\theta, \phi)\, p_\perp (\theta, \phi) + P_{||} G_{||} (\theta, \phi)\, p_{||} (\theta, \phi) \right] \sin\theta \, d\theta \, d\phi \tag{6.3}$$

Now, $P_\perp$ and $P_{||}$ are the mean received powers in the perpendicular and parallel polarisations with respect to the ground plane while $p_\perp (\theta, \phi)$ and $p_{||} (\theta, \phi)$ represent the perpendicular and parallel components of the angular density

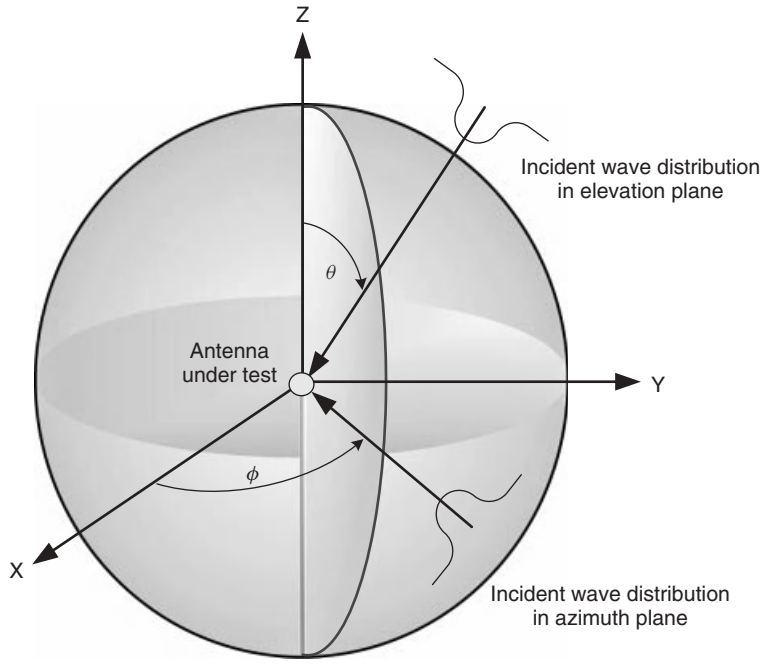

Figure 6.2 Spherical coordinates system and representation of a hypothetical incident wave distribution model. Reproduced by permission of © 2012 IEEE.

functions of the incoming waves respectively, as shown in Figure 6.1. P_{incident} arriving at the mobile GPS terminal is then

$$P_{\text{incident}_{\text{GPS}}} = P_{\perp} + P_{||} \tag{6.4}$$

The ratio between the mean powers received in the two polarisations is called the Cross-Polarisation Ratio (XPR) and described as

$$\text{XPR} = \frac{P_{\perp}}{P_{||}} \tag{6.5}$$

Using Equations 6.3–6.5, the MEG expression for the GPS antenna can be formulated as [22, 23]

$$\text{MEG}_{\text{GPS}} = \int_0^{2\pi} \int_0^{\pi} \left[\frac{\text{XPR}}{1+\text{XPR}} G_{\perp}(\theta,\phi) p_{\perp}(\theta,\phi) + \frac{1}{1+\text{XPR}} G_{\parallel}(\theta,\phi) p_{||}(\theta,\phi) \right] \sin\theta \, d\theta d\phi \tag{6.6}$$

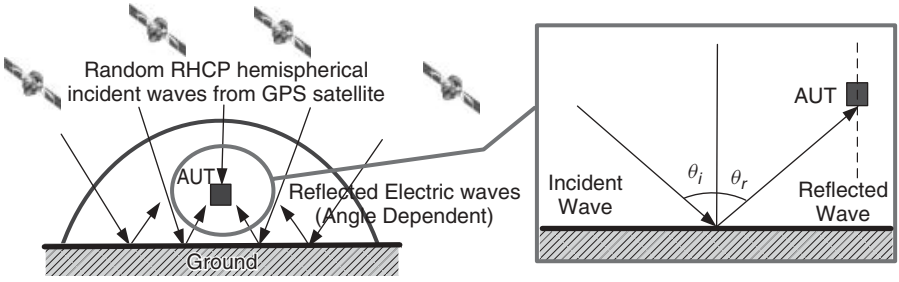

Figure 6.3 Multipath environment model around the mobile terminal GPS receiver antenna [22]. Reproduced with permission from IET.

Since XPR governs the polarisation of the incoming wave in this model, the circular polarised (CP) nature of the incoming GPS satellite signal is accumulated by making XPR = 0 dB. It employs the fact that simultaneous transmission of two LP waves that have a phase difference of $\pi/2$ (radians) results in the generation of a CP wave.

6.2.2 *GPS Angle of Arrival Distribution* (AoA_{GPS})

The AoA_{GPS} gives a statistical definition of the direction of arrival of the incident radio waves, arriving at the mobile terminal GPS antenna. Both the azimuth and elevation planes should be considered separately to replicate the multipath environment.

The incident radio waves are reflected, diffracted and scattered from the objects located in the surroundings of the receiving antenna. Since these objects vary in height and shape, the direction of arrival of the incident waves is random. This random occurrence is dealt with by a uniform angular density function in azimuth, similar to the case of the land mobile environment [1–3]. For the GPS environment, reflections from the ground (Figure 6.3) should also be considered in the elevation plane. The elevation plane is therefore divided into incident and reflection regions. Due to the lack of available measurement data for the direction of arrival of the GPS waves, the angular density function is assumed to be uniform in the incident region. In the reflection region, it is no longer uniform and reduced by a factor governed by the reflection coefficients. Also, the favourable use of the multipath signal in the mobile terminal GPS antennas for quick link establishment leads to use the summation of the received powers in the incident and reflected regions.

In accordance with the preceding assumptions, the statistical model for the GPS antenna in an open field multipath environment with ground reflections is

proposed as follows [22, 23, 25]:

$$p_{\perp}(\theta,\phi) = \begin{cases} 1 & 0 \le \theta \le \pi/2 \\ A(\theta)_{\perp} & \pi/2 \le \theta \le \pi \end{cases} \tag{6.7}$$

$$p_{\parallel}(\theta,\phi) = \begin{cases} 1 & 0 \le \theta \le \pi/2 \\ A(\theta)_{\parallel} & \pi/2 \le \theta \le \pi \end{cases} \tag{6.8}$$

$A(\theta)$ depends upon the reflection coefficients for the perpendicular and parallel components that vary with angle of incidence (θ_i) as [26]

$$A(\theta_i)_{\perp} = \frac{\cos\theta_i - \sqrt{(\varepsilon_2/\varepsilon_1) - \sin^2\theta_i}}{\cos\theta_i + \sqrt{(\varepsilon_2/\varepsilon_1) - \sin^2\theta_i}} \tag{6.9}$$

$$A(\theta_i)_{||} = \frac{(\varepsilon_2/\varepsilon_1)\cos\theta_i - \sqrt{(\varepsilon_2/\varepsilon_1) - \sin^2\theta_i}}{(\varepsilon_2/\varepsilon_1)\cos\theta_i + \sqrt{(\varepsilon_2/\varepsilon_1) - \sin^2\theta_i}} \tag{6.10}$$

In this study, the open field ground is considered to be of a semi-grassy, semi-concrete type with a relative permittivity of 4.5 [27, 28]. It makes the model a replication of the open field working environment. Having the knowledge of $\mathrm{AoA}_{\mathrm{GPS}}$, the model could be easily adapted to an urban environment.

6.2.3 GPS Coverage Efficiency (η_c)

Coverage efficiency of the receiving GPS antenna is another important parameter. It defines the capability of the antenna to receive the signals coming directly from the satellites.

The GPS antenna can receive signals from all directions that lie within its coverage area. However, the performance of a GPS antenna is currently characterised by its ability to receive the signals for elevation angles higher and lower than 10° (from the horizon) [12]. Defining the antenna coverage based on this criterion fails to describe its overall coverage in the upper hemisphere. The concept of coverage efficiency overcomes this drawback by providing information about the antenna coverage in the whole upper hemisphere.

The coverage efficiency of the antenna under test is calculated as the ratio of the solid angles subtended by its coverage area to the total area [22, 23]:

$$\eta_c = \frac{\text{coverage area}}{\text{total area}} \tag{6.11}$$

These calculations are based on the RHCP gain pattern of the antenna under test to suit the RHCP incoming radio waves. The coverage area depends on

a carefully calculated received signal threshold level. Signals below this level are considered too weak to have an impact and hence wasted. The maximum coverage that can be obtained by a reference GPS antenna is termed the total area. It is considered to be the half-hemispherical solid angle of 2π for an isotropic antenna. Figure 6.4 illustrates the η_c calculations. The box encloses the incident region (upper hemisphere) with the horizon at 0° and the zenith at 90°. The cross-hatched part indicates the coverage area.

An appropriate threshold level is worked out using the GPS link budget for the L1 (1575.42 MHz) frequency band [29]:

$$P_r = P_t + G_t - L_p - L_m + G_r \tag{6.12}$$

where P_r is the receiver sensitivity while P_t is the transmitted output power including the transmitter losses. G_t and G_r indicate the gains of the transmitting and receiving antennas respectively, while L_p is the free space loss and L_m indicates the miscellaneous losses including polarisation mismatch and atmospheric losses. The link budget is calculated as follows:

Satellite altitude $R = 20\,180$ km

$G_t = 13$ dBi [29, 30]

$P_t = 16.99$ dBW (corresponds to 50 W typically) [29]

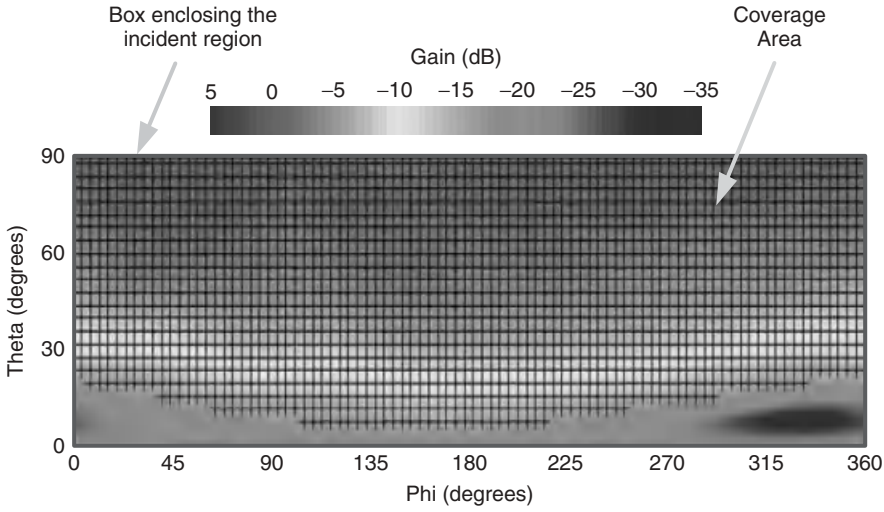

Figure 6.4 Illustration of η_c calculations based on RHCP radiation pattern of a GPS antenna with cross-hatched regions indicating coverage area (where signal is above −13 dBi) [25]. Reproduced by permission of © 2012 IEEE.

However, in practical scenarios P_t could be reduced to 14.3 dBW due to impedance mismatches and circuit losses [30]:

$$L_p = (4\pi R/\lambda)^2 = 182.5\,\text{dB}$$

$$L_m = 2\,\text{dB [29, 30]}$$

$$P_r = -160\,\text{dBW (corresponds to} - 130\,\text{dBm typically)}$$

Different GPS vendor specifications indicate that P_r could be as high as -175 dBW [31]. Submitting these values in Equation 6.12 gives $G_r = -17.8$ dBi. It shows that a minimum threshold level of -17.8 dBi is required to calculate the coverage efficiency of the GPS antenna. However, a threshold level of -13 dBi has been selected to investigate the worst case scenarios. This selection is validated in the following sections by a close agreement between η_c values calculated using the proposed model and observed in the open field tests.

6.3 Open Field Test Procedure

A detailed open field test procedure is adopted to verify and validate the model's predictions.

6.3.1 Measurement of GPS Mean Effective Gain

For MEG_{GPS}, the received signal power (P_{signal}) should be known. The signal-to-noise ratio (SNR) is a measure that is used to evaluate the performance of the designed GPS antennas. It indicates how strongly the satellite's radio signal is being received. It SNR is computed as a ratio of the signal power to the noise power corrupting the signal:

$$\text{SNR (dB)} = P_{\text{signal}}\ \text{(dBm)} - P_{\text{noise}}\ \text{(dBm)} \tag{6.13}$$

Also [30]:

$$P_{\text{noise}}\ \text{(dBm)} = P_{\text{sr}}\ \text{(dBm)} + \text{NF (dB)} \tag{6.14}$$

Here, NF is the noise figure representing the noise generated within the GPS receiver while P_{sr} is the temperature-dependent source resistance noise power. At a temperature of 25°C and a system bandwidth of 1 Hz [32]

$$P_{\text{sr}}\ \text{(dBm)} = kTB = 1.380 \times 10^{-23} \times 298.15 \times 1$$
$$= -174\ \text{dBm} \tag{6.15}$$

where k is Boltzmann's constant and T is temperature in kelvin. Now, putting these values in Equation 6.15, the following expression is obtained:

$$P_{\text{signal}}\ (\text{dBm}) = \text{SNR}\ (\text{dB}) + \text{NF}\ (\text{dB}) - 174\ \text{dBm} \tag{6.16}$$

This implies that the signal strength delivered to the GPS receiver is linearly dependent on the SNR if NF is constant in Equation 6.16. Hence, mean received power (P_{received}) of a GPS antenna in Equation 6.1 can be calculated using the mean SNR level for that antenna. The mean SNR level of the reference antenna (typically dipole antenna) gives the total mean incident power (P_{incident}). Finally, MEG_{GPS} is calculated by taking the ratio of the mean SNR levels of the two antennas.

6.3.2 Measurement of GPS Coverage Efficiency

The coverage efficiency describes how well the antenna can view the sky and receive the satellite signal. In the field, this quality corresponds to the number of tracked GPS satellites. It is obtained by taking the ratio of the mean value of the tracked satellites (representing the coverage area of the antenna under test in Equation 6.11) and the maximum number of tracked satellites observed during the whole measurement process (representing the total area in Equation 6.11):

$$\eta_c = \frac{N_{\text{mean}}}{N_{\text{maximum}}} \tag{6.17}$$

6.3.3 Measurement Set-Up

The DG-100 GPS receiver from GlobalSat Technology is used in the measurements. This receiver has an embedded SIRF Star-III chipset module with 20 channels (can track 20 satellites). The sensitivity of the receiver is −145 dBm. The data for the number of tracked satellites and received SNR by the antenna under test is collected using a satellite status chart. The field test set-up is illustrated in Figure 6.5. The antennas are connected to the GPS receiver via an MMCX-to-SMA jumper cable.

The designed antennas are tested for GPS signal reception in an outdoor open environment in both horizontal and vertical orientations with respect to the ground. In this suburban environment, the height of buildings in the vicinity of the test point ranges from ∼10 to 60 m and they are located at a distance of ∼30–50 m. The GPS receiver and the antennas are placed at a height of 1 m from the ground. The antennas are rotated horizontally and eight readings of

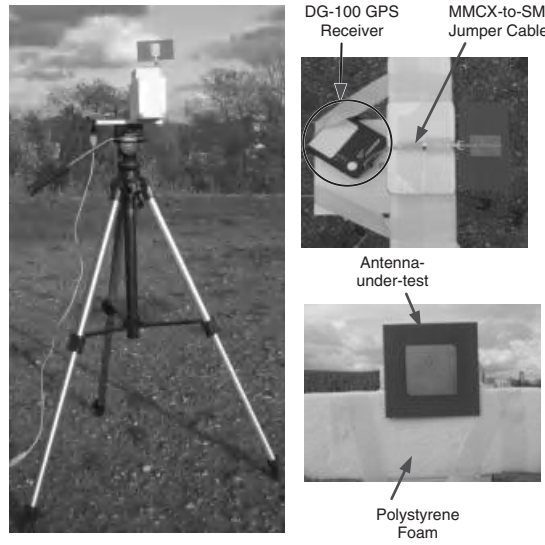

Figure 6.5 Open field test set-up for measurement of MEG_{GPS} and η_c for GPS antennas [25]. Reproduced by permission of © 2012 IEEE.

the satellite status chart are recorded for the following angles:

$$\phi = n \times \frac{\pi}{4} \qquad n = 0, 1, 2, \ldots, 7 \tag{6.18}$$

This effectively provides the average reception of the signal in this environment. The information for the eight best values of the received SNR are used to calculate the mean SNR level for each antenna. Hence

$$\text{SNR}_{\text{mean}} = \frac{1}{N} \sum_{i=1}^{N} \text{SNR}_i \tag{6.19}$$

MEG_{GPS} is then calculated by dividing SNR_{mean} of the antenna under test by SNR_{mean} of the reference antenna. Coverage efficiency is calculated using the mean number of tracked satellites (N_{mean}) and dividing by 12, which appeared to be maximum number of tracked satellites (N_{maximum}) during the measurements.

6.4 Performance Assessment of GNSS Mobile Terminal Antennas in Multipath Environment

Two approaches have been adopted to establish the accuracy and efficiency of the proposed statistical model to predict GPS antenna performance in the

multipath environment as described in the following sections. A number of commonly used GPS antennas, both generic and mobile terminal types, are analysed in the open field multipath environment to benchmark the working of the proposed model. The generic antennas include the dipole, microstrip patch and generic PIFA, while the mobile terminal antennas include the PIFA, IFA, DRA, helix and mono-loop. The mobile terminal antennas use a ground plane of $100 \times 40\,\text{mm}^2$ that represents the size of a standard mobile phone.

6.4.1 Design of Tested GPS Antennas

6.4.1.1 Dipole

The use of a standard simple antenna with known characteristics is needed to bench mark the model. A half-wavelength dipole antenna, similar to the one discussed in Chapter 2, working at 1575.42 MHz, is chosen for this purpose due to its simplicity and wide usage as a standard antenna.

The fabricated prototype of the antenna is shown in Figure 6.6a. The antenna performs well in the L1 frequency band with -10 dB bandwidth of 153 MHz as depicted by the measured S_{11} response in Figure 6.6b. The 3D gain patterns of the antenna are measured in an anechoic chamber using Satimo's Stargate 64 measurement system. The patterns for the perpendicular and parallel polarisations of the antenna in horizontal and vertical orientations are illustrated in Figures 6.6c and d.

6.4.1.2 Microstrip Patch Antenna

A CP truncated-corner microstrip patch antenna as discussed in Chapter 2 is used in this study. Figure 6.7a shows the geometry of the fabricated antenna. The free space S_{11} response of the antenna in Figure 6.7b shows good impedance matching in the L1 band with centre frequency at 1578 MHz. The measured 3D radiation patterns for perpendicular and parallel polarisation of the antenna for both the horizontal and vertical orientations are illustrated in Figures 6.7c and d.

6.4.1.3 Generic PIFA

The PIFA is a popular choice for a wide range of GPS applications. The antenna used in this study is shown in Figure 6.8a. The measured S_{11} curve of the antenna shown in Figure 6.8b indicates that the PIFA operates well in the L1 band having -10 dB bandwidth of 45 MHz. Figures 6.8c and d give an account of the measured 3D radiation patterns for perpendicular and parallel polarisations of the antenna in both horizontal and vertical orientations.

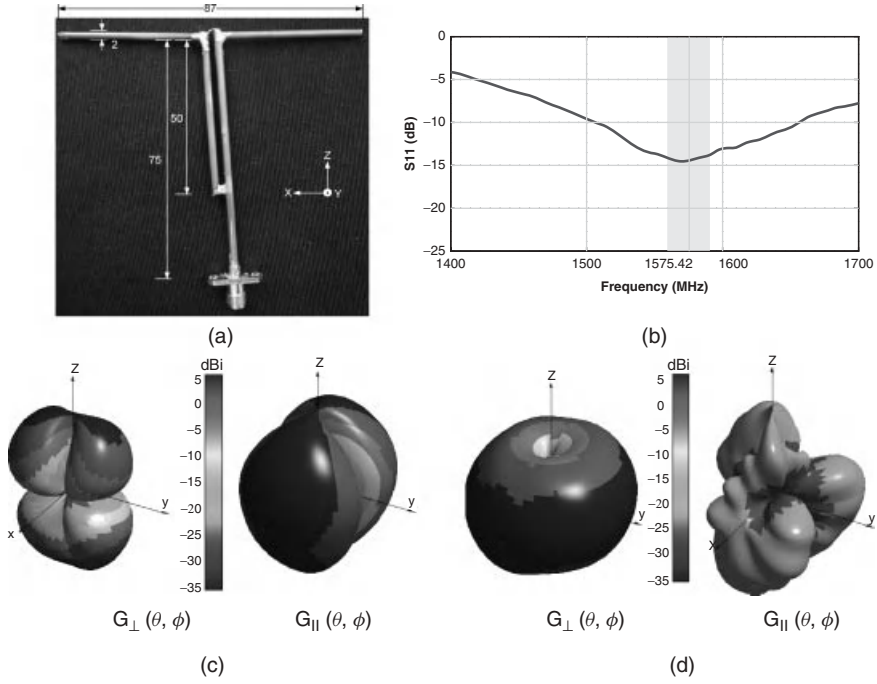

Figure 6.6 Geometrical structure of dipole antenna with measured S_{11} and 3D power gain patterns for perpendicular and parallel polarisations in horizontal and vertical orientations: (a) Antenna geometry (lengths are in mm), (b) Measured S_{11}, (c) Gain patterns for horizontal orientation and (d) Gain patterns for vertical orientation [25]. Reproduced by permission of © 2012 IEEE.

6.4.1.4 Mobile Terminal PIFA

The mobile terminal PIFA is designed using an FR4 substrate of 1.6 mm thickness. Figure 6.9a shows the geometrical structure of the prototype while Figure 6.9b presents the measured S_{11} curve for the antenna. The antenna has 4.1% of −10 dB impedance bandwidth for a frequency range of 1560 to 1625 MHz, adequate for GPS operation. The measured 3D gain patterns for the antenna at 1575.42 MHz for vertical and horizontal orientations are depicted in Figures 6.9c and d.

6.4.1.5 IFA

The IFA is designed on a metal plate of 0.45 mm thickness, 100 mm length and 40 mm width. The radiating element is mounted on the left side of the metal plate and has similar thickness (Figure 6.10a). The antenna is fed using

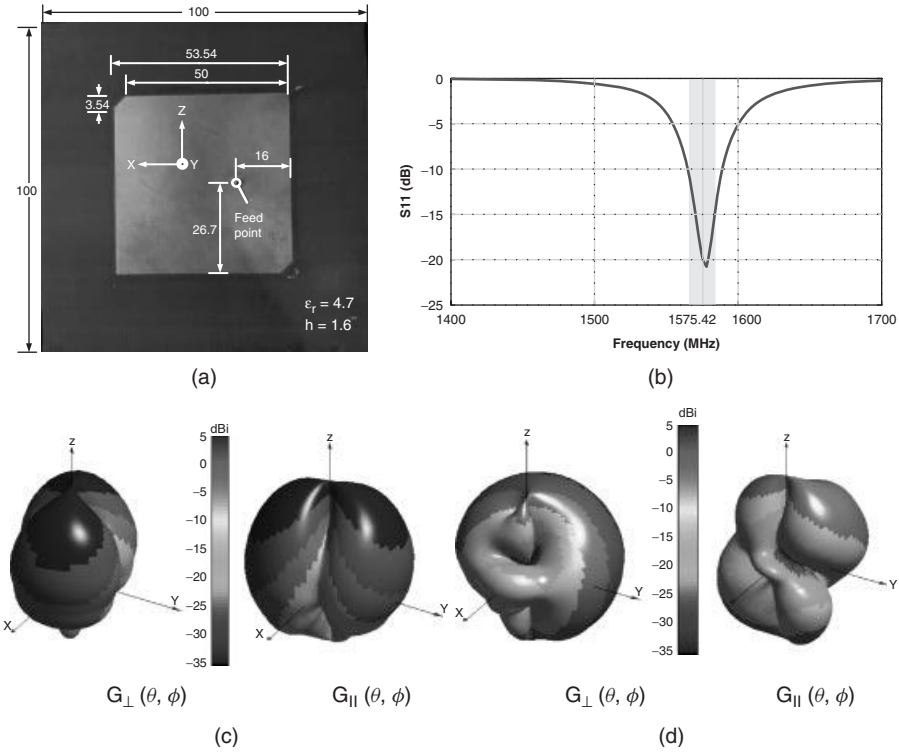

Figure 6.7 Geometrical structure of truncated-corner microstrip patch CP antenna with measured S_{11} and 3D power gain patterns for perpendicular and parallel polarisations in horizontal and vertical orientations: (a) Antenna geometry (lengths are in mm), (b) Measured S_{11}, (c) Gain patterns for horizontal orientation and (d) Gain patterns for vertical orientation [25]. Reproduced by permission of © 2012 IEEE.

a standard 50 Ω coaxial port. The antenna shows good performance for GPS operation with −10 dB bandwidth of 11.9% covering frequencies from 1480 to 1668 MHz. Figure 6.10b shows the measured S_{11} response for the antenna while Figures 6.10c and d illustrate the measured 3D radiation patterns for the antenna at 1575.42 MHz for vertical and horizontal orientations.

6.4.1.6 DRA

Ceramic antennas are another popular choice for embedded antennas due to their smaller size. The DRA designed for this study is loaded with a dielectric of $\varepsilon_r = 21$. The ground plane is lossy copper type with $\sigma = 5.8 \times 10^7$ S/m.

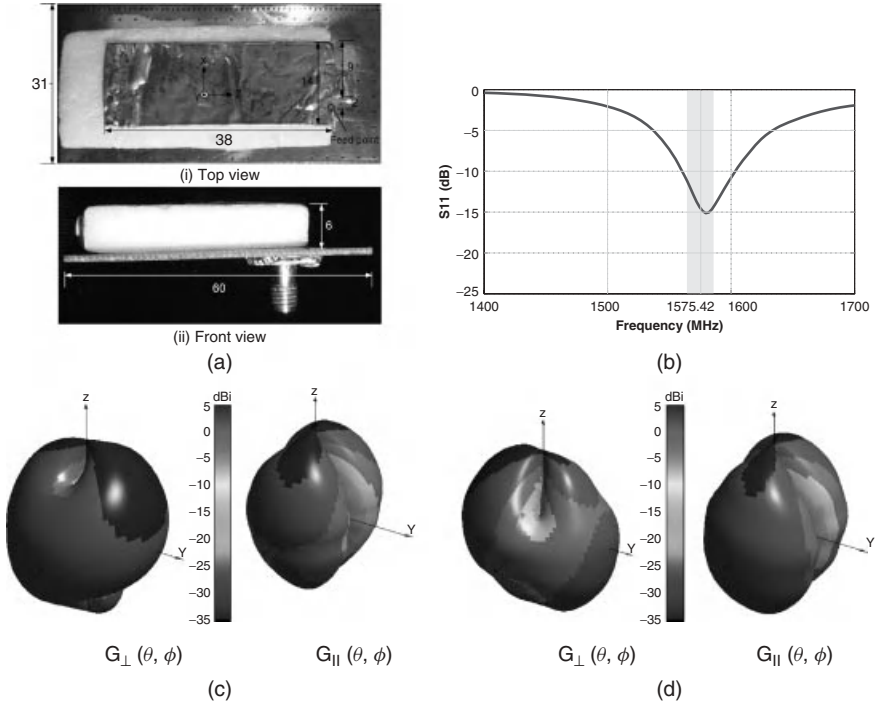

Figure 6.8 Geometrical structure of PIFA with measured S_{11} and 3D power gain patterns for perpendicular and parallel polarisations in horizontal and vertical orientations: (a) Antenna geometry (lengths are in mm), (b) Measured S_{11}, (c) Gain patterns for horizontal orientation and (d) Gain patterns for vertical orientation [25]. Reproduced by permission of © 2012 IEEE.

The loaded dielectric is covered with lossy silver having $\sigma = 6.17 \times 10^7$ S/m. The antenna is fed using a 50 Ω coaxial port as shown in Figure 6.11a. The measured S_{11} illustrated in Figure 6.11b indicates that the antenna works well in the L1 band with 2.8% of −10 dB bandwidth that covers frequencies from 1553 to 1597 MHz. The measured 3D gain patterns for the antenna at 1575.42 MHz for vertical and horizontal orientations are described in Figures 6.11c and d.

6.4.1.7 Helix

External antennas, like the helix, are not used widely in portable applications nowadays. However, studies of these kinds of antennas are good for the performance comparison. The helix antenna used in this study is mounted on the

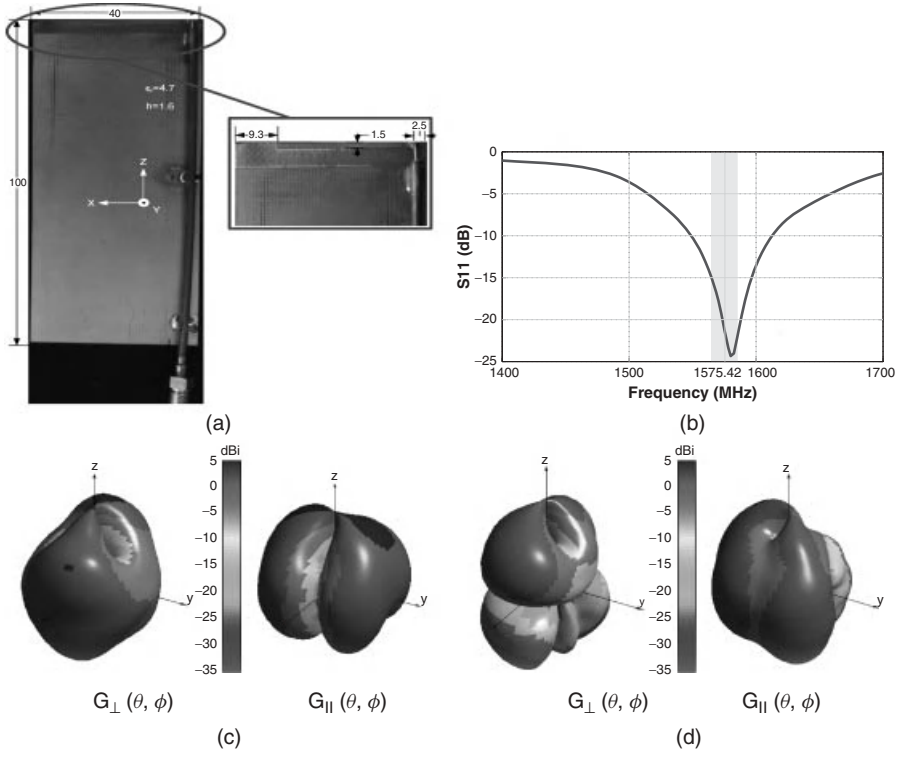

Figure 6.9 Geometrical structure of mobile terminal PIFA antenna with measured S_{11} and 3D power gain patterns for perpendicular and parallel polarisations in horizontal and vertical orientations: (a) Antenna geometry (lengths are in mm), (b) Measured S_{11}, (c) Gain patterns for horizontal orientation and (d) Gain patterns for vertical orientation.

top left of the metallic ground plane, shown in Figure 6.12a. The radius of the helix wire is 0.45 mm with a length of 26 mm. The antenna is fed through a 50 Ω coaxial port. The S_{11} response plotted in Figure 6.12b describes that the antenna works well in the L1 band having a −10 dB bandwidth of 9% ranging from 1495 to 1638 MHz frequencies. The measured 3D radiation patterns of the antenna in vertical and horizontal orientations are shown in Figures 6.12c and d.

6.4.1.8 Mono-Loop

This antenna is designed as a combination of the monopole and loop antenna and is termed mono-loop antenna. The ground plane size is only $18 \times 80\,\text{mm}^2$. The radiating element consists of 11 loops of $23.2 \times 2\,\text{mm}^2$. The antenna

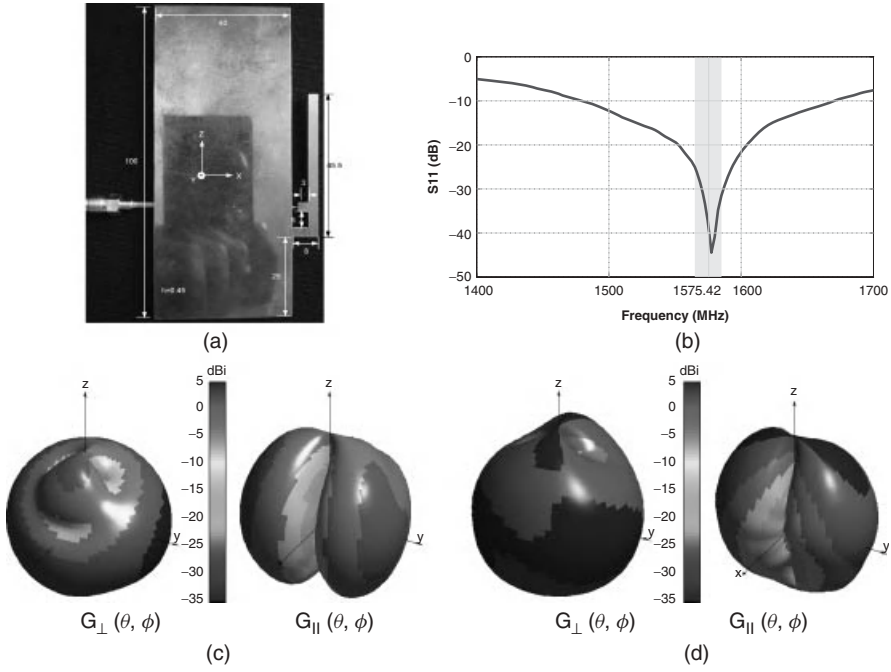

Figure 6.10 Geometrical structure of IFA antenna with measured S_{11} and 3D power gain patterns for perpendicular and parallel polarisations in horizontal and vertical orientations: (a) Antenna geometry (lengths are in mm), (b) Measured S_{11}, (c) Gain patterns for horizontal orientation and (d) Gain patterns for vertical orientation.

exhibits a −10 dB impedance bandwidth of 107 MHz covering the frequencies from 1520 to 1627 MHz. Figure 6.13a illustrates the geometrical structure and Figure 6.13b shows the measured S_{11} curve for the antenna. Figures 6.13c and d depict the measured 3D patterns for the antenna.

6.4.2 Comparison Based on Simulated and Measured 3D Radiation Patterns

Firstly, statistical calculation results of the model are compared for two different input methods. The three generic antennas, namely dipole, CP patch and generic PIFA, are analysed in the open field multipath environment to benchmark the working of the proposed model. The 3D gain patterns of the three antennas obtained through the simulations and the anechoic chamber (Satimo Stargate 64) measurements are used for the comparison. The results

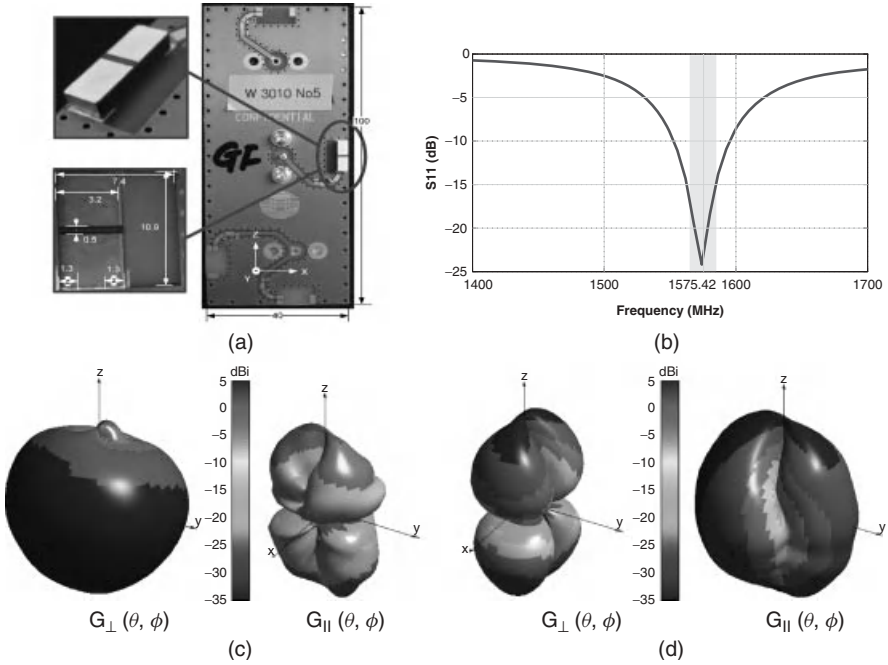

Figure 6.11 Geometrical structure of DRA antenna with measured S_{11} and 3D power gain patterns for perpendicular and parallel polarisations in horizontal and vertical orientations: (a) Antenna geometry (lengths are in mm), (b) Measured S_{11}, (c) Gain patterns for horizontal orientation and (d) Gain patterns for vertical orientation.

summarised in Table 6.1 show good agreement between the calculated results of η_c and MEG_{GPS} using the simulated and the measured 3D gain patterns. A maximum difference of 0.6 dB has been observed in MEG_{GPS} values in the actual reflection environment and 4% in η_c values. This difference is assigned to antenna fabrication errors.

Theoretically, the performance of a GPS antenna in terms of its MEG_{GPS} in the actual reflection environment (ARE) should lie between two extreme ideal environments (i.e. total reflection environment (TRE)) and no reflection environment (NRE) as part of the incident wave is reflected back, depending upon the reflection coefficients for a ground permittivity of 4.5 [27, 28]. The results in Table 6.1 indicate that the proposed model works well, exhibiting the expected theoretical behaviour.

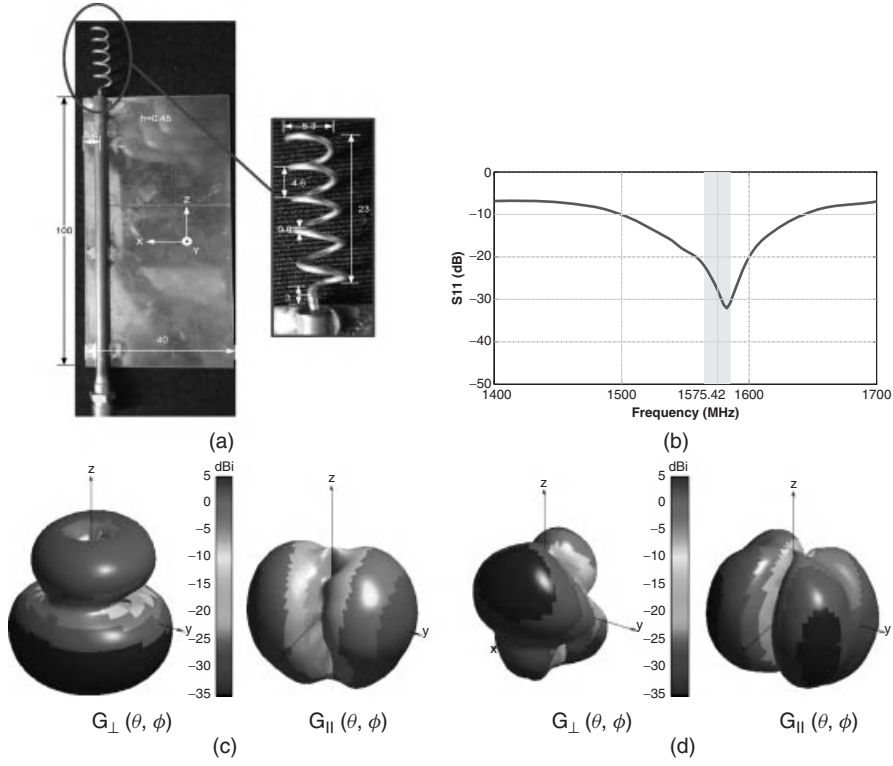

Figure 6.12 Geometrical structure of helix antenna with measured S_{11} and 3D power gain patterns for perpendicular and parallel polarisations in horizontal and vertical orientations: (a) Antenna geometry (lengths are in mm), (b) Measured S_{11}, (c) Gain patterns for horizontal orientation and (d) Gain patterns for vertical orientation.

6.4.3 Comparison Based on Measured 3D Radiation Patterns and Actual Field Tests

The comparison of the model's calculations to open field measurements serves as a crucial step in the validation process. The horizontal dipole antenna is used as a reference antenna in this study. Both the calculated (obtained through the proposed model using 3D measured gain patterns) and measured (mean SNR level observed in the actual field test) values of MEG_{GPS} are normalised to the corresponding values for the horizontal dipole antenna and described in dBd. Hence, −5.4 dB (in the actual reflection environment given in Table 6.1)

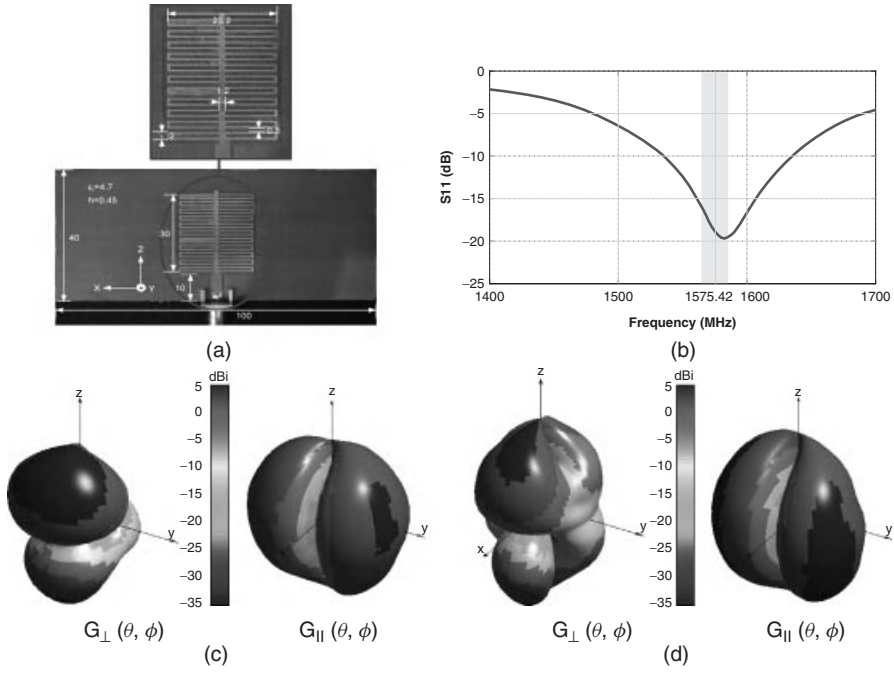

Figure 6.13 Geometrical structure of mono-loop antenna with measured S_{11} and 3D power gain patterns for perpendicular and parallel polarisations in horizontal and vertical orientations: (a) Antenna geometry (lengths are in mm), (b) Measured S_{11}, (c) Gain patterns for horizontal orientation and (d) Gain patterns for vertical orientation.

Table 6.1 Comparison of calculated η_c and MEG_{GPS} of tested GPS antennas in different reflection environments using simulated and measured 3D power gain patterns for validation of proposed GPS multipath model (TRE = Total Reflection Environment, NRE = No Reflection Environment, ARE = Actual Reflection Environment)

Antenna	Model calculations using simulated 3D patterns				Model calculations using measured 3D patterns			
	η_c (%)	MEG_{GPS} (dB)			η_c (%)	MEG_{GPS} (dB)		
		TRE	NRE	ARE		TRE	NRE	ARE
Horizontal dipole	95	−3.2	−6.1	−5.2	97	−3.7	−6.4	−5.4
Horizontal CP patch	100	−5.2	−5.7	−5.4	99	−5.8	−6.2	−6.0
Horizontal PIFA	98	−4.0	−5.8	−4.6	94	−4.3	−6.3	−5.1

and 40.2 dB (in the open field test) are being used as the reference levels for the calculated and measured results, respectively. The antennas are placed horizontally with respect to the ground. The results are summarised in Table 6.2.

In these assessments, the repeatability of the measurement procedure must also be known. Therefore, in these as well as the following investigations, MEG_{GPS} and η_c are calculated performing three sets of measurements for each antenna and reporting the mean values. The standard deviation of these three measurements (averaged over various tested scenarios) is 0.6 dB and 5% for MEG_{GPS} and η_c, respectively.

Table 6.2 Comparison of calculated η_c and MEG_{GPS} of tested GPS antennas in horizontal and vertical orientations using measured 3D power gain patterns with the actual field test measurements

Antenna	Orientation	Model calculations using measured 3D patterns		Open field test measurements	
		η_c(%)	MEG_{GPS}(dBd)	η_c(%)	MEG_{GPS}(dBd)
Dipole	Horizontal	97	0 (corresponding to calculated value of −5.4 dB in ARE)	96	0 (corresponding to measured average SNR of 40.2 dB)
	Vertical	94	−0.2	92	−0.2
CP patch	Horizontal	99	−0.6	97	−0.4
	Vertical	72	−2.1	72	−2.2
Generic PIFA	Horizontal	94	0.3	94	0.2
	Vertical	97	−0.5	97	−0.8
Terminal PIFA	Horizontal	83	−2.2	81	−2.3
	Vertical	95	−3.3	92	−3.1
IFA	Horizontal	100	0.6	97	0.4
	Vertical	79	−0.4	81	−0.3
DRA	Horizontal	95	−0.6	94	−0.5
	Vertical	94	−0.5	90	−0.5
Helix	Horizontal	97	−1.2	96	−1.5
	Vertical	87	−0.6	87	−1.0
Mono-loop	Horizontal	80	−2.0	82	−1.6
	Vertical	78	−1.6	80	−1.8

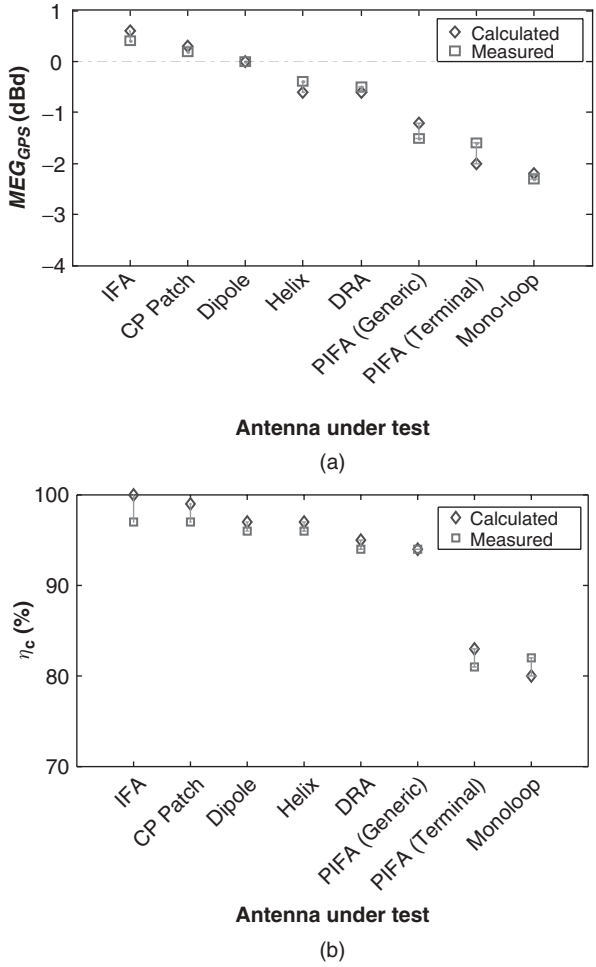

Figure 6.14 Comparison of calculated and measured values of MEG_{GPS} and η_c showing performance ranking of GPS antennas in horizontal orientation: (a) MEG_{GPS} taking horizontal dipole as a reference (0 dBd); (b) η_c.

The field test results show good agreement with the model's predictions for MEG_{GPS} and η_c values for the mobile terminal GPS antennas. Figure 6.14 indicates that a similar performance ranking of the tested antennas has been achieved in both the calculations and measurements. It confirms that the model can successfully translate and predict the working of GPS antennas in a multipath environment. A maximum difference of 0.4 dB is noted for MEG_{GPS} values and 3% for η_c values between the model's calculations and open field

measurements. These differences are well below the accepted levels reported in the literature [1, 2, 5]. They are mainly attributed to random factors arising from atmospheric errors and weather conditions.

The results also indicate that the two parameters of MEG_{GPS} and η_c do not rely greatly on each other. An antenna with good η_c may exhibit poor MEG_{GPS} and vice versa, for example in the case of the generic PIFA antenna. However, the multipath performance of GPS antennas could only be characterised by a combined consideration of the two parameters. MEG_{GPS} incorporates the whole environment taking into account both the direct and multipath signals, especially the ground reflections. On the other hand, η_c only considers the direct link. An antenna having low values of MEG_{GPS} and η_c would be unable to establish a quick GPS link as the direct signal is weak while the multipath impact is less significant. The performance of the antenna with high values of MEG_{GPS} should be analysed further in terms of its η_c. A high η_c shows that the direct signal is stronger than the multipath signal enabling the antenna to achieve an overall good performance with quick GPS link and low multipath errors. On the contrary, low η_c shows a weaker direct signal with a greater impact of the multipath signal. An antenna exhibiting such a performance could build satellite link quickly but with high errors. The CP patch and IFA belong to the first category while the generic PIFA lies in the second category. However, an optimal performance could only be achieved with an antenna exhibiting good MEG_{GPS} and η_c.

6.5 Performance Dependence on GNSS Antenna Orientation

Antenna orientation plays a vital role in multipath wireless communication. Varying orientation changes the antenna main lobe direction inflicting link losses. The mobile terminals operate in a dynamic environment with ever-changing orientations of the antennas depending on the user's holding position. The effects of these changes on mobile terminal GPS antennas is characterised in this section. The antennas are placed in a vertical orientation (with respect to the ground) and performance is studied in comparison with the horizontal orientations.

The calculated and measured results using the proposed statistical model and open field test are presented in Table 6.2. Figure 6.15 shows the comparison of the antenna rankings in terms of their MEG_{GPS} and η_c based on the two methods. It is further established that the model delivers precise results with a close agreement to the field test observations. A maximum relative difference of 0.4 dB in MEG_{GPS} and 4% in η_c has been noted.

These results also show that change in the antenna orientation has a profound effect on the performance of GPS antennas. Comparing the vertically oriented

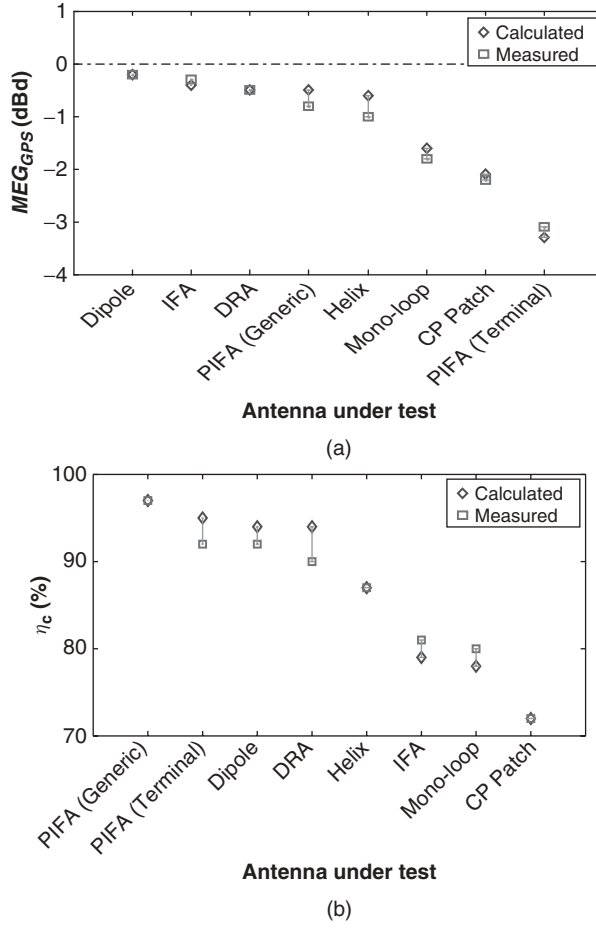

Figure 6.15 Comparison of calculated and measured values of MEG_{GPS} and η_c showing performance ranking of GPS antennas in vertical orientation: (a) MEG_{GPS} taking horizontal dipole as a reference (0 dBd); (b) η_c.

antennas with those in the horizontal orientation (Figure 6.16), the horizontal configurations show an overall better performance in terms of MEG_{GPS}. These variations in MEG_{GPS} are associated with the antenna gain patterns. MEG_{GPS} incorporates overall changes in the antenna gain pattern for both polarisations and its response to the multipath environment in terms of AoA_{GPS} (that also includes ground reflections). Hence, it shows that the antenna gain and polarisation respond better to the nature of the incident plane waves when placed horizontally. The higher values of the antenna gain, especially in the upper

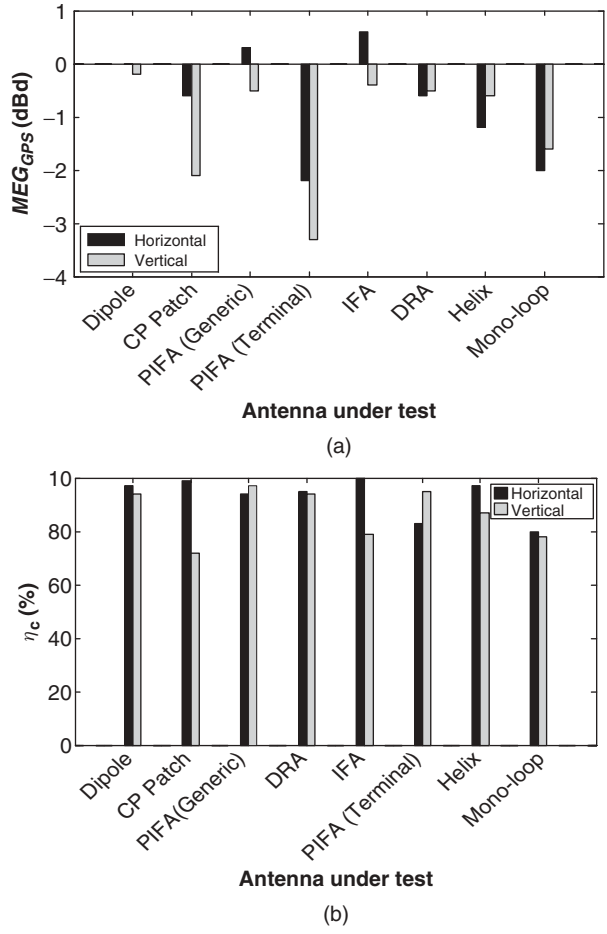

Figure 6.16 Performance comparison of GPS antennas with effects of change in orientation in terms of calculated MEG_{GPS} (taking horizontal dipole as reference) and η_c: (a) MEG_{GPS} taking horizontal dipole as a reference (0 dBd); (b) η_c.

hemispherical space, in both the perpendicular and parallel polarisations (as presented in the gain pattern figures), are a key contributor.

The majority of the tested antennas including the CP patch, IFA and helix also exhibit better η_c in the horizontal orientation as more open sky view is available. It increases the number of tracked satellites and hence the level of the received signal in the incident region ($0^\circ \leq \theta \leq 90^\circ$). As a result, the wasted signal is reduced, improving the overall η_c. The change in antenna η_c with changing orientation (with respect to the ground) is attributed to the sensitivity

of the antenna to receive the incoming GPS signal. Since the incoming GPS signal is RHCP, antenna RHCP gain patterns are evaluated in order to study the relation between η_c and RHCP gain with change in antenna orientation. The RHCP gain patterns of the tested antennas are measured using Satimo's Stargate 64 measurement system. Figures 6.17 and 6.18 present the comparison of measured RHCP gains in the incident region for the tested antennas in both the horizontal and vertical orientations. In these figures, the cross-hatched area indicates useful angles having a gain level above -13 dBi, contributing to η_c.

The comparison of the presented plots clearly indicates that η_c of the antenna depends upon the strength of the RHCP gain in the incident region. For example, in the case of the CP patch antenna, the vertical orientation exhibits much lower η_c of 72% compared with 99% for the horizontal orientation. It shows that the antenna has more clear sky view and a larger coverage area when placed horizontally. The RHCP gain patterns also support this theory. Figure 6.17b(i) shows that all of the incident region is above the required threshold level of -13 dBi when the antenna is working in the horizontal orientation. A decreased η_c for the vertically orientated antenna is caused by comparatively less area meeting this threshold. The presence of the RHCP gain levels lower than -13 dBi (non-hatched area) in Figure 6.17b(ii), particularly in the angles $30^\circ \leq \theta \leq 90^\circ$, $0^\circ \leq \phi \leq 60^\circ$ and $40^\circ \leq \theta \leq 90^\circ$, $330^\circ \leq \phi \leq 360^\circ$, gives rise to wasted signals resulting in a lower η_c. Similarly, η_c of the horizontal IFA is 100% but only 79% for the vertical IFA. The RHCP gain patterns in Figure 6.18a(ii) illustrate that the whole incident region fulfils the -13 dBi threshold for the horizontal orientation while a wide area in $30^\circ \leq \theta \leq 90^\circ$, $0^\circ \leq \phi \leq 140^\circ$ fails to meet this criterion for the vertical orientation. Similar behaviour could be observed for the helix antenna.

The tested antennas can be divided into three groups. The first group shows a tendency of improved MEG_{GPS} with enhanced η_c and vice versa on varying orientation. The dipole, CP patch and IFA come under this group. In the second group, if MEG_{GPS} increases, η_c decreases and vice versa. The generic PIFA, mobile terminal PIFA, helix and mono-loop antennas exhibit such behaviour. The third group consists of the antennas that have little impact of the changing orientation on their MEG_{GPS} and η_c. The DRA shows this stable performance.

It has been observed that the CP patch is more vulnerable to change in the orientation as MEG_{GPS} and η_c vary significantly. The vertical CP patch has lost 1.6 dB of its MEG_{GPS} and 27% of its coverage compared with the horizontal CP patch. This indicates that the multipath signal has little impact upon the CP patch antenna and it relies more on the direct signal lowering its capability to establish a quick satellite link in arbitrary orientations. The performance of

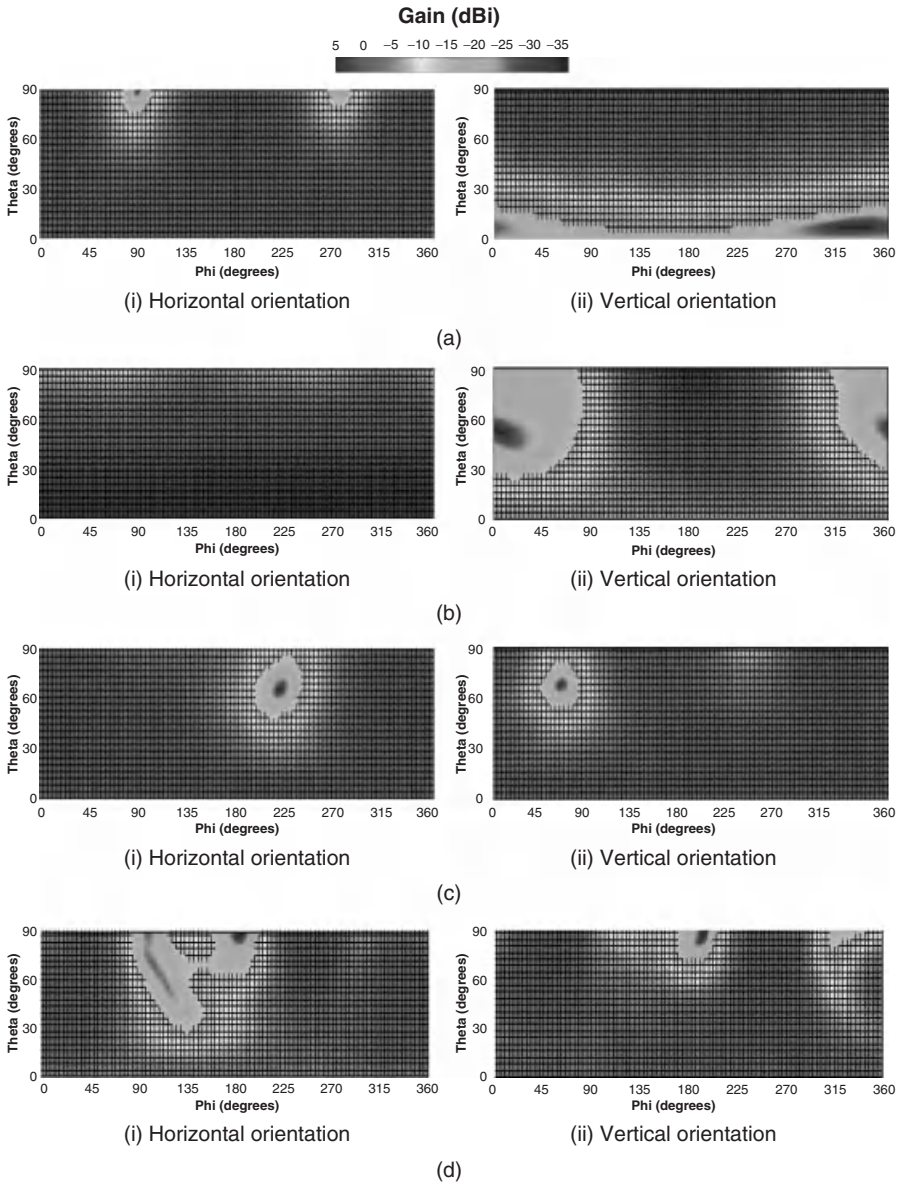

Figure 6.17 Measured RHCP gain patterns in the incident region for dipole, CP patch, PIFA (generic) and PIFA (terminal) GPS antennas in horizontal and vertical orientations (cross-hatched regions indicate where signal is above −13 dBi): (a) Dipole, (b) CP Patch, (c) PIFA (Generic) and (d) PIFA (Terminal) [25]. Reproduced by permission of © 2012 IEEE.

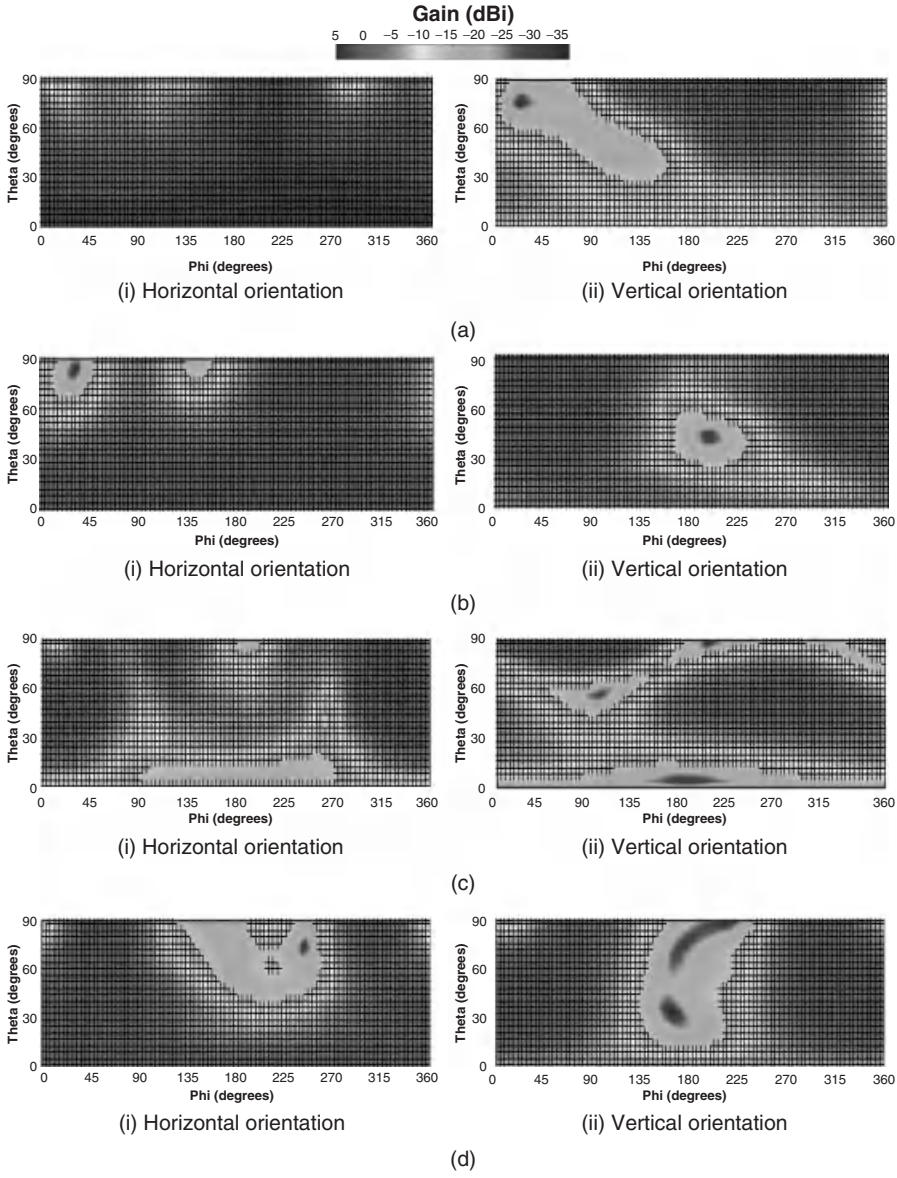

Figure 6.18 Measured RHCP gain patterns in the incident region for IFA, DRA, helix and mono-loop GPS antennas in horizontal and vertical orientations (cross-hatched regions indicate where signal is above −13 dBi): (a) IFA, (b) DRA, (c) Helix and (d) Mono-loop.

the IFA is also affected, but less significantly compared with the CP patch antenna, with a reduction of 1 dB in MEG_{GPS} and 21% in η_c. On the other hand, MEG_{GPS} of the vertical generic PIFA has reduced by 0.8 dB but its η_c has improved by 3%. A similar trend is observed for the mobile terminal PIFA. It depicts that the direct signal is playing a greater part in antenna performance. The ability of these antennas to make good use of the multipath signal in the horizontal orientation and the direct signal in the vertical orientation enables it to establish a faster GPS link regardless of the orientation (at the expense of comparatively higher multipath errors in the horizontal orientation). Hence, a combined consideration of antenna gain, polarisation, the radio environment (i.e. the AoA_{GPS} distributions) and the orientation in terms of MEG_{GPS} and η_c shows that the two PIFAs could deliver better performance in the multipath environment compared with the CP patch antenna.

The vertical helix and vertical mono-loop antennas have attained improved MEG_{GPS} at the expense of η_c compared with their horizontal counterparts. This also shows that these antennas can use the multipath signal constructively and are able to establish a quick GPS link. However, their performance is relatively poor compared with the generic PIFA. The DRA appears to be the most suitable antenna for mobile terminal GPS applications, showing a very stable performance. It has little impact of varying orientation as MEG_{GPS} and η_c change only by 0.1 dB and 1%, respectively.

The results show that MEG_{GPS} and η_c are an efficient measure to characterise antenna performance in the multipath environment. This simplifies the practical evaluation of antenna performance as it is based on the antenna gain pattern measurements in an anechoic chamber. It describes the antenna performance incorporating both the polarisation properties of the antenna under test and the directional properties of the radio environment. For example, from the perspective of antenna efficiency and maximum gain, the CP antennas (CP patch and helix) should out perform the tested linear antennas for GPS operation. However, MEG_{GPS} results show that these methods are not enough to depict the performance of the antennas in practical scenarios. A combined consideration of gain, polarisation and the radio environment (i.e. the AoA_{GPS} distributions) in terms of MEG_{GPS} makes the DRA and generic PIFA better performing antennas in the multipath.

6.6 Performance Enhancement of GNSS Mobile Terminal Antennas in Difficult Environments

It is apparent from the discussion in the previous section that the multipath environment degrades the performance of GPS mobile terminal antennas. The

time taken for the receiver to lock the GPS satellite (time to first fix (TTFF)) can reach up to 10 minutes, which is unacceptable for emergency calls. Provision of a reliable navigation service demands mitigation of these degrading effects. The performance of the terminal antennas in a cluttered environment can be enhanced by employing different techniques including assisted GPS, GPS signal reradiation, beamforming and diversity antennas.

6.6.1 Assisted GPS

Assisted GPS, also termed A-GPS, is a system where external sources including an assistance server with greater computing power and reference network provide the GNSS receiver with aiding information. Precise information of the GPS satellite orbit, clock data, initial position and time estimate is provided by the assistance server that gets help from the reference network [33]. The assistance server uses a wireless link to communicate with the GPS receiver. Provision of this data reduces the workload of the GPS receiver so it can operate more quickly and efficiently with assistance from the network. The TTFF can be decreased by a factor of 10, increasing the receiver's sensitivity [34]. This system is employed in mobile telecommunication networks. However, it requires network access which is not always available and can also compromise the user's privacy.

6.6.2 GPS Signal Reradiation

This approach is based on the use of GPS repeaters. It consists of an outdoor GPS receiver antenna and an indoor GPS amplifier. The receiving antenna is placed at a location where it has the best clear sky view, for example on the roof of a building or on a high pole. The GPS signal received outdoor by the receiver antenna is then amplified and reradiated inside the premises. The position solution is calculated by the receiver inside the building relating to the information obtained by the external antenna [35]. This method is a simple and cost-effective solution for large shadowed areas with no access to the GPS signal, including indoors and underground. However, the position of the indoor receiver could always be the same, representing the location of the outdoor antenna. Furthermore, the regulatory bodies have placed special regulations on the use of GPS repeaters to avoid signal jamming and interference with adjacent frequency bands. The European Telecommunications Standards Institute (ETSI) limits the overall gain of the repeater to a maximum of 45 dB while the National Telecommunications and Information Administration (NTIA) and Ofcom forbid the use of such devices (with the exception of specially permitted government

agencies) in the USA and UK [36, 37]. It undermines the deployment of this technology for commercial purposes.

6.6.3 Beamforming

Beamforming is another technique used to improve the performance of GNSS antennas. It is digitally implemented using signal processing methods. The direction of signal reception (i.e. antenna directivity) can be controlled by exploiting the elemental space and phase characteristics in an antenna array. The signals in some particular direction experience constructive interference while others undergo destructive interference. This directs the signal in a specific direction. Beamforming could use fixed weights and phases or adaptive criteria for combining the signal [38]. It is an option for the suppression of the multipath and jamming signals in GNSS applications. However, intensive computations and the cost of beamforming antennas have inhibited its use in commercial applications [39].

6.6.4 Diversity Antennas

A number of solutions are being proposed to improve GPS antenna performance including dielectric loading, high-value substrates, active circuits and diversity antennas. It has been reported that diversity antennas have the potential to enhance performance while maintaining a relatively low profile, small size and low cost [40, 41]. Since this technique is more relevant to the topic of this book, dual-element GNSS antenna designs are considered and performance in the multipath environment is analysed for the mobile terminal PIFA and mono-loop antenna. This will show the benefit of using diversity antennas in modern-day navigation devices to counter multipath degradations.

6.6.4.1 Tested Diversity Antennas

Dual-Element Mobile Terminal PIFA

A dual-element PIFA is designed based on the mobile terminal PIFA described in the previous section. The fabricated prototype of the two-element design is shown in Figure 6.19a. The elemental dimensions are the same as described in Figure 6.9a. The measured S_{11} and S_{21} curves are shown in Figures 6.19b and c, respectively. The antenna exhibits -10 dB impedance bandwidth of 55 MHz covering the frequency range from 1552 to 1607 MHz. The mutual coupling of the antenna is not very great as the S_{21} value at 1575.42 MHz appeared to be -11.4 dB. Figure 6.20 illustrates the measured 3D gain patterns for the perpendicular and parallel polarisations of the dual-element PIFA.

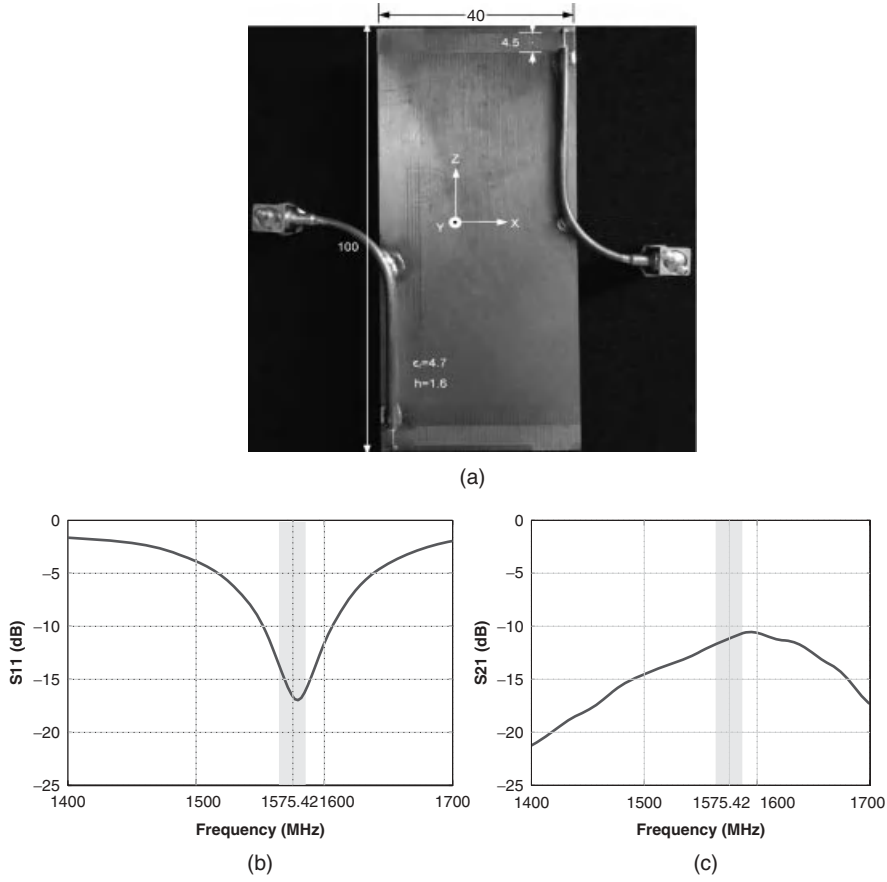

Figure 6.19 Geometrical structure of GPS mobile terminal dual-element PIFA diversity antenna with measured S_{11} and S_{21} curves: (a) Antenna geometry (lengths are in mm), (b) Measured S_{11} curve and (c) Measured S_{21} curve.

Dual-Element Mono-loop Antenna

The dual-element mono-loop antenna is also designed to study the enhancement of GPS antenna performance in the multipath environment using diversity [42]. The elemental dimensions are similar, as illustrated in Figure 6.13a, with a distance of 41.8 mm between the two elements. Figure 6.21a shows the fabricated prototype of the designed antenna while Figures 6.21b and c describe the measured S_{11} and S_{21} curves respectively for the antenna. The antenna has a -10 dB impedance bandwidth of 250 MHz covering all the frequencies ranging from 1385 to 1635 MHz. An acceptable level of coupling between the two elements is observed with the measured S_{21} of -14.1 dB at 1575.42 MHz. The measured

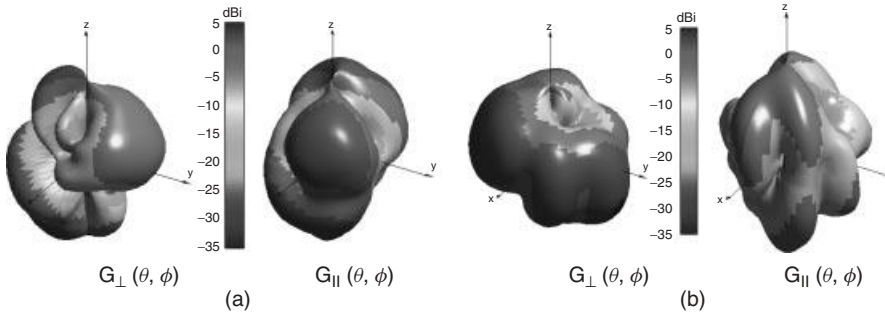

Figure 6.20 Measured 3D gain patterns for perpendicular and parallel polarisations of GPS mobile terminal dual-element PIFA diversity antenna in horizontal and vertical orientations: (a) Gain patterns for horizontal orientation; (b) Gain patterns for vertical orientation.

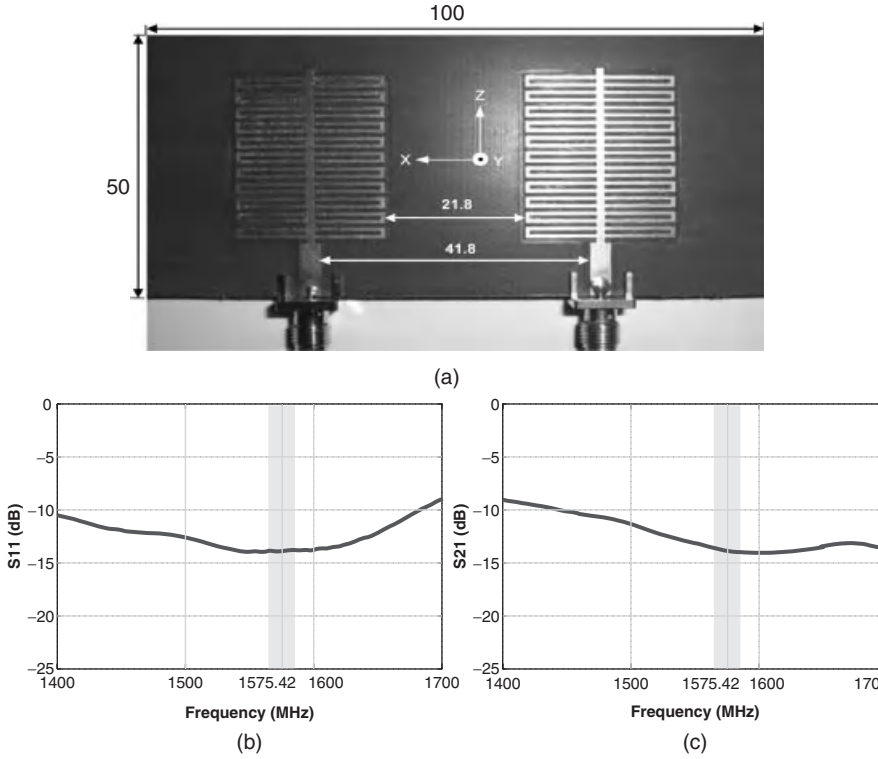

Figure 6.21 Geometrical structure of GPS mobile terminal dual-element mono-loop diversity antenna with measured S_{11} and S_{21} curves: (a) Antenna geometry (lengths are in mm), (b) Measured S_{11} curve and (c) Measured S_{21} curve.

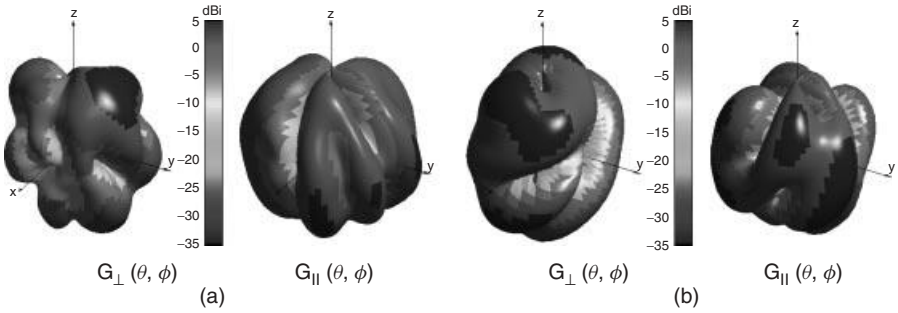

Figure 6.22 Measured 3D gain patterns for perpendicular and parallel polarisations of GPS mobile terminal dual-element mono-loop diversity antenna in vertical and horizontal orientations: (a) Gain patterns for horizontal orientation; (b) Gain patterns for vertical orientation.

3D gain patterns for the perpendicular and parallel polarisations of the dual-element mono-loop antenna are illustrated in Figure 6.22.

6.6.4.2 Performance of GPS Diversity Antennas in Multipath Environment

The performance of the two diversity antennas in the multipath GPS environment is evaluated using the proposed statistical model and verified through open field test measurements. A power combiner is used to combine the signal from the two elements with an insertion loss of 0.5 dB. The vertical orientation of the two antennas is taken into account. The 3D gain patterns of the antenna configurations are input to the model. The effectiveness of the diversity is analysed in terms of η_c and MEG_{GPS} with the horizontal dipole antenna taken as the reference.

Table 6.3 summarises the MEG_{GPS} and η_c results for the two antennas while a comparison with the performance of respective single-element (non-diversity) antennas is presented in Figure 6.23.

Figure 6.23 shows that the use of the diversity antennas increases MEG_{GPS} for the GPS multipath operation significantly. The extent of this enhancement is different for the two antennas with a 0.6 dB increase achieved by the dual-element PIFA while a 1.4 dB increase is offered by the dual-element mono-loop.

Similarly, a significant improvement in the coverage of the incoming GPS signal has been exhibited by the dual-element mono-loop with an η_c increment of 17%. The η_c of the dual-element PIFA has also increased by 2% which is not very significant but shows a tendency of improvement.

Table 6.3 Performance evaluation of mobile terminal GPS diversity antennas in horizontal and vertical orientations using the multipath environment model in comparison with the measured results

Antenna	Model calculations using measured 3D patterns		Open field test measurements	
	η_c (%)	MEG_{GPS} (dBd)	η_c (%)	MEG_{GPS} (dBd)
Horizontal dipole (reference)	97	0 (corresponding to calculated value of −5.4 dB in ARE)	96	0 (corresponding to measured average SNR of 40.2 dB)
Vertical terminal PIFA	95	−3.3	92	−3.1
Vertical dual-terminal PIFA	97	−2.7	97	−2.6
Vertical mono-loop	78	−1.6	80	−1.8
Vertical dual mono-loop	95	−0.2	96	−0.3

The higher values of MEG_{GPS} and η_c achieved for the two diversity antennas are a result of enhanced gain patterns. The use of spatial diversity has broadened the antenna's clear sky view, modified the gain patterns and increased the gain levels as illustrated in Figures 6.20 and 6.22. The modified gain patterns have enabled the antennas to cover a wider range of AoA_{GPS}. This, combined with an overall increased gain level, has resulted in comparatively larger values of MEG_{GPS} for the diversity antennas. The enhanced gain values have also increased the coverage of the antennas and hence their η_c as this depends on the solid angle subtended by the area where gain levels are higher than −13 dBi in the upper hemisphere. The results show that the diversity is good for the mono-loop antenna but its benefit is marginal for the PIFA. The less resounding performance of the dual-element PIFA is related to fabrication errors that lead to higher mutual coupling between the two elements. The S_{21} measurements, presented in Figures 6.19c and 6.21c, show that the dual-element PIFA has a mutual coupling of −11.4 dB as compared with −14.1 dB for the dual-element mono-loop at 1575.42 MHz. It reduces the performance of the dual-element PIFA to a greater extent resulting in less significant improvement in MEG_{GPS} and η_c values compared with the dual-element mono-loop antenna.

Overall, the dual-element diversity antennas have shown better performance in the multipath environment compared with their single-element counterparts. It is therefore deduced that diversity is a viable solution in terms of effective GPS reception. Further optimisation of the antenna designs and minimisation

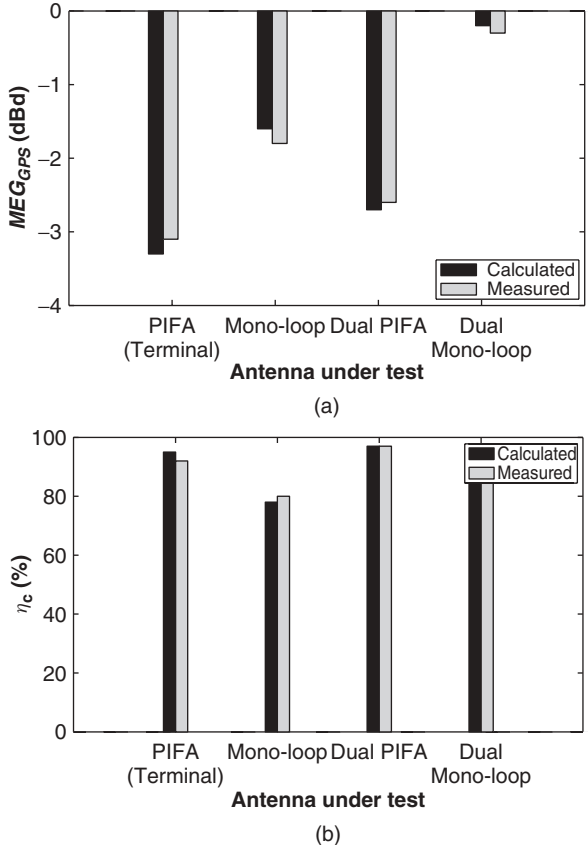

Figure 6.23 Performance enhancement of GPS diversity antennas in multipath environment in comparison of single-element designs in terms of calculated MEG_{GPS} (taking the horizontal dipole as reference) and η_c: (a) MEG_{GPS} taking horizontal dipole as a reference (0 dBd); (b) η_c.

of the fabrication errors would result in more enhanced GPS operation of the mobile terminal.

Besides its precise predictive capabilities, the proposed statistical model is only suitable for open field (suburban) GPS environments due to the assumption of uniform AoA_{GPS} in the azimuth and elevation planes. For urban area operation with a greater number of reflecting objects, more practical AoA_{GPS} representing a greater probability of arrival of the GPS signal near the zenith compared with the horizon angles, for example Gaussian and elliptical distributions, should be considered.

References

1. Taga, T. "Analysis for mean effective gain of mobile antennas in land mobile radio environments", *IEEE Transactions on Vehicular Technology*, **39**, 117–131, 1990.
2. Kalliola, K. Sulonen, K. Laitinen, H. *et al*. "Angular power distribution and mean effective gain of mobile antenna in different propagation environments", *IEEE Transactions on Vehicular Technology*, **51**, 823–838, 2002.
3. Carro, P. and de Mingo, J. "Mean effective gain of compact WLAN genetic printed dipole antennas in indoor-outdoor scenarios", International Conference on Personal Wireless Communications (PWC), pp. 275–283, September 2006.
4. Ando, A. Taga, T. Kondo, A. Kagoshima, K. and Kubota, S. "Mean effective gain of mobile antennas in line-of-sight street microcells with low base station antennas", *IEEE Transactions on Antennas and Propagation*, **56**, 3552–3565, 2008.
5. Nielsen, J. and Pedersen, G. "Mobile handset performance evaluation using radiation pattern measurements", *IEEE Transactions on Antennas and Propagation*, **54**, 2154–2165, 2006.
6. Krogerus, J. Ichelun, C. and Vainikainen, P. "Dependence of mean effective gain of mobile terminal antennas on side of head", European Conference on Wireless Technology (ECWT), pp. 467–470, October 2005.
7. Axelrad, P. Comp, J. and MacDoran, P. "SNR-based multipath error correction for GPS differential phase", *IEEE Transactions on Aerospace and Electronic Systems*, **32**, 650–660, 1996.
8. Wu, J. and Hsieh, C. "Statistical modeling for the mitigation of GPS multipath delays from day-to-day range measurements", *Journal of Geodesy*, **84**, 223–232, 2006.
9. Spangenberg, M. Tourneret, J. Calmettes, V. and Duchteau, G. "Detection of variance changes and mean value jumps in measurement noise for multipath mitigation in urban navigation", A silomar Conference on Signals, Systems and Computers P, October 2008.
10. Hannah, B. "Modelling and simulation of GPS multipath propagation", PhD thesis, Queensland University of Technology, March 2001.
11. Bancroft, R. *Microstrip and printed antenna design*, 2nd edn, SciTech Publishing, Raleigh, NC, 2009.
12. Moernaut, G. and Orban, D. "GNSS antennas: an introduction to bandwidth gain pattern, polarization and all that" *GPS World*, **20**(2), 42–48, February 2009.
13. Boccia, L. Amendola, G. and Di Massa, G. "A shorted elliptical patch antenna for GPS applications", *IEEE Antennas and Wireless Propagation Letters*, **2**, 6–8, 2003.
14. Miller, G. "Adding GPS applications to an existing design", *RF Design*, pp. 50–57, March 1998.
15. Langley, R. "A primer on GPS antennas", *GPS World*, pp. 50–55, July 1998.
16. Pathak, V. Thornwall, S. Krier, M. *et al*., "Mobile handset system performance comparison of a linearly polarized GPS internal antenna with a circularly polarized antenna", Antennas and Propagation Society International Symposium (AP-S), Vol. 3, June 2003.
17. Kingsley, S. "GPS antenna design for mobile phones", *Electronics Weekly*, 11 April 2007.
18. Haddrell, T. Ricquier, N. and Phocas, M. "Mobile-phone GPS antennas: can they be better?", *GPS World*, **21**(2), 29–35, February 2010.
19. Fujimoto, K. and James, J. R. *Mobile antenna systems handbook*, 2nd edn, Artech House, Boston, MA, 2001.
20. Chen, Z. N. *Antennas for portable devices*, John Wiley & Sons, Ltd, Chichester, 2007.
21. Ur Rehman, M. Gao, Y. Chen, X. Parini, C. and Ying, Z. "Analysis of GPS antenna performance in amultipath environment", Antennas and Propagation Society International Symposium (AP-S), July 2008.

22. Ur Rehman, M. Gao, Y. Chen, X. Parini, C. and Ying, Z. "Environment effects and system performance characterisation of GPS antennas for mobile terminals", *IET Electronics Letters*, **45**, 243–245, 2009.
23. Ur Rehman, M. Gao, Y. Chen, X. Parini, C. and Ying, Z. "Characterisation of system performance of GPS antennas in mobile terminals including environmental effects", European Conference on Antennas and Propagation (EuCap), March 2009.
24. Jakes, W. *Microwave mobile communications*, John Wiley & Sons, Inc., New York, 1974.
25. Ur Rehman, M. Chen, X. Parini, C. and Ying, Z. "Evaluation of statistical model for the characterization of multipath affecting mobile terminal GPS antennas in sub-urban areas", *IEEE Tran. Antenna and Prop.*, Vol. 60, No. 2, 2012.
26. Cheng, D. *Field and wave electromagnetics*, 2nd edn, Addison-Wesley, Reading, MA, 1989.
27. Jemai, J. Kurner, T. Varone, A. and Wagen, J. "Determination of the permittivity of building materials through WLAN measurements at 2.4GHz", IEEE International Symposium on Personal, Indoor and Mobile Radio Communications, September 2005.
28. Klysza, G. Balayssaca, J. and Ferriresb, X. "Evaluation of dielectric properties of concrete by a numerical FDTD model of a GPR coupled antennaparametric study", *NDT & E International*, **41**, 621–631, 2008.
29. J. Reed, *Software radio: A modern approach to radio enginenering*, Prentice-Hall, Englewood Cliffs, NJ, 2002.
30. Tsui, J. *Fundamentals of Global Positioning System Receivers: A software approach*, 2nd edn, John Wiley & Sons, Inc., New York, 2000.
31. "Ultra low power superior sensitivity GPS modules", URL http://www.starsnav.com/MTI-8T.htm (accessed 30 September 2011).
32. Pozar, D. *Microwave engineering*, 3rd edn, John Wiley & Sons, Inc., New York, 2005.
33. Hoffmmann-Wellenhof, B. Lichtenegger, H. and Wasle, E. *GNSS-Global navigation satellite systems*, Springer Vienna, 2008.
34. Van Diggelen, F. S. T. *A-GPS: Assisted GPS, GNSS, and SBAS*, Artech House, London, 2009.
35. Samama, N. *Global positioning: Technologies and performance*, John Wiley & Sons, Inc., Hoboken, NJ, 2008.
36. ETSI, "EN 302645 draft on standardization of GNSS repeater", http://www.etsi.org/deliver/etsi_en/302600_302699/302645/01.01.01_20/en_302645v010101c.pdf (accessed 2 November 2011).
37. NTIA, "Manual of regulations and procedures for federal radio frequency management", http://www.ntia.doc.gov/files/ntia/publications/manual_5_11.pdf (accessed 2 November 2011).
38. Kaplan, E. and Hegarty, C. *Understanding GPS: Principles and applications*, 2nd edn, *Artech House*, London, 2005.
39. Fu, Z. Hornbostel, A. Hammesfahr, J. and Konovaltsev, A. "Suppression of multipath signals by digital beamforming for GPS/Galileo applications", *GPS Solutions*, **6** 257, 2003.
40. Gao, Y. Chen, X. and Parini, C. G. "Study of diversity antennas for Galileo/GPS receivers", European Navigation Conference (ENC-GNSS), April 2008.
41. Douglas, M. Okoniewski, M. and Stuchly, M. "A planar diversity antenna for handheld PCS devices", *IEEE Transactions on Vehicular Technology*, **47** 747–754, 1998.
42. Ur Rehman, M. Gao, Y. Chen, X. and Parini, C. "Dual-element diversity antenna for Galileo/GPS receivers", 13th World Congress of International Association of Institutes of Navigation (IAIN), October 2009.

7

Human User Effects on GNSS Antennas

7.1 Interaction of Human Body and GNSS Antennas

The GNSS devices in wireless body area networks (WPANs) and wireless personal area networks (WBANs) typically operate either in on-body positions (held by the user) or in near-body positions (working in the proximity of the human body). In either case, the presence of the human body in the vicinity degrades the performance of the embedded GPS antennas of such devices.

It is now a well-established phenomenon that the human body is a very lossy medium that affects the performance of the antenna in three ways: reduction in efficiency due to electromagnetic absorption in the tissues; degradation of the radiation pattern; and variation in the feed point impedance [1–7]. Characterisation of these effects is a challenging but necessary task to provide guidelines for the design of an optimal performance antenna resilient to these degrading factors [8–11].

Following the land mobile antennas, the performance of GPS antennas also tends to deteriorate when placed near the human body [12]. It increases the magnitude of degradations in the mobile terminal GPS antennas operating in the multipath environment, that already have been suffering from reflections, diffraction and scattering of the incoming radio waves from surrounding objects [13, 14]. This results in attenuation, delay and distortion of the communication link. To guarantee a reliable navigation system that can also meet the Federal Communications Commission's (FCC's) mandate E911 of provision of precise location of the mobile user to ensure public safety [15] requires that the GPS

Antennas for Global Navigation Satellite Systems, First Edition.
Xiaodong Chen, Clive G. Parini, Brian Collins, Yuan Yao and Masood Ur Rehman.

mobile terminal antennas should cope with these deteriorations. Therefore, these antennas must be tested not only for the effects of the multipath environment, but also for the presence of the human body in this environment.

The effects of the human head presence in the multipath environment have been studied and reported in [16–18]. The mean effective gain (MEG) of the antenna is taken as a figure of merit for the antenna performance in these studies. Since the calculations of antenna MEG are based on the antenna power gain patterns, this simplifies antenna performance evaluation in practical scenarios including antenna on-body placements as follows [17,19–21]:

- The gain degradations due to radiation pattern deformations can be easily accommodated.
- The degradations of the antenna efficiency as a result of variations in the input impedance can also be accounted for, irrespective of whether it is caused by proximity of or absorptions by the human body.

The fast-growing demand for portable navigation devices necessitates the extension of this investigation to mobile terminal GPS antennas. The effects of the presence of the human body on the performance of GPS mobile terminal antennas is studied and characterised using the statistical model for the GPS multipath environment discussed in Chapter 6.

7.2 Effects of Human Body on GNSS Mobile Terminal Antennas in Difficult Environments

The investigation is carried out using realistic numerical models of the human head, hand and the whole body to study the behaviour of various mobile terminal GPS antennas. The study is conducted in two parts: firstly, investigating the effects of the presence of the human head and hand; secondly, investigating the effects of the presence of the whole body in the vicinity of the antennas. Different possible on-body scenarios are investigated including antenna held in user's hand, antenna placed beside user's head, antenna held in user's hand near to the head in talking position and antenna placed at user's pocket position. Effects of a multi-layered human head are also taken into account. The performance of GPS mobile terminal antennas is characterised in terms of $\mathrm{MEG}_{\mathrm{GPS}}$ and η_c. Since these parameters are calculated using simulated 3D power gain patterns that only consider the power absorptions in human body tissues [22], it is essential to include the mismatch losses caused by the antenna detuning in these on-body configurations. These losses are accumulated in $\mathrm{MEG}_{\mathrm{GPS}}$ and

η_c employing the concept of 'realised gain', calculated using the following equation [23]:

$$\text{Gain}_{\text{realised}} = \text{Gain} \times \eta_m \tag{7.1}$$

where Gain is the simulated gain that takes material losses into account. η_m represents the antenna mismatch efficiency that accounts for the antenna detuning losses and is calculated as follows:

$$\eta_m = 1 - |S_{11}|^2 \tag{7.2}$$

CST Microwave Studio® provides an embedded option for the realised gain mode [22].

7.2.1 Design of Tested GPS Antennas

Three types of GPS mobile terminal antennas are considered in this study to investigate the human body effects. The three antennas include the PIFA, DRA and helix antenna and are similar in design as described in Chapter 5. The antennas operate at the GPS frequency of 1575.42 MHz. The PIFA is designed using an FR4 substrate of 1.6 mm thickness. The PCB size is $100 \times 40\,\text{mm}^2$. The DRA is loaded with a dielectric of $\varepsilon_r = 21$. The ground plane is $100 \times 40\,\text{mm}^2$ of lossy copper type while the loaded dielectric is covered with lossy silver. The helix has no substrate and is mounted on the left side of the metallic ground plane of dimension $100 \times 40 \times 0.45\,\text{mm}^3$. The PIFA and DRA are fed using discrete ports with 50 Ω impedance to represent the commonly used 50 Ω coaxial port feed. Figures 7.1–7.3 show the schematic layout of the three antennas. The antenna prototypes were fabricated and tested in the Antenna Measurement Laboratory at Queen Mary University of London and results have been reported in Chapter 6. In the current study, however, only the simulation results are of interest.

7.2.2 Effects of Human Hand and Head Presence

In the first part of the study, only the effects of the presence of a realistic human head and hand model are investigated for the performance of GPS mobile terminal antennas in a multipath environment.

7.2.2.1 Test Set-up

A high-resolution realistic model of the human head and hand with dimensions for an average human is used as shown in Figure 7.4. The

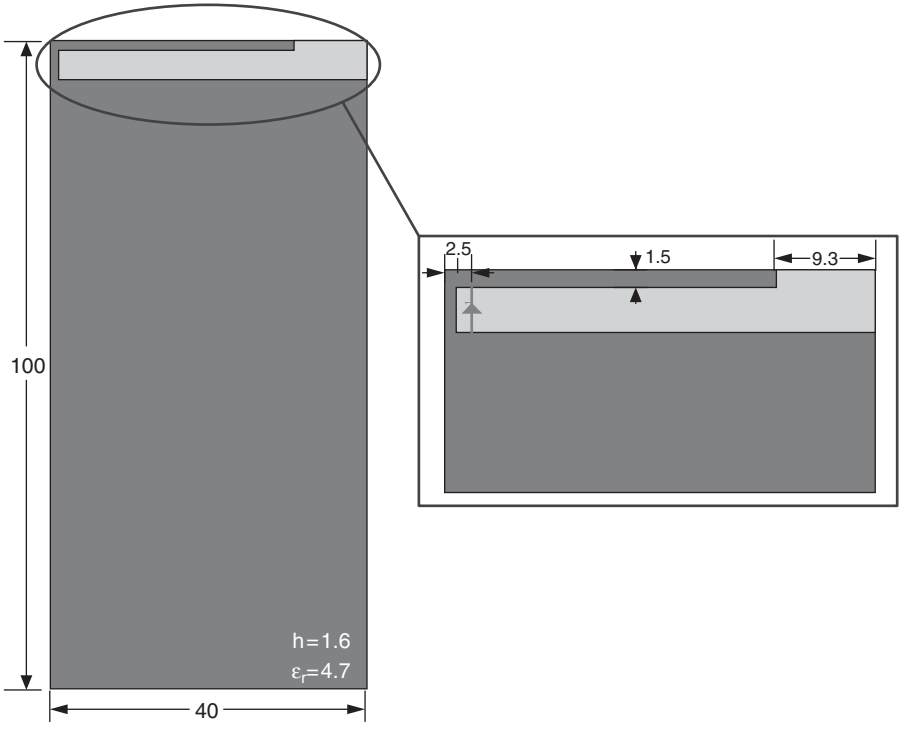

Figure 7.1 Geometric structure of GPS mobile terminal PIFA used to study the effects of human body presence on the antenna performance in a multipath environment (all lengths are in mm).

electrical properties of the muscle tissues are considered for the homogeneous head and hand models at 1575.42 MHz with a permittivity of 53.86 and conductivity of 1.22 S/m [24–26]. An inhomogeneous multi-layer head model is also employed to characterise the effects of different head tissues on the working of the antenna. Five head tissues including skin, muscle, skull, brain and spinal cord are incorporated in this inhomogeneous model. Table 7.1 summarises the electrical properties of these tissues at 1575.42 MHz and Figure 7.4e depicts a cross-sectional view of the multi-layer head model with anatomical details. An adaptive mesh is employed with different cell sizes that reduces the number of volume cells (voxels) in the computational domain significantly. The perfectly matched layer (PML) absorbing boundary conditions [22] are used with a maximum cell size of 10 mm near the

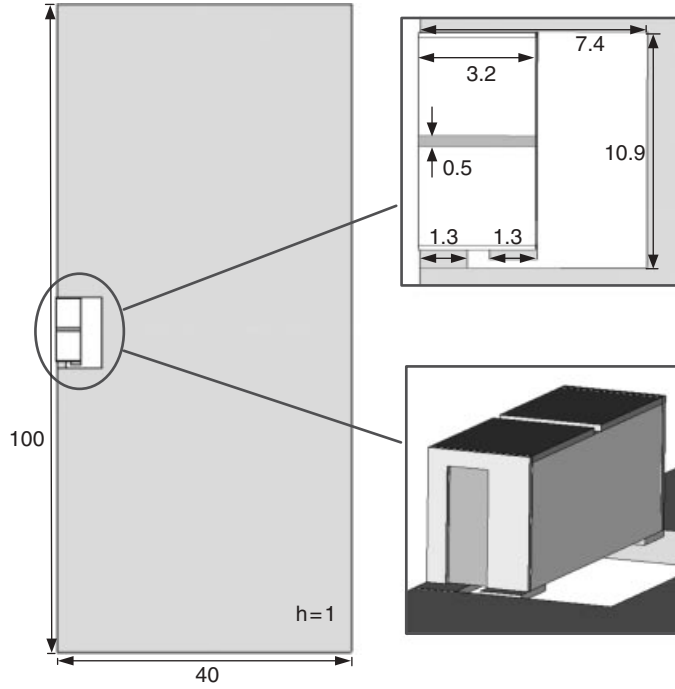

Figure 7.2 Schematic layout of GPS mobile terminal DRA to study the effects of human body presence on the antenna performance in a multipath environment (all lengths are in mm).

boundaries and a minimum size of 0.08 mm at the edges of the solids in the computational region.

Various on-body scenarios including the antennas placed beside the homogeneous head, held in hand and held in hand near to the head in talking position are taken into consideration to investigate the added effects of the human head and hand on antenna performance in the GPS multipath environment. The effects of the multi-layer head model in all the above configurations are then analysed. The antennas are placed beside the head inclined at 45° with respect to the z-axis for the talking positions. A separation of 10 mm between the antenna and the head is kept to allow clearance for the mobile casing. The statistical analysis of antenna performance in the multipath environment in these on-body configurations needs information of the 3D gain patterns in the perpendicular and parallel polarisations. Therefore, the simulated 3D gain patterns for all the test set-ups are recorded.

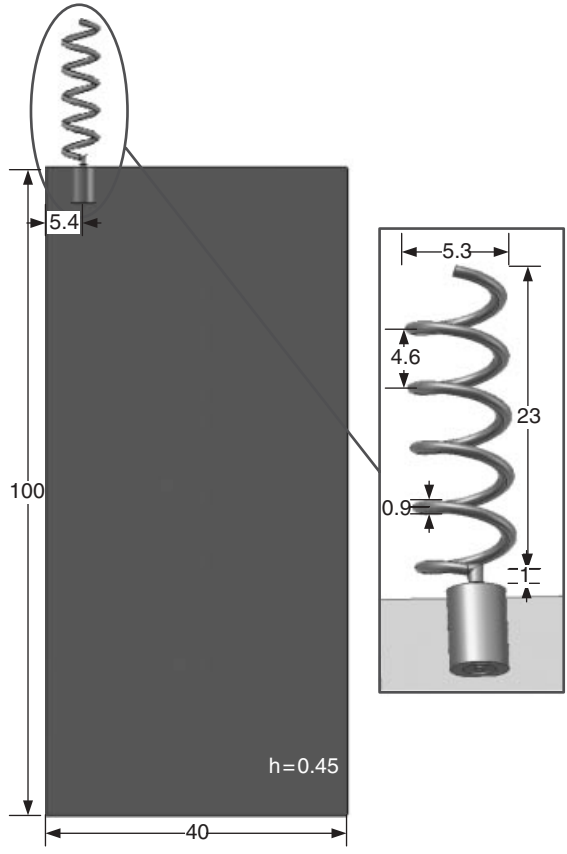

Figure 7.3 Geometry and dimensions of GPS mobile terminal helix antenna for the study of the presence of human body effects on the antenna performance in a multipath environment (all lengths are in mm).

7.2.2.2 Evaluation of GPS Antenna Performance

The S_{11} response of the three antennas is shown in Figures 7.5–7.7. These figures confirm the well-known phenomenon of antenna detuning caused by the presence of the human body. The amount of this detuning varies from antenna to antenna. The most resilient antenna to this detuning effect has proved to be the helix, which offered the required -10 dB bandwidth of ± 5 MHz (desired for efficient GPS operation) in all the cases due to its wide bandwidth. The S_{11} responses for the DRA (Figure 7.6) makes it the most sensitive of the three tested antenna types to the human body effects. It has shown greater detuning than the PIFA and helix antenna, though losing -10 dB impedance

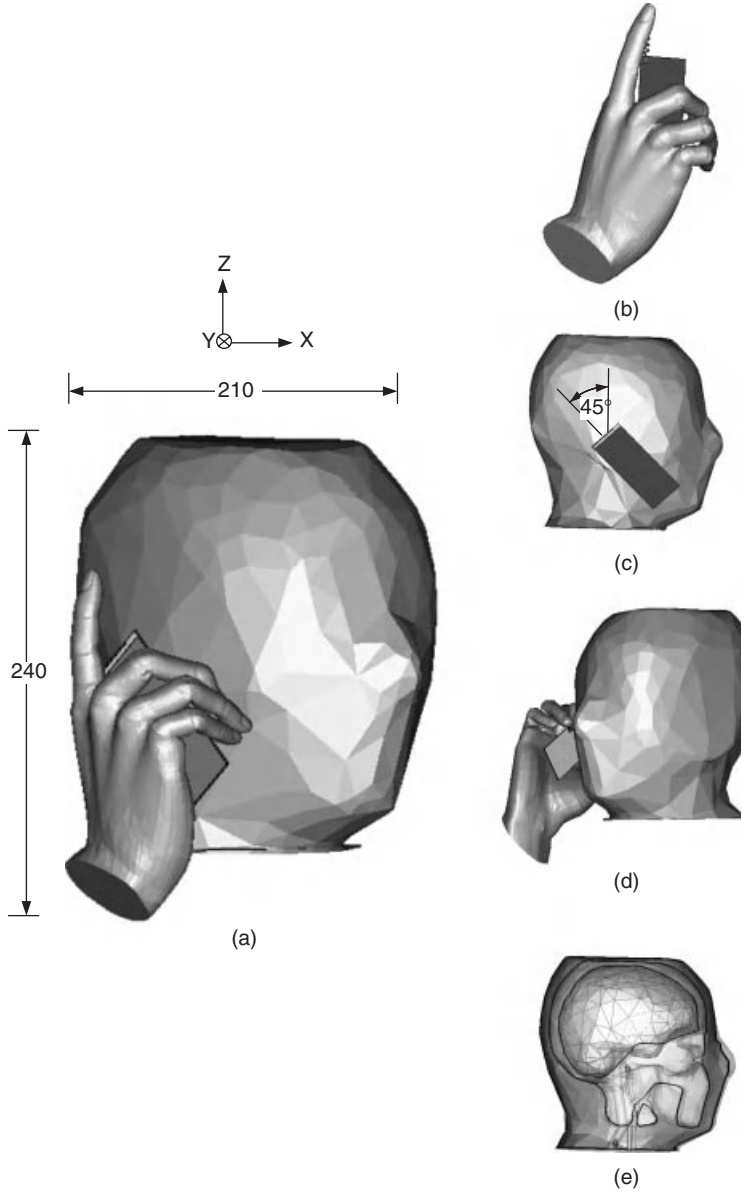

Figure 7.4 High-resolution model for human head and hand with different test configurations for three GPS antennas under test (all lengths are in mm): (a) Realistic head and hand model configuration, (b) Antenna held in hand, (c) Antenna placed beside realistic head model, (d) Antenna held in hand beside realistic head model in talking-on-phone position and (e) X-section view of multi-layer head model.

Table 7.1 Electrical properties of specific human tissues at 1575.42 MHz used within the constructed inhomogeneous multi-layer head model

Tissue	Electric properties	
	Dielectric constant (ε_r)	Tissue conductivity (σ)(S/m)
Skin (dry)	39.28	1.10
Muscle	53.86	1.22
Skull (average bone)	12.33	0.27
Brain (average grey and white)	43.96	1.04
Spinal cord	31.17	0.77

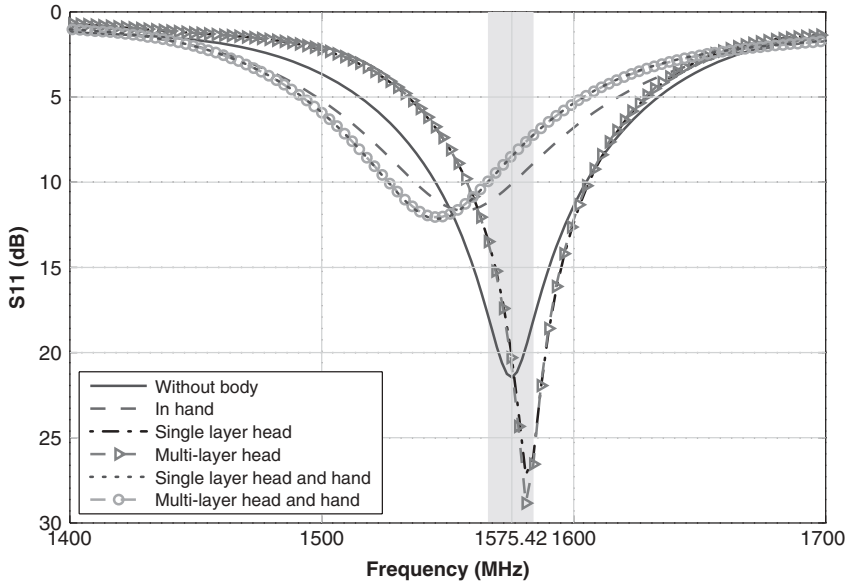

Figure 7.5 S_{11} curves for PIFA with effects of different placements near human hand and head.

bandwidth in the desired ±5 MHz L1 band for held-in-hand and the talking positions (antenna held-in-hand placed beside head). The performance of the PIFA is also degraded greatly, while the antenna held in the talking position has suffered worse. These results also show that the S_{11} response is similar

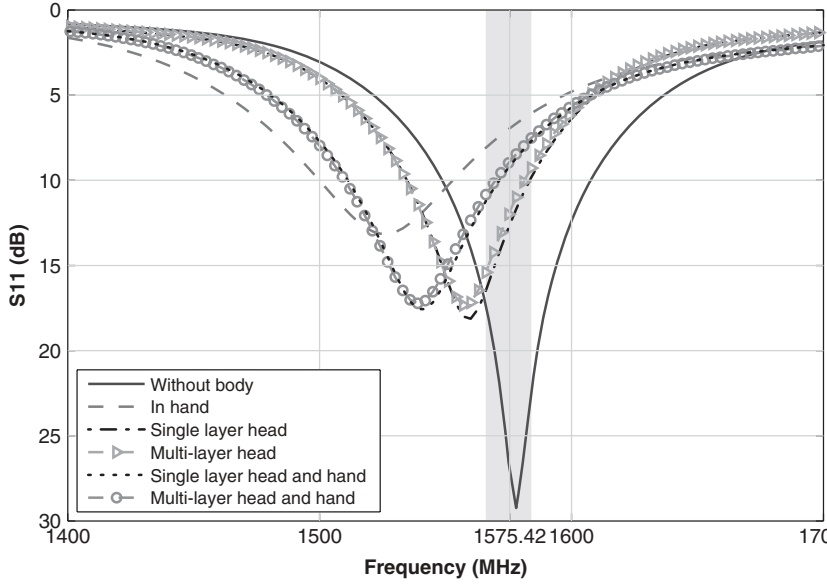

Figure 7.6 S_{11} curves for DRA with effects of different placements near human hand and head.

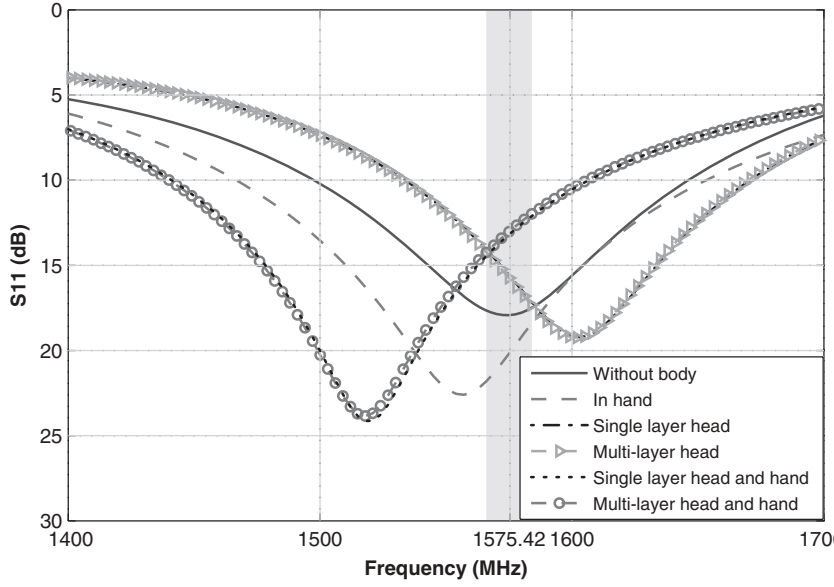

Figure 7.7 S_{11} curves for helix with effects of different placements near human hand and head.

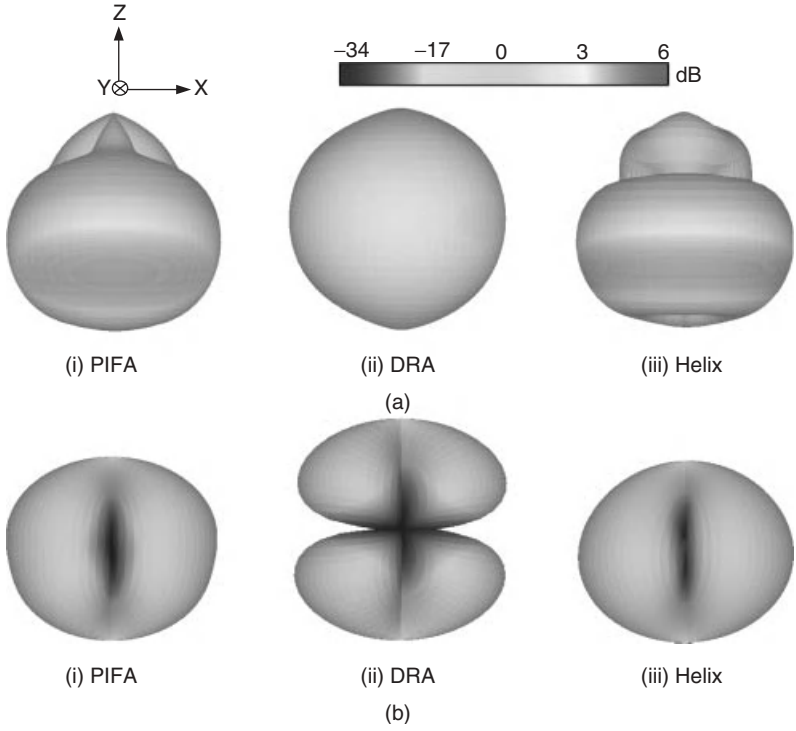

Figure 7.8 Simulated 3D gain patterns for perpendicular and parallel polarisations of PIFA, DRA and helix GPS mobile terminal antennas in free space: (a) $G_{\perp}$; (b) $G_{\parallel}$.

for the single-layer and multi-layer head models and that the inner organs incorporated in the inhomogeneous multi-layer model have little impact. This is due to the fact that input impedance is a relatively local phenomenon. It is influenced more significantly by the objects located close to the antenna feed point while the inner organs of the multi-layer head are comparatively more displaced [1].

Figures 7.8–7.13 illustrate the simulated 3D gain patterns for the perpendicular and parallel polarisations of the PIFA, DRA and helix antenna, operating in different scenarios near the human hand and head. It is evident from these results that the antenna detuning effect is also replicated in the radiation pattern deformations depending on the posture of the human hand and head.

In the held-in-hand position (Figure 7.9), the radiating element of the PIFA is in the negative x-direction while the DRA is in the positive x-direction. Hence, the PIFA is affected more by the gripping fingers especially the index finger and the DRA suffers more from the absorptions in the palm. For the

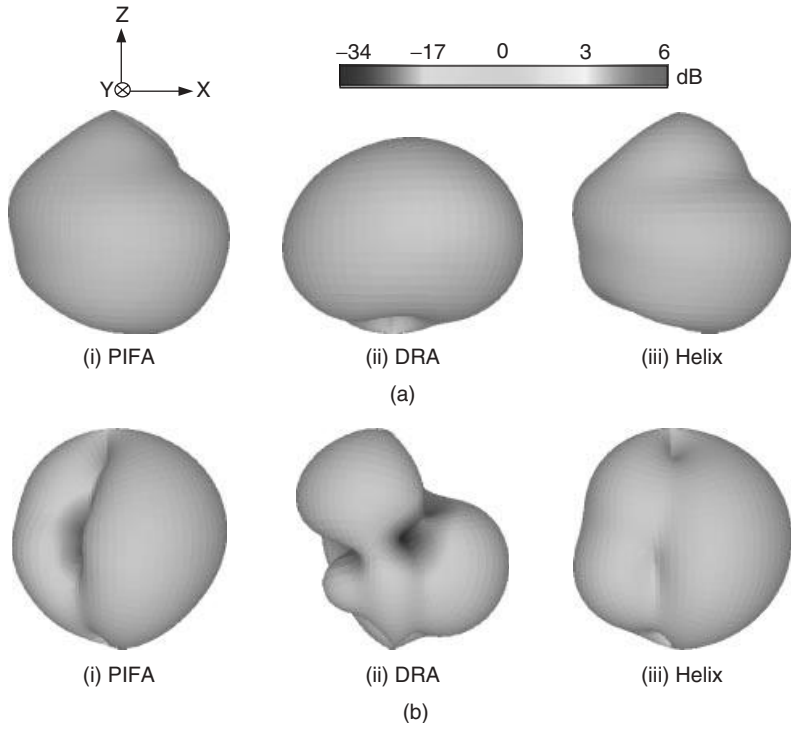

Figure 7.9 Simulated 3D gain patterns for perpendicular and parallel polarisations of PIFA, DRA and helix GPS mobile terminal antennas held in user's hand: (a) $G_{\perp}$; (b) $G_{\parallel}$.

helix in free space, the ground plane is a major contributor to the radiation. Therefore, it is also affected by the gripping fingers. When the antenna is placed near the head, a greater body mass reduces the radiation of the three antennas in the positive x-direction making the gain patterns directive in the negative x-direction as shown in Figures 7.10 and 7.11. It can also be observed from these results that gain levels are less in the upper hemisphere compared with the lower hemisphere. When the antenna is held in the user's hand in the talking position, the presence of both the hand and head on the two sides of the antenna give rise to electromagnetic absorptions and the reflected fields are minimum. This defragments the antenna radiation greatly and causes poor gain levels in all directions, depicted in Figures 7.12–7.13.

The performance of the PIFA, DRA and helix GPS mobile terminal antennas in the multipath environment is evaluated using the discussed statistical model in terms of MEG_{GPS} and η_c. The simulated 3D gain patterns of the designed

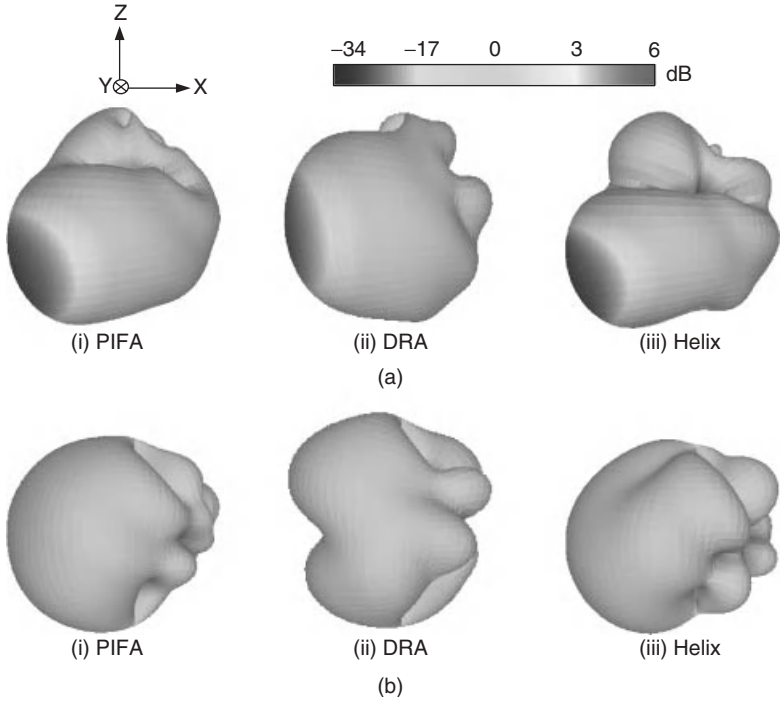

Figure 7.10 Simulated 3D gain patterns for perpendicular and parallel polarisations of PIFA, DRA and helix GPS mobile terminal antennas placed beside user's homogeneous single-layer head: (a) $G_{\perp}$; (b) $G_{\parallel}$.

antennas in different configurations, shown in Figures 7.8–7.12, are input to the model. The ground plane (earth) is considered as made of dry concrete with a relative permittivity of 4.5 [27, 28] to include the ground reflections.

Table 7.2 summarises the calculated values of η_c and MEG_{GPS} for the three tested antennas in different near-body configurations. Note that the presence of the lossy human body tissues causes significant degradation of the antenna performance due to electromagnetic absorptions in the tissues and field reflections from the surface of the human body. This results in gain pattern deformations compared with that without the presence of the human body, illustrated in Figures 7.9–7.13. This deterioration of the gain patterns reduces the coverage and MEG_{GPS} of the GPS antennas and their ability to pick up the GPS satellite signal suffers drastically.

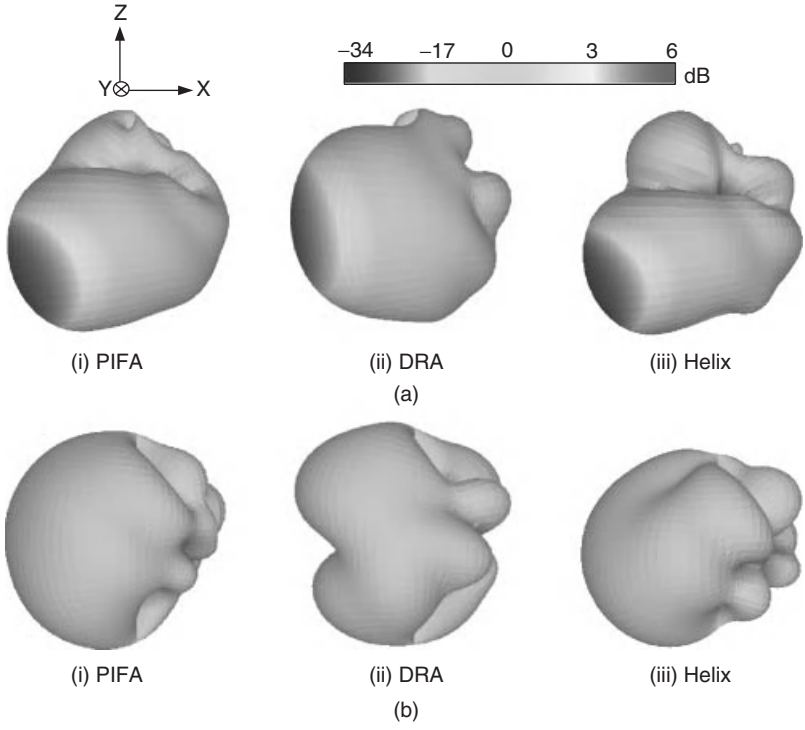

Figure 7.11 Simulated 3D gain patterns for perpendicular and parallel polarisations of PIFA, DRA and helix GPS mobile terminal antennas positioned beside user's inhomogeneous multi-layer head: (a) $G_{\perp}$; (b) $G_{\parallel}$.

Note also that the reduction in η_c depends mainly on the extent of available clear sky view to the radiating element. The more the antenna radiating element is covered by the user, the lesser is its η_c. The amount of body mass present in the vicinity of the GPS antenna also plays a key role.

Figure 7.14a compares the coverage of the three antennas in the above described test configurations. In the case of the PIFA, the radiating element is in the negative x-direction. For the held-in-hand position, the radiating element (top edge of the PCB) is not covered by the palm or the gripping fingers. Only a small disturbance comes from the index finger resulting in η_c of 89%, that is 3% lower than the free space value. When the antenna is placed beside the head, greater body volume produces larger detuning due to the surface

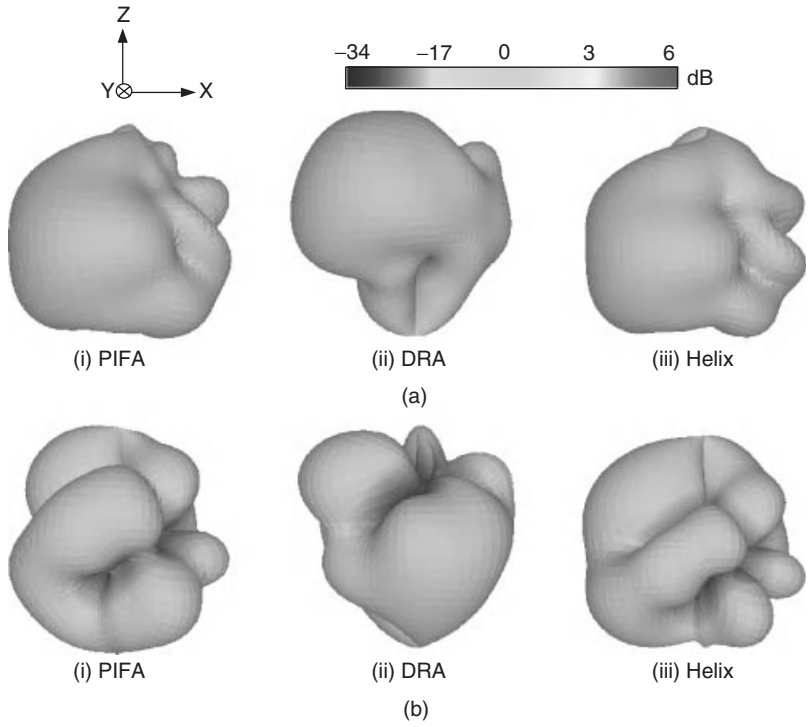

Figure 7.12 Simulated 3D gain patterns for perpendicular and parallel polarisations of PIFA, DRA and helix GPS mobile terminal antennas held in user's hand and placed beside the user's homogeneous single-layer head: (a) $G_{\perp}$; (b) $G_{\parallel}$.

reflections and energy absorptions and, hence, η_c decreases to 75%. Placing the antenna in the talking position shields its clear sky view on both sides by the user's holding hand and head reducing the antenna's coverage to 42%.

On the contrary, the radiating DRA is in the positive x-direction, located in the middle of the PCB and, hence, affected more by the palm. The gripping fingers also cover most of the radiating element, resulting in a reduced η_c value of 58% compared with the free space value of 95%. Placing the antenna beside the head blocks its view only on one side, resulting in an η_c of 76%, but the presence of both the hand and head shields most of the useful angles and, hence, η_c becomes 36%.

For the helix, the radiating element is mounted on the top left of the ground plane, having the feed in the negative x-direction. The index finger restricts the view of the radiating element on one side when held in the hand. The palm

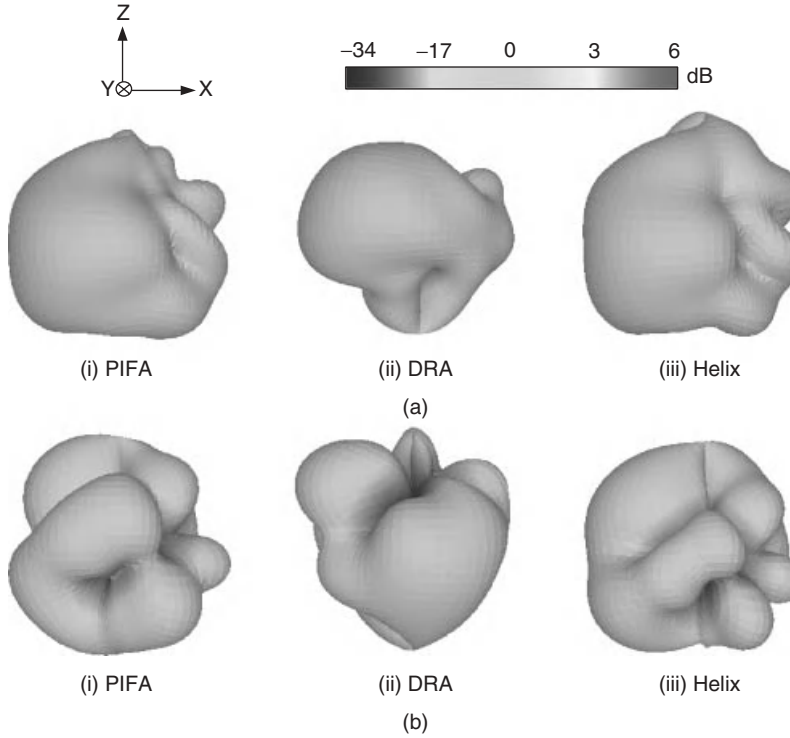

Figure 7.13 Simulated 3D gain patterns for perpendicular and parallel polarisations of PIFA, DRA and helix GPS mobile terminal antennas held in user's hand and placed beside the user's inhomogeneous multi-layer head: (a) $G_{\perp}$; (b) $G_{\parallel}$.

of the holding hand and gripping fingers also disturb the major radiation area as is evident by comparing Figure 7.8a(iii) and Figure 7.9a(iii). It causes η_c to drop from 88% for free space to 78%. The placement of the antenna beside the head is affected by the surface reflections. The antenna experiences clear sky view on one side but the other half is completely blocked causing η_c to drop to 66%. The talking position of held in hand and placed near head restricts the clear sky view of the antenna on both sides in a similar fashion, as noted for the PIFA and DRA, resulting in a poor η_c of 58%.

The loss due to the presence of the human body is also replicated in MEG_{GPS} values, shown in Figure 7.14b. Since MEG_{GPS} is the average performance of the antenna in the multipath environment, it depends on the overall gain pattern, taking into account both the power absorptions in the human body tissues and the antenna detuning, rather than the extent of the radiating element's clear

Table 7.2 Calculated GPS coverage efficiency and GPS MEG of three mobile terminal GPS antennas operating at 1575.42 MHz in multipath environment in proximity of human body with effects of human hand and head

Test set-up in presence of human hand and head	Model calculations using simulated 3D patterns in actual reflection multipath environment					
	PIFA		DRA		Helix	
	η_c (%)	MEG_{GPS} (dB)	η_c (%)	MEG_{GPS} (dB)	η_c (%)	MEG_{GPS} (dB)
Antenna without human body presence	92	−8.2	95	−5.7	88	−5.8
Antenna held in user's hand	89	−11.2	58	−10.6	78	−7.8
Antenna placed beside user's single-layer head	75	−10.0	76	−8.2	66	−7.4
Antenna placed beside user's multi-layer head	74	−10.1	73	−8.4	65	−7.5
Antenna held in talking position beside user's single-layer head	42	−15.9	36	−14.9	58	−11.0
Antenna held in talking position beside user's multi-layer head	41	−16.0	34	−15.2	57	−11.1

sky view. Therefore, the three GPS antennas have been affected by the human head and hand in a similar fashion. The performance degradation is less in the held-in-hand position and worst in the held-in-hand beside the head position compared with the MEG_{GPS} value for an antenna operating in a multipath environment without human body presence. From Figure 7.8, it is clear that the three antennas have stronger radiation in the azimuth plane with the main lobes in the negative y-direction. Therefore, when these antennas are held in the user's hand restricting most of the azimuth angles, gain values decrease sharply with almost equivalent levels in both the azimuth and elevation planes (Figure 7.9) resulting in decreased MEG_{GPS} values.

When the antennas are placed beside the user's head, the lossy human tissues are present on one side of the antennas. This produces reflected electromagnetic fields resulting in highly directive gain patterns as illustrated in Figure 7.10.

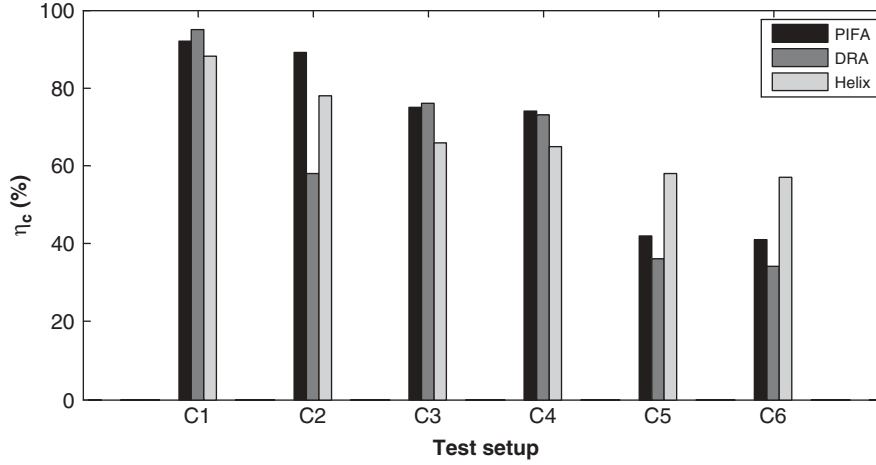

C1: Antenna without human body presence
C2: Antenna held in hand
C3: Antenna placed beside signal layer head
C4: Antenna placed beside multi-layer head
C5: Antenna in talking position with single layer head
C6: Antenna in talking position with multi-layer head

(a)

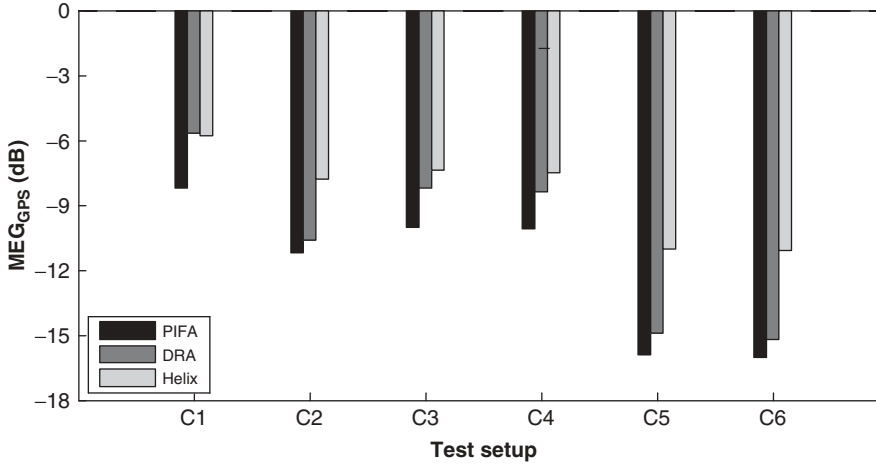

C1: Antenna without human body presence
C2: Antenna held in hand
C3: Antenna placed beside signal layer head
C4: Antenna placed beside multi-layer head
C5: Antenna in talking position with single layer head
C6: Antenna in talking position with multi-layer head

(b)

Figure 7.14 Multipath environment performance of three GPS mobile terminal antennas in free space and in different on-body positions with effects of human head and hand: (a) Coverage efficiency of GPS antennas; (b) MEG of GPS antennas.

This increase in directivity at certain azimuth angles fails to make a greater impact because of a reduction in the gain levels in other directions, especially in the upper hemisphere. It lowers the overall performance of the antenna resulting in decreased MEG_{GPS}.

Finally, when the GPS antennas are placed in the talking position, they are covered by the user's hand on one side and by the head on the other. The electromagnetic absorptions in the lossy tissues and reflections from the head and hand surfaces lead to greater degradation in the gain values causing MEG_{GPS} to reach its lowest value (of the observed cases).

A reduction of 1.8–7.7 dB (in comparison with the MEG_{GPS} for no human body present) is observed in the case of the PIFA while this reduction is between 2.5 and 9.2 dB and 1.6–5.2 dB for the DRA and helix antenna, respectively.

The effects of the presence of a multi-layer head near the three GPS mobile terminal antennas when placed beside the head with and without a holding hand are also studied. The comparison of η_c and MEG_{GPS} obtained for these scenarios with that of the single-layer head model, presented in Figure 7.14, clearly indicates that the internal organs have no significant effect on antenna performance. The reduction in the values of η_c and MEG_{GPS} is between 1–3% and 0.1–0.3 dB respectively with varying permittivity and conductivity values of the internal head organs increasing the losses. However, the penetration depth is only slightly changed from 30.2 mm for the single-layer head model to 33.5 mm (average) for the multi-layer case at 1575.42 MHz. It minimises the increase in the power absorption having little impact on MEG_{GPS} and η_c. It is therefore concluded that study of the antenna performance in the multipath environment with single-layer human body models containing the electrical properties of the muscle tissues provides reasonably accurate results and computational time could be saved by not employing multi-layer models.

Overall, the DRA offers better performance in the multipath environment with no human body presence, in comparison with the PIFA and helix antenna, with wider coverage and good MEG_{GPS}. However, the performance of the helix antenna is good and more consistent in the presence of the human head and hand.

7.2.3 Effects of Complete Human Body Presence

The previous section has given an overview of the effects of the user's hand and head on the performance of GPS mobile terminal antennas. However, in actual working scenarios, these antennas have to operate in the vicinity of the user's whole body that can further reduce their performance due to greater absorptions and reflections from the body surface. Therefore, it is pertinent to

take into account the effects of the whole body presence on the working of GPS mobile terminal antennas.

7.2.3.1 Test Set-up

In this study, a medium-resolution realistic complete human body model is considered. The human body is modelled as a single-layer homogeneous object, based on the observations made in the previous section for the single-layer and multi-layer head models. This model offers not only faster computations as a result of reduced complexity, but also flexibility in terms of repositioning the body parts [29, 30]. It makes it easy to represent the talking-on-phone and holding-the-phone positions. A high-resolution hand is also added to realise the antenna held-in-hand scenarios, shown in Figure 7.15. The dielectric properties of the muscle tissue at 1575.42 MHz are used with a permittivity of 53.86 and conductivity of 1.22 S/m [24–26].

The three similar types of GPS antennas used in mobile terminals discussed in Section 7.2.1, namely the PIFA, DRA and helix, are used to analyse the effects of human body presence in the multipath environment. Three possible scenarios of on-body placement of the GPS mobile terminal antennas are considered. For the device kept in the user's pocket, GPS antennas are placed on the bottom left torso at the pocket position on the body as shown in Figure 7.15b. The separation between the antenna and the body is kept at 10 mm to allow clearance for the mobile casing. In the scenario where the GPS mobile terminal antenna is being watched by the user, the antennas are modelled to be held in the user's hand in front of the body, at a distance of 175 mm from the body surface, as illustrated in Figure 7.15c. Lastly, the effects of the presence of the human body on GPS mobile terminal antennas are investigated for a common position of talking on the phone. This configuration is modelled by repositioning the human body in such a way that the antenna is held in the user's hand beside the head, as depicted in Figure 7.15d. The separation is again kept at 10 mm between the antenna and the head to allow the covering assembly, whereas the antennas are inclined at 45° with respect to the z-axis. Figures 7.16–7.18 illustrate the details of position and orientation of the radiating elements of the three antennas in the considered on-body placements.

7.2.3.2 Evaluation of GPS Antenna Performance

The S_{11} curves of the three antennas working in the on-body placements are plotted in Figures 7.19–7.21. The antenna detuning is evident from these results caused by the presence of the human body.

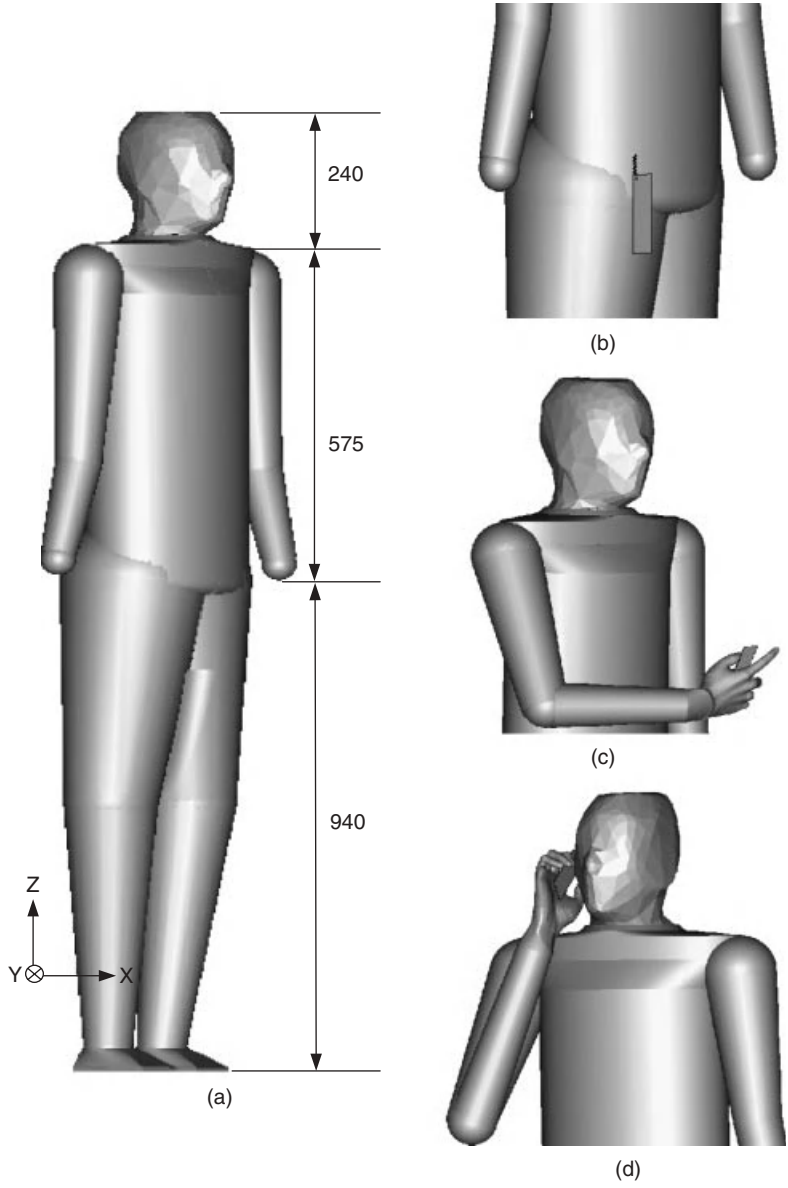

Figure 7.15 Medium-resolution single-layer homogeneous realistic human body model used to study effects of body presence on performance of GPS antennas with different placements of the antennas on the body (all lengths are in mm): (a) Realistic whole body model, (b) Placed at pocket position, (c) Watching position and (d) Talking position.

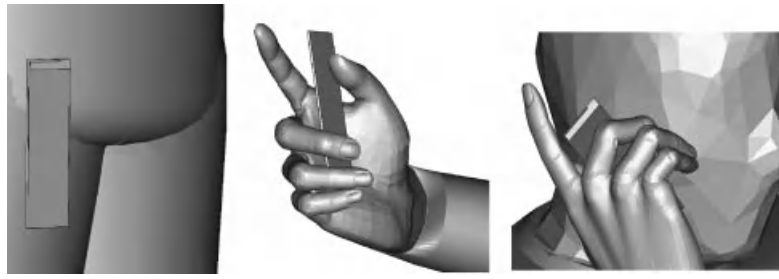

Figure 7.16 Various on-body placements of GPS mobile terminal PIFA: (a) Pocket position, (b) Watching position and (c) Talking position.

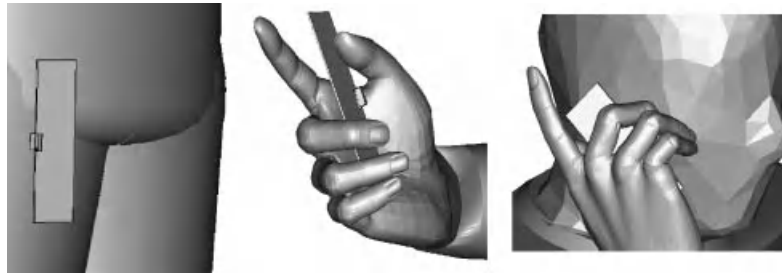

Figure 7.17 Various on-body placements of GPS mobile terminal DRA: (a) Pocket position, (b) Watching position and (c) Talking position.

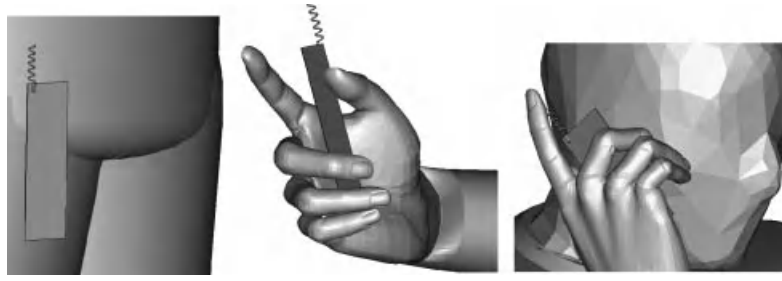

Figure 7.18 Various on-body placements of GPS mobile terminal helix: (a) Pocket position, (b) Watching position and (c) Talking position.

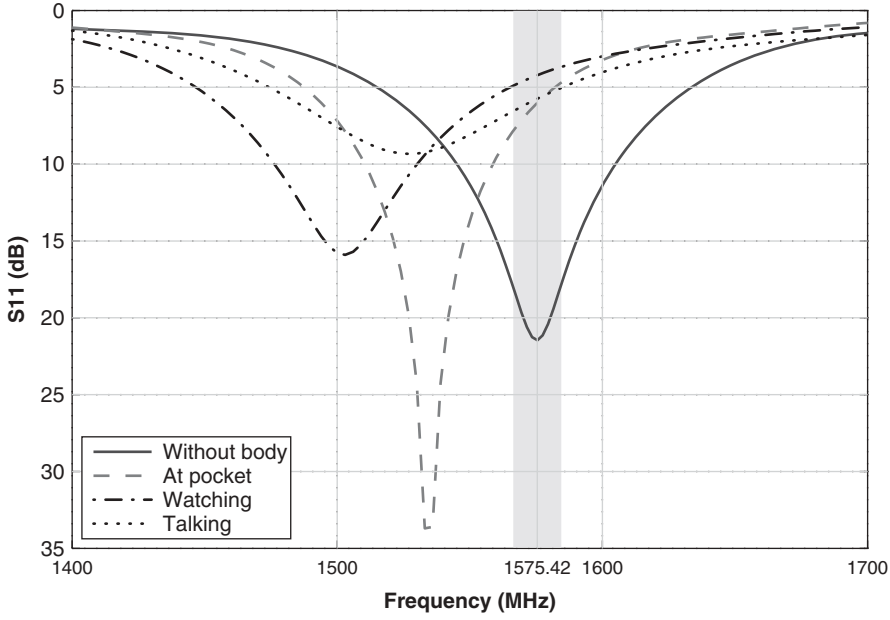

Figure 7.19 S_{11} response of PIFA operating in different on-body positions.

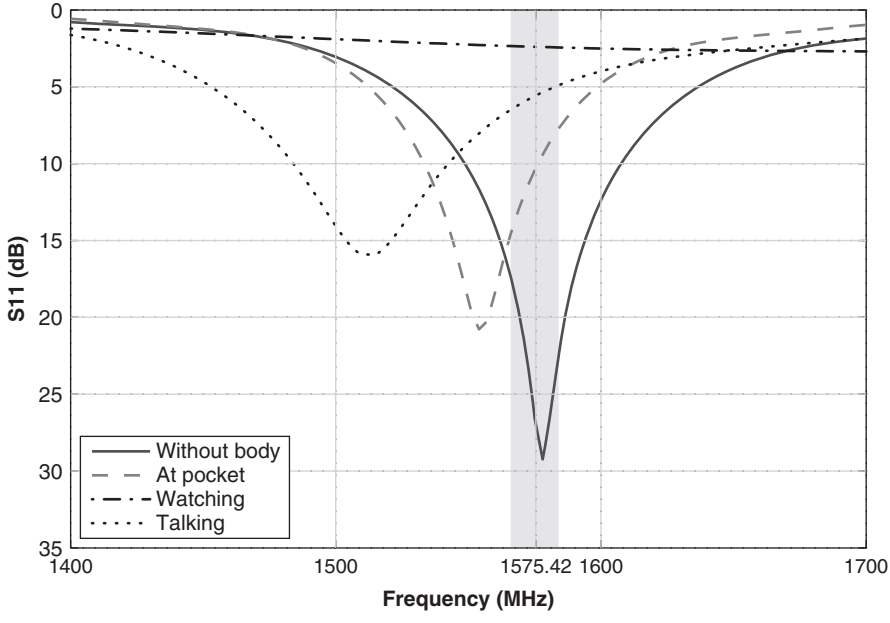

Figure 7.20 S_{11} response of DRA operating in different on-body positions.

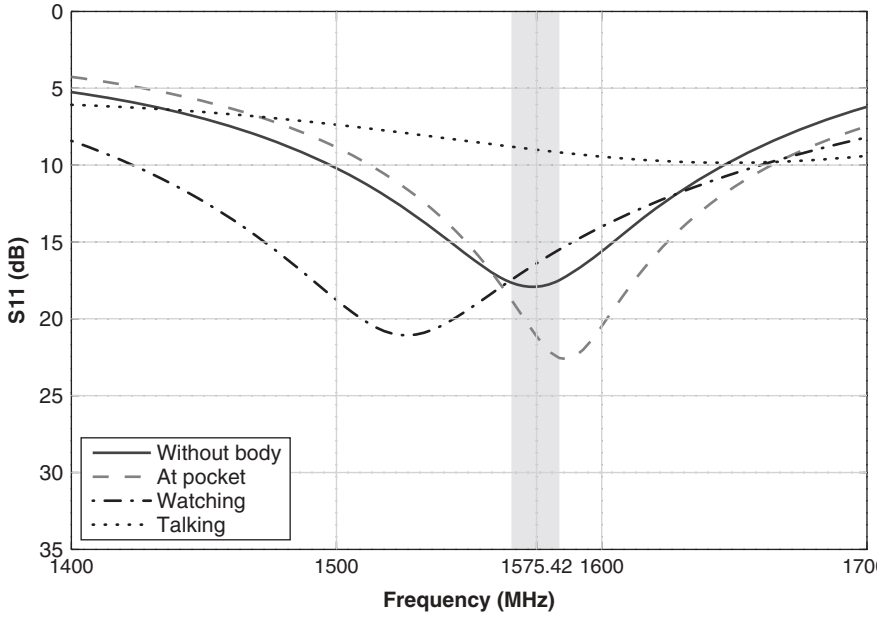

Figure 7.21 S_{11} response of helix operating in different on-body positions.

The PIFA is affected most as it has failed to exhibit the desired −10 dB impedance bandwidth of ±5 MHz in the three on-body configurations (Figure 7.19). The DRA has also shown a poor performance as it completely detuned in the watching and talking positiosn while achieving −10 dB impedance bandwidth of 5 MHz covering the frequency range of 1570 to 1575 MHz in the placed-at-pocket position, shown in Figure 7.20. The helix antenna has again shown a less sensitive behaviour to the detuning effects caused by the human body. It has fulfilled the ±5 MHz impedance bandwidth requirement in the L1 band for the placed-at-pocket and watching positions, while managing to attain a comparatively reasonable −8 dB impedance bandwidth of ±5 MHz when operating in the talking position (Figure 7.21). Overall, the three antennas have performed poorly in the talking position compared with the other scenarios.

The greater detuning of the DRA in the watching position and the helix in the talking position is due to electromagnetic absorptions in the palm of the holding hand and the gripping fingers. The two antennas could perform better if the radiating element was cleared from the palm of the hand and the gripping fingers. Therefore, the DRA in the watching position and the helix in the talking

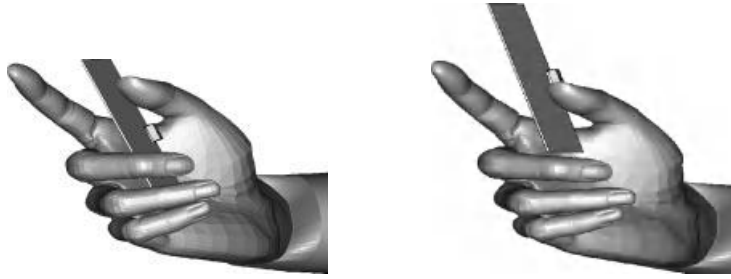

(a) (b)

Figure 7.22 Modified watching position for GPS mobile terminal DRA to investigate S_{11} response: (a) Original watching position; (b) Modified watching position (d_z = 40 mm).

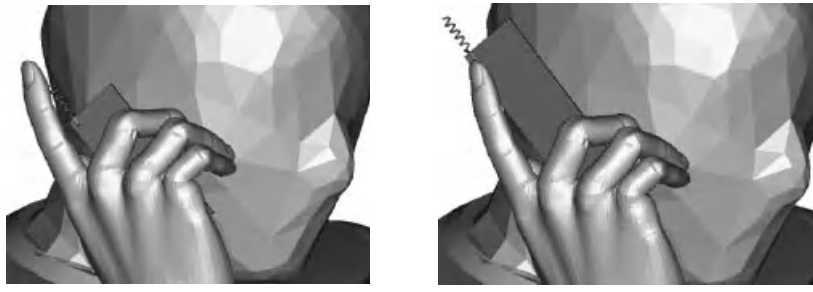

(a) (b)

Figure 7.23 Modified talking position for GPS mobile terminal helix to investigate S_{11} response: (a) Original talking position; (b) Modified talking position ($d_z = 40$ mm).

position are tested by moving the antenna 40 mm in the z-direction (d_z). The two tested configurations are shown in Figures 7.22b and 7.23b in comparison with the original positions (Figures 7.22a and 7.23a).

The S_{11} responses of the DRA and helix in the modified watching and talking scenarios are plotted in Figures 7.24 and 7.25, respectively. It can be observed from these results that the two antennas exhibit better impedance matching when placed at $d_z = 40$ mm compared with the original positions. It is therefore evident that the way a user holds the antenna plays a vital role in defining the extent of antenna detuning.

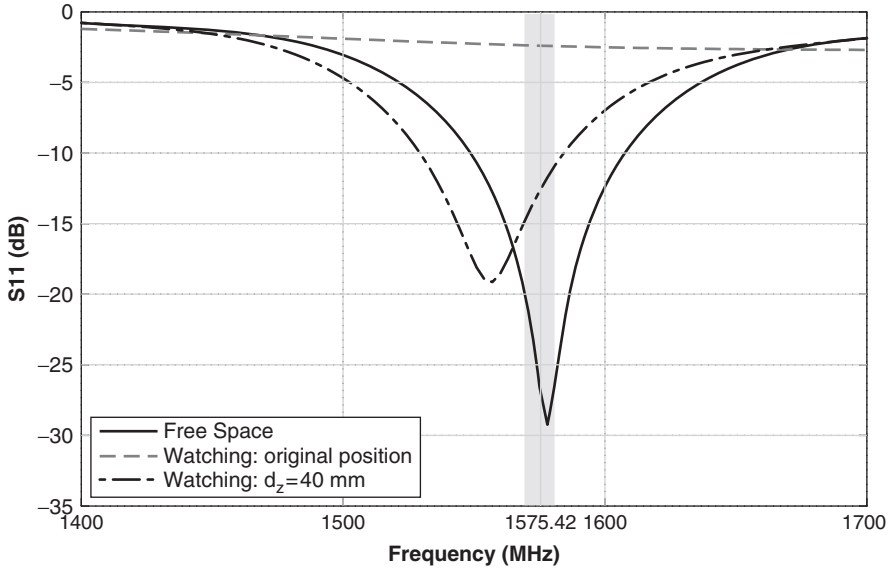

Figure 7.24 Comparison of S_{11} curves for DRA in original and modified watching positions.

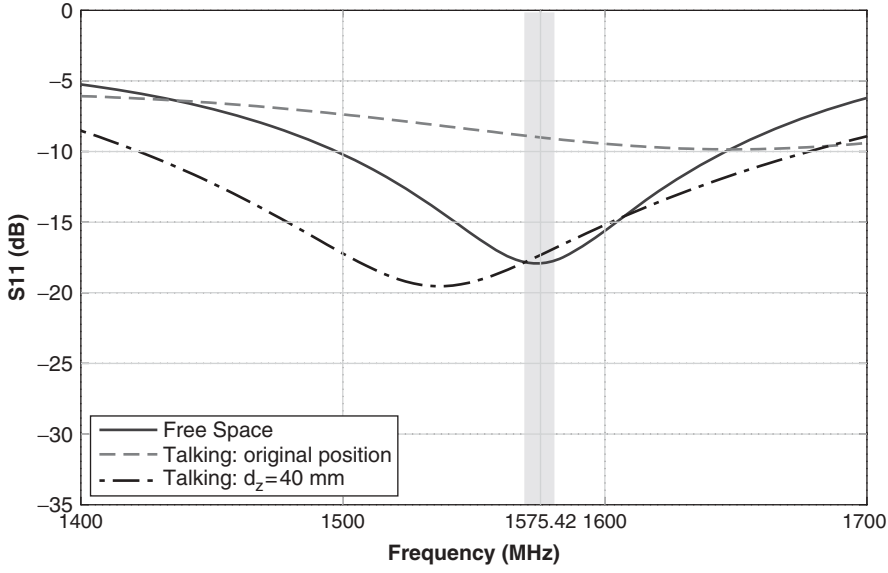

Figure 7.25 Comparison of S_{11} curves for helix in original and modified talking positions.

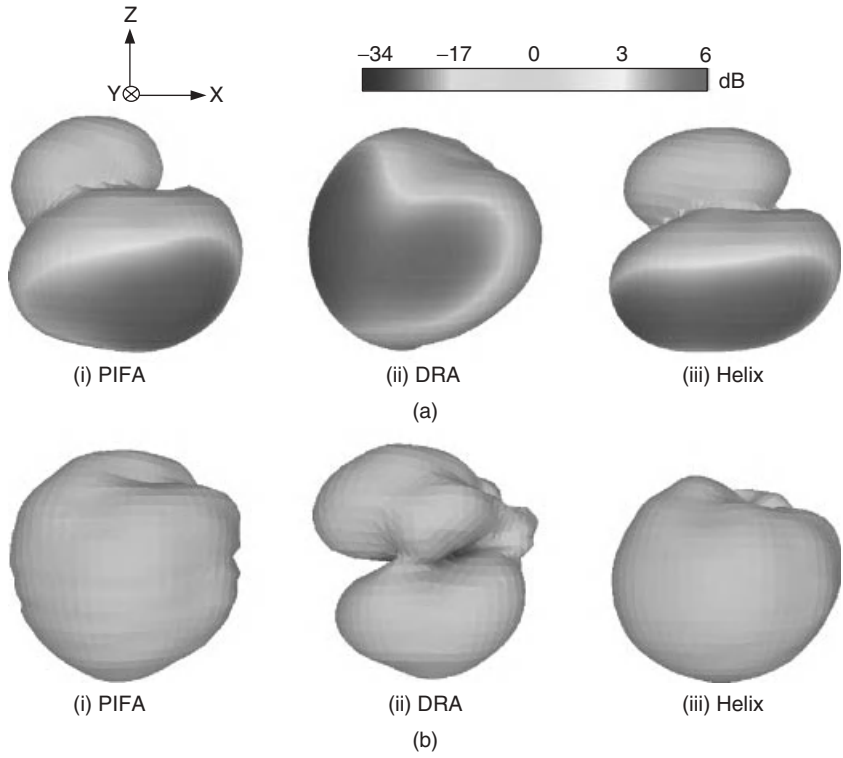

Figure 7.26 Simulated 3D gain patterns for perpendicular and parallel polarisations of PIFA, DRA and helix GPS mobile terminal antennas placed at user's pocket position to evaluate effects of body presence on performance of GPS antennas: (a) $G_{\perp}$; (b) $G_{\parallel}$.

The 3D simulated gain patterns of the three antennas in different on-body positions are also observed and recorded, and depicted in Figures 7.26–7.28. The proposed statistical model for the GPS multipath environment is used for the evaluation and comparison of the performance of the antennas in the three on-body configurations. The realised gain is used in the calculations of η_c and MEG_{GPS} to incorporate both the power absorption and detuning effects caused by the human body. Table 7.3 summarises these results in comparison with the values observed when the antennas operate without the presence of the human body.

Figure 7.29 compares η_c and MEG_{GPS} for the three antennas. These results further strengthen the fact that GPS mobile terminal antennas in the multipath environment undergo performance degradations due to the presence of the lossy

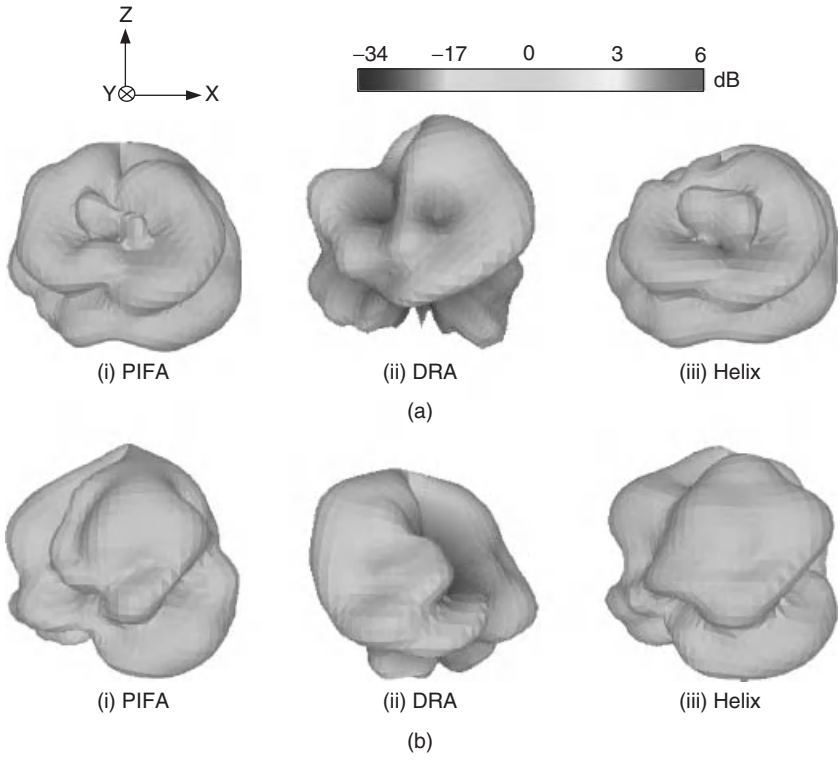

Figure 7.27 Simulated 3D gain patterns for perpendicular and parallel polarisations of PIFA, DRA and helix GPS mobile terminal antennas held in user's hand at watching position to evaluate effects of body presence on GPS antennas' operation: (a) $G_{\perp}$; (b) $G_{\parallel}$.

human body. The operation of the three antennas depends upon the factors discussed in the previous section, including clear sky view, shielding body mass and antenna placement.

Human body presence causes a minimum drop of 3% in the GPS antenna's η_c and 1.5 dB in MEG_{GPS}. The three antennas perform reasonably well in the placed-at-pocket position. A greater clear view of the sky and enhanced gain levels in directions away from the body, due to reflections from the surface of the body, act to minimise the degradations caused by the presence of the human body. The DRA antenna has shown the best performance because of stronger radiation in the upper hemisphere with an η_c of 58% and MEG_{GPS} of −7.2 dB. In the watching position, a larger gap between the torso and the

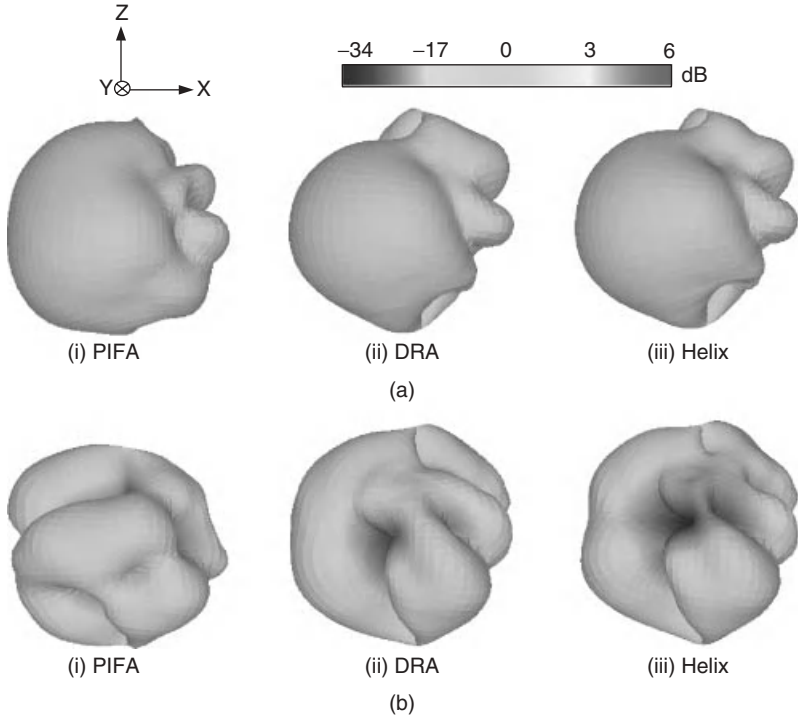

Figure 7.28 Simulated 3D gain patterns for perpendicular and parallel polarisations of PIFA, DRA and helix GPS mobile terminal antennas held in user's hand beside head in talking position for the evaluation of GPS antenna performance near the human body: (a) $G_{\perp}$; (b) $G_{\parallel}$.

antenna has reduced the tissue losses. The presence of the holding hand has proved the major source of degradation in this case. The PIFA and helix antenna have exhibited an improved η_c of 69% and 85%, respectively, as a combined result of a less shielded radiating element and increased gain in the upper hemisphere because of the reflections from the palm and arm. However, this increased coverage is made less effective by a reduced MEG_{GPS} of -13.2 dB and -8.0 dB, respectively, due to pattern deformations. On the other hand, the performance of the DRA has suffered greatly since the radiating element is blocked to a larger extent by the palm and gripping fingers of the holding hand. It has reduced its η_c to just 3% and MEG_{GPS} to -24.8 dB.

Table 7.3 Calculated GPS coverage efficiency and GPS MEG of three mobile terminal GPS antennas working in the vicinity of the human body in multipath environment with effects of whole human body presence

Test set-up in presence of complete human body	Model calculations using simulated 3D patterns in actual reflection multipath environment					
	PIFA		DRA		Helix	
	η_c (%)	MEG_{GPS} (dB)	η_c (%)	MEG_{GPS} (dB)	η_c (%)	MEG_{GPS} (dB)
Antenna without human body presence	92	−8.2	95	−5.7	88	−5.8
Antenna placed at pocket position	52	−10.7	58	−7.2	53	−7.3
Antenna held in watching position	69	−13.2	3	−24.8	85	−8.0
Antenna held in talking position	34	−17.5	17	−18.5	20	−13.8

The three antennas have again exhibited a poor performance in the talking position. The electromagnetic shielding by the lossy head and hand tissues on both sides has limited the reception of the signal from all directions. The η_c values are observed to be 34%, 17% and 20% for the PIFA, DRA and helix antenna, respectively. The MEG_{GPS} is noted to be −17.5, −18.5 and −13.8 dB for the three antennas, respectively. The ranking of the antenna performance is similar to that observed in the previous section (in the presence of both the head and hand) whereas added losses have been introduced mainly by the shoulder and arm.

Overall, the helix has shown a better capability to operate in the vicinity of the human body in the three tested scenarios, exhibiting reasonable levels of MEG_{GPS} and η_c with lesser detuning in comparison with the PIFA and DRA. Therefore, it could be deduced that size and position of the radiating element also play an important role in reducing the losses introduced by the human body tissues.

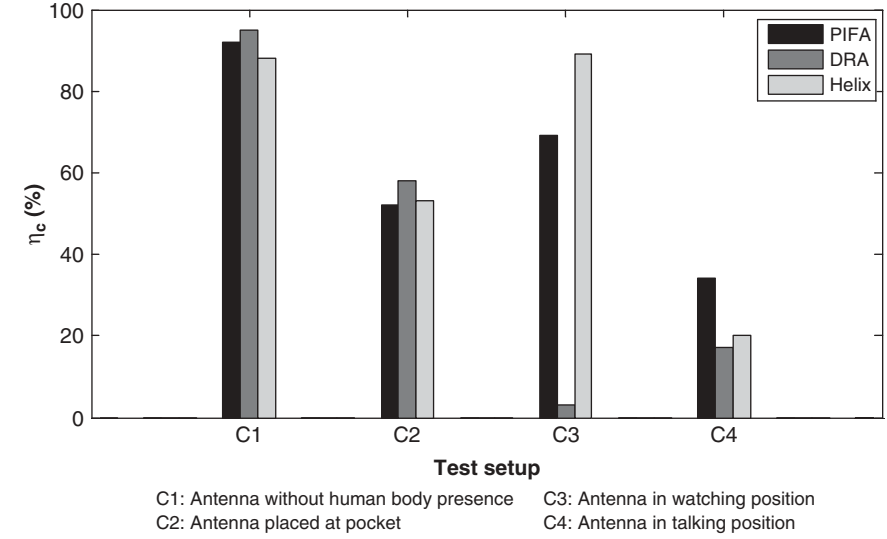

(a)

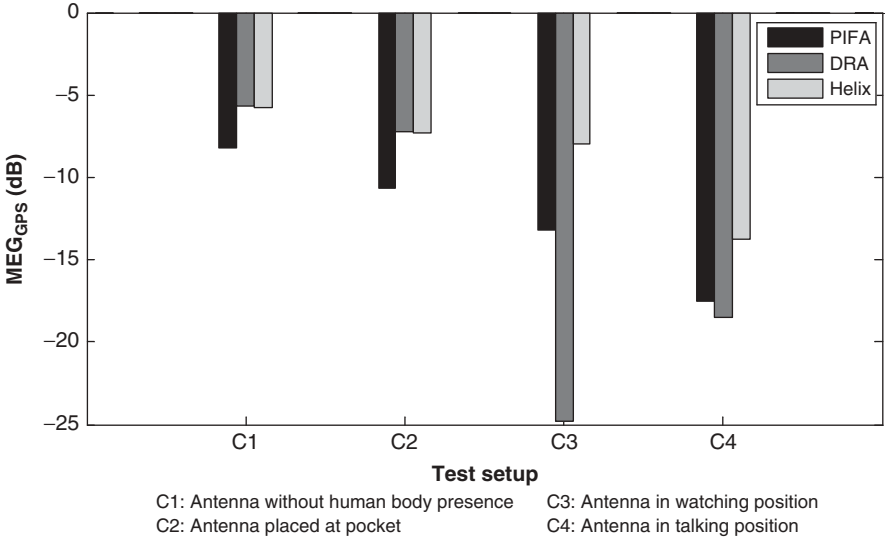

(b)

Figure 7.29 Multipath environment performance of GPS mobile terminal antennas in free space and in different on-body scenarios with effects of complete human body presence: (a) Coverage efficiency of GPS antennas; (b) MEG of GPS antennas.

References

1. Jensen, M.A. and Rahmat-Samii, Y. 'EM interaction of handset antennas and human in personal communications', *IEEE Transactions on Antennas and Propagation*, **83**, 7–17, 1995.
2. Toftgard, J. Hornsleth, S. and Anderson, J.B. 'Effects on portable antennas of the presence of a person', *IEEE Transactions on Antennas and Propagation*, **41**, 739–746, 1993.
3. Okoniewski, M. and Stuchly, M.A. 'A study of the handset antenna and human body interaction', *IEEE Transactions on Microwave Theory and Techniques*, **44**, 1855–1864, 1996.
4. Mason, P.A. Hurt, W.D. Walters, T.J. et al. 'Effects of frequency, permittivity and voxel size on predicted specific absorption rate values in biological tissue during electromagnetic field exposure', *IEEE Transactions on Microwave Theory and Techniques*, **48**, 2050–2058, 2000.
5. Hall, P.S. and Hao, Y. *Antennas and propagation for body-centric wireless networks*, Artech House, London, 2006.
6. Wang, J. and Fujiwara, O. 'EM interaction between a 5GHz band antenna mounted PC and a realistic human body model', *IEICE Transactions on Communications*, **E88-B**, 2604–260, 2005.
7. G.A. Conway and W.G. Scanlon, 'Antennas for over-body-surface communication at 2.45 GHz', *Transactions on Antennas and Propagation*, **57**, 844–855, 2009.
8. M. Sanad, 'Effect of the human body on microstrip antennas', IEEE Antennas and Propagation Society International Symposium (AP-S), Vol. 1, pp. 298–301, June 1994.
9. H.R. Chuang, 'Human operator coupling effects on radiation characteristics of a portable communication dipole antenna', *IEEE Transactions on Antennas and Propagation*, **42**, 556–560, 1994.
10. Colburn, J.S. and Rahmat-Samii, Y. 'Human proximity effects on circular polarized handset antennas in personal satellite communications', *IEEE Transactions on Antennas and Propagation*, **46**, 813–820, 1998.
11. CENELEC, European Specification, 'Considerations for the evaluation of human exposure to electromagnetic fields (EMFs) from mobile telecommunication equipment (MTE) in the frequency range from 30 MHz-6 GHz', ES-59005:1998 E, 1998.
12. Ur Rehman, M. Gao, Y. Chen, X. and Parini, C.G. 'Effects of human body interference on the performance of a GPS antenna', European Conference on Antennas and Propagation (EuCap), November 2007.
13. Ur Rehman, M. Gao, Y. Chen, X. Parini, C.G. and Ying, Z. 'Mobile terminal GPS antennas in multipath environment and effects of human body presence', Loughborough Antennas and Propagation Conference (LAPC), November 2009.
14. Ur Rehman, M. Gao, Y. Chen, X. Parini, C.G. and Ying, Z. 'Impacts of human body on built-in GPS antennas for mobile terminal in multipath environment', European Conference on Antennas and Propagation (EuCap), April 2010.
15. Federal Communication Commision, 'FCC's wireless 911 rules', http://www.fcc.gov/guides/wireless-911-services (accessed 25 September 2011)
16. Nielsen, J.O. and Pedersen, G.F. 'Mobile handset performance evaluation using radiation pattern measurements', *IEEE Transactions on Antennas and Propagation*, **54**, 2154–2165, 2006.
17. Krogerus, J. Ichelun, C. and Vainikainen, P. 'Dependence of mean effective gain of mobile terminal antennas on side of head', European Conference on Wireless Technology (ECWT), pp. 467–470, October 2005.

18. Douglas, M.G. Okoniewski, M. and Stuchly, M.A. 'A planar diversity antenna for handheld PCS devices', *IEEE Transactions on Vehicular Technology*, **47**, 747–754, 1998.
19. Fujimoto, K. and James, J.R. '*Mobile antenna systems handbook*,' 2nd edn, Artech House, Boston, MA, 2001.
20. Pedersen, G.F. and Andersen, J.B. 'Handset antennas for mobile communications: integration, diversity, and performance,' *Radio Science Review* Oxford University Press, Oxford, 1999.
21. Ogawa, K. and Uwanao, T. 'Mean effective gain analysis of a diversity antenna for portable telephones in mobile communication environments,' *Electronics and Communication in Japan (Part I: Communications)*, **83**, 88–96, 2000.
22. CST Microwave Studio®, 2010 User Manual.
23. Balanis, C. *Antenna theory analysis and design*, 2nd edn, John Wiley & Sons, Inc., New York, 1997.
24. Gabriel, C. 'Compilation of the dielectric properties of body tissues at RF and microwave frequencies', Brooks Air Force Technical Report, *AL/OE-TR-1996-0037*, 1996.
25. 'Calculation of the dielectric properties of body tissues,' Institute of Applied Physics, Italian National Research Council, http://niremf.ifac.cnr.it/tissprop (accessed 1 November 2011).
26. Federal Communication Commision, 'Body tissue dielectric properties,' /www.fcc.gov/oet/rfsafety/dielectric.html (accessed 2 November 2011).
27. Jemai, J. Kurner, T. Varone, A. and Wagen, J.F. 'Determination of the permittivity of building materials through WLAN measurements at 2.4 GHz', IEEE International Symposium on Personal, Indoor and Mobile Radio Communications, September 2005.
28. Klysza, G. Balayssaca, J.P. and Ferriresb, X. 'Evaluation of dielectric properties of concrete by a numerical FDTD model of a GPR coupled antenna parametric study', *NDT & E International*, **41**, 621–631, 2008.
29. Ur Rehman, M. Gao, Y. Alfadhl, Y. *et al*. 'Study of human body exposure to RF signal at UHF frequencies,' Joint Meeting of Bioelectromagnetics Society and the European Bioelectromagnetics Association (BioEM), June 2009.
30. Ur Rehman, M. Gao, Y. Wang, Z. *et al* 'Investigation of on-body Bluetooth transmission,' *IET Microwaves, Antennas and Propagation*, **4**, 871–880, 2010.

8

Mobile Terminal GNSS Antennas

8.1 Introduction

This chapter deals with the limitations of antenna size and shape that are imposed when GNSS functions are to be added to small devices such as mobile handsets and personnel trackers. It is shown how the radiation patterns and polarisation properties of the antenna can be radically changed by factors such as the positioning of the antenna on the platform. The presence of a highly sensitive receiver system imposes severe constraints on the permitted levels of noise that may be generated by other devices on the platform without impairing the sensitivity of the GPS receiver; the chapter will describe the design precautions that must be taken to reduce these to an acceptable level. The case studies provide measured results from real applications, illustrating a number of typical performance defects and indicating possible solutions.

The essential properties of an antenna for a GNSS receiver are that it has a radiation pattern that covers as much of the sky as possible with the user device in its normal operating position, and that it has as high a gain, for an RHCP signal, as is consistent with the wide pattern beamwidth.

Almost all low-cost mobile terminals use only the L1 signal from the GNSS satellites. This has the advantage that the antenna can operate in only one frequency band, although to cover all the available and near-future systems, the L1 signal frequencies differ between systems as shown in Table 1.1.

Antennas for Global Navigation Satellite Systems, First Edition.
Xiaodong Chen, Clive G. Parini, Brian Collins, Yuan Yao and Masood Ur Rehman.

The last few years have seen a huge upsurge in the number and variety of consumer equipment making use of GNSS-derived location data. In many consumer platforms, for example mobile phone handsets and cameras, there is inadequate space for a conventional GNSS antenna, and the physical orientation of the platform when in use may make it difficult to provide an antenna with a clear view of the sky. Fortunately there is substantial latitude in the antenna requirement and a variety of solutions has been used successfully.

Mobile user equipments (UEs) present several problems in their use of GNSS services. A UE will frequently be used at locations in which the device has a limited view of the sky. A user standing immediately outside an isolated building will have a view of only one-half of the sky. This immediately halves the number of satellites that are potentially visible, perhaps from 10 to 5, which is likely to result in a fix with lower precision than would have been expected under open sky conditions. Thus:

- The total amount of positional information is halved – there are fewer independent estimates of position which can be used to produce the position information received by the user.
- The geometry of the available satellites is likely to result in a larger dilution of precision than would have been possible with a view of the whole sky.
- The strongest signals may be lost because the satellites that would have provided them are shielded from view by the building.

In a city street among high buildings the chance of a fast and accurate fix is further reduced. The number of satellites in view falls because only a small strip of sky is visible, most of the visible satellites are roughly in line with the direction of the street, so the fix will have poor precision in the transverse direction, and signals from satellites that are not directly visible will be received via reflections – perhaps multiple reflections – from the surrounding buildings.

A mobile UE has the additional penalties of lack of physical space in which to accommodate antennas (it often has to use small antennas) and of limited battery life (it may have reduced possibilities to maintain or refresh positional information while the device is not in use). A further design issue is the potentially close physical spacing between the GNSS antennas and other antennas and associated electronic devices on the platform, such as processors, cameras and memory. As well as the obvious possibilities of interference from strong transmitted signals, many of these devices produce broadband noise at levels which may exceed that of the signals received from distant satellites.

It will be seen from this short summary that the use of GNSSs on small user platforms presents a number of challenges, many of which are beyond

the control of the antenna designer. However, when a proven GNSS receiver is fitted to a new mobile device and the time to first fix is long, the carrier-to-noise ratio of the visible satellites is low, or the resulting position data is less accurate than expected, the problem is often taken to the antenna designer who is expected to be able to provide a solution. It is therefore important for antenna engineers to know something of the operation of the whole GNSS, and also for system-level device designers to understand the issues that relate to antenna design and placement on the platform.

8.2 Antenna Specification Parameters

We now review the specification parameters for any GPS antenna, and consider their impact on system performance.

8.2.1 Polarisation

GNSS satellites radiate RHCP signals, so an ideal user terminal will be provided with an RHCP antenna. Reflected signals will have reached the receiver with a longer flight time than direct signals, so any calculations made from them will be inaccurate. After a single reflection, signals will have left hand polarisation, so they can be suppressed by ensuring that the antenna will respond only to RHCP signals. The ground is a potent source of reflected signals, but to reject ground-reflected signals from satellites at low elevation angles the antenna needs a high axial ratio at these angles. Unfortunately, the polarisation radiated by most RHCP antennas in the rear hemisphere is LHCP, so the only way to reject ground reflections is by ensuring a high rate of roll-off of sensitivity at elevation angles below 10° or so from the horizon.

A real UE will often be used in city streets in which there may be multiple reflections, many of which will have RHCP. As with many other characteristics of the antenna (radiation pattern, gain and impedance), its polarisation depends heavily on the interaction between the antenna and the platform on which it is mounted. Any unbalanced (single-terminal) antenna operates because it creates currents in the groundplane of the platform; these groundplane currents radiate, so their directions and phases, together with the direct radiation from the antenna, determine the polarisation of the whole device. To complicate matters further, the effective polarisation will vary substantially with satellite direction and the orientation of the platform.

As a result of all these factors, the difference in performance of antennas with differing polarisations is less than might be expected, and it is common to find antennas with both nominal RHCP and nominal linear polarisation in

use with apparently equal success. A linearly polarised antenna occupies less area than a patch and is likely to be less loaded; if so it may outperform the smaller patches [1].

It seems reasonable that antenna/platform assemblies are compared by measuring their performance when illuminated by an RHCP signal, and the results shown in this chapter adhere to this convention except where explicitly stated otherwise. In the same way, all references to the shape and direction of radiation patterns relate to the RHCP component.

8.2.2 Radiation Patterns

The radiation pattern of a GNSS antenna should cover as much of the sky as possible when the platform is in its use position. The use position of different platforms may be substantially different – for example, typical in-car PNDs are mounted with the display almost vertical, while a smartphone or other handheld device will often be used with the screen uppermost. A device intended for vehicle location may be mounted in a concealed position with a very limited view of the sky and in close proximity to metal surfaces, while a handheld device may interact strongly with the user's body.

In general, the ideal radiation pattern for a GNSS antenna is an upward-looking hemisphere, providing gain to all satellites that are visible in the sky. An antenna with too small a beamwidth may have a correspondingly higher gain, but provided that the received signal is adequate to provide a carrier-to-noise (C/N_0) ratio in excess of around 35 dB, a more accurate fix is provided by acquiring more satellites rather than simply increasing the signal from those satellites lying within a limited effective antenna beamwidth.

8.2.2.1 Radiation Pattern Measurement

Passive radiation patterns are measured using standard techniques, illuminating the device under test (DUT) with an RHCP antenna fed by a signal source in the usual way. Using a measuring receiver we can plot the gain of the antenna/platform combination in two or three dimensions, depending on the capabilities of the measurement range. These measurements will allow us to optimise the position of the antenna on the platform and measure RHCP gain and efficiency. Measurements of this kind are usually made at the beginning of the development cycle for a new UE and they provide an indication of the general level of performance that can be anticipated from the proposed device if

other design aspects are well managed. In particular, they will serve to confirm that the polarisation and radiation patterns are suitable.

A better indication of the performance of a working platform is provided by illuminating the DUT by means of a satellite simulator, and equipping the DUT with an on-board operational GNSS receiver. The C/N_0 ratio recorded by the receiver is then plotted as a function of bearing of the signal source from the platform. To avoid the enhancement of the signal which may be caused by the connection of a cable to a very small UE, the output from the receiver may be transmitted by radio (including GPRS, Wi-Fi or Bluetooth), by an optical fibre, or by a carefully decoupled and isolated data cable.

If this measurement is carried out on a fully working UE, the result includes any interference produced on the UE platform. We can compare the measured C/N_0 performance with what we expect, given the measured antenna gain and known receiver noise figure. If these fail to match, we can then seek the cause, which is likely to be radiated or conducted noise, spurious emissions from other devices, or blocking from other transmitters on the platform. While these are not 'antenna problems', it is usually the antenna engineer who has the test gear and expertise to investigate and cure them.

Electromagnetic compatibility (EMC) issues on small mobile platforms, with closely integrated antennas, are more likely than with separate 'active' antennas (with an associated low-noise amplifier (LNA)), simply because the separate antenna is not subject to the noise environment on the platform and the increase in signal level provided by the LNA reduces the relative level of on-platform interference. In general, this is not a function of the type of antenna used, but is caused by the proximity of the antenna and the intrinsically higher level of interaction when the antenna is mounted directly on the platform.

8.2.3 Impedance

In general we require the antenna to provide a close match to 50 Ω. In the case of a UE provided with a radio transmitter – for the cellular communications bands, Wi-Fi, Bluetooth or other interfaces – the receiver is likely to be preceded by a bandpass SAW filter, so the possibility of employing noise-matching rather than power-matching at the receiver input is limited. While almost all compact GNSS antennas have an unbalanced output, some receiver chips have a balanced (differential) input, so a balun network or chip component may be needed between the antenna and the receiver – some SAW filters provide a single-ended input and balanced output for this application. The input

impedance of a SAW filter may be mismatched from 50 Ω and some improvement in performance may be provided by providing an input matching network between the antenna and the filter. The provision for a matching network also allows for the compensation of the effects of the platform – including that of the plastic case – on the impedance of the antenna.

An antenna requires only a very small fractional bandwidth to cover the L1 frequency band, but the tendency of platform designers to demand ever-smaller antennas has led to the progressive reduction of patch antennas from the original $25 \times 25\,\text{mm}^2$ to as little as $12 \times 12\,\text{mm}^2$. This reduces the available bandwidth and many antenna designs rely on individual tuning by trimming its dimensions – a process often carried out using a laser. Some of these small antennas are easily detuned by surrounding objects or by the presence of the user. Other antenna designs that are heavily loaded to reduce their dimensions may suffer the same problem. Mismatch reduces the effective sensitivity of the receiver and is therefore to be avoided.

The VSWR of an internal antenna is only significant in its impact on signal transfer to the receiver. Optimising the impedance of the antenna is part of the optimisation of its efficiency; the 'best' impedance is whatever provides the highest sensitivity and delivers the highest C/N_0 ratio in a given signal environment.

If an external antenna is used, its VSWR is important because any significant deviation from 50 Ω may result in critical dependence on the exact electrical length of the interconnecting coaxial cable – something which the user may adjust, for example to suit the fit in a vehicle. For this reason the VSWR should typically be less than 2:1.

8.2.4 Gain/Efficiency

Given the very low signal strength available from the GNSS satellites, it is clear that we should obtain as much gain from the antenna as possible. Unfortunately the requirement that the antenna must have an approximately hemispherical radiation pattern restricts the directivity, and hence the gain, we can realise. If the antenna were lossless and we could obtain an efficiency of 100%, its gain would be 3 dBic; with a more realistic efficiency we would do well to achieve a mean gain over a hemisphere of 1 dBic. We can degrade this, by poor polarisation matching or poor design of the antenna or the platform, but we can do little to increase it.

The only option open to us to increase the sensitivity of the receiver is to ensure that its noise figure is a small as possible. If the receiver already has a very low noise figure – less than say 1.2 dB – we must avoid degrading it

by introducing loss between the antenna and the receiver. If the noise figure is higher than this we should consider preceding the input to the receiver with an LNA – typically with a gain of 16–20 dB and a noise figure less than 1 dB. If the UE has provision for the optional use of an external antenna connected by a coaxial cable, this antenna would usually incorporate an LNA – a so-called *active antenna*. Introducing too much front-end gain in an effort to reduce the noise figure is not good practice – the resulting C/N_0 reported by the receiver may look impressively low, but the dynamic range of the system may be severely reduced and susceptibility to blocking correspondingly increased.

8.2.5 Weight

In today's compact, but highly complex consumer electronics, weight is a significant issue, and every opportunity is taken by designers to reduce the weight of every component. Even an antenna that weighs 2 g is too heavy if the same result could have been obtained from one weighing only 1 g!

8.2.6 Bandwidth

In the earlier chapters of this book we have described a wide variety of antennas that are suitable for use with GPS receivers. For some GPS applications the first priority is to obtain position or navigation data which has the highest possible accuracy. Such applications include surveying and aircraft navigation. To achieve high accuracy, the most obvious steps are to compensate for the errors created by the propagation medium and to reduce the extent to which reflected signals can enter the receiver. A further major increase in accuracy may be obtained by using the phase of the signals received from the satellites for the calculation of position. All these have requirements in terms of the performance of the antenna.

Compensation of ionospheric propagation delays requires that we receive signals at more than one frequency. These will typically be the L1 and L2 signals at approximately 1575 MHz and 1227 MHz. The delay caused by ionospheric effects is a function of the transmission frequency and of the elevation and direction of the path from each satellite. By receiving signals from each satellite at two well-spaced frequencies it is possible to compute the excess delay caused on each path, reducing the potential uncertainty in the estimated position of the receiver. In order to do this, we need a dual-frequency antenna.

In practice, although the uncertainties of propagation give rise to the largest contribution to clear sky error in a modern GPS system, at the time of writing most portable devices use only the L1 signal.

8.2.7 Phase Performance

Use of the phase of the received signal to refine the position estimate requires that, to the extent possible, it should not be a function of its angle of arrival relative to the antenna. For surveying, precision navigation and other applications requiring high position accuracy, perhaps down to a few centimetres, we must do whatever is necessary to achieve high accuracy. This requires the use of antennas which are designed to maintain stable phase characteristics and which can be used in an environment free from user influences. The objective of a completely stable and well-defined phase centre in both azimuth and elevation planes, and whose position is independent of frequency, is not really achievable, so a compromise is reached by applying measured calibration data to compensate the remaining variability in phase as a function of the direction of each satellite. This further implies that we know both the compass bearing and attitude of the antenna in order to apply these corrections accurately. For surveying applications the GPS antenna will be supported by a device similar to a theodolite, while for navigational purposes these additional variables may be obtained from independent sensors.

8.3 Classification of GNSS Terminals

8.3.1 Geodetic Terminals

These are the most accurate GNSS terminals and are typically found in fixed-site GNSS applications. Their antennas cover multiple frequency bands to enable compensation of propagation effects, and will increasingly provide reception of satellites for multiple GNSSs. This will provide higher reliability – resistance to ground sector failures and not just satellite failures – and greater accuracy, especially in situations with a restricted view of the sky. They are usually fitted with choke-ring antennas which provide the required radiation pattern performance but are relatively costly, large and heavy.

8.3.2 Rover Terminals

These are typically used in land survey, forestry, construction, and other portable or mobile applications. They provide the user with good accuracy while being optimised for portability. The antenna for a rover terminal is typically mounted on a handheld pole and fires vertically upwards. This controls the attitude of the antenna within reasonably narrow limits, although

the azimuth orientation of the antenna may be uncontrolled. The position and high front-to-back ratio of the antenna assist by reducing operator-reflection multipath and ground noise pickup. These antennas are designed to provide rapid roll-off at low elevation angles to reduce multipath and the maintenance of a low axial ratio to maximise receive signal gain and reduce phase centre variations as far as possible. Their size, weight, performance and cost are practical compromises based on the application to be served.

8.3.3 General Purpose Mobile Terminals

These provide sufficient accuracy for consumer applications such as in-car navigation, personnel trackers, geo-tagging of photographs and social media. They also serve a wide range of commercial applications such as the tracking of goods and vehicles, and the location of handheld payment and receipt terminals. These terminals use a variety of antenna types, mainly determined by their low cost and small occupied volume. Fortunately, for these applications a median error (CEP) of between 2 and 3 metres is acceptable and it can be achieved by modern GPS receivers using s single frequency and a simple low-cost antenna. It is important to understand that the use of these antennas on small consumer platforms represents a large compromise in potential performance, but for many purposes the convenience and low cost of these devices outweigh their limited accuracy.

Table 8.1 gives a summary of the general classification of GNSS mobile terminals.

Table 8.1 General classification of GNSS terminals

	Geodetic	Rover	Handheld
Frequency bands	Multiple	Single/multiple	Single, L1
Radiation patterns	Tightly optimised	Controlled	Uncontrolled
Phase behaviour	Characterised and compensated in 3D	Moderate, not compensated	Not relied upon
Multipath suppression	Excellent	Good	None
Dimensions	Large	Medium	Small/very small
Weight	Heavy	Portable	Almost none
Cost	High	Medium	Very low

Three additional constraints are important in many of the applications which we will consider in this chapter, as follows.

8.3.3.1 Sensitivity

For smartphones, personnel trackers and many other applications it is desirable that GNSS position should be available even in poor signal conditions – with limited sky view, or perhaps even no direct satellite view. It is also very desirable that position is reacquired as soon as possible when the device moves from a shadowed position into an area with better signal coverage.

- *Time to first fix (TTFF)*: It is important for many applications that position is acquired rapidly on start-up. Lack of sensitivity will result in slow acquisition of satellites on start-up, especially when the device has a partial view of the sky.
- *Battery drain*: All portable devices are limited by the capacity of their batteries. Most GNSS receivers have a variety of low-power 'sleep' modes available, in which they maintain only minimal memory contents and wake from time to time to refresh their clock offsets and ephemeris data. These activities require substantial battery current, so if they are prolonged by lack of signal the effective battery life will be substantially reduced.

8.4 Antenna Designs for Portable User Equipment

8.4.1 Short Quadrifilar Helices

Early antennas for UEs were usually in the form of short helices. These became popular after the introduction of dielectrically loaded resonant quadrifilar helices, and this form of antenna has proved remarkably durable. Its main drawbacks are a form factor which is not always easy to accommodate in a small, tightly packed UE, and a relatively high price by current standards. These antennas are typically only 12 mm high at 1575 MHz (0.063λ) but suffer the consequent penalties of low radiation resistance, high Q-factor and the need for tight production tolerances. The characteristic shape and size of their upward-projecting outline are still typical of many user devices. A quadrifilar helix has the advantage of being a balanced antenna, and when suitably dimensioned its radiation pattern can provide high efficiency for RHCP reception and a radiation pattern covering a wide arc of the sky. Being balanced, the antenna is much less dependent on currents generated in the device on which it is placed than is the case with an unbalanced antenna. As described in [2] and illustrated

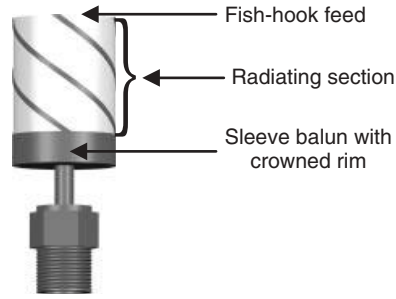

Figure 8.1 Short backfire quad-helix [2]. Reproduced with permission from IET.

in Figure 8.1, the antenna is realised as a copper track etched or deposited on a high-K dielectric core. An integral balun is formed as a short-circuit $\lambda/4$ coaxial sleeve, much shortened by the presence of the dielectric inside it. The antenna comprises two bifilar helical loops. One is adjusted to be slightly longer than resonant length to produce an input impedance with a phase angle of $+45^\circ$, and the other bifilar is adjusted to be shorter than resonance to produce an input impedance with a phase angle of $+45^\circ$. This produces the required 90° phase shift between the currents in the first bifilar winding with respect to the second bifilar winding.

The penalty for the substantial size reduction achieved by this very successful design is the low feed impedance ($R = 2\,\Omega$) and the consequent narrow bandwidth over which it can be matched to $50\,\Omega$.

This antenna provides a radiation pattern with a large beamwidth, aligned with the axis of the structure and directed away from the grounded end of the elements. In order to face the sky, this type of antenna is mounted on the upper edge of the host platform.

8.4.2 Patch Antennas

An alternative early form of small GNSS antenna was a square patch. When constructed using a suitable dielectric material between the substrate and the radiating patch, this is around 25 mm square, and with an off-centre feed and/or a truncated corner it can provide the desired circular polarisation. A patch creates a radiation pattern directed orthogonally away from the surface on which it is mounted. This is no problem if the surface is horizontal – like the roof of a car – but became a problem when integral antennas were needed for satellite navigation devices to be used inside cars. In this application the screen is oriented towards the driver and only the top of the package faces the

sky. Some user devices were provided with antennas supported on ancillary groundplanes, hinged so they could be flipped up to the horizontal position when the device was in use and folded down to avoid damage when the device was removed from the inside of the windscreen. This meant that the antenna must be connected to the receiver by a flexible cable, and a hinge mechanism was needed to support it in the stowed and operational configurations, both adding to the cost of implementation.

The dimensions of ceramic patch antennas have been progressively reduced by increasing the permittivity of the supporting dielectric, from 25 mm to 18 mm, 15 mm and currently to 12 mm square. Again, the disadvantage of reducing the size of any antenna is that its Q-factor increases, reducing its bandwidth and at the same time usually reducing its gain. Patch antennas on high-dielectric substrates have narrow bandwidths and their terminal impedance is affected both by the size and geometry of the supporting groundplane, as well as by the manufacturing tolerances of the dielectric and the conductive patch element.

The radiation pattern and polarisation characteristics of a patch mounted in the centre of a groundplane are well known, but mounting a patch in an off-centre location on a small groundplane can greatly modify both its pattern and polarisation.

8.4.3 Smaller Antennas

A further quest for smaller antennas has led to the use of simple linearly polarised antennas such as inverted-F antennas (IFAs), which have been dielectrically loaded where space is very restricted. Loops and convoluted coplanar dipoles have also been used with success. The performance of these antennas is very dependent on the geometry of the platform on which they are mounted and on their position on the platform. This dependence imposes requirements on the platform, as well as on the antenna and its placement.

8.5 The Function of the Platform

Any unbalanced antenna is a single-terminal device, and the current flowing into it is supported by currents and fields in the groundplane against which it is fed. The groundplane is physically much larger than the antenna, so its radiation patterns and input impedance are strongly determined by the groundplane. For this reason, successfully adding GNSS functionality to a UE depends on correct design of the UE as well as the choice of an appropriate antenna. When the UE design is incorrect it is usually the antenna designer who is given the

task of finding out what has gone wrong, and then persuading others that their design was inadequate to provide acceptable antenna performance. A much more satisfactory design method is to understand the way in which a successful platform is designed to provide the necessary RF performance. The effects to be considered are those on antenna efficiency (gain), noise environment, radiation pattern and polarisation.

8.5.1 Antenna Efficiency, Gain and Noise

A successful design requires that the host platform provides a continuous groundplane, with at least one dimension preferably approximating a free space half wavelength – this is around 65 mm. Ground currents will flow in the outermost conducting layer on the platform, so to avoid received power disappearing into DC feed lines, digital lines and other circuits, it is good practice to provide an essentially continuous copper ground conductor on the face of the PCB supporting the antenna. To ensure the highest antenna gain, the groundplane should not be interrupted by long tracks, especially those aligned at right angles to the antenna-induced currents. It is perfectly acceptable to provide holes in the groundplane so electronic components, fed from below, can be accommodated on the board. An even better result will be obtained if we provide a continuous copper layer on the other face of the PCB stack, and provide vias all around the edge of the PCB to tie the two outer groundplanes together. Not only has this provided a clear path for RF currents on both sides of the platform, but at the same time we have created a screened box, inside which lie all the noisy lines connected to processors, memory, clocks, switch-mode power supplies and other circuits which will raise the noise floor at the GNSS frequencies and reduce the ability of the receiver to see the very low-level signals arriving from GNSS satellites. While laying out the PCB it is prudent to allow for screening cans to be placed over all the chips supporting noisy functions. They may not be needed if the separation between the antenna and the chip is sufficient and the groundplane design is adequate, but if they are needed they can be added without the necessity of a board respin.

The environment of a small mobile UE is often very challenging for GNSS use, with co-sited transmitters and other electronic devices. The available isolation between small unbalanced antennas is often restricted by the presence of common-mode ground currents and there is little physical room to provide spatial separation – on a typical platform the available isolation may be as small as 12 dB. Fortunately, very high-Q bandpass SAW filters are available for the GNSS bands, and when cellular and GPS radios operate on the same platform it is general practice to fit SAW filters both preceding and following the LNA

at the front of the receiver. These naturally create a small reduction in receiver noise performance, but they effectively prevent blocking of the LNA by strong out-of-band signals.

A more insidious problem arises if a cellular transmitter has a poor out-of-band noise performance. Noise within the GPS band cannot be filtered by using a bandpass filter in front of the receiver, so the problem must be tackled by adding a notch filter in the transmitter output – or, better, by using a transmitter with lower broadband noise levels.

8.6 Comparing Antenna Performance on UEs

8.6.1 Drive Testing

An engineer who has designed a GNSS antenna for a portable UE will frequently be expected to demonstrate its functionality by conducting a 'drive test'. One or more portable UEs are taken in a vehicle and driven around while logging such parameters as the position of the vehicle, the number and C/N_0 ratios of the satellites used to provide each fix, and perhaps the TTFFs for various starting conditions. A test of this kind clearly in some way represents potential user experience, but as a method for comparing antennas, receivers or software it must be used with caution, and with an understanding of all the factors which can influence the performance of a GNSS receiver system.

One of the most important features of any test method must be that the result can be repeated. Unfortunately the constantly changing configuration of the GNSS satellites in orbit and the movement of a vehicle through the environment – particularly that of a high-rise city – effectively create a unique event. We cannot expect that carrying out the same test within an hour, or even at the same time on a different day, will provide the same results. They may be similar, but there may be wide variations in some parameters. These are to be expected – the vehicle may be in different positions on the road in subsequent tests and the satellite configuration will be different, causing large potential differences in the accuracy of position, especially in canyon streets. Effects of other traffic will vary; the duration of halts in traffic or at traffic signals will vary; the duration of periods out of range of signals may also vary – for example, while shadowed by tall buildings or waiting under bridges. The duration of a cold-start TTFF is a function of the time of start relative to the timing of data frames transmitted from the satellites; in urban conditions, and especially when on the move, the TTFF may be extended by shadowing from trees, buildings and other traffic and may be expected to differ widely between different cold starts even with the same equipment.

There are two methods by which this situation can be improved. Where possible, comparative trials should be conducted on two or more devices simultaneously, so the environmental variables are as near as possible the same for each; alternatively trials must be conducted a number of times and the results evaluated on a statistical basis.

There is always some conflict between the need to provide a user with some usable position information and the requirement for this to be accurate. This conflict has no unique solution, but the optimum for any user depends on the application. Many receivers provide configurable settings for parameters such as the lowest elevation angle for a satellite that will be used for navigation, or the lowest C/N_0 ratio that will be used, and these may be configured differently. Comparing antennas fitted to these receivers would give different results regarding the number of satellites used for navigation, but these would not necessarily have any relevance to a comparison of the performance of their antennas. The C/N_0 ratio reported by a receiver chip is a computed value, and not all types of receiver will provide the same value in identical circumstances – some always report higher than others, but though reporting different C/N_0 values, the receivers will usually be found to lose signal lock in very much the same conditions.

8.6.2 Non-Antenna Aspects of Performance

The most critical phase of the operation of a GNSS device is a cold start. In this condition the device has no current ephemeris data and no knowledge of the current GNSS time. Because the receiver knows neither the current exact orbital data of the satellites nor its own current location, it has no information with which to determine which satellites should be visible and cannot compute the Doppler shifts that will apply. The cold-start phase therefore requires that the receiver must correlate the incoming noise-like satellite signals with a range of Doppler shifts until it acquires and identifies some of the satellites that are in view. During this phase, a considerable amount of the available signal processing resource will be devoted to satellites which are not visible in the sky or are blocked from view, further reducing the efficiency of the acquisition process and potentially extending the TTFF. The TTFF will always be longer if the view of the sky is partially obstructed.

There are several system-level methods by which the TTFF can be reduced:

- Storing the last known position on the UE and reloading this to the receiver when it next starts; this allows the receiver to search for only those satellites that its internal almanac indicates will be visible from that location – rather

than searching for all the satellites in the constellation. No great precision of position is needed – in practice this will only fail if the user has taken a ride on an aircraft since the last fix. Approximate current position can be obtained from the IDs of local cellular base stations.
- Storing the last known position and the current ephemeris data; this will allow a faster start for some time after the receiver was last used, but becomes rapidly less useful after three hours.
- Providing intelligence in the receiver so it can predict the future ephemerides based on previous data received from the satellites it has seen while in use on previous occasions. The accuracy of this data is high for a few days and becomes less accurate as gravitational anomalies, solar radiation pressure and other effects reduce the accuracy of the predictions.
- Loading current ephemeris data to the receiver from dedicated network-connected servers; this may come directly from a mobile radio network or indirectly from a remote Internet-connected server.

While these procedures may seem unrelated to antenna design, any comparison between the performance of different UEs needs to be made with an understanding of these external factors which can heavily influence the results obtained. Even an apparently simple comparison of the C/N_0 ratios or TTFFs of two different devices conceals the fact that the C/N_0 ratios displayed by different receivers may not be directly comparable and the devices may have different resources to accelerate a first fix.

Many GNSS receivers have a noise performance which can be improved by adding an LNA in front of the receiver. 'External' antennas – connected to the UE by a coaxial cable – almost always include an LNA as part of the 'active antenna' package, and their use is common even with fully integrated antennas. The apparent performance of the receiver (as judged by the reported C/N_0 ratio) can often be 'improved' by increasing the LNA gain beyond the figure recommended by the receiver manufacturer. In the limit this leads to a system that is oversensitive to interference or external noise and which may exhibit unexpected behaviour in use. A characteristic anomaly is the reporting by the receiver of signals from satellites which are not visible above the horizon. This seems to occur because of aliasing of the short pseudo-random codes which are used to distinguish signals from different satellites.

This review of the system-related issues which result in different TTFF, position accuracy and reported C/N_0 ratio indicates some of the difficulties encountered when trying to compare the performance of antennas on a real GNSS user platform.

8.7 Practical Design

In a typical GNSS receiver the signals from multiple satellites are weighted according to their C/N_0 ratios such that the computed position is most reliant on the 'best' signals, with little or no weight given to those with low C/N_0 or from satellites with elevation angles below about 5°. When designing an antenna there is a clear trade-off between achieving maximum sky coverage (determined by the antenna beamwidth) and achieving maximum gain. What matters most is the performance of the antenna *in situ*, with the UE in its operating position and orientation, and including any operator effects such as hands or fingers which may cover a poorly placed antenna. The measurement of the radiation pattern and the gain of the antenna mounted on the target platform are simple and well-understood tasks and they can be conducted in a laboratory environment using standard techniques. The use of a satellite simulator allows the interactions of the antenna, bandpass filters, LNA and receiver to be included in the measurement, and for these components to be jointly optimised. However, interpreting laboratory results is never easy – given that for the same antenna designs mounted on different platforms, the radiation patterns, polarisation characteristics, mean gain and peak gain will all be different – and only an assessment of the real-world performance of the device, including the way its firmware and software behave in a non-ideal scenario, will provide a full insight into its operation.

8.7.1 Positioning the GNSS Antenna on the Application Platform

The use of a well-designed antenna is necessary to the achievement of good performance of the GNSS receiver, but even a good antenna will not perform according to expectations if it is incorrectly sited or if the supporting application PCB is not well designed. The following list indicates the main criteria that should be observed:

1. For a hand-portable device, the antenna position should not be covered by the user's hand when full GNSS functionality is needed. This is an easy constraint to understand, but with small application platforms there is great competition for antenna space and the GNSS antenna is often relegated to a suboptimal position.
2. As much area under and around the antenna should be provided with a copper groundplane, interrupted as little as possible by traces on the outer layer. As indicated, the existence of currents in the supporting groundplane are essential to the operation of a small unbalanced antenna. Any gaps in

the groundplane will interrupt these surface currents and cause energy to be coupled to traces in the inner board layers. Any noise present on inner lines is also likely to be radiated from the gap. The existence of small islands in the groundplane is acceptable, but linear interruptions, especially those which interrupt current flowing radially from the antenna feed point, are to be avoided. If such features are essential, the groundplanes on the front and back of the PCB should be connected with rows of vias along each side of the interruption.

3. The position chosen should provide a generally upward-looking radiation pattern when the device is held or positioned in the orientation in which it will be used. This is a relatively easy requirement to understand when using an antenna firing off the end of the application PCB, but is less easy to interpret when the antenna is mounted on one of its faces. In this case the position of the antenna and that of its feed point will have a strong effect on the resulting polarisation and radiation patterns. For any good commercial antenna the manufacturer should be able to provide application advice which should include measured radiation pattern data for typical antenna locations and orientations, measured when the device is illuminated with an RHCP signal. An insight into this aspect of performance can be obtained using standard electromagnetic simulation software. This aspect of design is a significant trap for the unwary; the same antenna may produce either RHPC or LHCP simply by changing its position and orientation. If the chosen position produces maximum RHCP gain below the horizon, the configuration will perform far below expectations, but the reason for this will not be easily seen by a typical platform design engineer whose skill lies in multi-layer PCB layout design.
4. The transmission line connecting the GNSS antenna to the receiver should be kept as short as practicable. It is vulnerable to local noise pickup and its attenuation will impair the thermal noise performance of the system. Either surface-mounted coplanar waveguide (with ground below) or buried triplate (stripline) designs may be used with success. The line should be edged with a row of closely spaced vias on each side to constrain the RF energy within the line and to reduce the possibility of noise pickup.
5. If there are other radio transmitters on the same platform it will be necessary to estimate the magnitude of the signals they will produce at the input to the GNSS receiver. If the level is high, then it will be necessary either to move one of the antennas or to provide a bandpass filter in front of the GNSS receiver chain (including the LNA). Small low-loss SAW filters are readily available for this application.

6. Great care must be taken to avoid noise entering the antenna or its connection to the front end of the receiver. On every platform it will be necessary to filter DC supplies, signal lines and other connections to the GNSS receiver. A GNSS receiver is the most sensitive radio receiver used for any mass-market application and it requires the most thorough platform noise suppression measures if it is to work correctly. It is relatively simple to provide too much filtering on a prototype build and to remove what is found to be unnecessary. It is much more difficult to provide too little filtering and then to find ways of fitting more components during trials, especially as some of the lines involved are likely to be buried in inner layers of the PCB stack. In the case of a complex platform it may be prudent to build the GNSS receiver and antenna on a small PCB and place it on the intended host platform, carefully checking the effects of major components on the reported C/N_0 ratios. There is a significant choice between GNSS antennas that operate over a groundplane and those which require a mounting area that is groundplane free. Although an on-ground-plane antenna will cause significantly less current to flow on the reverse side of the host PCB, there will still be currents in the ground, and in the display, but they will have lower amplitudes than would be the case where the antenna directly excites them.
7. The effects of major components such as batteries and display panels are always difficult to estimate. They can be evaluated by computer modelling, but the accuracy of the results is often limited by lack of precision in the model and lack of knowledge of the noise characteristics. As an example, the designer is unlikely to know the RF impedances presented by terminations at both ends of ribbon cables connecting displays, cameras and other hardware. However, their gross effects, and the effects of grounding them to the main PCB at different points, can certainly be seen. Antenna engineers are likely to be the only members of the design team able to use electromagnetic modelling software and their efforts to encourage others to redesign their circuit layouts may be greeted with mixed enthusiasm.
8. The effects of cases made from thermoplastics – typically PC-ABS or HIPS – are usually small. If possible a small physical clearance should be allowed between the GNSS antenna and the case moulding to reduce the effects of small dimensional tolerances and also to avoid the worst loading effects of fingers supporting the case. Some paints and other surface finishes – particularly those with a shiny metallic appearance – have significant conductivity and can severely compromise both the impedance of the antenna and its effective gain; these should be considered before they are specified for use.

The worst disasters of late redesign can often be avoided by building and testing simplified models of the product, but some risk will always remain until the final prototype is tested. Any design group with no in-house antenna engineer would be well advised to work closely with an experienced antenna design house, whose knowledge will often save the design team a great deal of time and expense.

8.7.2 Evaluating the Implementation

Once a prototype device has been built, the real-world performance of the GNSS receiving system can be assessed. All standard receivers provide output data, usually in the form of 'sentences' in standard NMEA format, listing the C/N_0 ratio for each of the satellites whose signals have been acquired. With an unobstructed view of the sky, in most locations it may be expected that the receiver will lock the signals for eight or more satellites, with several having reported C/N_0 ratios well in excess of 40 dB. The TTFF should be between 40 and 60 s for the time the receiver is powered up.

If the receiver sees only two or three satellites, or the C/N_0 ratios are below expectations, the first suspicion usually falls on the performance of the antenna. An early step in investigation should be to turn off everything on the platform other than GNSS receiver, to determine whether the reported C/N_0 ratios increase with the device in this state. If they do not improve significantly (say by more than 2 dB), the most significant problem lies in the antenna and its positioning, or in the receiver front end. If they improve by more than 6 dB, then the lack of performance is being caused by platform noise, which can be investigated using a spectrum analyser fitted with a small RF probe. (Between these figures, both causes need to be addressed.)

8.7.2.1 Expected Performance

The performance of a GNSS antenna/receiver on an application requiring very small antenna dimensions and operating on a very small platform is inevitably lower than that on a well-designed platform carrying little other than the GNSS. C/N_0 ratios exceeding 45 dB from a watch tracker are unlikely, while most dedicated evaluation kits using external full-size antennas should be able to provide them with ease. The practical result of the lower figure will be that location is less accurate – it will typically rely on fewer satellites – and is also more easily lost as the user moves into a location with only a partial view of the sky, or into an indoor environment. It will take longer, or may prove

impossible, to obtain a fix after a cold start in these environments, when a more sensitive platform could succeed.

8.8 Case Studies

The following case studies come from real applications and illustrate different aspects of the matters discussed in this chapter. Most of the examples use a modified PIFA [3], which is integrated with the GNSS receiver. The wide variety of patterns that are seen on different application platforms is caused by the platform size (in wavelengths) and the major components mounted close to the antenna. Displays, batteries and other hardware both block direct radiation and modify the radiating surface flowing in the ground of the platform.

We now examine some practical examples of GNSS antennas operating on typical small user devices. These include trackers (for persons or animals), alarms, in-car cameras and smartphones. Each example has been chosen as far as possible to illustrate one aspect of the optimisation challenge. Other examples suffered multiple causes of performance loss, so they would be less interesting to study here.

With one exception, the examples make use of a single-antenna configuration – a modified PIFA approximately $28 \times 13\,\text{mm}^2$ in area and 5 mm high. This antenna is mounted above the receiver chip and associated components, and normally lies parallel to the underlying host PCB. A planar meandered dipole design was used in one example; this is mounted orthogonal to the edge of the host PCB. All examples use the same receiver chip.

8.8.1 Measurement System

The measurement system is shown in Figure 8.2. The DUT is illuminated by an RHCP signal produced by a satellite simulator and radiated from a helical antenna. The receiver associated with the antenna generates output data which includes the computed C/N_0 ratio at its input. The level of the signal is arbitrary, so the C/N_0 ratios seen here are not necessarily those which would be seen from a satellite signal, although they are generally fairly similar. The signal level is, of course, left constant during any sequence of comparative measurements. Because of the small electrical dimensions of the platforms it is necessary to decouple the cable connecting the receiver inside the DUT to the computer that records the results; this is best done using a standard quarter-wavelength choke, as ferrites tend to introduce loss at the frequencies involved. In all the tests the LNA was protected from high-level signals in the cellular radio bands

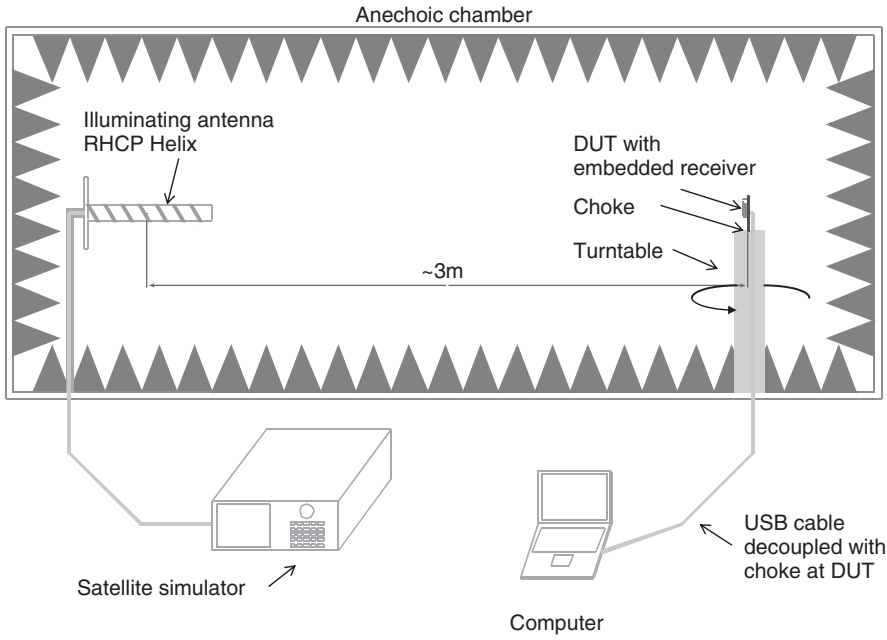

Figure 8.2 Typical arrangements for measuring GNSS device performance in an anechoic chamber.

by fitting a bandpass SAW filter at its input. The attenuation of this filter causes a small increase in system noise, but this protection is often essential.

Mounting the antenna on the application PCB, rather than placing the antenna on a separate PCB, perhaps separated from the main application board, provides a very compact solution, potentially at lower cost, but requires more care over implementation details because the antenna is inevitably closer to potential noise sources which must be quietened by screening or decoupling.

8.8.2 Case 1: Modified PIFA on Face of Small PCB

A modified PIFA is mounted on the face of an electrically small PCB ($35 \times 40\,\text{mm}^2$) with a GPRS antenna on the rear face of the same PCB. Figure 8.3 shows the arrangement. Small user devices may have very random physical orientation so the smooth, near-isotropic pattern of this device is potentially very useful. Both the GPS and cellular antennas are on-ground-plane designs, so the presence of the groundplane between the two antennas reduces their coupling – even so, their proximity is quite startling.

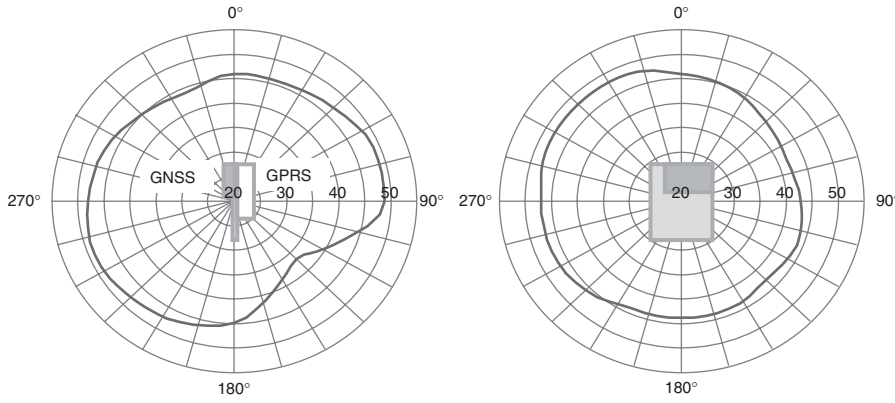

Figure 8.3 Case 1: Modified PIFA on face of small PCB. Platform dimensions: 35×40 mm^2. Smooth radiation patterns, with good sky coverage. Note close proximity of the GPRS antenna on the reverse face of the PCB.

8.8.3 Case 2: Meandered Dipole Antenna on Top Edge of Small PCB

Here a meandered dipole has been positioned at the top of a 55×48 mm^2 platform to provide it with a clear view of the sky. As may be seen in Figure 8.4, this design feature has failed to ensure that the radiation pattern is dominantly

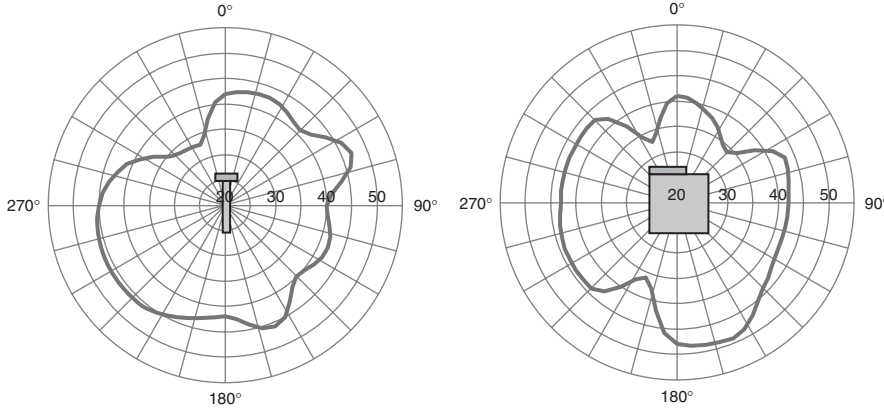

Figure 8.4 Case 2: Meandered dipole antenna on top edge of small PCB. Platform dimensions: 55×48 mm^2. Patchy upward coverage with higher gain in lower hemisphere.

upward looking. The positioning of the antenna, combined with the dimensions of the platform, has resulted in an irregular radiation pattern with significant minima in the upper hemisphere and high sensitivity in a generally downward direction. To safeguard against this outcome, the designer should either conduct some simple pattern measurements using a very rudimentary physical model of the platform – perhaps no more than an unetched PCB, an antenna, battery and display – or model the simplified structure and antenna using one of the available computer simulation packages.

8.8.4 Case 3: Modified PIFA above LCD Display on Smart-Phone-Size Device

This is an example of a platform of typical smartphone dimensions with the antenna mounted centrally above the LCD display. The initial disappointing performance (Figure 8.5, dashed line) was corrected by removing some of the groundplane below the antenna (solid line). The pattern minimum in the direction orthogonal to the display is probably unhelpful for operation with the device lying on a horizontal surface, but is probably caused by the display panel, which occupies much of the face of the PCB. Adjustments to the grounding positions on the display panel and the battery may also be helpful in optimising the radiation pattern.

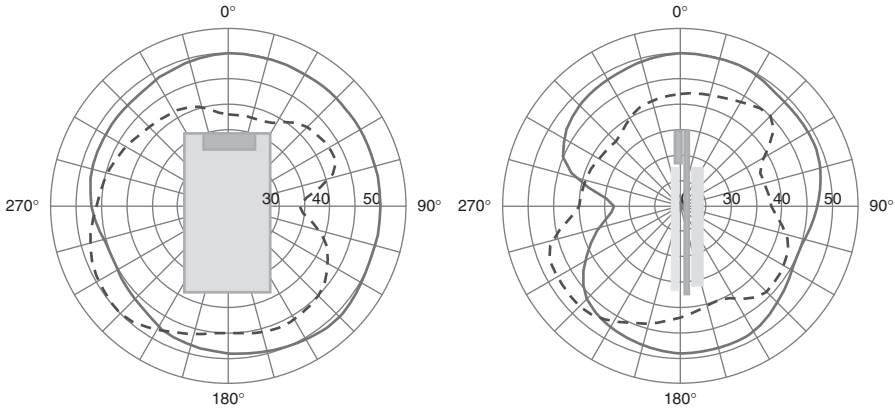

Figure 8.5 Case 3: Modified PIFA above LCD display on smart-phone-size device (dashed line) showing effect of partial groundplane removal under antenna (solid line). Platform dimensions: 55×110 mm^2, with battery in place behind PCB. Patchy upward coverage with higher gain in lower hemisphere.

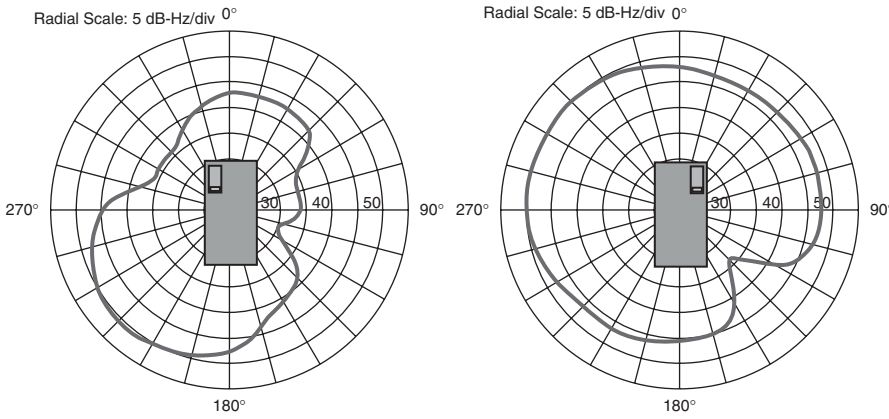

Figure 8.6 Case 4: Changes in radiation pattern of the modified PIFA when the antenna is moved from one corner of the platform to the adjacent corner.

8.8.5 Case 4: Moving Modified PIFA from One to Adjacent Corner of PCB

This is another example with a platform of suitable dimensions for a smartphone or PDA. In Figure 8.6 we see that moving the antenna from one corner of the platform to the adjacent corner – a simple translation with no associated rotation – has resulted in a radical change in the radiation pattern. In the original position (left hand plot) the polarisation was dominantly LHCP in the upward direction, with RHCP directed downwards. Moving the antenna changes the relationship between directly radiated fields and the fields created by currents flowing in the platform; in this example it has corrected the original polarisation so RHCP is now directed upwards.

This example again shows that comparatively simple experiments early in the design process can avoid substantial costs for later redesign.

8.8.6 Cases 5 and 6: Effects of Platform Electronics Noise

In Figure 8.7a we see the C/N_0 characteristics of a well-designed device with the platform firmware off (dashed line) and on (solid line).There is very little difference between the two conditions because platform noise has been well controlled.

In Figure 8.7b we see an example of poor noise design. The generally satisfactory response when the platform electronics is turned off (solid line) collapses to a very unsatisfactory response when the platform electronics is turned on. The sensitivity has fallen by around 25 dB! An expensive respin will be needed to correct this situation.

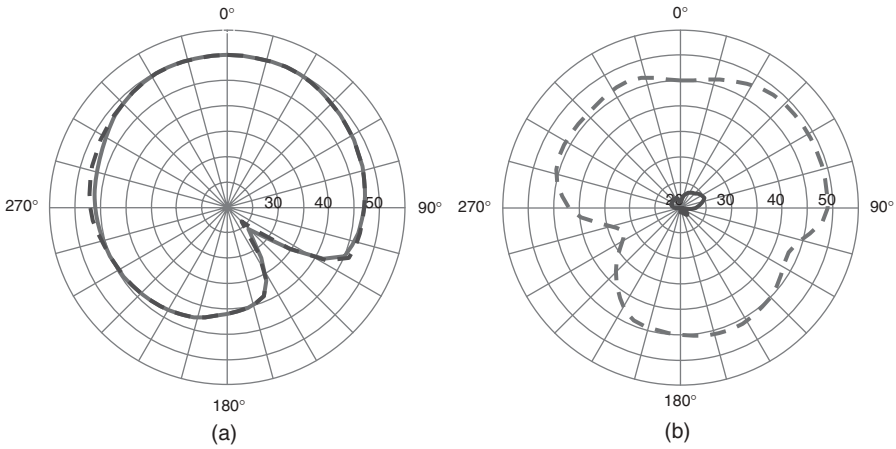

Figure 8.7 Extreme examples of performance with the platform electronics turned on (solid line) and off (dashed line): (a) Near-perfect example with no significant platform noise; (b) Example with high level of platform noise such that sensitivity is reduced by almost 25 dB.

8.9 Summary

In this chapter we have seen how simple low-cost antennas can provide adequate performance for use on a variety of handheld terminals, trackers and other simple devices. Success is achieved by using a well-designed antenna, siting it appropriately on the application and controlling locally generated noise by good PCB design.

References

1. Pathak, V., Thornwall, S., Krier, M. *et al.*, 'Mobile handset system performance comparison of a linearly polarized GPS internal antenna with a circularly polarized antenna', Antennas and Propagation Society International Symposium, Vol. 3, 22–27 June 2003, pp. 666–669.
2. Wingfield, A. and Leisten, O.P., 'Performance evaluation of small antennas for Global Positioning System (GPS)', Twelfth International Conference on Antennas and Propagation (ICAP), IEE Conference Publication No. 491, 2003.
3. UK Patent GB 2,459,020, Antenova Ltd.

Appendix A

Basic Principle of Decoding Information from a CDMA Signal

Figure A.1 shows how a spreading code of order 4 can be produced for a pair of messages to be sent via a CDMA link. This example is for illustration only, as 4 bits is not a practical length of code. Figure A.2 shows how the received signal (effectively the sum of the two signals from Figure A.1) can be decoded to reveal the two messages. The 'correlation' process is to take the spreading code used to encode the message to be decoded (in the case of GPS it is the spreading code for a particular satellite) and multiply it by the received signal. Over the length of the spreading code the result is then integrated and divided by the length of the spreading code and if a message exists a non-zero result is achieved. In the example in the second row of Figure A.2 the message $(+1, -1, +1)$ is successfully decoded. In a similar way the message sent via the second spreading code is decoded correctly in the third row of Figure A.2. In the fourth row of Figure A.2 another spreading code (which was not used to encode anything) is used and correctly shows a null message.

This is a very simple illustration and assumes that the spreading code and the received signal are synchronised (i.e. the start of the spreading code matches the start of a message frame). However, synchronisation is simply achieved

Antennas for Global Navigation Satellite Systems, First Edition.
Xiaodong Chen, Clive G. Parini, Brian Collins, Yuan Yao and Masood Ur Rehman.

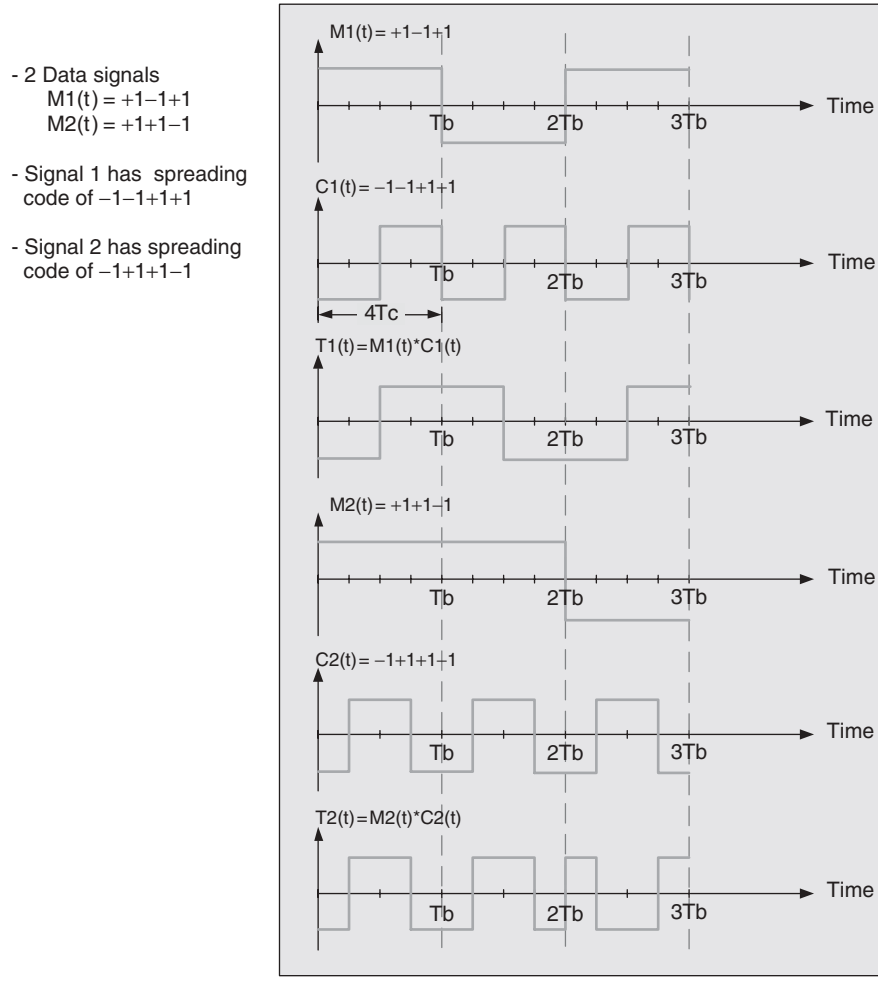

Figure A.1 Forming a simple CDMA signal with a spreading code of order 4.

by delaying the spreading code by one chip and recorrelating a frame until a non-null message is received or *N* delays have been undertaken where N is the length of the gold code. This is a process that can be rapidly undertaken even for large spreading codes by a digital signal processor.

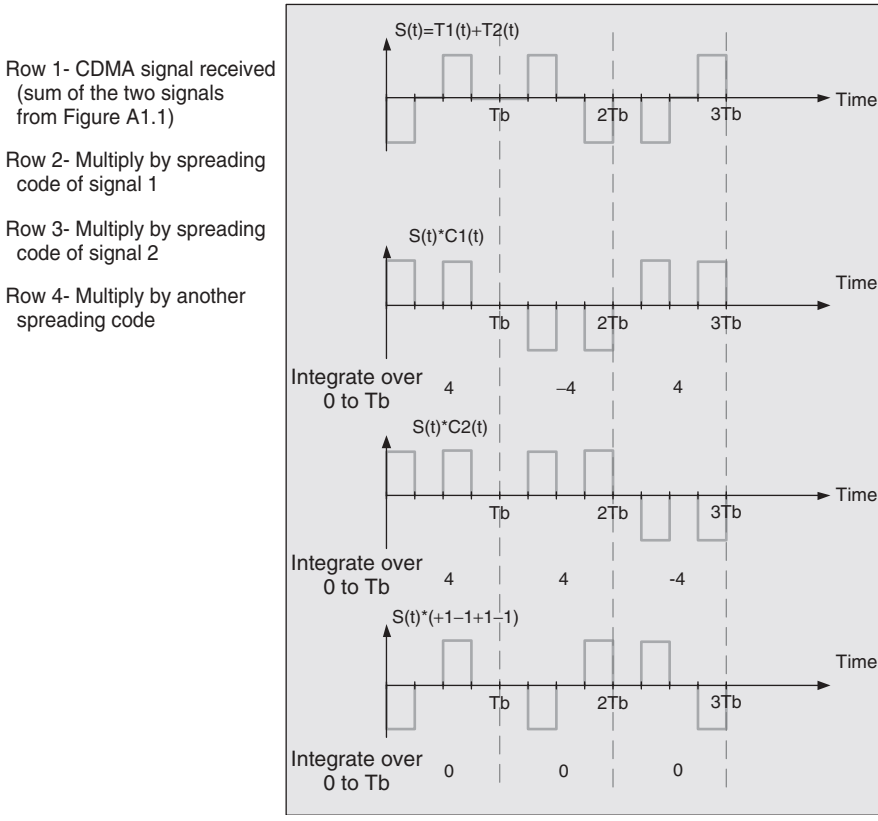

Figure A.2 Receiving the CDMA signal.

Appendix B

Antenna Phase Characteristics and Evaluation of Phase Centre Stability

The phase centre of a practical antenna varies in different azimuth and elevation angles, a phenomenon called phase centre dispersion. The antenna phase centre can only be kept relatively stable within a certain range of directions. The concepts of average phase centre, phase centre offset and phase centre variation are introduced to describe fully the characteristics of antenna phase response.

The average phase centre of an antenna is defined as the mean location of the antenna phase centre over a certain range of directions. The antenna reference point (ARP) is defined as the geometric centre of the antenna. The difference between the average phase centre and the antenna reference point is regarded as the phase centre offset (PCO). The offset between the phase centre in a particular direction and the average phase centre is known as phase centre variation (PCV) in that direction. These three parameters are illustrated in Figure B.1.

Typical antenna installations for surveying use the ARP as the reference point for phase measurements, so a correction must be made to allow for the PCO in the direction of the satellite signals. The average phase centre, or PCO, can be found by minimising the cost function:

$$\sum (\mathrm{PCV})^2 = \mathrm{Min}$$

In order to improve the reliability and accuracy of the GNSSs, we have to take into consideration the effect of antenna phase centre stability.

Antennas for Global Navigation Satellite Systems, First Edition.
Xiaodong Chen, Clive G. Parini, Brian Collins, Yuan Yao and Masood Ur Rehman.

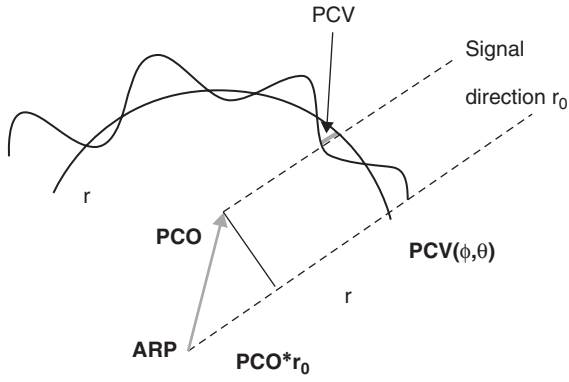

Figure B.1 Illustration of ARP, PCO and PCV [1]. Reproduced by permission of © 2010 IEEE.

B.1 Evaluation of Phase Centre Stability

As shown in Figure B.1, we can use the average phase centre as the origin to calculate the PCV as a function of azimuth and elevation angle. The phase centre stability is defined as half the PCV peak value across the main beam of the antenna. It can be expressed as

$$\Delta m = \frac{1}{2} \cdot \frac{\Delta\varphi}{360} \cdot \lambda \tag{B.1}$$

where Δm is phase centre stability, $\Delta\varphi$ is the peak value of PCV and λ is the corresponding wavelength.

B.2 Determination of the Average Phase Centre

A simple and practical method of computing average phase centre may be based on either simulated or measured antenna phase patterns [1]. We will use a least squares method and start with the equation of spherical phase expansion from its origin located at point phase centre (x, y, z) as shown in the equation below. A term c is added that can represent some constant. Azimuth and elevation angles are denoted as θ and ϕ, and the wavelength is λ. Thus

$$\text{Phase}(\phi, \theta) = \frac{2\pi}{\lambda}(x \cdot \cos\phi \sin\theta + y \cdot \sin\phi \sin\theta + z \cdot \cos\theta) + c$$

or in matrix form

$$F(\phi,\theta) = \frac{2\pi}{\lambda}[\cos\phi\sin\theta \;\; \sin\phi\sin\theta \;\; \cos\theta] \cdot \begin{bmatrix} x \\ y \\ z \\ c \end{bmatrix} \tag{B.2a}$$

$$\Rightarrow F = M \cdot P \tag{B.2b}$$

To find phase centre P, we use Equation B.2b, hence

$$P = M^{-1} \cdot F \tag{B.3}$$

$$\begin{bmatrix} x \\ y \\ z \\ c \end{bmatrix} = \frac{\lambda}{2\pi}\,[\cos\phi\sin\theta \;\; \sin\phi\sin\theta \;\; \cos\theta]^{-1} \cdot F(\phi,\theta) \tag{B.4}$$

We are now ready to assemble a solution matrix using either simulated or measured data obtained from sampling the phase pattern of the antenna to obtain a mean value of PCO:

$$\begin{bmatrix} x \\ y \\ z \\ d \end{bmatrix} = \frac{1}{2\pi} \cdot \begin{bmatrix} \cos\phi_1\sin\theta_1 & \sin\phi_1\sin\theta_1 & \cos\theta_1 & 1 \\ \cos\phi_2\sin\theta_1 & \sin\phi_2\sin\theta_1 & \cos\theta_1 & 1 \\ \vdots & \vdots & \vdots & \vdots \\ \cos\phi_N\sin\theta_1 & \sin\phi_N\sin\theta_1 & \cos\theta_1 & 1 \\ \cos\phi_1\sin\theta_2 & \sin\phi_1\sin\theta_2 & \cos\theta_2 & 1 \\ \vdots & \vdots & \vdots & \vdots \\ \cos\phi_N\sin\theta_K & \sin\phi_N\sin\theta_K & \cos\theta_K & 1 \end{bmatrix} \cdot \begin{bmatrix} \varphi_1(\phi_1,\theta_1)\cdot\lambda \\ \varphi_2(\phi_2,\theta_1)\cdot\lambda \\ \vdots \\ \varphi_N(\phi_N,\theta_1)\cdot\lambda \\ \varphi_{N+1}(\phi_1,\theta_2)\cdot\lambda \\ \vdots \\ \varphi_{N\cdot K}(\phi_N,\theta_K)\cdot\lambda \end{bmatrix} \tag{B.5}$$

where

$$\phi_i = 0 : 2\pi/N : 2\pi, \quad \theta_i = 0 : \pi/2K : \pi/2 \;\; \text{(upper hemisphere)}$$

Reference

1. Waldemar, K., 'Antenna phase center effects and measurements in GNSS ranging applications', 14th International Symposium on Antenna Technology and Applied Electromagnetics (ANTEM) & the American Electromagnetics Conference (AMEREM), Ottawa, Canada, 5–8 July 2010.

Index

Antennas for Global Navigation Satellite Systems, First Edition.
Xiaodong Chen, Clive G. Parini, Brian Collins, Yuan Yao and Masood Ur Rehman.